COASTAL OCEAN MODELING USING VARIATIONAL METHODS FOR FRESHWATER DISPERSAL STUDY, DATA ASSIMILATION AND OBSERVING SYSTEM DESIGN

by

WEIFENG ZHANG

A dissertation submitted to the

Graduate School-New Brunswick

Rutgers, The State University of New Jersey

In partial fulfillment of the requirements

For the degree of

Doctor of Philosophy

Graduate Program in Oceanography

Written under the direction of

Dr. John L. Wilkin

And approved by

_____

_____

_____

_____

_____

New Brunswick, New Jersey

October, 2009

ABSTRACT OF THE DISSERTATION

Coastal ocean modeling using variational methods for freshwater dispersal study, data assimilation and observing system design

By WEIFENG ZHANG

Dissertation Director:

Dr. John L. Wilkin

Coastal oceans as highly productive components of the global ocean play crucial roles in global carbon cycle and climate change. The wide continental shelf off US east coast is a typical coastal environment that serves as a buffer zone between human activities and open oceans. This thesis investigates the dispersal pattern of Hudson River outflow in the New York Bight (NYB). It applies adjoint sensitivity, Incremental Strong Constraint 4D Variational Data Assimilation (IS4DVAR) and representer-based optimal observation to integrate coastal ocean modeling and observation capabilities.

Firstly, analysis of a 2-year model simulation identifies three freshwater pathways: along (i) the New Jersey coast, (ii) the Long Island coast, and (iii) a Mid-shelf Pathway. It is shown that the New Jersey coast Pathway dominates winter months and the Mid-shelf Pathway summer months. It is also demonstrated that wind is the primary force for

spreading freshwater into mid- and outer-shelf and presence of the Hudson Valley strengthens freshwater recirculation in the New York Apex area. Secondly, the Constituent-oriented Age and Residence time Theory is implemented to simulate the age and residence time of the Hudson River plume. Analysis shows strong seasonality of surface mean age and residence time consistent with seasonal variation of the circulation. Time series analysis shows that spatial and temporal variations of the time scales in NYB are largely buoyancy- and wind-driven.

Thirdly, adjoint sensitivity analysis applied on the New Jersey inner shelf identifies water sources and quantitatively compares the contributions of different variables to a chosen oceanic process. Fourthly, IS4DVAR is used to assimilate observational data collected by all instrument types during spring 2006. It reduces the model-observation misfit by 60% and improves forecast of temperature, salinity and velocity. Finally, a representer-based optimal observation system is applied to identify the optimal sampling locations for predicting salt transport within the Hudson Shelf Valley. The system is then used to compare the influence area of existing observations.

This work prototypes the integration of observation and modeling in a coastal environment and demonstrates the use of traditional and variational tools to reveal the physical processes in a shelf region.

Acknowledgements

There are many people to whom I owe gratitude for this dissertation. Firstly, I am indebted to my advisor, Dr. John Wilkin, for his guidance, encouragement and support throughout my time at Rutgers. He taught me not only academic knowledge but the attitude to science, enthusiasm, objectiveness and preciseness in particular. His generosity, kindness and sense of humor also impressed me deeply and will affect me through the rest of my life. I am extremely grateful to have John as my advisor and also a friend.

I would like to express sincere gratitude to my committee, Dale Haidvogel, Julia Levin, Andrew Moore, and Javier Zavala. Their overseeing of my doctoral work and insightful comments on my dissertation improved this work substantially. Their support over the years made my graduate school life much joyful.

I am very grateful to Dr. Hernan Arango for his guidance on using ROMS and choosing research topics. This dissertation is really built upon more than 10 years' efforts by all the ROMS developers, among whom Hernan serves as the center. Without their hard work and generosity over the years, this dissertation would be impossible.

I would like to acknowledge Dr. Robert Chant for his encouragement and the inspiring conversations we had over the years. As an academic uncle of mine, Bob has always been supportive to my ideas. His sense of humor also made my time in IMCS much enjoyable.

I would also like to thank other colleagues over the years. The technical support from David Robertson, John Evans and Eli Hunter helped my research tremendously. The initial guidance of using ROMS from Dr. Byoung-Ju Choi made that experience much less

painful. The friendship with Gregg Foti brought a lot of fun to the office we shared for 3 years. The numerous discussions with Dr. Greg Gerbi improved the dissertation.

I am also very grateful to the Coastal Ocean Observation Laboratory (COOL) at Rutgers for providing me all the data. Without their data, much of my PhD research would be impossible. COOL also offered me many opportunities to learn operating numerous instruments, from which I realize the difficulties of ocean observation and start to appreciate more the observational data.

I would also like to thank all the graduate students at IMCS, especially Yonghua Chen, Grant Law, Felisa Wolfe-Simon, Matt Oliver, Yongcheng Ji, Alex Kahl, Sindia Sosdian, Jason Sylvan, Naomi Fleming, Carrie Fraser, Brian Gaas, Hui Liu, Rachel Sipler, Donglai Gong, Katye Altieri, Jaimie Tirado, Michele LaVigne, Eleni Anagnostou, Nicole Raineault, Joe Jurisa, Yi Xu, Maria Aristizabal, and Dove Guo, for all the happy time we spent together.

My deepest appreciation goes to my family, who supported me throughout this journey with their unfailing love, faith and patience: my father, Xiangnian Zhang, my mother, Yuqin Wang, my sister, Weihong Zhang, my brother, Weidong Zhang, and other family members. Finally, I dedicate this dissertation to my wife, Jing Chen, whose love and encouragement over the years are immeasurable, and my baby boy, Ray Yanrui Zhang, whom I love deeply.

Table of Contents

Lists of Tables

List of Figures

CHAPTER 1. INTRODUCTION

1.1. New York Bight

The wide continental shelf off US east coast is a major component of the global ocean in terms of the carbon cycle (Hofmann et al. 2008) and primary productivity (Schofield et al. 2008b). It is an important place for human activities, like fishing and recreation. The New York Bight (NYB) is the part of the shelf that is half enclosed by the New Jersey and Long Island coasts and heavily influenced by anthropogenic forces through river discharge. Studies of the physical and biogeochemical processes in the NYB will therefore contribute to the understanding of the changes that coastal oceans are undergoing in the context of climate change.

In the NYB, bathymetry, tides, freshwater input, air-sea exchange, and large-scale shelf-wide circulation all interact to create a coastal zone with complicated dynamics and short time and space scales of variability (Chant et al. 2008a, Choi and Wilkin 2007, Yankovsky 2003). It has been the subject of numerous studies, both modeling and observational (Castelao et al. 2008a, Chant et al. 2008a, Chant et al. 2008b, Johnson et al. 2003, Tilburg and Garvine 2003, Wilkin et al. 2005, Wong 1999, Yankovsky et al. 2000), with most of them focusing on the influences of the Hudson River discharge and winds on the local circulation. The Hudson River is a major supplier of freshwater, nutrients and suspended matter to the NYB and the dispersal pattern of the river plume in the shelf has dramatic influences on local physical and biochemical processes. Despite the cited studies, the overall picture of the dispersal pattern of the Hudson River plume in the NYB and the detailed effects that different forces have on the dispersal pattern are still largely unknown.

The effects that wind-driven coastal upwelling and down-welling have on the Hudson River plume in the apex area of the NYB have been studied intensively, but studies of the influence of winds on the pathways and eventual fate of the freshwater are lacking. Southwestward along-shelf mean currents of approximately 5 cm s^{-1} occur in the NYB (Beardsley and Boicourt 1981, Chapman and Beardsley 1989) and presumably steer the river plume once it reaches the mid- and outer-shelf. But details of the effects of the ambient current are still unknown. One distinct feature in the NYB is the Hudson Shelf Valley (HSV) which cuts through the entire shelf from the shelf break to the mouth of the Hudson River. It is expected that the HSV affects local circulation and plume dispersal (Chant, personal communication), but few systematic studies exist. The first two parts of this dissertation aim at these unknown mechanisms and offer a thorough description of the dispersal pattern of the Hudson River plume in the NYB.

The NYB is one of the most well-observed coastal areas on the world and has seen pioneering deployments of new observing instruments and platforms, including Autonomous Underwater Vehicles (gliders), High Frequency (HF) coastal radar system, and cabled observatory moorings. The NYB has also been studied through the comprehensive use of multiple satellites together with shipborne and moored instruments during a series of intensive multidisciplinary observational programs, e.g., LEO-15 (Long-term Ecosystem Observatory), LaTTE (Lagrangian Transport and Transformation Experiment), and MARCOOS (Mid-Atlantic Regional Coastal Ocean Observation System). Monitoring of water conditions in the NYB using these observing platforms has become a routine operation in the Coastal Ocean Observation Laboratory (COOLroom) at Rutgers University (Schofield et al. 2008a, Schofield et al. 2007). Meanwhile, numerical

simulations with Regional Ocean Modeling System (ROMS) have also been carried out to study the physics of the region (Choi and Wilkin 2007, Wilkin et al. 2005) and forecast the ocean conditions in real time.

The operation of the instruments on a quasi-continuous basis and the real-time simulation of ROMS makes the NYB an ideal location to learn how to integrate observation and modeling capabilities. The last three parts of this dissertation demonstrate how to employ variational methods to gain an understanding of coastal oceanic dynamics, and prototype a comprehensive integrated coastal ocean predictive capability that contributes directly to building a coastal ocean forecast and observation design system for the NYB.

1.2. Variational methods

Derived from control theory (Bertsekas 1982), variational methods have been used for decades in numerical weather prediction for applications such as data assimilation. The use of variational methods in oceanography is relatively new but has under-gone significant increase recently. One crucial component that underlies the variational approach is the adjoint model, or more precisely, the adjoint of a tangent linear approximation to a conventional forward ocean simulation model. Besides data assimilation, there are many other applications of the adjoint model that include parameter estimation, general stability analysis, sensitivity analysis, and optimal observation design. These are all useful tools for the study of oceanic processes and dynamics.

Regional Ocean Modeling System (ROMS) is a finite difference numerical ocean model. It utilizes a terrain-following coordinate system in the vertical that allows high

resolution in shallow shelf seas. Details of the computational kernel of nonlinear ROMS are described by Shchepetkin and McWilliams (1998, 2003, 2005) and Haidvogel et al.(2008). The adjoint and tangent linear component models in ROMS, together with drivers that link these models for adjoint sensitivity, optimal perturbation, 4-Dimensional Variational (4DVAR) data assimilation and observation sensitivity have been developed recently by the ROMS Adjoint Group (Moore et al. 2004) and used in numerous applications (Broquet et al. 2009, Di Lorenzo et al. 2007, Moore et al. 2008, Moore et al. 2004, Powell and Moore 2008, Powell et al. 2008, Powell et al. 2009, Veneziani et al. 2009). In this work, four of the ROMS adjoint model applications, namely adjoint sensitivity, residence time, Incremental Strong-constraint 4DVAR (IS4DVAR) and representer-based optimal observation, are applied to the NYB to test the theories, machineries, and applicability of these new analysis tools.

The adjoint sensitivity application uses the adjoint model to determine the sensitivity of selected model features to variations of initial conditions, boundary conditions, and surface forcing (Errico and Vukicevic 1992, Moore et al. 2008). The sensitivity signal can then be used to locate the dynamical upstream of the selected features and quantitatively compare the contributions of different possible sources to variation of the features.

In the residence time simulation, an adjoint of an age tracer equation (similar to a passive tracer conservation equation but with an additional aging term) is utilized to obtain the averaged duration it takes the water *at any time and any location* to be flushed out of a pre-defined control volume (Delhez 2006, Delhez et al. 2004).

IS4DVAR is one of the Data Assimilation (DA) methods that take the full dynamics into consideration while adjusting model control variables to fit observations (Courtier et

al. 1994, Powell et al. 2008, Weaver et al. 2003). Adjoint models are utilized here to provide the direction of the minimum search in a conjugate gradient algorithm. The algorithm is to find the optimal adjustment to model control variables that give the minimum model-observation mismatch.

Representer, the outcome of an adjoint model integration followed by a tangent linear model integration, gives the covariance of a selected model feature with model prior, present and posterior states (Bennett 2002). This covariance information can then be used to identify the most effective observation locations for more thorough understanding of the selected feature and to compare the influences of different observation strategies in a DA and forecasting system.

The applications of these four methods in this work will be the first test of their practical strengths and weaknesses on a broad, shallow, continental shelf. The extensive observational data already available for the NYB, and the many active projects in this region, afford the opportunity to immediately demonstrate the utility of the analysis methods for DA and observing system design for integrated coastal ocean observing systems of the type now being widely deployed internationally.

CHAPTER 2. PATHWAYS OF THE HUDSON RIVER PLUME

2.1. Introduction

Fresh water discharged into the coastal ocean from rivers and runoff is often observed to be incorporated into a narrow coastal current that is typically a few internal Rossby radii wide and rapidly transports freshwater down shelf, which appears similar to the classical model of buoyant outflow onto coastal oceans (Garvine 1999). However, more recent theoretical, modeling and laboratory studies (Avicola and Huq 2003b, Fong and Geyer 2002, Nof and Pichevin 2001) revealed a tendency for the formation of a recirculating bulge structure in the vicinity of the outflow in the absence of wind and alongshore current. In reality, the outflow pattern depends on outflow angle (Avicola and Huq 2003a, b, Garvine 1999), wind forcing (Fong and Geyer 2001, García Berdeal et al. 2002, Lentz and Chapman 2004), ambient current (Fong and Geyer 2002, García Berdeal et al. 2002, Hickey et al. 2005), tides, and local topography. These factors and forcing modify the pathways of the river plume and can make it similar to the classical theory. Given the temporal variation of some of the forcing, freshwater pathways are often highly mobile, and the unsteady freshwater transport pathways have important ecological implications regarding contaminant, larval, and nutrient transport (Cahill et al. 2008, Ciotti et al. 1995, Tilburg et al. 2005). Moreover, the details of freshwater dispersal processes can affect ocean stratification and parameterization of these processes impacts climate model results (Garvine and Whitney 2006).

In this study I use a numerical model to elucidate processes dispersing fresh water discharged from the Hudson River across the NYB. As mentioned in Chapter 1, southwestward along-shelf mean currents of approximately 5 cm s^{-1} occur in the NYB (Beardsley and Boicourt 1981, Chapman and Beardsley 1989). An analysis combining a simple steady model of the shelf-wide momentum balance and historical long-term moored current meter data (Lentz 2008) indicates that the vertically averaged along-shelf current is proportional to water depth, and hence the transport increases quadratically moving offshore. This suggests that while the southwestward mean flow may steer the Hudson's outflow once it reaches the outer shelf, on the inner shelf and particularly in the apex of the New York Bight in the shadow of Long Island, the ambient flow is relatively weak given its depth and its impact on fresh water pathways is unclear.

Observational and modeling studies have described a variety of freshwater transport pathways on the inner shelf and the NYB apex. For example, several studies describe the role of coastally trapped currents (Johnson et al. 2003, Münchow and Chant 2000, Yankovsky and Garvine 1998) while others note that the outflow is susceptible to bulge formation and is highly responsive to wind forcing (Chant et al. 2008a, Choi and Wilkin 2007). Chant et al. (2008a) presented evidence for rapid cross-shelf transport of the Hudson River injected freshwater during early summer. Relatively swift cross-shelf mixing is also evident in repeat autonomous coastal glider transects (Castelao et al. 2008a, Castelao et al. 2008b) that show the expansion of low salinity water over the entire shelf during summer months, and the cross-shelf transport is correlated with upwelling wind that dominates the NYB during summer months. This cross-shelf transport over summer is consistent with Mountain's (2003) analysis of historical hydrographic data that revealed

significant annual cycles of shelf water salinity in the NYB with a summer salinity minimum. However, the mechanisms that drive freshwater dispersal to mid-shelf and its subsequent fate on the mid- and outer-shelf are not fully known. One explanation given is that a fast cross-shelf pathway is created by upwelling favorable winds that drive short-term freshwater extension events (Castelao et al. 2008a), but beyond this there have been few studies that trace the fate of the river plumes in the region after their initial entry into shelf waters. The major objectives of this chapter are to characterize the shelf-wide spreading of freshwater input from Hudson River, describe its seasonal variability, and elucidate the dynamics that drive the variability. The Hudson River discharge has high levels of nutrients, phytoplankton, dissolved organic matter and contaminants, and characterizing its dispersal is of fundamental importance to regional studies of biogeochemical process.

The outline of this chapter is as follows: Section 2.2 introduces the model configurations and verification; Section 2.3 presents the simulated mean momentum dynamics, and the corresponding mean freshwater dispersal patterns are given in Section 2.4. In Section 2.5, the temporal variation of the freshwater transport on NYB is presented and discussed. The results are summarized in Section 2.6.

2.2. Model Configuration and Comparison to Observations

The model domain shown in Figure 2.1 covers the New Jersey coastal area from eastern Long Island to south of Delaware Bay and from the coast to approximately the 70-m isobath on the continental shelf. Two rivers, the Hudson and Delaware, are included. The model has 30 vertical layers and horizontal resolution of about 1 km. Chapman (1985)

and Flather (1976) open boundary conditions are used for sea level elevation and the barotropic component of velocity on the model perimeter, respectively. These conditions impose both a remotely forced, along-shelf mean flow described below, and tidal harmonic variability (7 components: K1, O1, Q1, M2, S2, N2, K2) extracted from a regional ADCIRC simulation (Mukai et al. 2002). For 3-dimensional velocity and tracers, tests comparing Orlanski-type radiation (Orlanski 1976) and simple 'gradient' conditions revealed little difference for the mean circulation and freshwater dispersal. All the results presented here are from simulations with gradient open boundary conditions for 3D velocity and tracers. To include the remotely forced, along-shelf currents associated with the large-scale pressure gradient I prescribed depth averaged normal flows on the open boundaries based on the water depth/flow speed linear relationship deduced by Lentz (2008). The normal flow on the off-shore boundary was smoothed to suppress the effect of small-scale undulations of the local topography and also to get a better fit with the CODAR data. The normal flow on the northeastern boundary was adjusted to conserve the total volume of the model domain, and the gradient of depth-averaged normal flow with respect to depth was preserved. In this study, the ambient current is assumed to be steady.

The model applies bulk formulae (Fairall et al. 2003) using marine boundary layer winds, temperature, humidity, and pressure from the North America Regional Reanalysis (NARR) (Mesinger et al. 2006), and ROMS sea surface temperature and current to compute air-sea fluxes of momentum and sensible, latent, and longwave heat. Quadratic bottom drag was used in all simulations with a drag coefficient of 0.003. It was found that results were insensitive to a bottom drag because shelf circulation and freshwater dispersal were similar in simulations with and without tides as will be discussed later in the chapter.

The river discharge was obtained from USGS Water Data (U. S. Geological Survey 2007) and modified to include ungauged portions of the watershed following Chant et al. (2008a). To avoid the ambiguity of reference salinity for ocean water in the NYB, and also to isolate the Hudson River from other sources of freshwater in the model, a passive tracer with unit concentration was introduced in the modeled Hudson River source. Following the simulated passive tracer concentration gives an unambiguous measure, anywhere in the model domain, of the volume fraction of water contributed by the Hudson River freshwater outflow. The model is initialized with zero 'freshwater' Hudson tracer concentration everywhere. Three-year-duration simulations were conducted with the first year used as a spin-up period; results presented here are from the analysis of the final two years of each simulation.

Five different simulations are discussed here. The first, with all the previously mentioned forces applied, is named the Full Physics Simulation (FPS). Four additional simulations were carried out to investigate the impact of remotely-forced along-shelf current, wind, tides, and the presence of the Hudson Shelf Valley (Figure 2.1), on the pattern and dynamics of freshwater spreading and mean circulation. The approach followed is to withdraw each of these factors individually from the FPS. The case with wind, shelf valley and tides but no along-shelf mean current is termed the no ambient-current simulation (NAS); the case with ambient current, valley, tides but no wind is the no-wind simulation (NWS); the case with along-shelf current, wind and tides, but with the model bathymetry altered to fill in the Hudson Shelf Valley, is called the no-valley simulation (NVS). For completeness, I also conducted a simulation with ambient current, wind and the original bathymetry, but omitted the tides. This no-tide simulation (NTS) is

discussed only partially in the interests of brevity. The other simulations are discussed in detail.

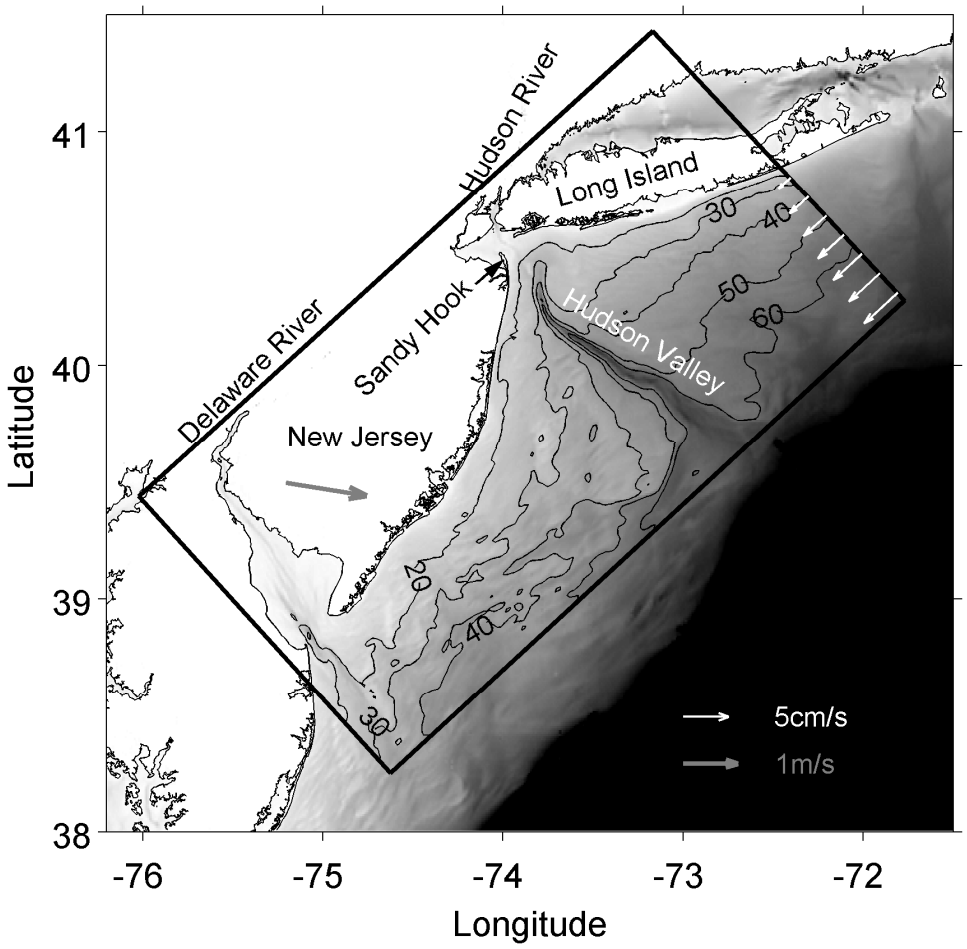

Figure 2.1. Bathymetry of the New York Bight (grayscale), mean wind over this area (gray arrow on land) over 2-year period 2005-2006, and barotropic inflow boundary condition (white arrows) on the northeast boundary of the model domain. The black frame indicates the model domain and contours are model isobaths in meters. Scale vectors for wind and inflow boundary velocity are given at the lower right corner.

Before proceeding to an analysis of the results, it should first be established that the full physics (FPS) modeled circulation has acceptable fidelity with respect to relevant observations. This study focuses on transport pathways of the buoyant freshwater discharge from the Hudson River, so the veracity of the modeled surface velocity field is a key requirement.

Throughout much of the NYB region we have available 2 to 5 years of surface current observations from land-based CODAR (Coastal Ocean Dynamics Applications Radar) high-frequency radar systems (Kohut et al. 2006a). Figure 2.2 compares the 2-year (2005 -2006) mean surface current from model and CODAR. The observed mean current is plotted only at locations where data are available for more than 70% of the time; the model results plotted are limited to the same area to aid comparison. Both model and observations show strong southward flow to the south of the mouth of the Hudson Shelf Valley. The triangular shaped zone of strong flow is somewhat more compact, stronger and located closer to the Valley in the model than in observations. This discrepancy may be due in part to the differing resolution of model and observation: 1 km in model and 10 km at this range for CODAR. Nevertheless, the pattern correlation coeffcient between the modeled and observed mean surface current is about 0.56 and the overall correspondence in pattern, direction and location is good.

To evaluate the simulated temporal variability, time series of the modeled and observed daily-averaged radial velocity across the arc depicted in Figure 2.2 are plotted in Figure 2.3. The arc is centered on the CODAR site at Sandy Hook (indicated by the star symbol in Figure 2.2) which measures the radial current speed across the arc directly, with somewhat greater accuracy than CODAR vectors derived from pairs of sites. In the analyses that

follow, freshwater transport across concentric pathways at varying range from Sandy Hook will also be presented. Figure 2.3 shows many similarities in model and observation: velocity south of the Hudson Shelf Valley is generally outgoing and to the north of the valley incoming; the timing and duration of the flow events are consistent in model and observation. A statistically significant cross-correlation of 0.69 is obtained between modeled and observed radial velocity in a 50-km wide band over the shelf valley where the CODAR observations have the most consistent availability. There are some issues regarding potential bias in the calculation of daily averaged CODAR values because sometimes, at some locations, there is only a handful of 1-hourly interval CODAR observations available to contribute to the 1-day average window, and the data gaps appear to correlate with low sea state and low current magnitude. Furthermore, the spatial resolution of model and observations differ. Despite these possible limitations to the model-data comparison, I feel that the model captures the temporal variability of the surface current well, and that, overall, the model is valid for the statistical long-term average simulation of freshwater spreading in the NYB.

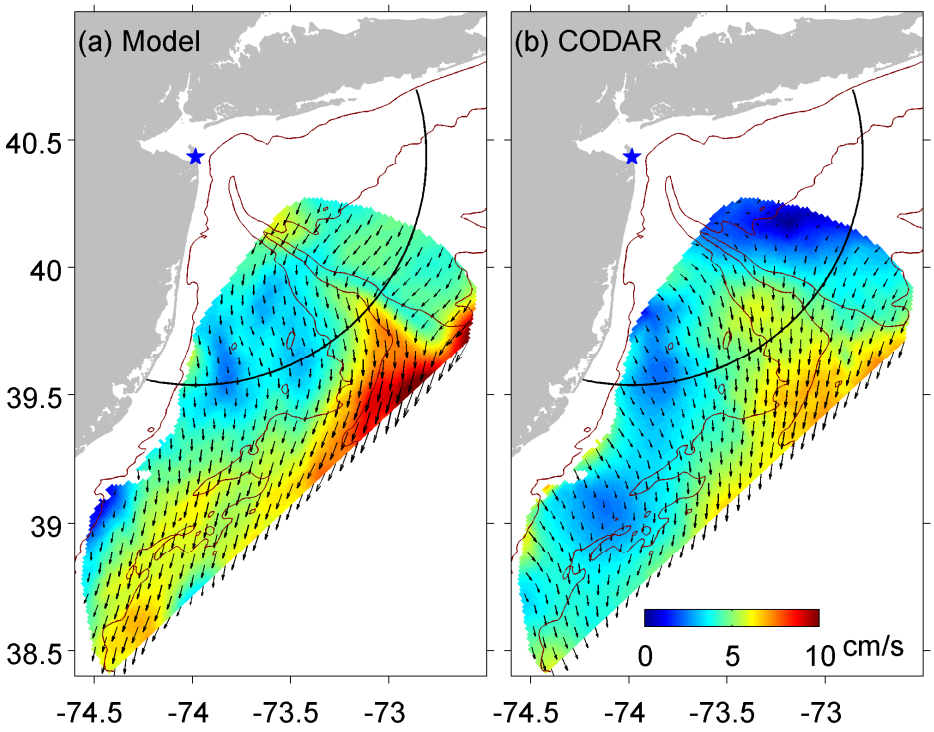

Figure 2.2. (a) Modeled and (b) observed mean surface current over the 2-year period 2005-2006. Color represents current magnitude and the arrows depict the direction. Red contours are 20 m, 40 m, and 60 m isobaths. The arcs of radius 100 km are centered at Sandy Hook (star symbol) and are used for the comparison of radial velocity in Figure 2.3.

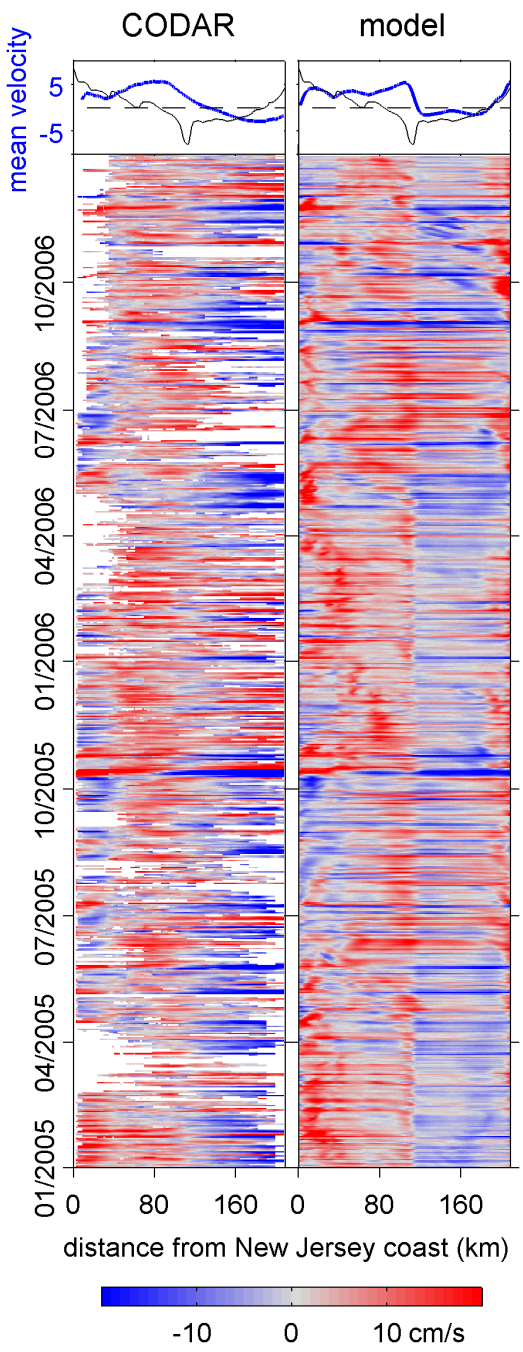

Figure 2.3. The time series (color plots) and 2-year mean (blue lines in the top panels) of modeled and observed radial velocity on the arc in Figure 2.2. Positive velocity is outgoing. Black lines in the top panels are the bathymetry along the arc with the y-axes spanning 0 to 80 meters.

2.3. Mean Dynamics

2.3.1. Sea Surface Height

Mean sea surface height (SSH) and surface current over the 2-year period for all the simulations are given in Figure 2.4. SSH contours (Figure 2.4a-d) generally follow isobaths and show a recirculation pattern in the NYB apex .The mean SSH pattern differs substantially between the different simulations. In the FPS case (Figure 2.4a), SSH contours are spaced closely on the mid- and outer-shelf with a riverward detour over the shelf valley. Without the ambient current (NAS) (Figure 2.4b), the SSH variation from coast to outer-shelf is three times weaker than in the FPS case. This shows that the remotely forced along-shelf circulation has a significant impact on the local mean sea level elevation on the mid- and outer-shelf, and this SSH variation is directly related with the surface mean geostrophic current that is described further in Section 3c. From the comparison of the FPS and NAS cases we can infer that about 75% of the local mean sea surface gradient, and therefore surface geostrophic current, is caused by the remotely forced shelf-wide circulation; it will be shown the remaining 25% is locally generated.

In the NWS case the mean SSH (Figure 2.4c) has a similar pattern to that in FPS, but the cross-shelf sea level gradient in NWS is much higher with SSH contours closer to each other on the inner- and mid-shelf. Given the absence of wind-driven lateral mixing of the freshwater, a stronger cross-shelf density gradient is expected that would cause stronger thermal wind and, ultimately, stronger sea level gradient across the shelf. This suggests that the locally generated geostrophic balance is largely driven by the influence of river discharge on the cross-shelf density gradient.

In the no-valley simulation (NVS) (Figure 2.4d), the mean SSH contours no longer detour over the valley on the mid- and outer-shelf, though they do still diverge somewhat on the broadest part of the shelf south of the shelf valley. Meanwhile, at the river mouth, the almost closed recirculation pattern trapped between the valley and the Long Island coast in FPS becomes a jug-handle-shaped bulge next to the New Jersey coast, which echoes the results of Fong and Geyer (2002) for idealized simulations of the freshwater bulge at a river mouth on a straight coast in the absence of an ambient current. This suggests that the Hudson Shelf Valley perturbs the surface current shoreward on the mid- and outer-shelf, traps freshwater on the north side of the valley in the apex area and forms a closed recirculation there.

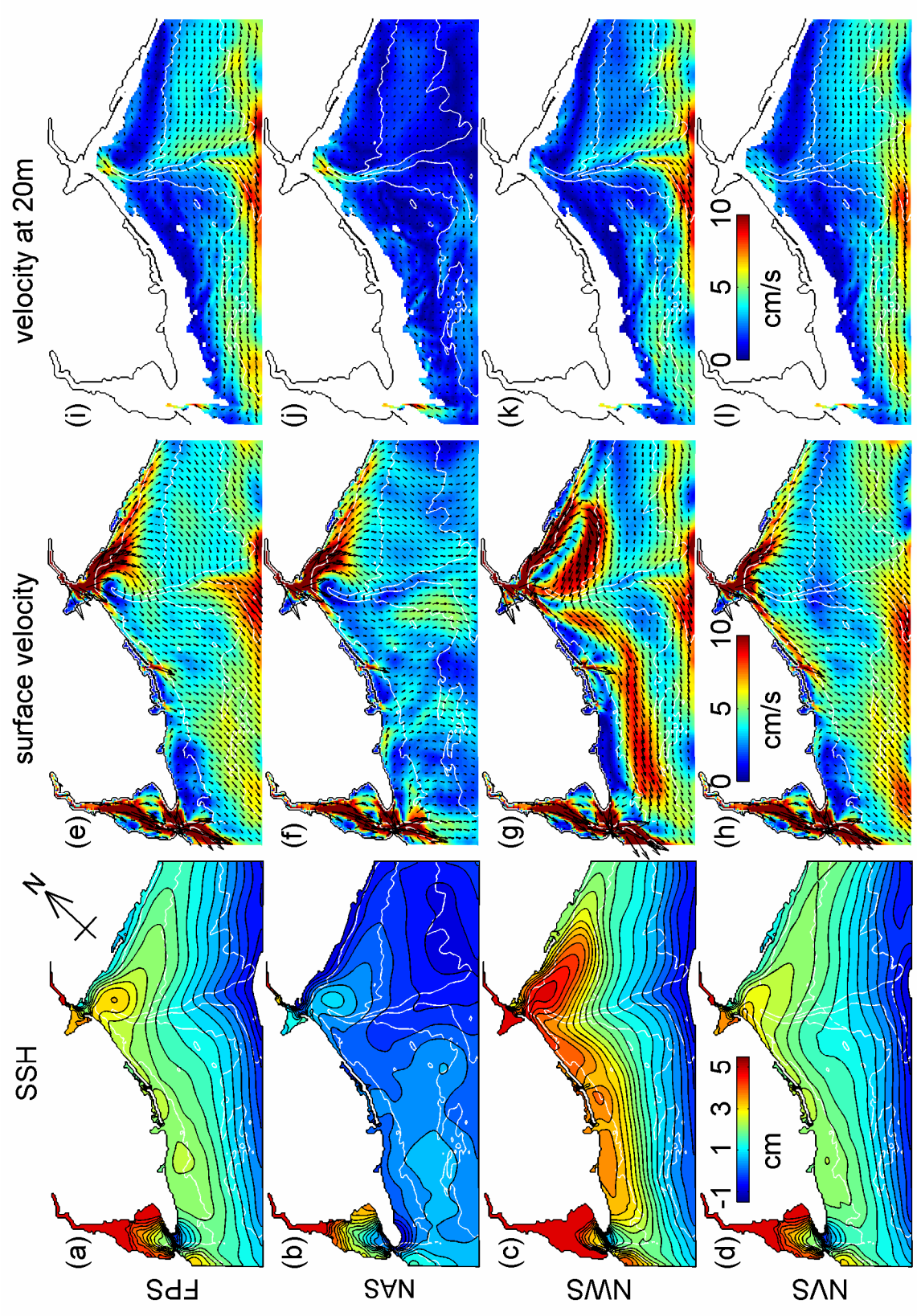
SSH
surface velocity
velocity at 20m
(a)
(b)
(c)
(d)
(e)
(f)
(g)
(h)
(i)
(j)
(k)
(l)
FPS
NAS
NWS
NVS
-1 1 3 5
cm
0 5 10
cm/s
0 5 10
cm/s

Figure 2.4. (a)–(d) Mean SSH contours, (e)–(h) mean surface current, and (i)–(l) mean current at 20 m depth over 2-year period of different simulations. In (e)–(l), color represents magnitude and arrows depict direction. Solid white lines are 20, 40, and 60 m isobaths; dash white lines in (d), (h) and (l) are the corresponding isobaths after the Hudson Shelf Valley is filled. The abbreviations: FPS - Full Physics Simulation, NAS - No Ambient-current Simulation, NWS - No Wind Simulation, and NVS - No Valley Simulation.

2.3.2.Sea Surface Current

The mean surface current in the FPS case (Figure 2.4e-h) shows outflow faster than 10cm s^{-1} at the river mouth directed along Long Island coast. A substantial part of this coastal current departs the Long Island coast and turns to the south, with a portion recirculating in the apex of the NYB in an approximately 30 km radius loop and the remainder crossing the Hudson Shelf Valley. The rest of the coastal current turns to the southeast gradually as it moves eastward along the Long Island Coast. On the New Jersey side, a southward coastal current forms at Sandy Hook. For most of the mid- and outer-shelf, water moves south-southeastward on the surface.

Without the remotely forced along-shelf flow (NAS), the mean surface current in Figure 2.4f is weakened substantially and directed more eastward on the mid- and outer-shelf. The region of strong southward current between the 40-m isobath and the valley on the outer-shelf in FPS disappears in NAS, but the inner-shelf circulation differs little. Thus the largely isobath-following, remotely forced ambient current does not have

much influence on the mean surface current on the inner-shelf or NYB apex area, but it magnifies the surface current on the mid- and outer-shelf, rotates the currents there clockwise, and forms the strong southward flow on the outer-shelf.

Dramatic differences exist between Figure 2.4g, the mean surface current of the NWS, and Figure 2.4e (FPS), especially for the inner- and mid-shelf. Without winds, the circulation pattern constitutes an elongated freshwater bulge greatly amplified compared to the bulge in FPS. Fong and Geyer (2002) demonstrated that the freshwater bulge in the vicinity of a river mouth can continually grow without reaching a steady state in the absence of any ambient current or surface mixing to aid its dispersal. The circulation here has similarities to Fong and Geyer's (2002) results, except that the bulge is squeezed between the coast and the bathymetry of the Hudson Shelf Valley, and the growth of the bulge is arrested by the remotely forced ambient current in the middle of the Long Island coast. The presence of the Long Island coast and the Hudson Shelf Valley makes the situation here much more complicated than that in Fong and Geyer (2002), and the extent to which bottom friction modifies the ballooning effect of the freshwater outflow, as described by Nof and Pichevin (2001), is uncertain. To discern this role clearly when the outflow is confined by coastline and the Shelf Valley would require further analysis that is beyond the scope of this dissertation. A strong southward coastal current emerges along the northern New Jersey coast that is joined by flow that crosses the shelf valley after branching off from the recirculation. This combined flow forms a strong current belt between the 40-m and 60-m isobaths that extends all the way to the mouth of Delaware Bay. The striking change from the FPS to NWS case (Figures 4e and 4g) indicates that wind plays a major role in shaping the circulation on the inner- and mid-shelf on very short

time scales, and strikes a cautionary note that simulation studies applying the bulk formulae in conjunction with low frequency (e.g. monthly average) climatological winds might neglect important dynamical influences in this area.

Consistent with the SSH comparison, the surface recirculation loop at the river mouth in FPS disappears in NVS (Figure 2.4h), and more of the river outflow turns to the south upon exiting the harbor to form a stronger New Jersey coastal current. In the offshore region, though the direction of surface velocity is similar in FPS and NVS, the dramatic change of velocity magnitude immediately downstream from the Hudson Shelf Valley is less abrupt in NVS. These results confirm that the Hudson Shelf Valley acts as a dynamic boundary that redirects the surface current on the mid- and outer-shelf and obstructs the southward flow of freshwater from the north side of the shelf valley in the NYB apex area.

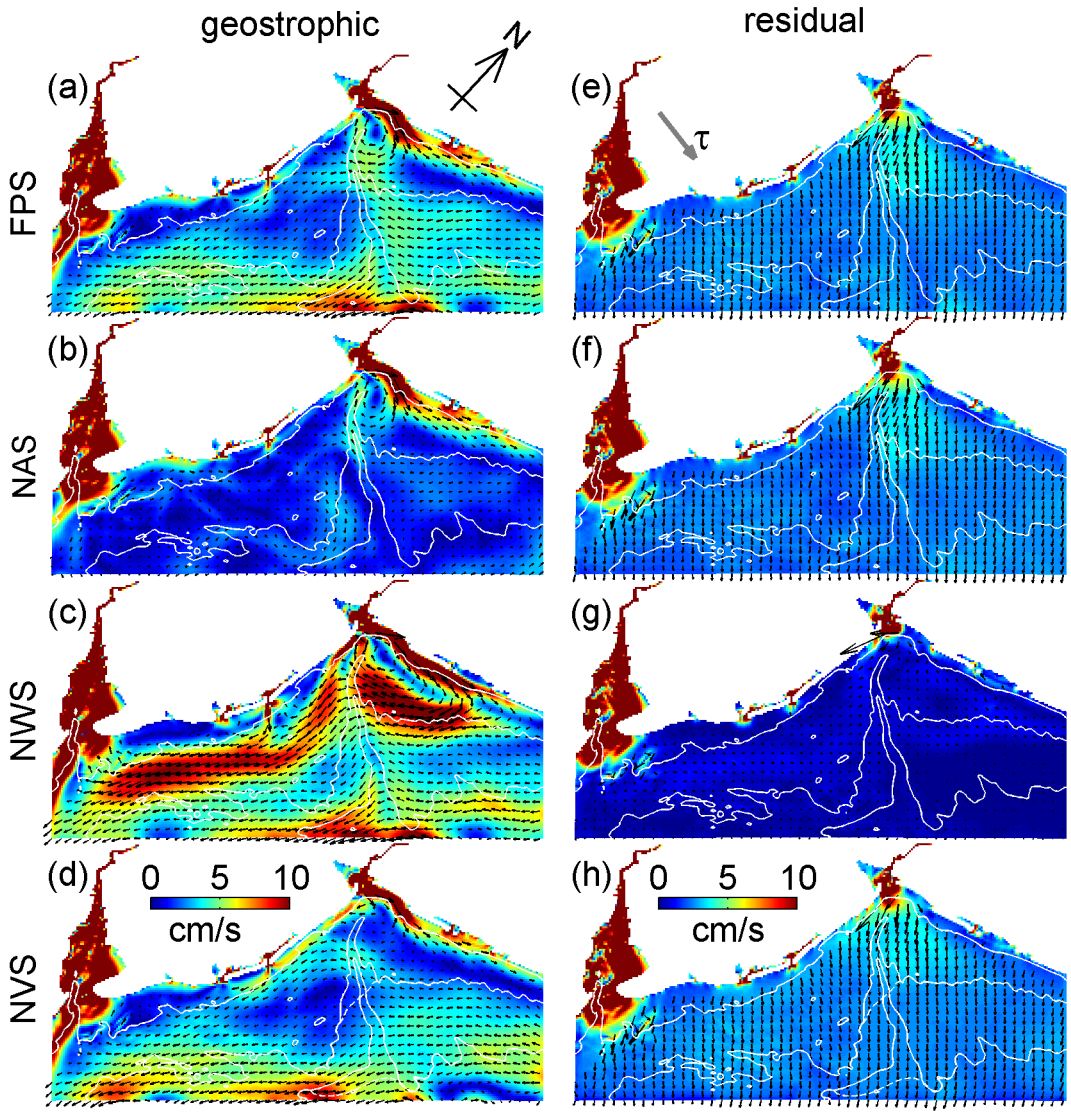

Figure 2.5. Two-year mean surface (a-d) geostrophic and (e-h) residual ageostrophic current of different simulations. Color represents magnitude and arrows depict direction. Solid white lines are 20, 40, and 60 m isobaths; dash white lines in (d) and (h) are the corresponding isobaths after the Hudson Shelf Valley is filled; the grey arrow in (e) is 2-year mean wind.

2.3.3. Decomposition of the surface current

To understand the dynamics in greater detail, the surface mean geostrophic current (Figure 2.5a-d) was computed from the 2-year mean of SSH enabling me to examine the mean residual ageostrophic current, i.e. the difference between surface current and surface geostrophic current (Figure 2.5e-h). Due to the strong nonlinearity in the estuaries created by tides and bottom friction, this linear decomposition is not informative inside the estuaries and is not discussed here. The surface mean geostrophic current of FPS (Figure 2.5a) is very similar to Figure 2.4e, especially the southwestward current on the outer-shelf, and the strong out-flow at the river mouth and Long Island coastal current; these major features of the surface current are geostrophically balanced, consistent with the conclusion drawn in Section 3a. But the direction of the flow everywhere in Figure 2.5a is rotated clockwise with respect to Figure 2.4e and the strong off-shore current on the outer-shelf is weakened. On the mid- and outer-shelf, and along the New Jersey coast, the residual flow vectors in Figure 2.5e are directed almost uniformly southeastward at a speed of approximately 2.5 cm s^{-1}. From later analysis we know that this residual flow is basically Ekman transport on the surface. Ekman transport is different at the New York Apex area because freshwater-outflow-generated stratification there is stronger than that on the rest of the shelf.

The changes from Figure 2.5a to 5b-d reinforce the three conclusions drawn in Section 3: (i) on the outer-shelf the geostrophic balance develops in response to the remotely forced along-shelf current; (ii) the action of the wind is to modify the pressure field and thence the mean geostrophic circulation; (iii) the Hudson Shelf Valley modifies the surface geostrophic balance.

The comparison between surface ageostrophic velocity in Figure 2.5e and Figure 2.5g suggests that the surface mean residual flow is basically wind driven. To confirm it is Ekman transport, drift current was estimated using Madsen's (1977) steady-state Ekman spiral equation. The average 10-m wind in the NYB in NARR is about 1.64 m s^{-1} southeastward (Figure 2.1), which is equivalent to wind stress of 0.02 N m^{-2} given a drag coefficient of 0.005 (Yelland and Taylor 1996). The estimated drift current at 0.15 m depth (average depth of the model surface layer) is about 3.8 cm s^{-1}, which is somewhat stronger than the mean surface residual current in FPS. The estimated deflection angle between the surface wind stress and the drift current at the corresponding depth is about 23^{o}, which is smaller than the 33^{o} deflection angle in FPS (Figure 2.5e). These discrepancies are consistent with the linear increase of vertical viscosity with depth in Madsen's theory being about half that computed by the model turbulence closure.

2.3.4. Mean subsurface circulation

The mean current at 20 m deep for the different simulations is plotted in Figure 2.4i-l. For the FPS case, southward flow is strongest offshore and this outer-shelf current deflects shoreward somewhat as it crosses over the Hudson Shelf Valley. On the mid- and inner-shelf at this depth the Hudson Shelf Valley guides a significant flow toward the apex of the New York Bight. When the remotely forced along-shelf flow is removed (NAS; Figure 2.4j) the southward current on the mid- to outer-shelf disappears showing that the mean subsurface current in the NYB is driven primarily by large scale shelf circulation. However, the shoreward flow intrusion at 20 m depth at the head of the valley head remains in NAS. In Figures 4i and 4k the subsurface circulation is much the same except the riverward intrusion at the valley head is weakened substantially in NWS. This

indicates that the 2-year mean up-valley flow at 20 m is, at least partially, the result of the prevailing westerly wind. This is consistent with winter-time observations of flow in the Shelf Valley by Harris et al. (2003). The mean current at 20 m in the NVS case (Figure 2.4l) differs from FPS in three respects: (i) not surprisingly the slight shoreward detour of the outer-shelf current over the Hudson Valley disappears, (ii) the abrupt increase of velocity magnitude over the valley is diminished, and (iii) the riverward water intrusion at the head of the Hudson Shelf Valley is weakened. Thus, on the mid- to outer-shelf the valley steers the surface and subsurface currents in a similar way, while on the inner shelf it acts to funnel subsurface currents that flow shoreward to feed surface offshore transport that is driven by wind and the river outflow.

The results from the NTS case (not shown), in which tides are omitted but all other forces and bottom drag coefficient are retained, are the same as those from FPS. This indicates that tidal processes in the NYB are mostly linear in the respect that there is no appreciable rectification of tidal currents into the mean circulation on the inner shelf or deeper waters. Moreover we can conclude that bottom friction is unimportant because the inclusion of tides dramatically increases bottom drag on the shelf, yet the mean flow patterns and freshwater pathways change little. The principal role of tides in this area is to influence mixing within the Hudson River estuary (Chant et al. 2007, Lerczak et al. 2006).

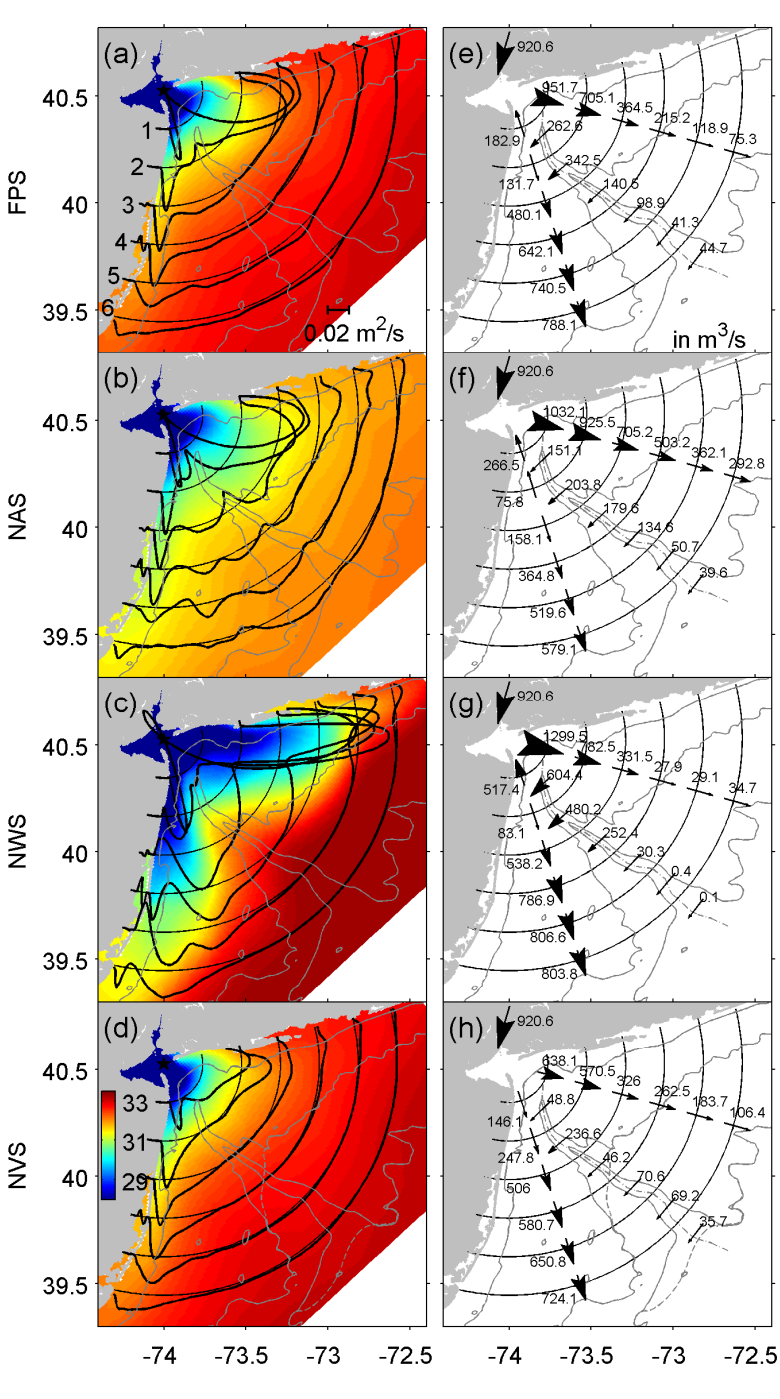

Figure 2.6. (a) – (d) Temporally-averaged vertically-integrated freshwater flux (thick black lines) across thin black arcs of radius 20, 40, 60, 80, 100, and 120 km, respectively, and 2-year mean surface salinity (in color). The arcs are centered at the entrance to New York harbor (star symbol). (e) - (h) Temporally-averaged spatially-integrated freshwater

transport across the segments of the arcs on either side of the Shelf Valley (gray dash-dot line), and the valley itself. The size of the arrow heads along with the numbers indicates the freshwater transport. Solid gray lines in all panels are 20, 40, and 60 m isobaths; dash gray lines in (d) and (h) are the corresponding isobaths after the valley is filled.

2.4. Mean Freshwater Dispersal

To examine the patterns of river-source freshwater spreading in the NYB I consider flow across six arcs (thin lines in Figure 2.6) centered at the entrance to New York harbor. The arcs of radius 20, 40, 60, 80, 100 and 120 km are numbered arc 1 through 6, respectively. The two-year (2005-2006) time-averaged, vertically-integrated freshwater flux across each arc is depicted by the thick lines in Figure 2.6a-d; the scale bar indicates freshwater transport per unit length of azimuth of arc. The two-year mean sea surface salinity is also given in Figure 2.6a-d for reference. To quantify the budget of freshwater dispersal to the shelf the freshwater fluxes across the segments of the arcs either side of the valley and across the valley itself are presented in Figure 2.6e-h.

In FPS three somewhat distinct freshwater transport pathways show in Figure 2.6a: (i) southward along the New Jersey Shore (which I name the New Jersey Pathway), (ii) eastward along the Long Island coast (which I name the Long Island Pathway), and (iii) along the southern flank of the Hudson Valley (which I name the Mid-Shelf Pathway). The Long Island Pathway located on the inshore northeastern shelf has been observed episodically (Chant et al. 2008a) and starts as a strong, broad feature that becomes thinner, weaker, and more coastally trapped, as it moves eastward. On the offshore northeastern shelf there is virtually no freshwater flux across the arcs. The New Jersey Pathway, located

on the inshore southwestern shelf, has been noted in observations before and is consistent with the dynamics of a buoyancy-driven coastal current. It starts as a sharp and thin feature on arc 1 and gradually broadens as it propagates southward. On the offshore southwestern shelf the Mid-shelf Pathway becomes distinct at arc 3. At arc 6, it is almost evenly distributed between the 20-m isobath and the valley with a local maximum on the southern flank of the valley. At arc 1 and 2, there is freshwater returning along a path over the Hudson Valley as part of the freshwater recirculation identified in Figure 2.4e. The freshwater budget in Figure 2.6e shows that in the long-term mean almost all river discharge goes first to the northeastern shelf at arc 1, but the southwestern shelf is the eventual destination for more than 90% of the freshwater discharge. Recirculation processes on the northeastern shelf ultimately guide the freshwater across the Hudson Shelf Valley onto the southwestern shelf, with most of the crossing occurring within 80 km radial distance from the harbor mouth. Inside arc 2 there is northward transport between New Jersey coast and the valley that creates a closed recirculation (Figure 2.4e) of about one fifth of the total freshwater discharge.

Comparing Figures 2.6a and 2.6b we see that without the remotely forced along-shelf current (NAS) the freshwater dispersal pattern changes in several respects: On the northeastern shelf the Long Island Pathway strengthens and a new, minor off-shore pathway emerges along the northern flank of the valley; the freshwater return over the Hudson Valley extends to arc 5 indicating an intensification of the bulge recirculation; and on the southwestern shelf the Mid-Shelf Pathway splits into two lobes at arc 4. The New Jersey Pathway remains the same as in FPS. Figures 2.6e and 2.6f quantify these differences. Compared to FPS, the NAS case has 50% stronger recirculation at the harbor

mouth (267 $m^3 s^{-1}$ compared to 183 $m^3 s^{-1}$) and a 40% weaker (355 $m^3 s^{-1}$ vs. 605 $m^3 s^{-1}$) flow crossing the valley inside arc 3 (60 km radius). About one third of the total freshwater exits the domain from the northeastern shelf at arc 6 in NAS compared to about one tenth in FPS. These differences show that the remotely forced ambient current weakens the bulge recirculation, suppresses the Long Island Pathway, and diminishes the net cross-shelf export of freshwater on the northern flank of the Hudson Shelf Valley. In terms of the eventual fate of material transported in the Hudson River discharge, the ambient current acts to direct water away from the Long Island coast and across the Hudson Shelf Valley toward the southwestern shelf.

When the effect of wind is removed (NWS; Figure 2.6c and 2.6g), the Long Island Pathway along arcs 1 and 2 grows substantially compared to FPS and there is a commensurate increase in the freshwater recirculation on the offshore northeastern shelf, especially on the inner four arcs. On the southwestern shelf, a strong and broad pathway forms at arc 2 and flows cross-shore and then along-shelf bounded by the 20 m to 40 m isobaths. This is the broad southward flow separated from the coast in Figure 2.4g. Along the New Jersey coast there is no longer a coherent southward coastal current, but rather the flow direction is reversed consistent with the recirculation seen in Figure 2.4g between the coast and the main pathway that turns offshore. Figure 2.6g shows that the net affect of these circulation changes when winds are absent are to first direct 35% more of the river discharge to the northeastern shelf, yet via a much stronger recirculation most of this flow crosses the Hudson Valley within 80 km of the harbor mouth. Taking the result in Section 3 into consideration, we can conclude that by mixing the ocean surface layer, wind is a major force for the mean surface circulation on NYB and the freshwater pathways. It plays an

important role in establishing the mean southward New Jersey coastal pathway, dispersing a portion of the discharge across the northeastern shelf, and suppressing the strength of the bulge recirculation.

Without the Hudson Valley (Figure 2.6d and h) the freshwater pathways differ from FPS such that the cross-shelf transport on the northeastern shelf is substantially weakened, the northward return flow in the Hudson Valley at arcs 1 and 2 disappears, the local maximum cross-shelf freshwater flux along the southern flank of the Hudson Valley at arcs 5 and 6 is absent, and the New Jersey Pathway is strengthened. These changes confirm the conclusion reached in Section 3: the valley helps trap freshwater on the northern shelf in the NYB apex area, promotes formation of the closed freshwater recirculation loop there, and guides freshwater export on the southwestern outer shelf parallel to the valley. Comparing Figures 2.6e and 2.6h we see that while in the NVS case less of the Hudson River discharge initially flows to the northeastern shelf across arc 1 (638 $m^3 s^{-1}$ vs. 952 $m^3 s^{-1}$ in FPS), the net export across the northern portion of the arc 6 is 40% greater, and therefore relatively *less* freshwater crosses the Hudson Valley from the north to the south when there is no shelf valley. This apparent paradox arises because by amplifying the recirculation in the NYB apex the shelf valley fosters stronger exchange from north to south between arcs 1 and 3 (FPS 605 $m^3 s^{-1}$; NVS 285 $m^3 s^{-1}$). In FPS, this vigorous flow bifurcates at the New Jersey coast, feeding both the northward coastally-trapped recirculation and the southward coastal current.

As was noted in Section 3, there is little difference in the freshwater dispersal pattern in FPS and NTS.

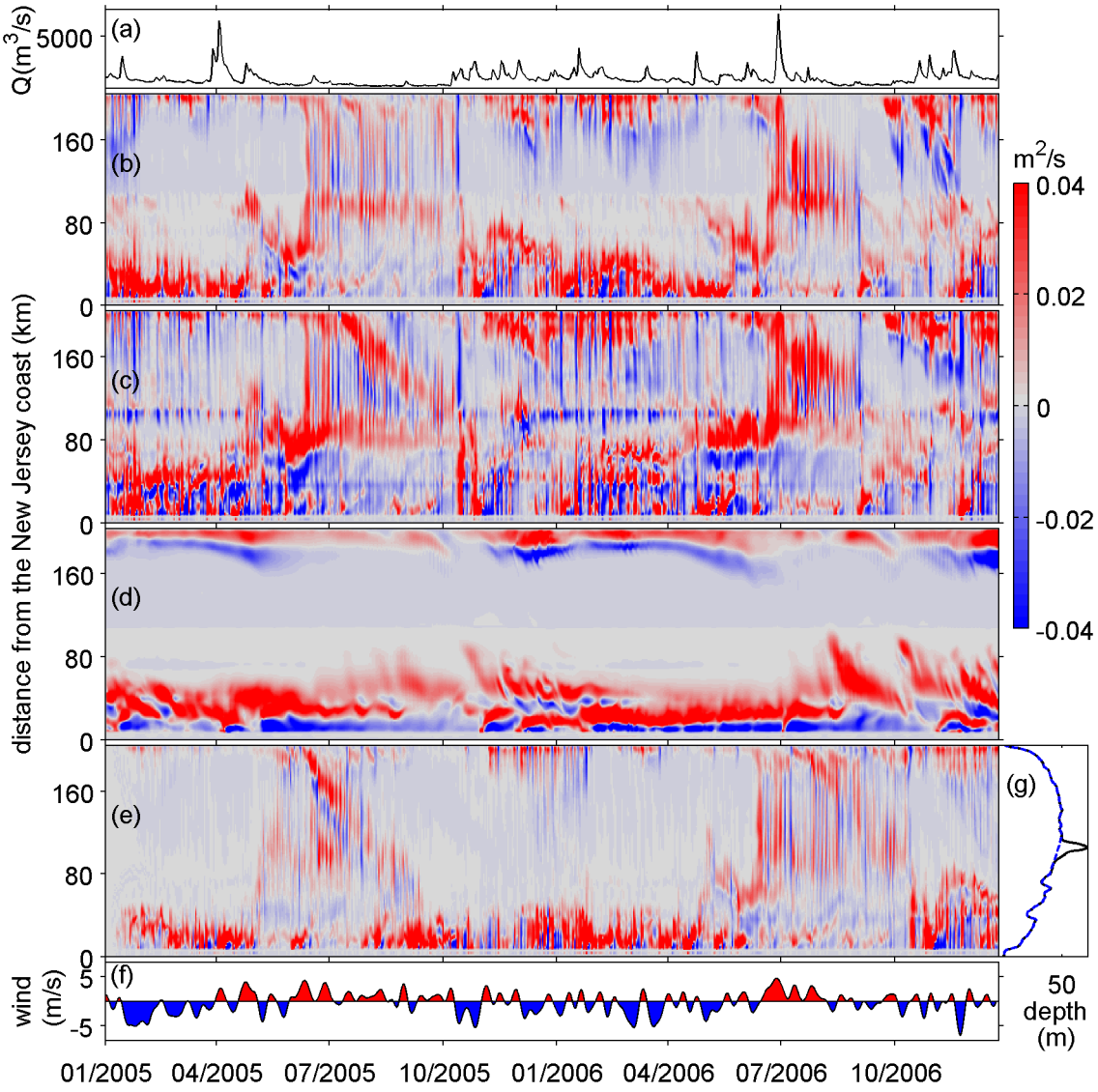

Figure 2.7. Time series of vertically integrated daily-averaged freshwater flux across arc 5 (Figure 2.6) of different simulations: (b) FPS, (c) NAS, (d) NWS, and (e) NVS. (a) River discharge and (f) meridional component of the wind over the same period, and (g) bathymetry along arc 5: black solid line is the original depth, blue dash is the depth after the valley is filled.

2.5. Temporal Variation of Freshwater Dispersal

The temporal variability of freshwater dispersal is presented in Figure 2.7 in terms of the vertically-integrated daily-averaged freshwater flux across arc 5 over the two-year period, along with the Hudson River discharge and the northward (parallel to New Jersey coast) component of the wind. (The water depth as a function of azimuth along arc 5 is shown to the right of Figure 2.7g.) Positive freshwater flux is defined as out-going from the harbor. The time series of wind has been low-pass filtered with cut-off period of 10 days.

In the FPS case (Figure 2.7b) most of the outgoing freshwater flux occurs on the southern shelf and along the New Jersey coast, as was noted in the mean freshwater flux patterns described in Section 4. A weak yet clearly discernable cutoff line over the valley distinguishes variability on the northern and southern shelves throughout the whole two-year period. Thus, the effect the valley has on the freshwater flux at this outer-shelf (arc 5) location is also exerted at daily time scales. There is a noticeable seasonality in the freshwater dispersal patterns in FPS. Between October and May outgoing flux is predominantly along the New Jersey coast with a weaker eastward flux in a narrow current along the Long Island coast. In contrast, between June and September outgoing flux across is primarily across the mid-shelf portion of the arc. Comparing the freshwater flux with the time series of along-shore wind (Figure 2.7f) we see that outgoing flux across the center portion of the arc coincides predominantly with periods of upwelling favorable wind (southerly). This is consistent with the results of Castelao et al. (2008a) in CODAR and surface float observations that a swift jet transports water from the New York Bight apex to the outer-shelf in summer and is significantly correlated with upwelling favorable winds.

Moreover, this is also consistent with historical observations that reveal a freshening of the outer shelf during summer months (Mountain 2003). The off-shore transport intensity differs between years, with the summer-time direct off-shore freshwater transport being stronger in 2006 than that in 2005. It appears this is caused by the peak in Hudson River discharge in 2006 coinciding with the beginning of the upwelling season (end of June), whereas the peak discharge in 2005 occurs some two months before the upwelling season. All these features of the flow variability are similar at arcs 3, 4 and 6 (not shown).

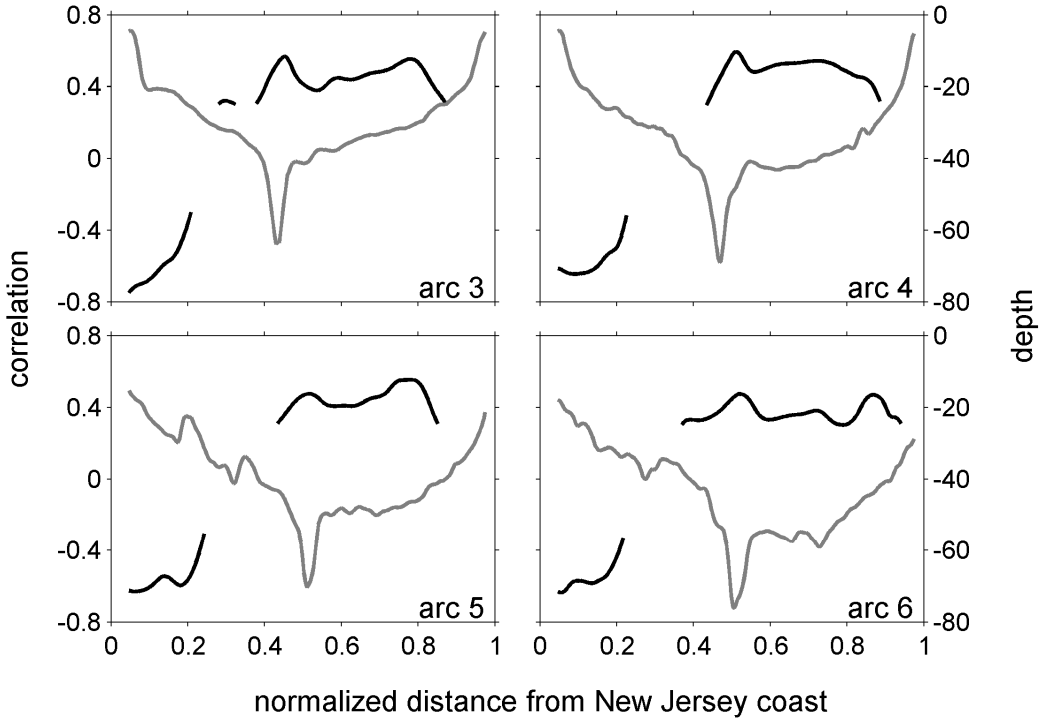

Figure 2.8. Correlation (dark lines) between filtered meridional component of the wind (southerly as positive) and filtered freshwater flux across four arcs in the Full Physics Simulation. The correlation is plotted only where it is significant at the 95% confidence level. The gray lines in each panel are bathymetry along the arcs.

To examine more quantitatively the relationship of freshwater transport to winds, correlations between time series of the wind at the New Jersey coast (northward positive) and freshwater flux across 5° azimuth intervals of each arc are considered. Using a similar analysis approach to that of Castelao et al. (2008a) applied to CODAR surface velocity in this region, a weighted running mean filter is first applied to the time series using the equation $f_k(t) = k^{-1}\int_{-\infty}^{t} f(t')e^{(t'-t)/k}dt'$ where $f(t)$ is the wind stress or freshwater flux at time t, and $f_k(t)$ is the resulting convolution with weights that decay exponentially with time scale *k* (Austin and Barth 2002). By doing this, the time history of the wind and the freshwater advection is considered. Here, *k* is chosen to be 4 days, being a time scale reflecting the 2-5 day variability in the synoptic wind field in the NYB and appropriate to the duration of wind events that could displace waters on the order of 70 km, at 20 cm s^{-1}, from the New Jersey coast to arcs 4-6. Of all wind directions, the component along the New Jersey shore has the highest correlation with the freshwater flux over the Hudson Shelf Valley area. The correlation between filtered along-shore wind and freshwater flux for the four outer arcs is presented in Figure 2.8. The correlation is plotted only where it is significant at the 95% confidence level. The results are similar for all four arcs: the negative correlation on the shelf adjacent to the New Jersey coast indicates southward (negative) wind favors the export of freshwater in the coastal current, while the positive correlation from the 40-m isobath on the south (New Jersey) side of the valley to approximately the 30-m isobath north of the valley indicates northward wind favors the off-shore freshwater advection in the Mid-shelf Pathway and the weak eastward freshwater advection on much the northern shelf. Similar conclusions were drawn by Choi and Wilkin (2007) using idealized simulations.

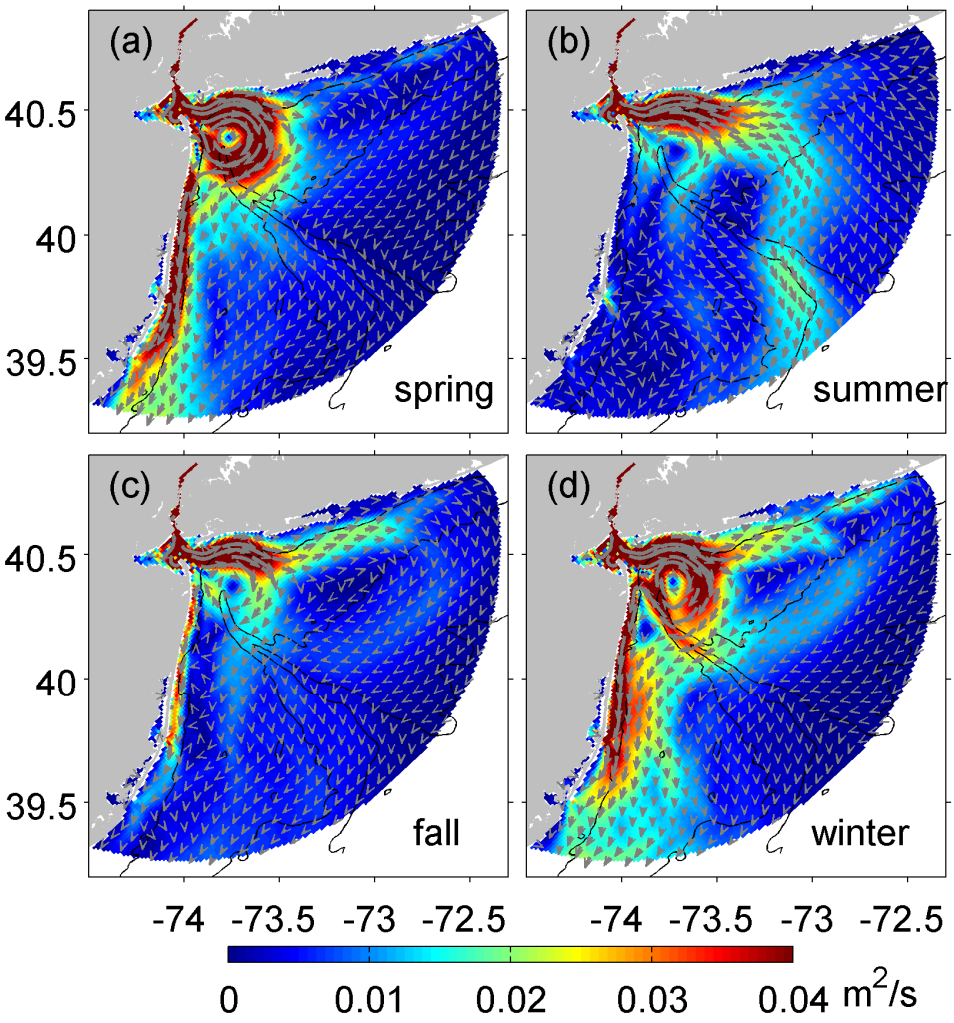

Figure 2.9. Temporally averaged vertically integrated freshwater transport within 140 km from the estuary entrance for (a) spring (March – May), (b) summer (June - August), (c) fall (September – November) and (d) winter (December – February) seasons. Color represents transport magnitude and vectors depict the direction. Black lines in both panels are 20, 40, and 60 m isobaths.

To depict clearly the seasonal variation of the freshwater pathways, Figure 2.9 shows the mean vertically integrated freshwater fluxes as a vector field on the model grid during

spring (March to May), summer (June to August), fall (September to November) and winter (December to February) months. Off-shore freshwater transport along the Mid-shelf Pathway dominates the summer period, eastward freshwater transport along the Long Island coast is the most obvious pathway in the fall period and southward freshwater transport along the New Jersey coast dominates the winter-spring period. In all seasons, freshwater first moves eastward after it exits the New York Harbor. In summer, part of the outflow turns to the south and forms a weak freshwater recirculation at the river mouth but the majority of it turns seaward at the 40-m isobath and crosses the Hudson Shelf Valley about 100 km from the harbor mouth, whereupon it moves offshore following the 60-m isobath. This path is similar to the episodic jet transport Castelao et al. (2008a) found in CODAR surface current observations. There is little freshwater movement along the New Jersey coast in summer. In fall, a relatively strong flow in the Long Island Pathway, weak recirculation at the harbor mouth and, a weak New Jersey Pathway transport are present. In winter-spring months, a strong New Jersey Pathway and a strong recirculation at the harbor mouth are distinctive features of the flow, and there is modest transport of freshwater eastward along the Long Island coast in the winter. There is little transport to the northern and central mid- and outer-shelf at this time.

We now return to consideration of the forces that influence variability in the freshwater spreading on short time scales. Time series of the freshwater flux across arc 5 in the NAS, NWS and NVS cases are shown in Figures 2.7c, d and e, respectively, to complement the FPS results discussed previously. The temporal variability of FPS and NAS are very similar, but in NAS (Figure 2.7c) the Hudson Shelf Valley appears clearly as a conduit for on-shore transport for much of the time, especially October through May when winds tend

to have a southward along-coast component (negative in Figure 2.7f). In summer, when wind is predominantly upwelling favorable (positive in Figure 2.7f), the NAS case shows stronger off-shore transport on the south flank of the valley that then spreads over the entire northern shelf.

The pattern in NWS (Figure 2.7d) is very different from FPS and NAS showing clearly that wind is the primary driving force for the daily time-scale variability of the freshwater flux and the spreading of freshwater onto the mid- and outer-shelf. Without wind, the freshwater only crosses the arc on either end, in coastal currents, leaving the middle of the shelf free of freshwater flux. Both of the coastal currents have recirculations that grow and decay in step with the respective outflows, indicating the freshwater movement largely follows the static path in Figure 2.4g.

Case NVS (Figure 2.7e) shows variability similar to the full physics simulation (Figure 2.7b) on time scales of days to seasonal, but the boundary at the valley that delineates northern and southern shelf regimes in FPS vanishes. This indicates the valley plays its role in blocking freshwater movement at all time scales. The boundary at the valley between the two regimes is evident even in the absence of any wind forcing (Figure 2.7d). Moreover, without the Hudson Valley, it appears that the southward freshwater transport on the New Jersey coast is more coastally trapped, consistent with the result in Section 4.

The time variability of freshwater flux across arc 5 in the NTS case (not shown) is the same as FPS, which shows that tides have no real effect on the freshwater transport to the mid- and outer-shelf, even on daily time scales.

2.6. Summary and Conclusions

I have conducted a study of the processes that influence the dispersal of the Hudson River discharge as it enters the New York Bight and spreads across the New Jersey shelf. Two-year simulations with ROMS were used to analyze the mean momentum dynamics and freshwater transport pathways. To investigate the influences of remotely forced along-shelf current, wind, the topographic control of the Hudson Shelf Valley, and tides, reduced physics simulations were conducted in which each of these respective factors was individually withdrawn from the model configuration.

In all simulations, mean sea surface current follows the isobaths on the mid- and outer-shelf and a freshwater recirculation occurs in the apex of the New York Bight near the harbor mouth. Analysis of the surface current identifies Ekman dynamics and geostrophic balance as the two major processes governing the mean surface circulation. The reduced physics simulations show that the large-scale remotely forced shelf circulation is the major driver for the surface geostrophic balance. Below the surface mixed layer most of the circulation is driven by the remotely forced shelf-wide circulation, except on the inner shelf where bathymetry funnels subsurface flow toward the head of the Hudson Valley. Tides have almost no influence on the mean shelf circulation.

The freshwater entering New York Bight from the Hudson estuary disperses along three principal transport pathways: (i) along the New Jersey coast, (ii) along the Long Island coast, and (iii) along a mid-shelf pathway that proceeds offshore guided by the southern flank of the Hudson Shelf Valley, consistent with recent analyses of CODAR surface current observations (Castelao et al. 2008a). In all cases, a freshwater recirculation

forms near the harbor mouth within the 40 km arc. In terms of the freshwater budget, all the simulations show that the majority of the river-source freshwater flows first onto the shelf north of the Shelf Valley but then crosses the valley within 80 km of the harbor mouth. In the simulation with all physics included, more than 90% of the freshwater flux eventually exits the region on the south side of the Hudson Valley.

From the reduced physics simulations the role of the remotely forced large scale shelf circulation is found to be decreasing the volume of freshwater recirculating, and pushing freshwater from the northern shelf across the Hudson Valley, subsequently dispersing it more evenly over the southern shelf. Wind is the most significant force pushing freshwater from the inner-shelf onto the mid- and outer-shelf. Winds also reduce the recirculation intensity at the river mouth but do little to change the ultimate fate of the freshwater. The bathymetry of the Hudson Shelf Valley is shown to have a significant role in forming the strong and closed recirculation at the harbor mouth and promotes cross-shelf transport of freshwater further down shelf. Tides have minor impact on the freshwater pathways.

There is seasonal variability in freshwater flux across the 100 km arc over the two-year period simulated. In the winter-spring period, the New Jersey coastal pathway dominates. During fall, the Long Island pathway is relatively strong. During summer, the mid-shelf pathway that directly transports river discharge to the mid- and outer-shelf dominates. The mid-shelf pathway is active when the wind is upwelling favorable, which supports the tentative conclusion drawn by Castelao et al. (2008a) that upwelling wind is the main driver of off-shore transport. The cross-correlation between a 4-day weighted temporal average of along-coast wind and freshwater flux across the four outer arcs considered shows significant positive correlation between the upwelling wind and mid-shelf out-going

freshwater flux. This result agrees with Choi and Wilkin's (2007) conclusion that southward wind favors the New Jersey pathway.

The comparison of the differing reduced physics simulations identifies wind as the primary source for the daily-scale variability of freshwater transport and the major force pushing the freshwater onto mid- and outer-shelf. Ambient current is shown to be a suppressive force for the outgoing freshwater flux on the northern shelf.

These results have implications for biogeochemical processes in the New York Bight because the Hudson River is a significant source of nutrients, organic matter, and dissolved and suspended contaminants to the inner shelf. The patterns of freshwater dispersal revealed here indicate that the destination of material transported in the Hudson River discharge changes rapidly on the time scales of a few days, but also with longer term seasonal differences. For river-borne material that is biologically or geochemically active on time scales of a few days to months, the transport pathways inferred here will influence deposition, availability to the regional marine ecosystem, and regions where material may be exported from the New York Bight by advection.

CHAPTER 3. AGE AND RESIDENCE TIME

3.1. Introduction

Timescale analysis (water age, residence time) has utility for estimating ventilation rates of lakes, estuaries, and ocean basins (England 1995, Hohmann et al. 1998, Jenkins 1987), inferring ocean circulation and mixing (Fine 1995, Haine et al. 1998, Schlosser et al. 2001, Wunsch 2002), and studying rates of biogeochemical processes (Hohmann et al. 1998, Sarmiento et al. 1990, Weiss et al. 1991). Water age is not directly observable, so transient tracers, isotopes and anthropogenic tracers are used to infer "age", by which it is generally meant the elapsed time since the water was last in contact with the tracer source. Most tracer age derivations assume negligible mixing and diffusion (Fine 1995, Hohmann et al. 1998, Jenkins 1987, Schlosser et al. 2001, Weiss et al. 1991), though these processes can substantially divert tracer-based age from real age (Deleersnijder et al. 2001, Delhez et al. 2003, Thiele and Sarmiento 1990, Waugh et al. 2003). In numerical modeling, a common approach is to release many tracers and extract timescale information from their differential transport (Gao et al. 2005, Monsen et al. 2002). This method requires substantial computation if spatial and temporal detail is sought. Methods for directly simulating these timescales were introduced by Jenkins (1987) and Sarmiento et al. (1990) who derived tracer-based age conservation equations. The concept of an ideal age tracer followed and has been compared with radiotracer age in idealized simulations (Thiele and Sarmiento 1990), and used to simulate global ocean ventilation rates in a general circulation model (England 1995).

Further developments in modeling timescales have followed two approaches: Constituent-oriented Age and Residence-time Theory (CART) (Deleersnijder et al. 2001, Delhez 2006, Delhez et al. 2004, Delhez et al. 1999) and Green's function based Transit Time Distribution theory (TTD) (Haine and Hall 2002, Hall and Plumb 1994, Holzer and Hall 2000). These approaches describe similar concepts from different perspectives. CART focuses on *mean tracer age*, defined as the mass-weighted, arithmetic average of the time elapsed since the tracer left the source region, and *mean residence time*, defined as the mass-weighted, arithmetic average of the time needed for tracer to leave a domain of interest. TTD emphasizes the transit time spectrum; this is an age spectrum when expressed as a probability density function (PDF) of transit times since tracer last had contact with its origin, and a residence time spectrum when the PDF is of transit time from a certain point to first contact with a location where it can exit a defined domain. Neither mean age nor mean residence time fully characterize the water mass movement (Hall and Haine 2002). Nevertheless, this information is still very useful for studying spatial patterns of circulation and mixing and their associated timescales, which is the main objective here and is instructive when considering many coastal ocean biogeochemical processes. Besides, the computation of full age and residence time spectra can be prohibitive for highly resolved coastal ocean applications even when exploiting the recently described transport matrix framework (Khatiwala 2007) to accelerate simulations.

Focusing on timescales associated with the spreading of river source waters across the inner shelf, this chapter applies CART to the circulation of the Hudson River discharge in the NYB. The Hudson River plume is a major source of suspended matter, nutrients, dissolved organic matter and contaminants to the NYB (Adams et al. 1998, Howarth et al.

2006, Schofield et al. 2009). Transport of these materials from the estuary to the shelf regulates local biogeochemical processes (Geyer et al. 2001, Moline et al. 2008, Schofield et al. 2009) for which timescales are key factors (Howarth et al. 2006, Malone and Chervin 1979).

The path of the Hudson River plume is highly mobile, largely controlled by local wind, and influenced by bottom topography (Chant et al. 2008a, Choi and Wilkin 2007). Under high discharge conditions, the plume often forms a low salinity "bulge" at the NYB apex area extending 30-40 km from the coast. The bulge recirculates water and potentially traps tracers there, causing less than ½ of the total freshwater outflow to enter the southward current along the coast of New Jersey. The freshwater outflow pathways vary with season (Chapter 2). In summer, when upwelling favorable winds prevail, the recirculation bulge is weak and the river plume tends to move directly offshore. During the rest of the year winds have a significant offshore component and the recirculation bulge is more prevalent, ultimately feeding a strong coastal current along the New Jersey coast and weaker current along the Long Island coast. The effect of these pathways on the timescale of freshwater dispersal onto and out of the NYB apex is the focus of this chapter.

The CART theory is summarized in Section 3.2. Section 3.3 introduces the regional model configuration and verification. Results of the mean age simulations are presented in Section 3.4, and those for mean residence time in Section 3.5. Section 3.6 summarizes the results and their relevance to regional ocean circulation.

3.2. Constituent-oriented Age and Residence Time theory (CART)

Following Delhez et al. (1999), Deleersnijder et al. (2001), Delhez et al. (2004), Delhez (2006), and Delhez and Deleersnijder (2006), derivations of mean age and residence time are summarized here.

3.2.1. Mean age

Suppose a water parcel located at **x** at time *t* contains dissolved tracer having an age spectrum concentration distribution $c(t,\mathbf{x},\tau)$, where τ is the age, i.e. the time since the tracer was released into the water. The equation for age spectrum concentration is

$$\frac{\partial c}{\partial t} = p - d - \nabla \cdot \left(\mathbf{u}c - \mathbf{K} \cdot \nabla c \right) - \frac{\partial c}{\partial \tau} \tag{3.1}$$

where p and d are the rates of production and destruction, respectively (in this application these terms are zero, with production effectively entering only in the river source boundary condition), **u** is the flow velocity and **K** is the eddy diffusivity tensor. The last term on the right-hand-side expresses the aging of the tracer. Equation (3.1) can be used to simulate the age spectrum concentration directly, but at considerable computational cost if hundreds of tracers are activated to resolve the age spectrum well.

The concentration of tracer in the fluid is the integral of the age spectrum with respect to age, $C(t,\mathbf{x}) = \int_0^\infty c(t,\mathbf{x},\tau)d\tau$, while the mean age, $a(t,\mathbf{x})$, is the first moment of the age spectrum, $a(t,\mathbf{x}) = \dfrac{\int_0^\infty \tau c(t,\mathbf{x},\tau)d\tau}{C(t,\mathbf{x})}$. If we define an age concentration tracer, $\alpha(t,\mathbf{x}) = \int_0^\infty \tau c(t,\mathbf{x},\tau)d\tau$, then

$$a(t,\mathbf{x}) = \frac{\alpha(t,\mathbf{x})}{C(t,\mathbf{x})}. \tag{3.2}$$

The $\lim_{\tau\to\infty} c(t,\mathbf{x},\tau) = 0$, so integrating (3.1) over τ gives the total concentration of the tracer:

$$\frac{\partial C}{\partial t} = P - D - \nabla\cdot\left(\mathbf{u}C - \mathbf{K}\cdot\nabla C\right). \tag{3.3}$$

Here, $P(t,\mathbf{x}) = c(t,\mathbf{x},\tau=0) + \int_0^\infty p(t,\mathbf{x},\tau)d\tau$ is the source of tracer, and

$D(t,\mathbf{x}) = \int_0^\infty d(t,\mathbf{x},\tau)d\tau$ is the sink. Equation (3.3) is the conservation equation solved in any numerical model. Multiplying (3.1) by τ, then integrating over τ and applying a reasonable assumption, $\lim_{\tau\to\infty} c(t,\mathbf{x},\tau) = 0$, we obtain the age concentration equation:

$$\frac{\partial \alpha}{\partial t} = C + \pi - \delta - \nabla\cdot\left(\mathbf{u}\alpha - \mathbf{K}\cdot\nabla\alpha\right) \tag{3.4}$$

where $\pi(t,\mathbf{x}) = \int_0^\infty \tau\, p(t,\mathbf{x},\tau)d\tau$, and $\delta(t,\mathbf{x}) = \int_0^\infty \tau d(t,\mathbf{x},\tau)d\tau$. The age concentration is coupled with (3.3) through the first term on the right-hand-side; if tracer is present in the fluid then $C > 0$ and the age concentration grows in time proportionately.

If there are no sources and sinks of tracers C and α in the domain interior, the terms π and δ can be removed from (3.4) and implemented though boundary conditions. Dividing (3.4) by C, we obtain

$$\frac{\partial a}{\partial t} = 1 - \nabla\cdot\left(\mathbf{u}a - \mathbf{K}\cdot\nabla a\right), \tag{3.5}$$

which is the ideal age equation of Thiele and Sarmiento (1990) and England (1995).

Equations (3.3) and (3.4) can be solved numerically using an ocean model. I set initial conditions for both C and α of zero and release tracer after the initial time from a source at

the head of the modeled Hudson River. I am therefore asking the question: "how long is it that the fraction of Hudson River water at **x,** *t* has been exposed to the ocean?" Equation (3.2) gives the mean age of river source water everywhere. Where the newly released tracer has not yet reached, *C* is zero and the mean age is undefined. This method is easily implemented in most Eulerian numerical models because it requires only two tracers and the addition of the first term on the right-hand-side of (3.4).

3.2.2. Residence time

We define residence time θ as the time taken by tracer to leave a control domain ω. Consider a mass of tracer located around $\mathbf{x}_0$ (inside the control domain) at time $t = t_0$ with volume V_0 and concentration $C(t_0,\mathbf{x}_0)$,

$$C(t_0,\mathbf{x}) = \begin{cases} C_0 & \mathbf{x} = \mathbf{x}_0 \\ 0 & \mathbf{x} \neq \mathbf{x}_0 \end{cases},$$

that leaves the control domain ω gradually. Some fraction of the tracer leaves the control domain at time t_f having residence time $\theta = t_f - t_0$. The mean residence time of the tracer body in the control domain is

$$\bar{\theta}(t_0,\mathbf{x}_0) = \frac{1}{V_0}\int_{V_0}(t_f - t_0)\mathrm{d}V\,. \tag{3.6}$$

Applying integration by parts and assuming that all of the tracer is flushed out of the control domain eventually, i.e. $V(t_f) = 0$ as $t_f \to \infty$ ($V(t)$ is the volume of the tracer remaining in ω at time t), we can express the mean residence time as

$$\bar{\theta}(t_0,\mathbf{x}_0) = \frac{1}{V_0}\int_{t_0}^{\infty} V(t_f)dt_f\,. \tag{3.7}$$

The volume of the tracer remaining in the control domain at time t_f is an integration of the tracer concentration over the whole control domain,

$$V(t_f) = \int_{\omega} C(t_f, \mathbf{x}) d\omega = \int_{\omega_T} C(t_f, \mathbf{x}) f(\mathbf{x}) d\omega \tag{3.8}$$

where ω_T is the volume of the total model domain which is larger than or equal to ω, and f is a function that delineates the control domain,

$$f(\mathbf{x}) = \delta_{\omega} = \begin{cases} 1 & \mathbf{x} \in \omega \\ 0 & \mathbf{x} \notin \omega \end{cases}.$$

These equations show how point injections of tracer in a model can be used to obtain the residence time. However, one injection only gives the residence time at one place at one time, and to resolve spatial and temporal variability requires many injections and simulations, at substantial computational cost. This problem can be circumvented.

We write (3.8) in inner-product form,

$$V(t_f) = \left\langle C(t_f, \mathbf{x}), f(\mathbf{x}) \right\rangle_{\omega_T} \tag{3.9}$$

and note that (3.3) can be written in propagator form (Moore et al. 2004) $C(t_f,\mathbf{x}) = \mathbf{R}(t_0, t_f)C(t_0,\mathbf{x})$ because it is linear in the concentration, C. Here, $\mathbf{R}(t_0, t_f)$ is the propagator matrix that advances the ocean state from time t_0 to t_f. Applying the bilinear identity of the adjoint operator (Lanczos 1961) to (3.9), we obtain

$$V(t_f) = \left\langle \mathbf{R}(t_0, t_f) C(t_0, \mathbf{x}), f(\mathbf{x}) \right\rangle_{\omega_T} = \left\langle C(t_0, \mathbf{x}), \mathbf{R}^{\dagger}(t_f, t_0) f(\mathbf{x}) \right\rangle_{\omega_T} = V_0 C^{\dagger}(t_0, \mathbf{x}_0) \tag{3.10}$$

Here, $\mathbf{R}^{\dagger}(t_f, t_0)$ is the adjoint operator of (3.3) that propagates information backward from t_f to t_0, and $C^{\dagger}(t_0,\mathbf{x}) = \mathbf{R}^{\dagger}(t_f, t_0)f(\mathbf{x})$ is the adjoint state. The corresponding adjoint equation is

$$-\frac{\partial C^{\dagger}}{\partial t_0} = \nabla \cdot \left(\mathbf{u} C^{\dagger} + \mathbf{K} \cdot \nabla C^{\dagger} \right), \tag{3.11}$$

which is integrated backward in time with initial conditions at t_f of $C^\dagger(t_f,\mathbf{x}) = f(\mathbf{x}) = \delta_\omega$. Equation (3.10) shows that $C^\dagger(t_0,\mathbf{x}_0)$ is the fraction of tracer that was initially located at $\mathbf{x}_0$ at time t_0 that remains in the control domain at time t_f, i.e.

$$C^\dagger(t_0,\mathbf{x}_0) = \frac{V(t_f)}{V_0},$$

and from (3.7), we have

$$\bar{\theta}(t_0,\mathbf{x}_0) = \int_{t_0}^{\infty} C^\dagger(t_0,\mathbf{x}_0)\,dt_f\,. \tag{3.12}$$

The ocean state is unsteady, so the fraction of tracer remaining differs for different time windows $[t_0, t_f]$ even with same window duration. That is, $C^\dagger$ is a function of both t_0 and t_f, i.e. $C^\dagger = C^\dagger(t_0, t_f, \mathbf{x})$.

Let us now define a time T_f far in the future, i.e. $T_f >> t_0$, when all tracer has been flushed out of the control domain, that is

$$C^\dagger(t_0,T_f,\mathbf{x}) = 0\,. \tag{3.13}$$

Integrating (3.11) over t_f from t_0 to T_f, applying Leibniz Integral Rule and using (3.12), we obtain the equation for the mean residence time:

$$-\frac{\partial\bar{\theta}}{\partial t_0} = \delta_\omega + \nabla\cdot\left(\mathbf{u}\bar{\theta} + \mathbf{K}\cdot\nabla\bar{\theta}\right). \tag{3.14}$$

Here, $\bar{\theta} = \bar{\theta}(t_0,\mathbf{x})$. Integration of (3.14), backward in time, gives the mean residence time everywhere in the control domain for any time within the simulation window. However, the initial condition $\bar{\theta}(T_f,\mathbf{x})$ is unknown. Delhez et al. (2004) proposed initializing (3.14) with $\bar{\theta}(T_f,\mathbf{x}) = 0$ and integrating sufficiently long that the influence of the initial condition vanishes; the required time can be determined from the solution to (3.11). The argument

goes as follows. The initial condition of (3.11) is $C^{\dagger}(t_f, t_f, \mathbf{x}) = \delta_{\omega}$, and due to the lack of forcing $C^{\dagger}(t_0, t_f, \mathbf{x})$ gradually diffuses away as the backward integration proceeds until $C^{\dagger}(t_0, t_f, \mathbf{x})$ approaches 0 and the effect of the initial condition vanishes. By virtue of the similarity of (3.11) and (3.14), we expect the effect of initial conditions to decay similarly in both equations. Therefore, we integrate (3.11) and (3.14) simultaneously and the solution to (3.14) becomes valid when the solution to (3.11) approaches zero.

If the model domain is larger than the control domain ($\omega \subset \omega_T$), there are two ways to treat the area beyond the control domain (Delhez 2006, Delhez and Deleersnijder 2006). The first is to force the adjoint model state $\overline{\theta}(t_0, \mathbf{x})$ to be zero everywhere beyond the control domain. This is termed the *strict mean residence time*. In the analysis of Lagrangian drifters this is equivalent to ceasing to track a drifter the first time it crosses the control domain boundary. The second way is to let the adjoint solution evolve freely outside the control domain. This approach essentially gives the accumulated time spent by tracer in the control domain, which is called the *exposure time* (Monsen et al. 2002). In tracking drifters, this allows for reentry into the control domain.

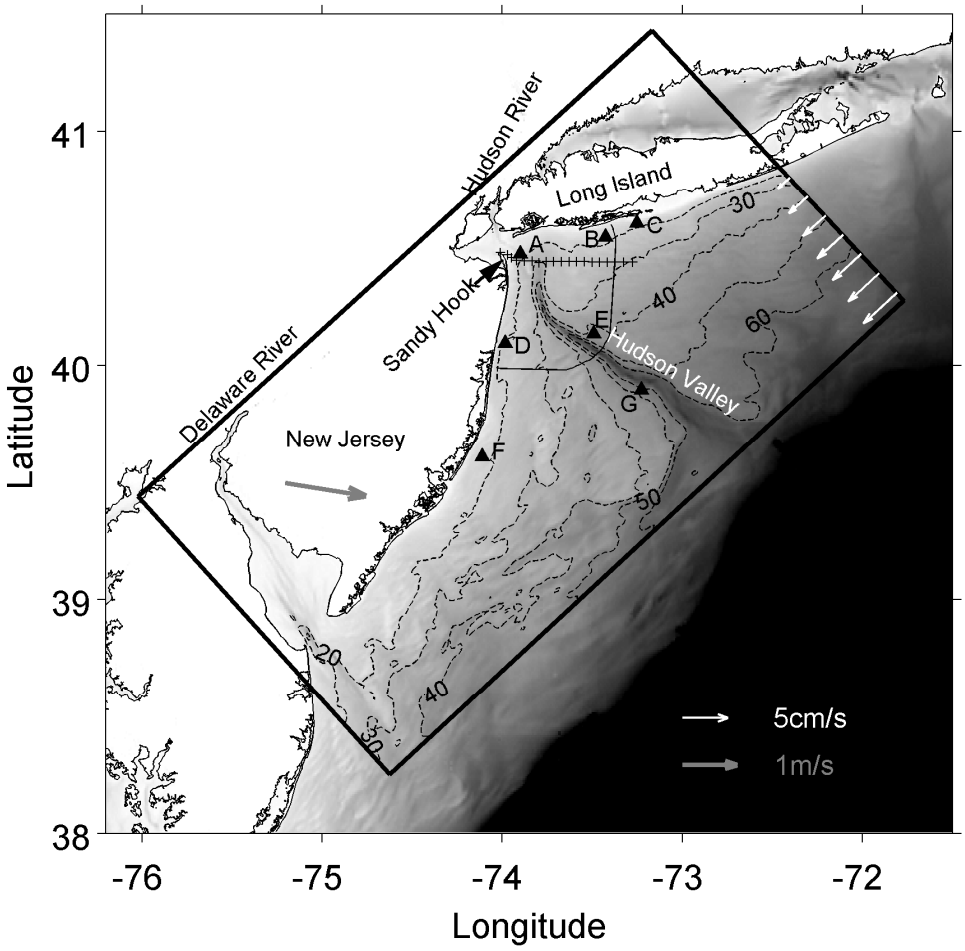

Figure 3.1. The study domain. The black frame indicates the model domain; Bathymetry of the New York Bight is in grayscale; Dashed lines are contours of model isobaths in meters; Gray arrow on land depicts the 2-year (2005-06) mean wind over this area; White arrows at the northeast boundary of the model domain represent barotropic inflow boundary condition on that boundary; Solid triangles are the sites for mean age and residence time referred to in the text; The line of plus symbols is the ship track on 9 Apr 2005 referred to in Section 3; The thin solid line depicts the control domain used in the residence time simulation.

3.3. Model configuration and verification

The first terms on the right-hand-sides of (3.4) and (3.14) were added to the ROMS code for this study. The model setup in this chapter is similar to the one in Chpater 2. Figure 3.1 depicts the model domain. The model has 30 vertical layers and horizontal resolution of about 1 km. Chapman (1985) and Flather (1976) conditions are used for sea level elevation and barotropic velocity on the model perimeter, respectively. Tidal harmonics extracted from a regional tide simulation (Mukai et al. 2002) and remotely forced along-shelf currents deduced by Lentz (2008) are imposed on the open boundaries. An Orlanski-type radiation (Orlanski 1976) open boundary condition is used for 3-dimensional momentum, temperature and salinity, and the age and residence time passive tracers are clamped to zero on the open boundaries. The model applies bulk formulae (Fairall et al. 2003) at the sea surface using atmospheric boundary layer conditions from the North America Regional Reanalysis (NARR) (Mesinger et al. 2006). River discharge was obtained from USGS Water Data.

A comparison of modeled and observed salinity along the ship track in Figure 3.1 is presented in Figure 3.2. The observations are from a ship-towed undulating instrument and surface CTD on 9 April 2005 (Chant et al. 2008a). The model and observations show agreement in the surface salinity and vertical variation of the halocline, although the model shows a bias toward higher salinity in deep water and the low salinity anomaly that reaches 73.4^{o}W in the observations does not extend so far eastward in the model. We note that there has been no assimilation of observations in this simulation. Model initial conditions based on a multi-year shelf-wide climatology are somewhat more salty than mid-shelf conditions

in 2005, and we expect this presents resistance to the spreading of the river plume, and prevents low salinity water penetrating far to the east.

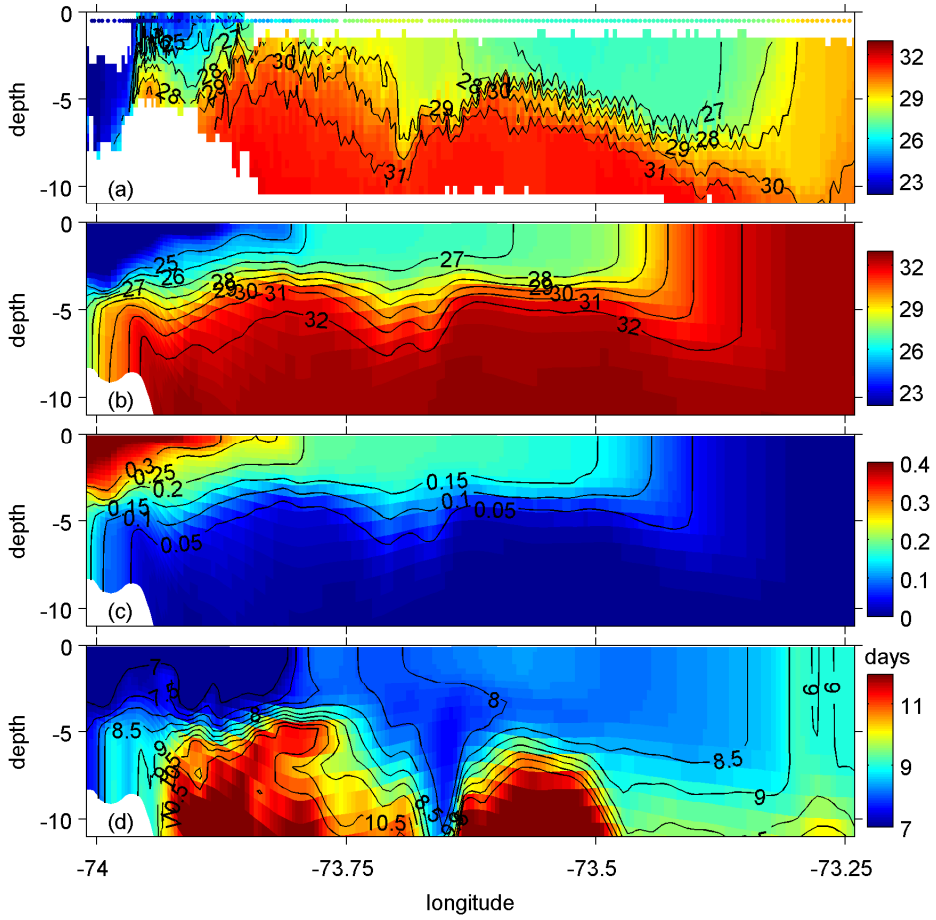

Figure 3.2. Cross-section of (a) observed salinity, (b) modeled salinity, (c) modeled freshwater concentration, and (d) modeled mean age along the ship track in Figure 3.1.

To simulate the mean age of Hudson River source water on the shelf, two tracers are activated in the forward ROMS model. The first is conservative and satisfies (3.3) with unit concentration in the Hudson River inflow, while the second represents the river water age concentration and satisfies (3.4). Its value is zero in the river inflow. Mean freshwater age is computed with (3.5). Regions where the concentration is lower than 10^{-5} are

assumed to be free of Hudson River source water and age there is undefined. To verify that the mean age calculation is correct, I conducted a 60-day simulation solving (3.1) with the full age spectrum discretized into 120 age intervals, while also computing the mean age from a concurrent simulation of C and α. The full age spectra at sites A and E in Figure 3.1 at day 60 are plotted in Figure 3.3; the mean age computed from the age spectra is marked, along with the corresponding mean age α/C from (3.2). Calculating mean age using the two-tracer approach clearly works well.

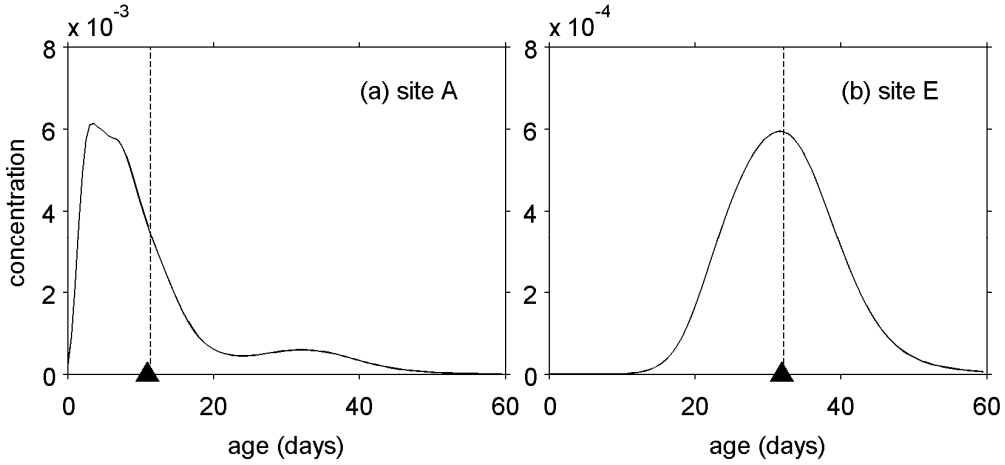

Figure 3.3. Concentration distribution function (solid curves) at (a) site A and (b) site E at May 10th, 2005; Dash lines indicate the mean age computed from the concentration distribution functions; triangles indicate the mean age given by the mean age model simulation at corresponding places and time.

Vertical cross-sections of modeled freshwater concentration and mean age are included in Figure 3.2 at times corresponding to the ship-board observations. The freshwater

concentration has the same pattern as modeled salinity, while the mean age outlines a body of relatively young (8.5 days) water around 73.4^{o}W at the place where a similar body of freshwater was observed. This supports the claim that river water reached that location in the model, but in a smaller amount.

In the results that follow, two years of simulation (2005-2006) following a spin-up year (2004) form the basis of the freshwater mean age analysis.

In the residence time simulations, the control domain is defined as the surfacemost 10 m of the smoothed rectangular area at the NYB apex shown in Figure 3.1. Ocean states from the 3-year model simulation are stored every three hours for the background state of the adjoint model. In the adjoint model, two tracers representing the fraction of tracer remaining and the mean residence time (equations (3.11) and (3.14)) are activated. The initial condition for the fraction of tracer remaining is one inside the control domain and zero everywhere outside; the mean residence time is initially zero everywhere. The adjoint model is integrated from the end of 2006 back to the beginning of 2005. No external constraints are applied to the adjoint model in the places beyond the control domain, which means residence time calculated here is the so-called exposure time. Because of tidal oscillations across the control domain perimeter, the strict residence time would misrepresent the total time river source water spends in the NYB area. For the sake of convenience, the term residence time is used here.

To test the validity of the adjoint-based residence time theory and model, simulations were conducted where passive tracers injected in the forward model at selected times and locations were followed for 120 days (Figure 3.4). Mean residence time computed from the

fraction of each tracer remaining in the control domain is indicated by the dashed lines in Figure 3.4. Comparison with the mean residence time obtained from the adjoint model (triangles in Figure 3.4) shows the two approaches agree.

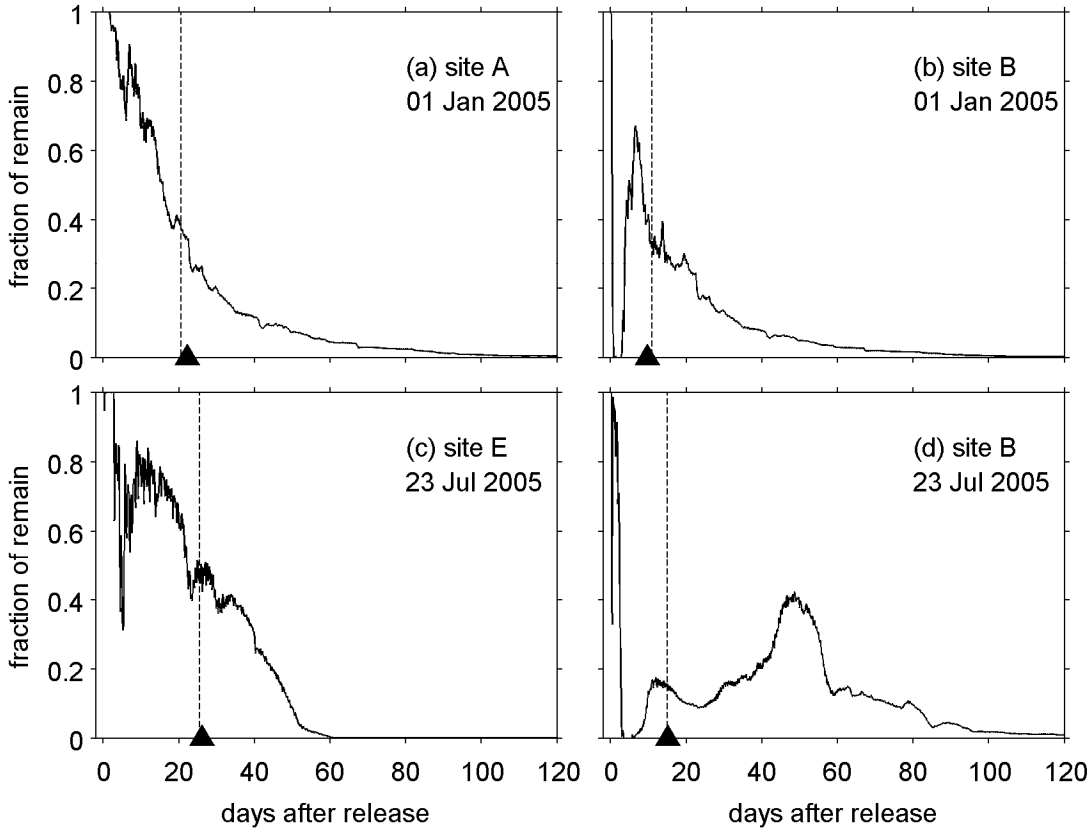

Figure 3.4. Fraction of tracer remaining in the control domain after unit releases at selected sites (see Figure 3.1) at different times; Dashed lines indicate the mean residence time computed from the time series; Triangles indicate the mean residence time at the corresponding places and times given by the mean residence time adjoint model simulation.

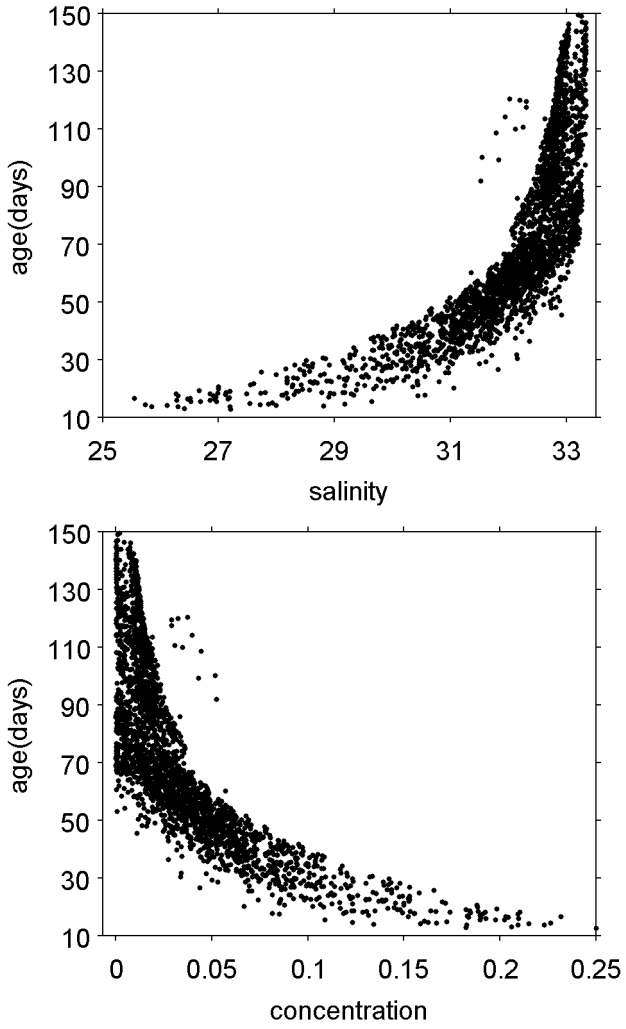

Figure 3.5. Relationship between (top) salinity and (bottom) freshwater concentration and mean age at random locations in the model domain.

3.4. Mean Age

In studies of river plume dispersal, scientists have long used salinity or concentration of a river tracer to estimate the time that river source water has been exposed in the ocean. To

contrast this approach with the more rigorous mean age calculation, Figure 3.5 compares mean age, salinity and freshwater concentration at selected locations in the model. A positive relationship between mean age and salinity, and inverse relationship between mean age and freshwater concentration can be seen, but by no means are the relationships linear. As the water becomes saltier and the concentration becomes lower, the range of the mean age become large. At salinity 33, the mean age is from 70 days to 150 days. This is to be expected because the volume of river water discharged over this timescale is much smaller than that into which it mixes, and once the salinity becomes close to the background value of mid-shelf water subsequent mixing changes the salinity little, yet the water continues to age. The same logic applies to the freshwater concentration. Figure 3.5 suggests that estimating age from salinity or tracer concentration has limited utility, and could be very misleading for timescales of more than two weeks in the case of the Hudson River plume.

3.4.1. Comparison between mean age and satellite measurements

One of the objectives in studying age and residence time is to provide estimates of the rate of physical dispersal and mixing of the river plume for future comparison to timescales of regional biogeochemical processes. I will not present here any biogeochemical process observations, or results of coupled biogeochemical simulations, but before presenting an analysis of the model results I compare snapshots of simulated mean age with an empirical proxy for river water age derived from satellite optical observations.

Waters near the coast are turbid and optically complex (Schofield et al. 2009). The major optical constituents of the Hudson plume are phytoplankton, sediment, colored dissolved organic matter (CDOM) and detritus, and the relative concentration and

therefore optical signal of these change over time (Cahill et al. 2008, Schofield et al. 2009). In river source plumes, CDOM is the dominant optical constituent; however as the plume ages the CDOM signal decreases relative to phytoplankton and detrital signatures. These changes produce a spectral shift in the remote sensing reflectance (Ramadurai 2008). The ratio of reflectance at 490 nm to 670 nm wavelengths is sensitive to the relative optical signatures of CDOM and phytoplankton, and therefore the time that river source waters have been exposed in the ocean waters. This ratio, which I henceforth refer to as the 490/670 band ratio, can be computed from satellite observations by the Sea-viewing Wide Field-of-view Sensor (SeaWiFS).

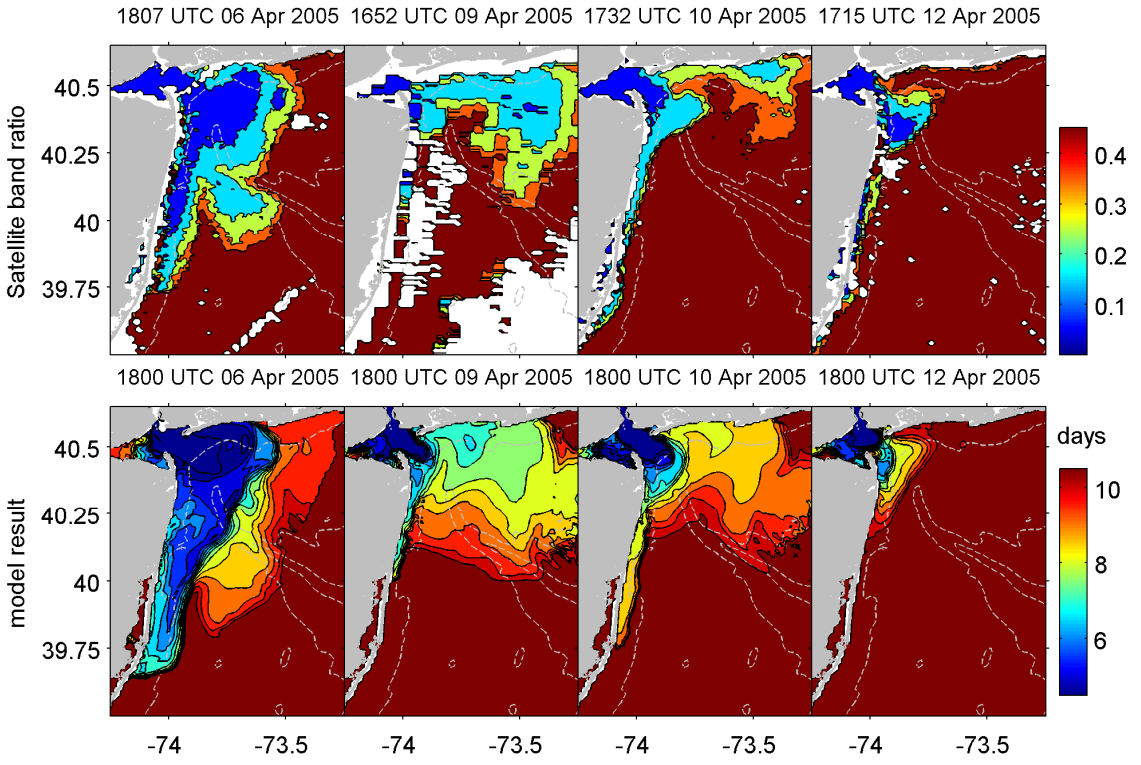

Figure 3.6. Snapshots of (top row) the ratio of SeaWiFS observed water leaving radiance at 490 nm to 670 nm and (bottom row) modeled freshwater mean age at the sea surface. Dashed lines show 20, 40 and 60 m isobaths.

Figure 3.6 shows many similarities in the patterns of observed 490/670 band ratio and modeled surface freshwater age during the 2005 LaTTE field experiment. Note that there has been no assimilation of satellite data in these simulations; the model reproduces well the transport pathways of river water dispersal (Chapter 2) and we expect some pattern correspondence in optical characteristics that are strongly related to the river source waters. If indeed the 490/670 band ratio is a useful proxy for water age, we further expect some correspondence in values across the 4 realizations in Figure 3.6. To quantify the relationship, the 490/670 band ratio and mean age within the river-influenced area are plotted in Figure 3.7. The correlation is 0.73, which is significant at the 95% level. A least square fit gives: $a = 1.3 + 25 \times r$, where a is the mean age and r is the band ratio. This simple relation may have applications in fieldwork where the age of the Hudson River influenced waters is needed in real time. I cannot yet comment on how robust this relationship is, or whether it can be employed for rivers other than the Hudson, but empirical relationships could likely be derived following the same methodology.

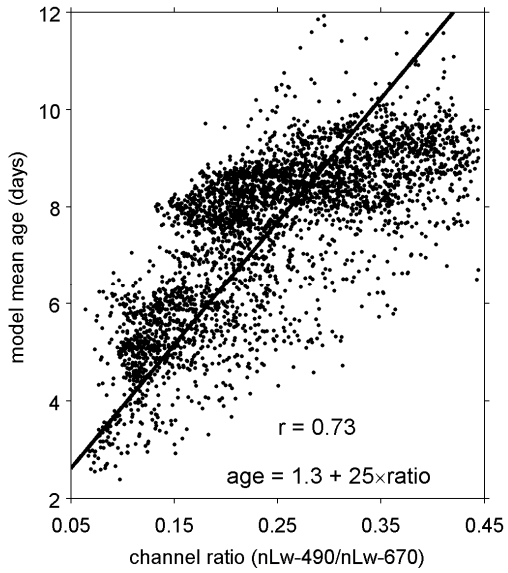

Figure 3.7. Relationship between modeled mean age and the ratio of satellite observed water leaving radiance (490 nm : 670 nm). The correlation coefficient r = 0.73 is significant at the 95% level. Solid line is the least square fit: mean age = 1.3 + 25 × radiance ratio.

3.4.2. Temporal variability of the mean age

To examine temporal variability of mean age, time series of surface freshwater water concentration and mean age at sites A, C, F, and G in Figure 3.1 are plotted in Figure 3.8 along with river discharge and wind. At all the sites, the mean age fluctuates dramatically between 10 and 170 days within a few days, similar to the timescale of wind variability. Fluctuations of mean age and freshwater concentration are inversely related. Site A near the estuary mouth shows the least variability with mean age fluctuating from 10 to 40 days out of phase with the freshwater concentration and river discharge (which are closely correlated). Not surprisingly, mean age at the estuary mouth is closely related to river

discharge. Site C near the Long Island coast lies in the pathway along which freshwater advects eastward, principally in fall and winter. Accordingly, the mean age at site C is arguably lower in winter. Site F falls in the New Jersey coastal pathway that Chapter 2 identified as dominating freshwater advection in winter and spring. Seasonality of this transport manifests itself in the time series of mean age: there are frequently lower age values in winter and spring and relatively high and unsteady values in summer and fall. Site G lies in the mid-shelf pathway that dominates the summer months and carries freshwater directly offshore – mean age at site G is generally low in summer. The mean age at site G is also low in winter 2005-2006, presumably because of persistent westerlies during that time. This will be seen later in the correlation between mean age and wind.

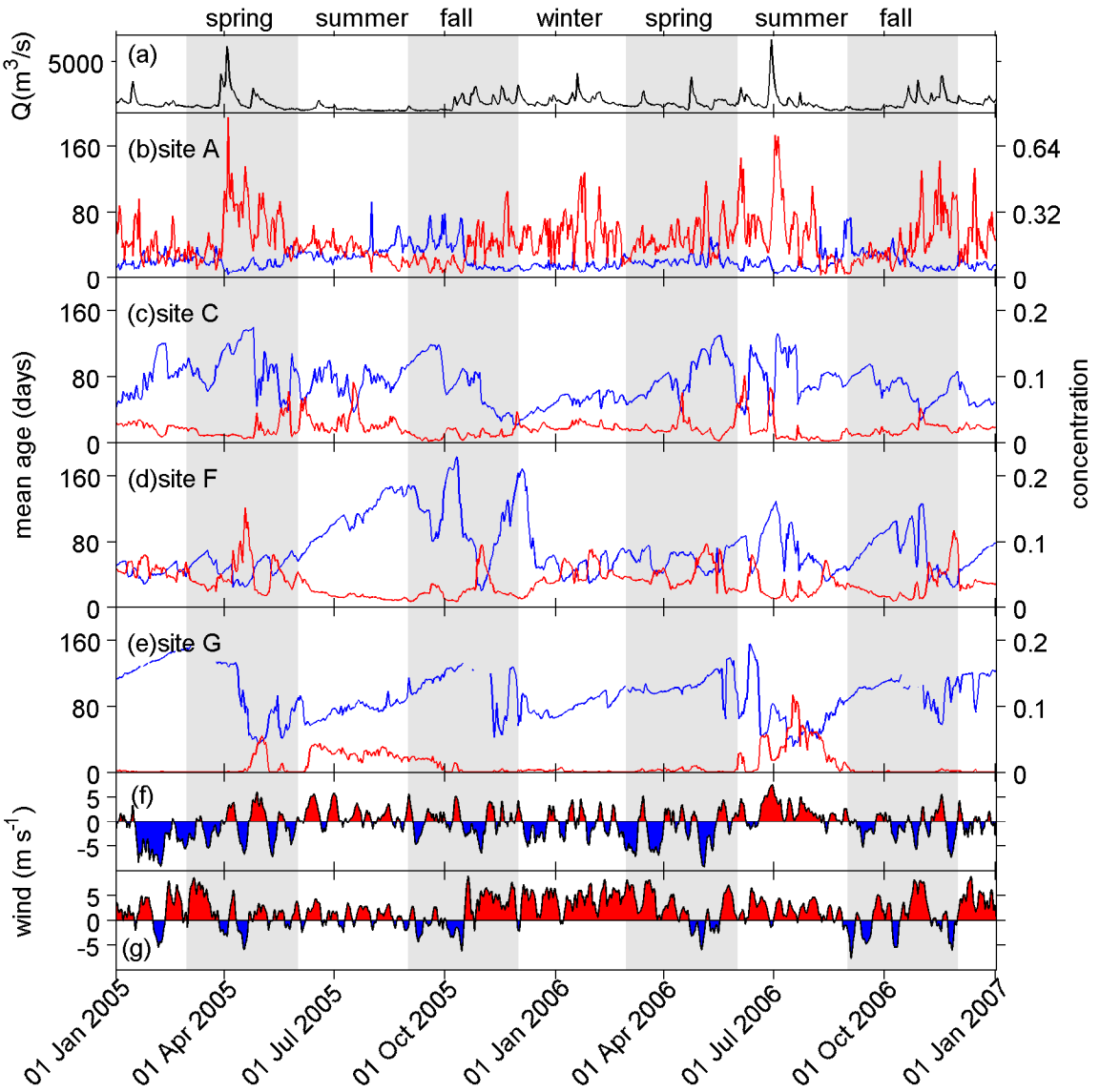

Figure 3.8. Time series of (a) the Hudson River discharge, (b-e) freshwater concentration (red lines) and mean age (blue lines) at different sites (see Figure 3.1 for locations of sites A, C, F and G). The bottom panels show the filtered (f) meridional (positive toward north) and (g) zonal (positive toward east) components of the wind in the New York Bight.

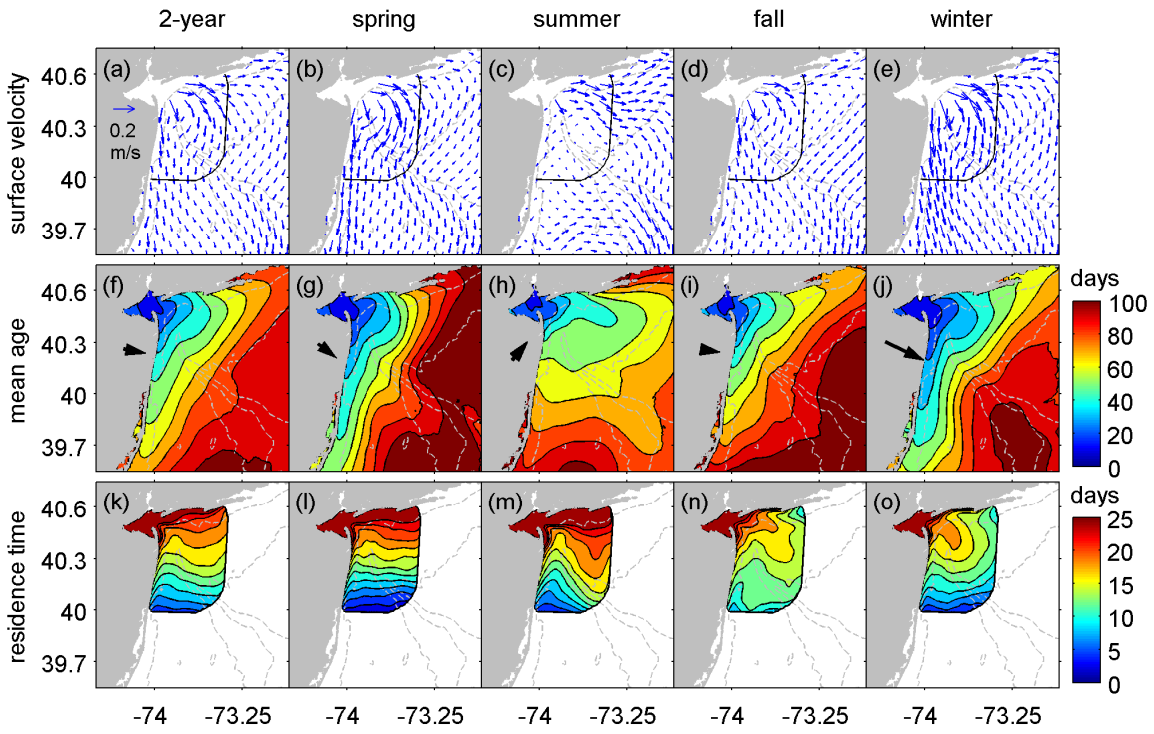

Figure 3.9. Two-year mean and seasonal averages of (top row) surface current, (middle row) surface mean age, and (bottom row) surface residence time. Black arrows in middle row figures indicate direction and relative strength of the average wind stress. Dashed lines show the 20, 40 and 60 m isobaths.

Figure 3.9 presents two-year and seasonal averages of the mean age and surface current. Consistent with the three-pathway pattern of surface freshwater dispersal described in Chapter 2, the two-year average shows furthest penetration of young water along the New Jersey coast, secondary penetration along the Long Island coast, and at about 40°N a weak offshore tongue of moderate age water along the HSV. The seasonal variation of mean age echoes the freshwater dispersal seasonality noted in Chapter 2. In spring, relatively young water penetrates along the New Jersey coast further than in the

two-year mean and the offshore extent of moderate age water is more obvious. In summer, transport of young water along the New Jersey coast is almost completely shut down. Instead, dispersal is towards the east and the tongue of moderate age water along the HSV is pronounced, consistent with the dominance of the mid-shelf freshwater pathway driven by upwelling favorable wind. The pattern in fall is similar to spring except that there is less young water along the New Jersey. In winter the coastal boundary currents are stronger and young water is found considerably further along both coasts than in the two-year mean, while evidence of offshore flow along the HSV is absent.

Patterns and seasonality of freshwater mean age are readily explained in terms of mean circulation and freshwater dispersal pathways, and we can conclude that advection processes control the dispersal of Hudson River source water in the NYB.

3.4.3. Relationship of mean age with river discharge and wind

In Figure 3.8, mean age at site A appears correlated with the Hudson River discharge while temporal variability at sites C, F, and G has timescales more akin to the wind. To quantify this, correlations of mean age with river discharge and wind are shown in Figures 3.10a and 3.11, respectively. (The wind time series used is the NARR data at 40.5^{o}N, 73.75^{o}W.) The mean age pattern depends on the freshwater travel history, so I apply a weighted running mean time filter to river discharge and the wind prior to the correlation analysis. This approach was used in Chapter 2 with the filter $f_k(t) = k^{-1}\int_{-\infty}^{t} f(t')e^{(t'-t)/k}dt'$, where $f(t)$ is the wind component at time t, and $f_k(t)$ is the resulting convolution with weights that decay exponentially with scale k (Austin and Barth 2002) chosen to be characteristic of freshwater advection events in the NYB. Tests with values of k from 1 to

50 days (not shown), and time lags between wind and mean age ranging from -10 to 10 days, show few differences in the correlation pattern. I use k =10 days and zero lag for results in Figures 3.10a and 3.11. Note that since I consider correlations between scalar and vector component time series, I need only show plots for wind direction in two quadrants – e.g. the pattern of correlation with a strictly southerly wind is the negative of the pattern for a northerly wind.

In Figure 3.10a the correlation between river discharge and mean age is negative for an area within 50 km from the New Jersey coast and as far south as Tuckerton, clearly outlining the area of direct influence of river discharge on coastal waters. Interestingly, the significant correlation extends much less far along the New York coast.

Results that are evident from Figure 3.11 are: (i) Easterly wind and mean age everywhere are positively correlated; (ii) as wind direction becomes increasingly southeasterly to southerly, a negative correlation emerges offshore and spreads shoreward; (iii) southerly wind is positively correlated with surface mean age on the New Jersey coast and negatively correlated with that offshore; and (iv) significant negative correlation occupies most of the coastal area when wind is westerly. What is occurring is that easterly wind pushes waters that have aged offshore back toward the coast, thereby increasing the mean age, while the opposite occurs for westerly winds that favor rapid dispersal of water offshore. Southerly winds cause upwelling on the New Jersey coast which drives younger water from the coastal current eastward and lowers mean age offshore, while uplifting older deep water to the surface at the coast increasing the mean age there.

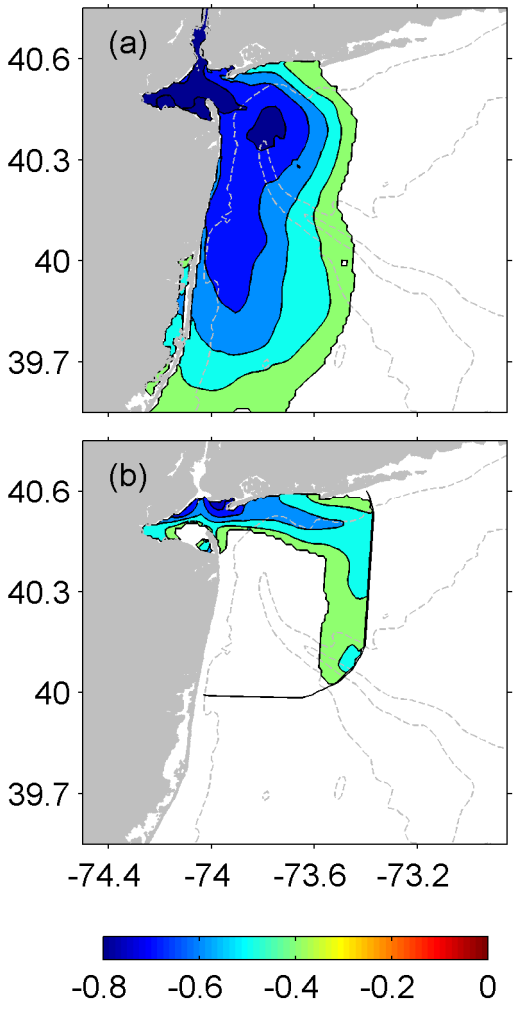

Figure 3.10. Correlation between (a) surface mean age and (b) surface mean residence time and 10-day time scale running mean low-pass filtered Hudson River discharge. Only correlations significant at the 95% level and greater than 0.3 are plotted. Contours are in 0.1 intervals. Dashed lines show the 20, 40 and 60 m isobaths.

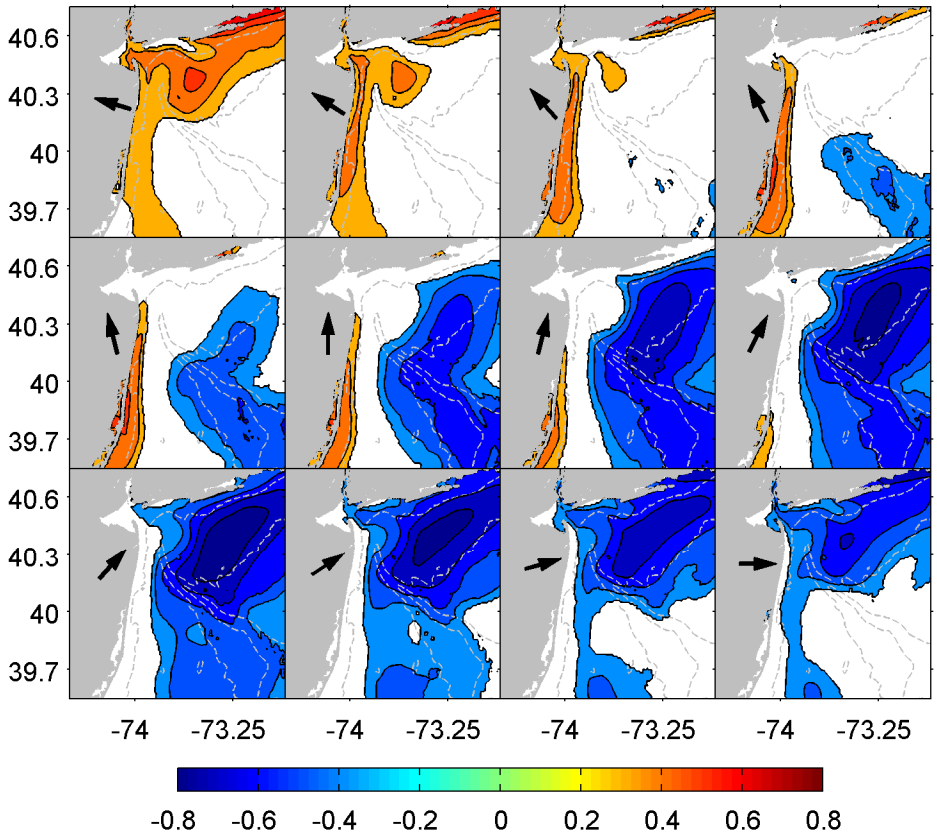

Figure 3.11. Correlation between surface mean age and 10-day time scale running mean low-pass filtered wind components in different direction. Arrows on land depict the wind direction. Only correlations significant at the 95% level and greater than 0.3 are plotted. Contour interval is 0.1. Dashed lines show the 20, 40 and 60 m isobaths.

3.5. Mean Residence Rime

Residence time has been used in coastal ocean studies of water renewal (Monsen et al. 2002) and biogeochemical processes (Brooks et al. 1999, Duarte et al. 2001). Residence time can be crudely estimated by dividing a total volume by a characteristic flushing rate,

or more accurately by releasing Lagrangian particles or Eulerian tracers into numerical models, the computational cost of which can be heavy. The capability, introduced here, of computing mean residence time for every location in a control domain at any time with a single adjoint model integration is a significant advance that provides the ability to study spatial and temporal heterogeneity of residence time and its connection with external forcing.

Because we are interested in the duration that river source water stays in the NYB, residence time in this study is defined as the numbers of days, on average, it takes the water *at a particular time and location* to be flushed out of the control volume defined as the surfacemost 10 m of the smoothed rectangular area shown in Figure 3.1.

3.5.1. Temporal variability of mean residence time

Time series of mean residence time at four different sites in the control domain are plotted in Figure 3.12 along with the fraction of tracer remaining at 1 January 2007 and wind. Recall from Section 2 that the residence time calculation is only valid once the fraction of remaining tracer in the adjoint integration is zero; by 1 September 2006 the tracer has vanished at all locations plotted in Figure 3.12 and the 4 months September-December 2006 is excluded accordingly from the analysis.

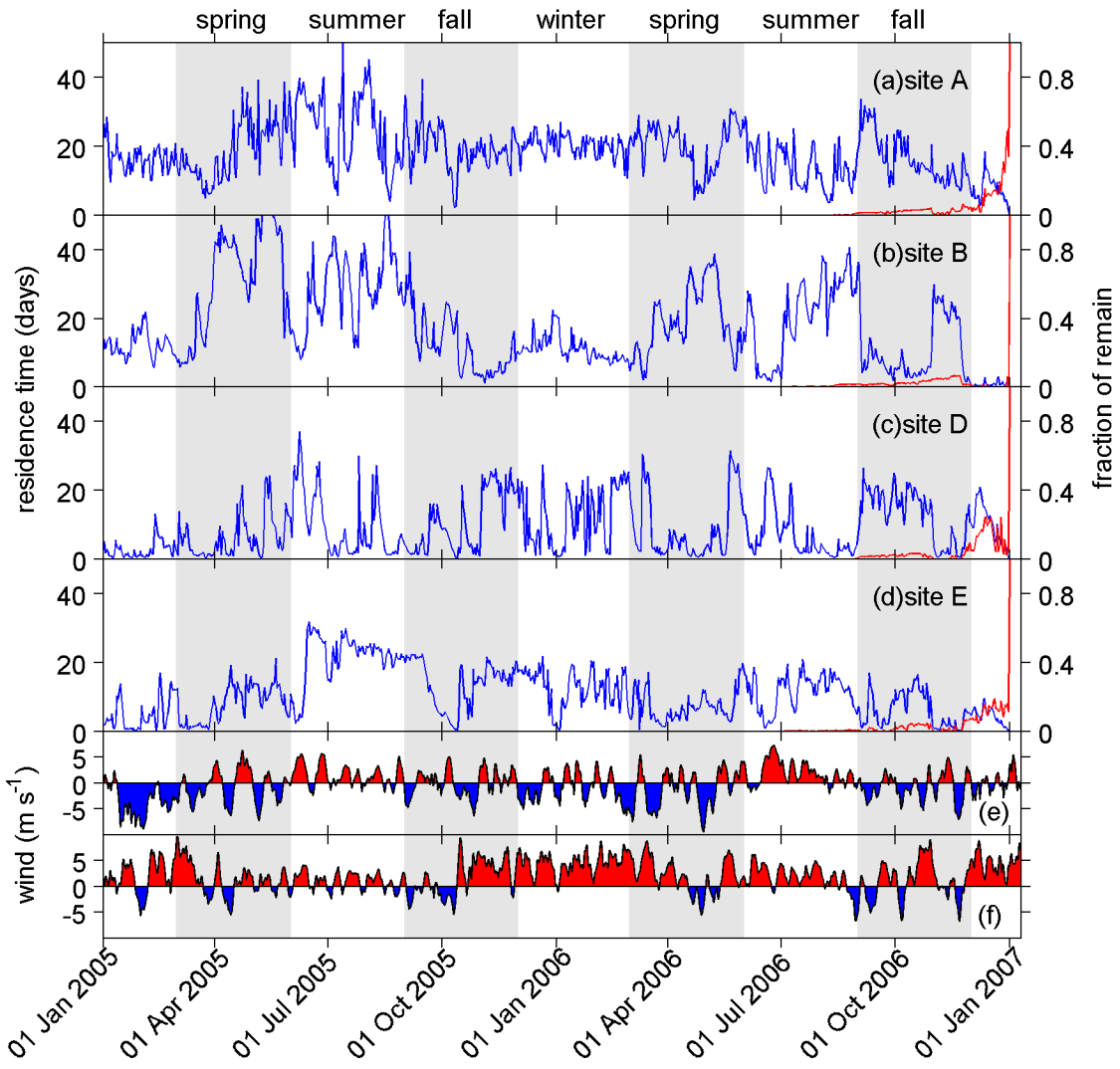

Figure 3.12. Time series at different sites (a-d) of mean residence time (blue lines) and fraction of tracer remaining in the control domain (red lines) (see Figure 3.1 for site locations), and 10-day running mean filtered wind components in the (e) meridional and (f) zonal direction.

Before discussing these results, I restate what is being calculated in this application of the adjoint-based residence time method: Each blue time series in Figure 3.12 shows the time scale in days, after any particular date in the time series, that it will subsequently take

for passive tracer released at that location to be flushed out of the control volume. Residence time at site A near the harbor mouth stays around 20 days except during summer 2005 when it often reaches 40 days. At site B, close to the eastern boundary of the control domain, residence time is generally low in winter but higher in spring and summer. The residence time at site D on the New Jersey coast does not show obvious seasonal dependence but generally varies in opposition to site B – the correlation between the time series for sites B and D is -0.36, and is significant at the 95% level. Sites B and D are located at opposite ends of the control domain and a negative correlation is not unexpected. At site E mid-shelf the residence time is generally lower than 20 days except during summer 2005. The correlation between residence times at site D and B is 0.27, which is significant (95% level). These sites are both located north of the HSV, which Chapter 2 showed places them in a related circulation regime and the similarity in residence time variability is therefore reasonable. The residence times at sites A, B and E all exhibit generally high values in summer, which is clear in the seasonal average residence time in Figure 3.9 (bottom row).

The 2-year average residence time shown in Figure 3.9 has highest values in the estuary and along the Long Island coast and lower values south of the HSV, and these features are shared by all the seasonal averages though differences between the seasonal averages exist. Mean residence time along the Long Island coast in spring and summer is much higher than in fall and winter, consistent with the sense we obtained from the time series (Figure 3.12). In summer, the HSV clearly serves as a barrier between zones of relatively high residence time to the north, and low residence time to the south. The influence of the HSV in other seasons is not as obvious. In winter, a circular feature of high residence time occurs in the

New York Bight apex area that is similar to the river water bulge in Chapter 2, indicating that in winter the recirculating bulge traps water and prolongs its residence in the NYB apex.

Residence time is very large along the Long Island coast in summer, all the way to the eastern edge of the control volume, despite there being a strong eastward surface current that transports water swiftly along the Long Island coast enabling it to quickly exit the control domain. The mechanism behind this apparent paradox is revealed by the concentration of a passive tracer released at site B during summer 2005; the time series of the fraction of tracer remaining in the control domain is plotted in Figure 3.4d. There is indeed a rapid decline of tracer right after release, but as time proceeds a substantial fraction of the tracer returns: some 40% of the initial release at site B reenters the control domain 50 days later . What has occurred is that eastward flow along the Long Island coast in summer has carried the tracer out of the control domain, but the tracer has remained nearby on the inner shelf and the change to southwestward flow in the fall has pushed tracer back into the control domain, from which it subsequently exits through the southern boundary. Flow across the eastern boundary of the control domain is only a temporary outlet for tracers in the NYB apex – it is transport across the southern boundary that is the real exit.

This reentry process is given full consideration in the adjoint-based residence time method because I compute the accumulated tracer exposure time as explained in Section 3. This is potentially very important when employing residence time estimates in studies of, for example, river-borne pollutant dispersal, degradation and bioaccumulation, phytoplankton growth and secondary productivity, or larval transport and settlement. All

of these are influenced by processes active on timescales of a few to several tens of days, and the *strict mean residence time* as opposed to *exposure time* could represent timescales significantly differently.

3.5.2. Relationship of mean residence time with river discharge and wind

Figures 3.10b and 3.13 shows correlations of residence time with the Hudson River discharge and the wind, respectively. Because the dispersal of water over the finite expanse of the control region relies on the accumulated effect of buoyancy- and wind-driven flow over some time, the river discharge and wind components were weighted using a running mean filter, $f_k(t) = k^{-1}\int_t^{+\infty} f(t')e^{(t-t')/k}dt'$, similar to that used in Section 4.3. Note that the filter acts on times strictly *after* the release time, because it is river discharge and wind in the future that subsequently influences the dispersal and residence time of the tracer. Different filter scales *k* and time lags were tested but, again, few differences occur in the correlation patterns (not shown). Ten days filter time scale and zero lag are used in the results in Figures 3.10b and 3.13.

Figure 3.10b shows that significant correlation between river discharge and residence time occurs only along the Long Island coast and eastern boundary of the control domain, and is negative, i.e. high river discharge decreases residence time for waters starting from a those locations. This pattern of negative correlation echoes the outer boundary of the circular freshwater pathway in the NYB shown in Chapter 2. It presumably occurs because high river discharge accelerates the bulge and sweeps water at the outer extent of the recirculation from the control domain.

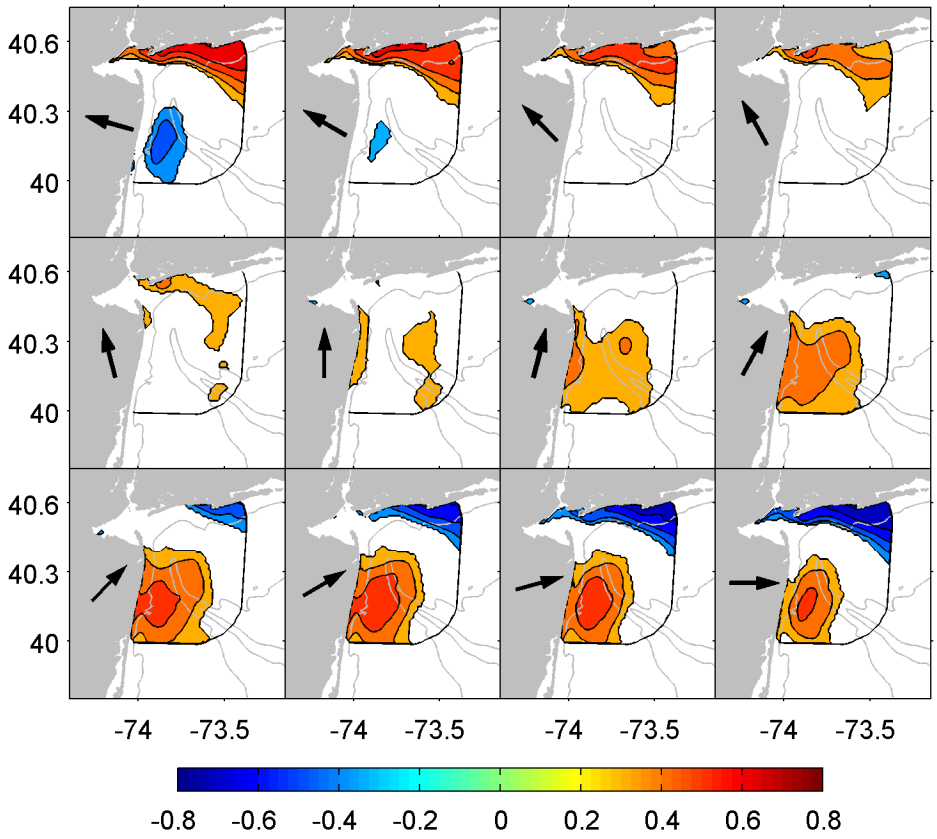

Figure 3.13. Correlation between surface mean residence time and filtered wind components in different directions. Arrows on land depict the wind direction. Only correlations significant at the 95% level and greater than 0.3 are plotted. Contour interval is 0.1. Gray lines show the 20, 40 and 60 m isobaths.

Figure 3.13 shows easterly wind is positively correlated with residence time near the Long Island coast, but negatively correlated with residence time between the New Jersey coast and HSV. We have already seen that easterly winds drive westward flow along the Long Island coast that prolong residence time there, whereas westerly winds flush Long Island coastal waters and lower residence time. But easterly wind also pushes to the west

surface waters that lie between the New Jersey coast and the HSV, strengthening the New Jersey coastal current (Choi and Wilkin 2007) and lowering the time waters from this region stay in the control domain. When winds are more southeasterly, the pattern of negative correlation between New Jersey and the HSV disappears. A positive correlation between residence time and winds from the south and west occurs along the New Jersey coast and inner shelf because either upwelling (southwesterly wind) directs surface water northward and eastward, extending the time water next to the New Jersey coast stays in the control domain, or downwelling (northeasterly wind) pushes surface water into the coastal current which promptly exits the control domain, or both.

3.6. Summary

This study extends modeling studies in Chapter 2 and by Choi and Wilkin (2007) to consider in detail the timescales associated with dispersal of Hudson River source water within the New York Bight. I have restated Constituent-oriented Age and Residence-time Theory and summarized application of the theory in ROMS – including verification that two-tracer-based mean age and adjoint-based residence time methods give the same results as more conventional multi-tracer methods.

The mean age results here should be interpreted as the mean time since water at a given location and time entered into the ocean via the Hudson River. The *mean* recognizes that a water mass at any location comprises some younger water that has traveled relatively rapidly to the site, mixed with older waters that have taken a less direct route.

The model results show that mean age and inner shelf salinity are related, as is typically assumed in river-influenced areas, but this relationship is not linear; there is value in

directly simulating age if the objective is explicit consideration of dispersal and dilution timescales. A more linear relationship, though noisy, was found between modeled surface mean age and the ratio of satellite-measured radiances at 490 and 670 nm, which has been proposed as an empirical proxy of age. A least-square fit of age on band ratio is a potentially useful tool for estimating water age from remotely sensed observations, though analysis of a more extensive data set is required to formulate a robust relationship.

Time series of mean age at different sites in the NYB show significant temporal and spatial variation in mean age, indicating that the tracer field is being stirred but has not yet been homogenized by mixing processes. Within 50 km of the New Jersey coast, mean age is strongly influenced by the river discharge, but no such influence is obvious for the area beyond. Rather, temporal variability of mean age on the scale of days is consistent with a dominant influence from wind, and this carries through to seasonal differences in mean age patterns related to seasonality in prevailing wind. The patterns of seasonally averaged mean age are consistent with knowledge of the mean circulation from previous studies: young water penetrates furthest along the New Jersey coast in winter and spring when river discharge feeds into a southward coastal current that is unopposed by winds in these seasons; an offshore directed tongue of young and moderate age water appears in summer when more prevalent southerly upwelling favorable winds drive offshore movement of surface waters. Analysis of correlations between mean age and wind shows that easterly winds increase mean age of surface water adjacent to the coasts, whereas southerly winds raise the mean age along the New Jersey coast and lower mean age in the east.

What we gain in this age analysis over conventional simulations of mean velocity and salinity is explicit information on timescales. Figure 3.9 shows that in the long-term

average, Hudson River influenced waters take some 60 days to reach the LEO-15 (Long-term Ecosystem Observatory) site on the Jersey Shore (near site F in Figure 3.1). Most ecosystem and geochemical processes that would act on river-borne material could reasonably be expected to be mature by this time, suggesting it is unlikely there is much direct influence of the Hudson on the coastal ocean this far south. The mean age at LEO-15 almost halves to roughly 35 days in winter and spring, allowing the likelihood of a significantly greater impact from the river during those seasons. The time series for site F in Figure 3.8d shows that at LEO-15 the mean age can plunge dramatically from highs far exceeding 100 days to low values less than 30 days in the course of a few weeks or less, seemingly with the onset of northwesterly winds (Figure 3.11). Such rapid changes indicate patches of rather different mean age water exist on the inner shelf, so close to shore and well south of New York Harbor the waters originating from the Hudson River are still not laterally well mixed. Further offshore at site G, age fluctuates much less and waters are more homogeneous.

The adjoint model residence time analysis is based on slightly less than two years of simulation. Here, I defined a control volume encompassing most of the NYB within 50 km of the mouth of the Hudson estuary. Our interpretation of residence time is the number of days it takes for a tracer to be flushed out of this control volume and not return. The results are dependent not only on starting location (i.e. proximity to the edge of the control domain) but also time, because of variation in the transport pathways by which tracer is exported from the control domain.

As was the case for age and passive tracers, the mean residence time exhibits strong temporal fluctuations on the scale of days in response to river discharge and wind, and

seasonal averages show some differences in spatial pattern. In all seasons, residence time is long near to the estuary mouth and along the Long Island coast. High values near the estuary are unsurprising, but along the Long Island coast where a strong but variable eastward boundary current forms, long residence times were somewhat unexpected. What occurs is that in spring and summer, water that previously exited the control domain reenters when winds change to easterly. Thus the flow crossing through the eastern boundary of the control domain makes only a temporary exit. Residence time is low in all seasons along the southern boundary of the control domain. Water near this boundary is quickly lost from the domain, and thus it is the southern boundary that is the permanent exit for Hudson River waters entering the NYB. This result is consistent with mean circulaton but now we know the timescales of motion along these pathways. From the mouth of New York Harbor it takes the river discharge on average 20 days, in all seasons, to depart the NYB. Waters that find their way into the Long Island coastal current reside longer than this (over 30 days), while those that flow into the New Jersey coastal current, or have crossed the HSV from north to south, will take some 10 days further, on average, to exit the control domain.

The recirculating low salinity bulge at the estuary mouth that forms during high river discharge events and is a conspicuous feature of winter circulation is a trap that extends residence times by 5 to 10 days compared to waters outside the bulge. The correlation between residence time and winds shows that easterlies increase the residence time of water along the Long Island coast but reduce residence time of waters between the New Jersey coast and the HSV.

The Hudson River is the major source of nutrient and contaminants for the NYB, and the apex region has historically been the site of significant dumping of urban waste. Age and residence time have important implications for the extent to which biogeochemical processes might act on human-impacted waters as they move through this region. The time it takes river-injected tracers to reach places on the shelf is a key factor in estimating the uptake rate of nutrients by phytoplankton (Schofield et al. 2009) and to measure enzyme activities (Gaas et al., unpublished manuscript), to give two examples for this region. Age information assists the selection of rate parameters in ecosystem modeling.

It has been demonstrated here that temporally and spatially resolved information on these timescales can be computed in a coastal ocean model using mean age calculated from just two model tracers (conservative, and age concentration) and residence time provided by a single integration of an adjoint model. The formulation of control domains, and age tracer release scenarios, are readily adapted to address questions of specific relevance to other applications.

CHAPTER 4. ADJOINT SENSITIVITY ANALYSIS

4.1. Introduction

The sector of the Mid-Atlantic Bight adjacent to the coast of New Jersey is separated from the Slope Sea by a wide, shallow shelf, largely insulating the circulation of the New Jersey inner shelf from remotely generated deep-ocean forcing. Historical observations show that ocean variability in the area is most energetic at relatively short time and space scales further suggesting likely dominance by local forcing. In recent years, the region has been the focus of studies designed to examine the dynamics of wind-driven coastal upwelling and buoyancy-driven coastal currents (Choi and Wilkin 2007, Johnson et al. 2003, Münchow and Chant 2000, Tilburg and Garvine 2003, Wong 1999, Yankovsky and Garvine 1998, Yankovsky et al. 2000). These studies indicate that tides, river runoff and air-sea exchanges all have influence, with no single forcing mechanism controlling the regional dynamics. Details of the coastline (Yankovsky 2003, Yankovsky and Garvine 1998) and bathymetry variations (Chant et al. 2004, Garvine 2004, Kohut et al. 2004) also affect the local ocean response.

Using in-situ observations on the New Jersey inner shelf, Yankovsky and Garvine (1998) first found the interaction between wind-driven coastal upwelling and buoyancy intrusions; Wong (1999) discovered cross-shelf inhomogeneity in the ocean's reaction to wind and attributed it to the buoyancy-driven coastal current on the inner shelf; Yankovsky et al. (2000) showed the spatial variability of mesoscale currents driven by the interaction of buoyancy and wind; Chant (2001) concluded that near-inertial motions are mainly driven by local wind, and subsequently propagate gradually into the thermocline;

Tilburg and Garvine (2003) and Yankovsky (2003) both investigated the 3-dimensionality of the flow generated by the combination of wind and buoyancy intrusions; Chant et al. (2004) further proved the 3-dimensionality of the wind-driven flow by studying coastal flow reversals during upwelling conditions; Johnson et al. (2003) described two dynamic states of the coastal ocean: a river plume state and an upwelling state; Garvine (2004) investigated the influence of buoyancy intrusion and wind forcing on the vertical structure of the flow, especially the thickness of surface mixed layer and bottom mixed layer; Kohut et al. (2004) demonstrated strong correlation between wind and surface current on the seasonal scale; Castelao et al. (2008b) identified local wind as a significant role player in driving coastal dynamics and spreading the plume. In numerical model studies, Choi and Wilkin (2007) concluded that wind, and to a lesser extent buoyancy forces, together determine the pattern of horizontal freshwater dispersal; Chapter 2 of this thesis identified wind as the primary force to spread the river-injected freshwater onto the mid- and outer-shelf. All these studies proved wind and buoyancy are two significant competing forces on the New Jersey inner shelf. Their influences on SST on the coast are exactly what are intended to be quantified in this study.

As mentioned in Chapter 1, in the New York Bight the operation of many sensors continues on a quasi-continuous basis and the area is presently the nation's most densely routinely observed coastal region. Consequently, this is an attractive location in which to explore the integration of advanced observation, modeling and DA capabilities for the purposes of implementing coastal ocean forecast systems.

The work presented here uses one of the variational calculus based methods – specifically, the adjoint sensitivity technique – to identify conditions and forcing that are

dynamically upstream, to quantify the relative significance of buoyancy and wind forcing to coastal dynamics in the New York Bight, and to characterize coherent patterns of circulation variability that deserve consideration in the deployment of regional coastal observing systems. Adjoint model sensitivity analysis is a step toward developing a comprehensive 4-dimensional variational (4DVAR) DA system that will exploit the diversity of coastal ocean observation technologies available, and direct their deployment.

Beginning in the 1980s, meteorologists established the theory of adjoint sensitivity and used it to study how selected features of a model forecast vary with respect to prior model states (Errico and Vukicevic 1992). More recently, adjoint sensitivity studies have been applied in oceanography (Dutkiewicz et al. 2006, Galanti and Tziperman 2003, Hill et al. 2004, Junge and Haine 2001, Li and Wunsch 2004, Losch and Heimbach 2007, Marotzke et al. 1999, van Oldenborgh et al. 1999) but with a focus on mesoscale to gyre-scale physics in ocean general circulation models. In one of the first coastal ocean applications, albeit still in the predominantly deep waters of the California Current System, Moore et al. (2008) examined how coastal upwelling, eddy kinetic energy variability and baroclinic instability are affected by surface forcing. In this chapter, a related adjoint sensitivity approach is applied, but to a different class of analyses.

On the New Jersey inner shelf the prior ocean state influences how the ocean responds to direct forcing; quite different ocean responses can occur under similar forcing conditions if the oceanic preconditioning differs. In adjoint sensitivity analysis, oceanic response is characterized by some particular aspect of the model variation expressed in terms of a user-defined scalar functional. The analysis quantifies how this aspect of the model varies with respect to initial conditions and forcing over some finite time interval.

The methodology is effective at revealing the spatial and temporal extent of the oceanic conditions and forcing that are "dynamically upstream" to a region or feature of interest. In this chapter, I emphasize how this analysis approach is a tool for addressing two questions that frequently drive observing system design: (i) Can we quantify the aspects of the ocean state that dominate the dynamics under differing circulation conditions? and (ii) can we identify the most useful places and times at which to make observations in order to better estimate the true ocean state?

There are a number of challenges to adjoint modeling in limited area coastal domains. The first is open boundary conditions, which are formally ill-posed in any nonlinear forward model and can become worse in an adjoint model. This is because any information that propagates out of the open boundaries in the forward tangent linear model is simply lost to the backward mode of the adjoint, unless tangent linear model states on the open boundaries are stored completely. Nonlinearity of coastal currents and abrupt gradients induced by local vertical mixing can pose further difficulties. The issue here is that the adjoint model is formulated for perturbations (the tangent linear approximation) along a trajectory of the nonlinear model, and validity of the linear perturbation assumption needs to be ascertained. This study is also a demonstration of how to deal with these difficulties in practice. The technique exhibited here can also be applied to determining which features of the regional oceanography dominate other local phenomena of interest such as freshwater anomaly transport, the trajectory of a phytoplankton bloom or reactive biogeochemical component, and so on.

The outline of this chapter is as follows. An alternative mathematical derivation of adjoint sensitivity is given in section 2a to better illustrate the interpretation of the adjoint

variables. This is followed by an explanation of adjoint sensitivity in section 2b. Section 2c gives the definition of scalar sensitivity index, *J*, and guidelines on its formulation. The model configuration and proof of the linearization are given in section 3. Model output is presented in section 4 and summarized in section 5.

4.2. Adjoint Sensitivity

4.2.1. An alternative derivation of adjoint sensitivity

Different approaches have been used to describe the mathematical and conceptual formalism of adjoint sensitivity. Errico (1997) combined a Taylor series expansion with a temporal discrete consideration of the model. Marotzke et al. (1999) extended this method by applying an automatic differentiation to derive an adjoint code. However, these time-step-by-time-step derivations do not give a mathematically concise form of adjoint sensitivity. The propagator-based approach adopted by Moore et al. (2008) showed that backward in time integration of the adjoint model gives the sensitivity to initial conditions, forcing and boundary conditions. Here, an alternative explanation also using the propagator algorithm and variational data assimilation theory is presented to show the sensitivities from a different angle.

Following Moore et al. (2004), let us represent the forward ocean model as

$$\begin{cases} \dfrac{\partial \mathbf{\Phi}(t)}{\partial t} = M(\mathbf{\Phi}(t)) + \mathbf{F}(t) \\ \mathbf{\Phi}(0) = \mathbf{\Phi}_i \\ \mathbf{\Phi}(t)\big|_{\Omega} = \mathbf{\Phi}_{\Omega}(t) \end{cases} \tag{4.1}$$

where M is the model nonlinear operator; $\mathbf{\Phi}(t)$ is a state vector $[\mathbf{u}\ \mathbf{v}\ \mathbf{T}\ \mathbf{S}\ \boldsymbol{\zeta}]^{\mathrm{T}}$ comprised of the velocity, temperature, salinity and sea surface height at all model grid points at time t;

$\mathbf{F}(t)$ is the external forcing; $\mathbf{\Phi}_i$ are the initial conditions; and $\mathbf{\Phi}_\Omega(t)$ are boundary conditions along boundary Ω. I let $\mathbf{\Phi}_0$ denote a solution to the nonlinear problem (4.1) and introduce perturbations $\boldsymbol{\varphi}_i = \delta\mathbf{\Phi}_i$, $\boldsymbol{\varphi}_\Omega(t) = \delta\mathbf{\Phi}_\Omega(t)$, and $\mathbf{f}(t) = \delta\mathbf{F}(t)$ to initial conditions, boundary conditions and forcing respectively. Then, using a Taylor expansion around base state $\mathbf{\Phi}_0$, we obtain the so-called tangent-linear model

$$\begin{aligned} &\frac{\partial \boldsymbol{\varphi}}{\partial t} = \left(\frac{\partial M}{\partial \mathbf{\Phi}} \right)\Bigg|_{\mathbf{\Phi}_0} \delta\mathbf{\Phi} + \delta\mathbf{F}(t) = \mathbf{C}\boldsymbol{\varphi} + \mathbf{f}(t) \\ &\boldsymbol{\varphi}(0) = \boldsymbol{\varphi}_i \\ &\boldsymbol{\varphi}(t)\big|_\Omega = \boldsymbol{\varphi}_\Omega(t) \end{aligned} \tag{4.2}$$

where $\boldsymbol{\varphi} = \delta\mathbf{\Phi} = \mathbf{\Phi} - \mathbf{\Phi}_0$ is the departure from the base state $\mathbf{\Phi}_0$. When discretized in space and time, the tangent linear model yields a system of linear equations:

$$\mathbf{A}\boldsymbol{\varphi} = \mathbf{b} \tag{4.3}$$

Here, $\mathbf{A}$ is a coefficient matrix and $\mathbf{b}$ is a right hand side vector which consists of boundary conditions, initial conditions and external forcing, as,

$$\begin{bmatrix} \cdots & \cdots & \cdots & \cdots \\ \cdots & \cdots & \cdots & \cdots \\ \cdots & c_{ij}^{k} & c_{ij}^{k+1} & \cdots \\ \cdots & \cdots & \cdots & \cdots \end{bmatrix} \begin{bmatrix} \vdots \\ \varphi_{ij}^{k} \\ \varphi_{ij}^{k+1} \\ \vdots \end{bmatrix} = \begin{bmatrix} \vdots \\ \\ \hat{b}_{ij}^{k} + f_{ij}^{k}\Delta t \\ \vdots \end{bmatrix}$$

where φ_{ij}^{k} is the tangent linear state variable at the k^{th} time step at location (i , j), c_{ij}^{k} is the corresponding coefficient coming from discretization and model physics, Δt is the time step, $\hat{b}_{ij}^{k}$ is discretized initial condition or boundary condition and f_{ij}^{k} is discretized forcing. If the trivial equations, $f_{ij}^{k}\Delta t = f_{ij}^{k}\Delta t$, are added to the system, matrix $\mathbf{A}$ and vector $\mathbf{b}$ can be modified to incorporate the forcing terms into the state vector thus:

$$\begin{bmatrix} \cdots & \cdots & \cdots & \cdots & \cdots \\ \cdots & \cdots & \cdots & \cdots & \cdots \\ \cdots & c_{ij}^{k} & c_{ij}^{k+1} & \cdots & -1 \\ \cdots & \cdots & \cdots & \cdots & \cdots \\ 0 & 0 & 0 & 0 & 1 \end{bmatrix} \begin{bmatrix} \cdots \\ \varphi_{ij}^{k} \\ \varphi_{ij}^{k+1} \\ \cdots \\ f_{ij}^{k}\Delta t \end{bmatrix} = \begin{bmatrix} \cdots \\ \cdots \\ \hat{b}_{ij}^{k} \\ \cdots \\ f_{ij}^{k}\Delta t \end{bmatrix}.$$

Now, each element in the right hand side vector **b**is a discretized element of initial conditions, boundary conditions or forcing. Following Errico (1997), let us define a scalar functional, J, that describes a chosen aspect of the model state for which we wish to explore the sensitivity

$$J = G(\mathbf{\Phi}(t)). \tag{4.4}$$

Applying the method of Lagrange multipliers (Bertsekas 1982), we can define a corresponding scalar index (or cost function for DA)

$$J = G(\mathbf{\Phi}) = G(\mathbf{\Phi}) + \boldsymbol{\mu}^{T}\left(\mathbf{A}\boldsymbol{\varphi} - \mathbf{b}\right) \tag{4.5}$$

which has the same minimum as (4.4) for all φ that satisfy (4.3). Here, $\boldsymbol{\varphi}$ is the tangent linear state vector which incorporates $f\Delta t$ as discussed before; $\boldsymbol{\mu}$ is a vector of Lagrange multipliers; and **b** is the right hand side of the tangent linear model, including initial conditions, boundary conditions, and forcing.

Setting $\delta J/\delta\boldsymbol{\mu}$ to zero (Bennett 2002), we recover the tangent linear model (4.3); setting $\delta J/\delta\boldsymbol{\varphi}$ to zero results in the adjoint system:

$$-\mathbf{A}^{T}\boldsymbol{\mu} = \frac{\partial G}{\partial \boldsymbol{\varphi}} = \frac{\partial G}{\partial(\boldsymbol{\varphi} + \mathbf{\Phi}_{0})} = \frac{\partial G}{\partial \mathbf{\Phi}}. \tag{4.6}$$

This shows that $\partial G/\partial\mathbf{\Phi}$ is the adjoint forcing, $\mathbf{A}^{\mathrm{T}}$ the adjoint operator, and the Lagrange multipliers μ are the adjoint variables. Additionally,

$$\frac{\delta J}{\delta \mathbf{b}} = \frac{\delta G}{\delta \mathbf{b}} = \boldsymbol{\mu} \tag{4.7}$$

indicating that $\boldsymbol{\mu}$ are the sensitivities of J with respect to all the components of $\mathbf{b}$. In other words, the adjoint variables μ reveal how J depends on perturbations to all of the initial conditions, boundary conditions, and forward model forcing. For J defined as the mismatch between the model state and observations, the sensitivity information can be used to adjust initial conditions to obtain a better model-observation match (Courtier et al. 1994); this is the underlying principle of variational DA. If J is a scalar measure of some aspect simulated in the nonlinear model, the adjoint sensitivity identifies locations and variables which are important to this feature.

4.2.2. Dimensional considerations

In the discrete model, a perturbation is distributed over the small yet finite-sized grid cell that contains the perturbation point. ROMS utilizes orthogonal curvilinear coordinates that allow for variable grid sizes which must be accounted for in the formulation in order to make the correct physical interpretation of adjoint sensitivity. In practice, sensitivity is most readily interpreted as the gradient of J with respect to equivalent masses or volumes of water (Lewis et al. 2001). In ocean applications, mass-weighted and volume-weighted sensitivity differ little, and the latter is used in this study. The horizontal grid here is almost uniform so I show horizontal fields of adjoint sensitivity without any scaling. However, the ROMS terrain-following vertical coordinate is stretched significantly where bathymetry varies and the consequent changes in grid cell thickness change the cell volume. Accordingly, the vertical grid cell thickness is used to scale the vertical fields of adjoint sensitivity presented in Section 4.

Adjoint sensitivity allows comparison of the relative contributions of different variables to the variation of the model aspect of interest. Consider the total variation of J,

$$\delta J = \frac{\partial J}{\partial u_0}\delta u_0 + \frac{\partial J}{\partial T_0}\delta T_0 + \frac{\partial J}{\partial \tau_{x0}}\delta \tau_{x0} + \frac{\partial J}{\partial \nu_{h0}}\delta \nu_{h0} + \cdots, \tag{4.8}$$

where $\frac{\partial J}{\partial u_0}$, $\frac{\partial J}{\partial T_0}$, $\frac{\partial J}{\partial \tau_{x0}}$, $\frac{\partial J}{\partial \nu_{h0}}$ … are the adjoint variables (sensitivities), and δu_0, δT_0, $\delta \tau_{x0}$, δv_{k0} … are variations of forward model variables (i.e. the state variables, but also forcing) at time zero. The relative contributions of different variables to the variation of J, i.e. the respective terms in equation (4.8), can be expressed in appropriate dimensional units by multiplying the adjoint variables by estimates of the magnitude of uncertainty in the corresponding nonlinear model variables. This procedure identifies those state variables or parameters that contribute most to the variation of J. This knowledge is readily applied to the question of determining which variables, where, and when, are crucial to obtaining a good estimate of J, and therefore pertinent to directing observing system design and deployments targeted at capturing a particular event or phenomenon characterized by the appropriate J (Köhl and Stammer 2004). It should be noted that adjoint sensitivity does not immediately reveal the underlying dynamics of the event, though it might point to, or eliminate, certain event triggers at particular places or times. The real triggers will need to be identified through further model analysis.

4.2.3. Definition of scalar index, J

The scalar functional $J = G(\mathbf{\Phi}(t))$ (equation (4.4)) is defined according to the question of interest. Moore et al. (2008) give several definitions for different applications. I would like to add two comments on defining J. First, caution should be exercised in defining J precisely targeting the aspect of interest, especially when the aspect of interest is too vague to define a J specifically. Once a particular J is chosen, the sensitivity of J with respect to

initial conditions or boundary conditions ought to be interpreted precisely according to the definition. Second, the cost function in variational DA is non-dimensionalized by model and observation error covariance which gives the tangent linear model variables the same units as the forward model variables. However, for adjoint sensitivity analysis, there is no necessity to non-dimensionalize *J* because the factor would be a single constant and would make no difference to the interpretation of sensitivity patterns. In this work, *J is* dimensional.

A characteristic feature of New Jersey coastal ocean dynamics is the occurrence of wind-induced upwelling and down-welling that leads to low and high, respectively, SST along the coast (Chant 2001, Münchow and Chant 2000). I study these events here by defining a *J* that is the SST anomaly variance within a localized area adjacent to the New Jersey coast:

$$J = \frac{1}{2(t_2 - t_1)A} \int_{t_1}^{t_2} \int_A (T_S - \overline{T_S})^2 \, dA dt \quad , \tag{4.9}$$

where T_S is SST and $\overline{T_S}$ is its temporal mean, and the definition considers temperature anomaly within an area A during a time interval t_1 to t_2. Here, the time period is chosen to be the last three hours of the simulation time window. Note that *J* is defined as a quadratic form to prevent the cancellation of positive and negative anomaly inside area *A*.

Being a scalar that characterizes local temperature variability, *J* could be affected by temperature through two different mechanisms: (i) transport, i.e. advection or diffusion of temperature as a tracer, and (ii) dynamics, i.e. the contribution of temperature to density and thereby to baroclinic pressure gradients and stratification that impacts vertical turbulent mixing. To separate the sensitivity of *J* due to advection/diffusion from that due

to the density effects, Marotzke et al. (1999) introduced a decomposition in which J is rewritten as a function of temperature and salinity with density and temperature as intermediates,

$$J = J(T,S) = J(q(T), \rho(T,S)) \tag{4.10}$$

Here, $q = T$ denotes the contribution of temperature in J only when it is being advected or diffused and has no relation with salinity, which implies $(\partial q/\partial T)|_S = 1$ and $(\partial q/\partial S)|_T = 0$.

Applying the chain rule, the sensitivity of J to temperature can be expressed as,

$$\begin{aligned} \left.\frac{\partial J}{\partial T}\right|_S &= \left.\frac{\partial J}{\partial q}\right|_\rho \left.\frac{\partial q}{\partial T}\right|_S + \left.\frac{\partial J}{\partial \rho}\right|_q \left.\frac{\partial \rho}{\partial T}\right|_S \\ &= \left.\frac{\partial J}{\partial q}\right|_\rho + \left.\frac{\partial J}{\partial \rho}\right|_q \left.\frac{\partial \rho}{\partial T}\right|_S \\ &= \left.\frac{\partial J}{\partial T}\right|_\rho - \alpha\rho \left.\frac{\partial J}{\partial \rho}\right|_q \end{aligned} \quad , \tag{4.11}$$

where α is the thermal expansion coefficient. The first term on the right-hand side of (4.11) is the sensitivity to temperature due to the processes of advection or diffusion, while the second term describes the density effect. These can be separated by considering the sensitivity to salinity:

$$\left.\frac{\partial J}{\partial S}\right|_T = \left.\frac{\partial J}{\partial q}\right|_\rho \left.\frac{\partial q}{\partial S}\right|_T + \left.\frac{\partial J}{\partial \rho}\right|_q \left.\frac{\partial \rho}{\partial S}\right|_T = \beta\rho \left.\frac{\partial J}{\partial \rho}\right|_q \tag{4.12}$$

Here, β is the haline contraction coefficient. From (4.11), we can isolate the sensitivity of J to temperature due to the dynamic influence on density:

$$\left.\frac{\partial J}{\partial T}\right|_q = -\alpha\rho \left.\frac{\partial J}{\partial \rho}\right|_q = -\frac{\alpha}{\beta} \left.\frac{\partial J}{\partial S}\right|_T ; \tag{4.13}$$

Combining (4.11) and (4.12), we obtain the sensitivity to temperature due to advection and diffusion:

$$\left.\frac{\partial J}{\partial T}\right|_{\rho} = \left.\frac{\partial J}{\partial T}\right|_{S} + \frac{\alpha}{\beta}\left.\frac{\partial J}{\partial S}\right|_{T} \tag{1.14}$$

4.3. Model Configuration and Experiments

The model domain is shown in Figure 4.1. Circulation in the apex of New York Bight is mainly locally driven (Chapter 2) so gradient open boundary conditions are applied on all open boundaries. Forcing scenarios are idealized in this study to develop experience with the adjoint model while also studying the regional ocean dynamics; here, tides and surface water exchange are neglected and both rivers have a steady discharge of 500 $m^3 s^{-1}$ which is typical outside of high discharge storm or freshet events. Because the focus of this study is the oceanic dynamical upstream, the surface heat exchange, an apparent factor for SST variation, is simply neglected. Three adjoint sensitivity experiments are conducted to study the buoyancy-driven coastal circulation and wind-driven upwelling and down-welling that are major features of the dynamics in this area. In Experiment 1, no surface wind is applied, and a coastal current is generated by river buoyancy input. In Experiment 2, both river input and a southward 5 m s^{-1} wind are applied. The wind is switched to northward and coastal upwelling is generated in Experiment 3. The initial conditions for the spin-up of these experiments are from the corresponding model outputs of Choi and Wilkin (2007) in which the ocean has had 3 months to adjust to a realistic state. The SST and surface current at the end of 3-day spin-up periods for the respective experiments are shown in Figure 4.2; the patterns are similar to those identified by Choi and Wilkin (2007) for these forcing scenarios.

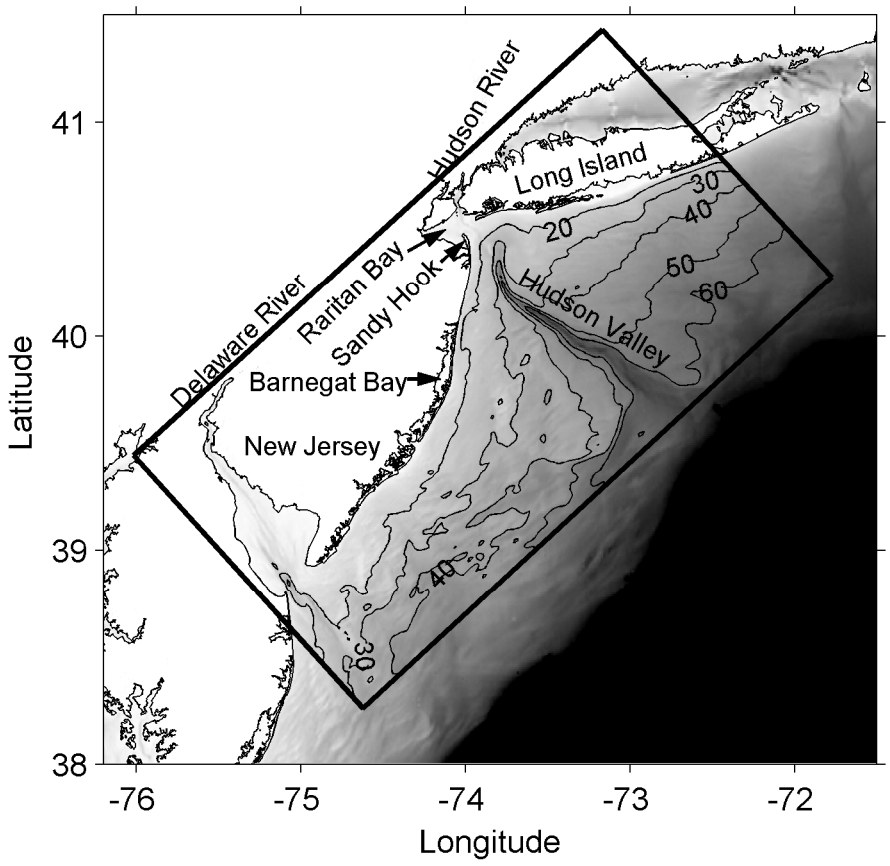

Figure 4.1. Model domain (black frame) and bathymetry of the New York Bight. Depth contours are in meters.

The Adjoint and Tangent Linear component models for ROMS, together with drivers that link these models for Adjoint Sensitivity, Optimal Perturbation, Incremental Strong Constraint 4-Dimensional Variational (IS4DVAR) and Weak constraint 4DVAR (W4DVAR) DA have been developed by the ROMS Adjoint Group (Di Lorenzo et al. 2007, Moore et al. 2004). The Adjoint Sensitivity driver runs the ROMS adjoint model backward in time with zero initial condition. Adjoint forcing is prepared offline and given to the model.

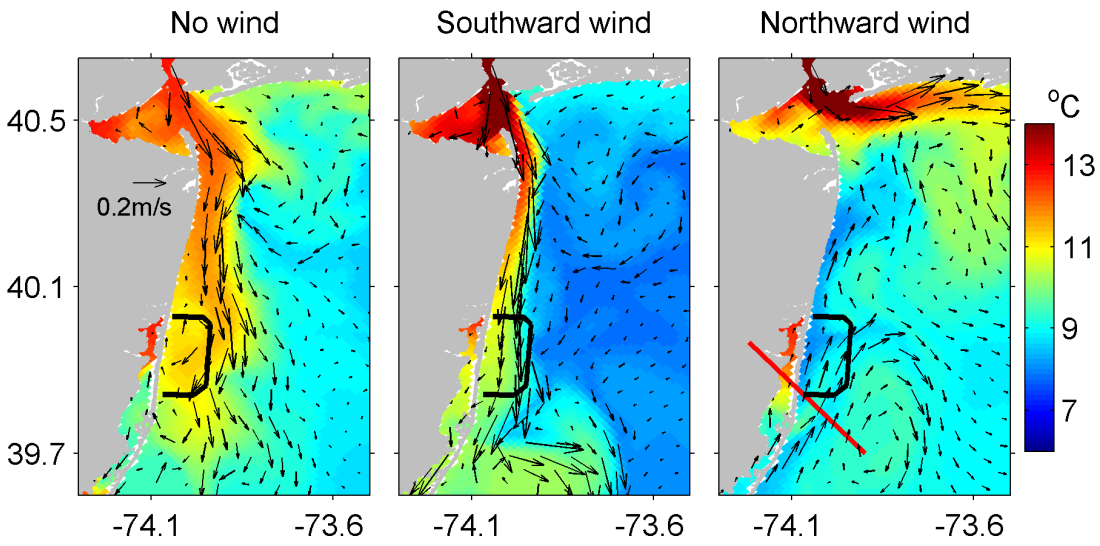

Figure 4.2. Forward model SST and surface current at the end of the three day period for Experiments 1 (no wind), 2 (southward wind) and 3 (northward wind). The thick black frame indicates the adjoint sensitivity region, *A*. The red line in the right-hand figure indicates the location of the cross-section in section 4c.

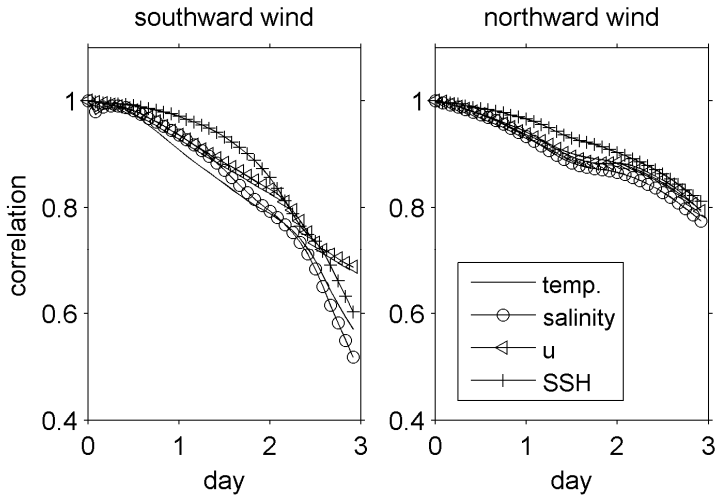

Figure 4.3. Pattern correlation between tangent linear model solution and the difference of two nonlinear model solutions (perturbed minus control, see text) for two idealized configurations: southward wind (left) and northward wind (right). High correlation indicates validity of the tangent linear approximation.

The validity of the tangent linearization should be verified prior to performing an adjoint sensitivity analysis. This is done by using the ROMS Optimal Perturbation driver, based on General Stability Theory (Farrell and Moore 1992, Moore and Farrell 1993), to first obtain the perturbation to initial conditions that has the most rapid energy growth among all singular vectors of the tangent linear system. The perturbation pattern is then scaled by a factor to give the initial condition perturbation a magnitude characteristic of model uncertainty (0.3 m s^{-1} for velocity, 0.2 ^{o}C for temperature, 0.2 for salinity) in this area. Three simulations are conducted for each experiment: the first is the control case, and is the nonlinear forward simulation used as the basic state of the adjoint model; the second, a perturbed nonlinear model, has the scaled perturbation added to the initial conditions of the control simulation; the third, a tangent linear model, is initialized with the scaled perturbation itself. The difference of the nonlinear forward models (perturbed minus control) is compared with the corresponding tangent linear model solution, and the similarity is evaluated by centered pattern correlation analysis (Santer et al. 1993). Figure 4.3 shows the comparison for Experiments 2 and 3. For Experiment 1 (not shown) the similarity is much higher, presumably because of the absence of wind-induced mixing. The similarity of nonlinear and tangent linear solutions for Experiments 2 and 3 decreases gradually from 1 as time advances and the accumulated effects of nonlinearity become important. After 3 days, the correlation is about 0.6 for southward wind (Experiment 2) and about 0.8 for northward wind (Experiment 3). Therefore, I am confident the linearization around the nonlinear model trajectory is valid for the 3-day duration time window of the adjoint model simulations presented here.

4.4. Model Output and Discussion

4.4.1. Experiment 1: No wind

In the nonlinear forward model of this experiment a purely buoyancy-driven coastal current is generated. As shown in Figure 4.2a, and examined in detail by Choi and Wilkin (2007), when the Hudson River volume discharge is modest a low salinity plume exits Raritan Bay and flows southward along the New Jersey coast. The current separates from the coast at about 40.2 ^{o}N but southward flow continues on the eastern side of a weak anticyclonically recirculating feature. SST is higher at the coast than offshore due to warm river water within the plume.

In the absence of wind, vertical mixing is low and it is anticipated that coastal SST will be largely determined by the advection of temperature from upstream. I test this hypothesis using the SST anomaly adjoint sensitivity function, *J,* introduced in equation (4.9), evaluated for the area, *A,* adjacent to the coast indicated by the thick black frame in each panel of Figure 4.4, and for a time interval t_1 to t_2 that spans the final 3 hours of the 3-day window. The adjoint variables ($\partial J / \partial T$ and $\partial J / \partial S$) show how SST in region *A* at the end of the time window is influenced by the distribution of temperature and salinity in the preceding 3 days.

Figure 4.4 shows the evolution, backward in time (from left to right), of this temperature and salinity sensitivity evaluated at the surface. Surface values are plotted because the circulation is predominantly horizontal in this instance, though I emphasize that the adjoint variables are defined over all 3 spatial dimensions. As we shall see below, this can be particularly instructive for deducing 3-dimensional transport pathways. The

sensitivity to surface temperature (Figure 4.4, top row) at day 2.9 is simply the temperature anomaly pattern within region A that determines J, and is proportional to $T_S - \overline{T}_S$. This is apparent if one considers the derivative of (4.9) with respect to T_S. The pattern shows positive sensitivity (anomaly) in the southern half of A, and negative in the north.

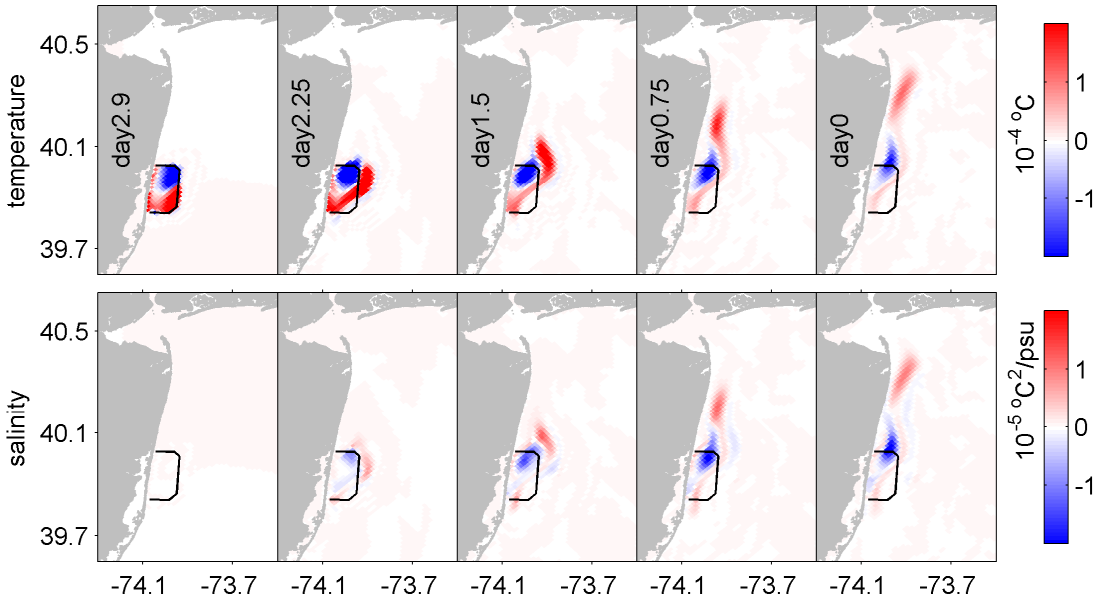

Figure 4.4. For Experiment 1 (no wind), the sensitivity of J to surface temperature (top row) and salinity (bottom row) at different times during the three-day period. Time retreats backwards from left to right. The region A over which J is evaluated, i.e. the adjoint forcing area, is indicated by the black frame.

As time proceeds backward, the southern part makes a cyclonic motion first, stretches out, and moves northward following the track of the river plume (Figure 4.2a). The zone of maximum positive sensitivity lies at Sandy Hook at day 0, with a trail of sensitivity along almost the entire plume track. This means that surface temperature throughout most of the

river plume at day 0 contributes to the surface temperature anomaly in region *A* three days later; but the leading contribution comes from waters immediately southeast of Sandy Hook so this can be considered the principal upstream source location. Sensitivity greater than zero means that higher plume temperatures at day 0 at Sandy Hook would give stronger SST anomaly in the frame (i.e. larger *J*) at day 3. In contrast, the negative sensitivity patch in the northern half of the frame persists for the whole period. From Figure 4.2a we can see that this region is relatively cool and static, being surrounded by warmer waters of the detached plume which evidently trap the cool anomaly in place. The cool waters also contribute to *J* because it is defined as the square of SST anomaly, but the gradient of *J* with respect to SST there is negative. This states that had cooler waters in the northern part of *A* been warmer during days 0 to 3, *J* would decrease. This is consistent with warming making the cool anomaly and plume temperatures more similar, decreasing the anomaly within *A*, and thereby decreasing *J*.

A significant role of advection in driving the coastal SST anomaly is evident from the sensitivity to surface salinity shown in the bottom row of Figure 4.4. Sensitivity to salinity starts from zero since changes in salinity will not affect *J* at the time for which it is defined. Proceeding backward in time, salinity sensitivity gradually grows along the plume track eventually exhibiting a pattern very similar to the sensitivity to SST. Using equations (4.12) through (4.14), the sensitivity to density, sensitivity to temperature associated with density effects, and sensitivity to temperature via passive advection are shown in Figure 4.5c, d and e. Temperature sensitivity due to density related effects is about two orders of magnitude smaller than the sensitivity due to advection. I conclude that the sensitivity of

SST anomaly is dominated by advection, and the pattern shows clearly the trajectory of the source waters over the preceding 3 days.

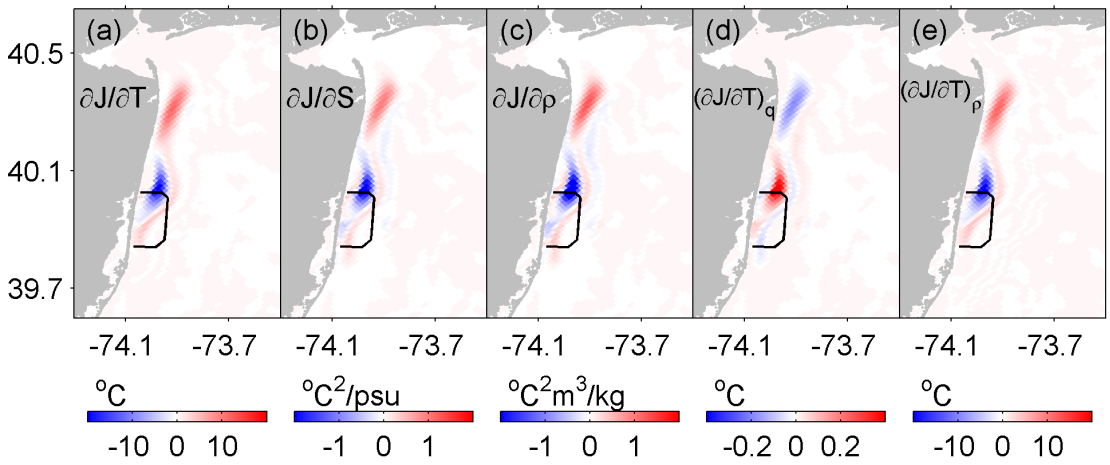

Figure 4.5. At day 0 of Experiment 1 (no wind), the sensitivity, evaluated at the sea surface, of *J* with respect to (a) temperature, (b) salinity, (c) density, (d) temperature density effect, and (e) temperature advection and diffusion effect. (a) and (b) are full adjoint variable, (c) is computed using with equation (4.12), and (d) and (e) are computed with equation (4.13) and (4.14), respectively. All the fields here are multiplied by 10^5.

The similarity in the patterns of sensitivity to surface salinity and temperature at day 0 (Figure 4.4) is striking. To reveal the physical mechanism that leads to this, I make a small 0.01 salinity perturbation to the nonlinear forward model surface initial condition and trace its impact on the circulation. The perturbation is placed southeast of Sandy Hook where sensitivity to salinity is greater than 5×10^{-6} °C^2. Figure 4.6 shows the evolution through time of the difference between the perturbed and unperturbed solutions for surface current and salinity (top row) and surface temperature (bottom row). As we would expect from the adjoint sensitivity results (Figure 4.4), a positive salinity perturbation to the initial

condition produces an increase in SST in the southern half of sensitivity area, *A,* that increases *J*. Throughout the 3 days, the positive salinity anomaly always coincides with surface convergence anomaly and a dipole of positive and negative SST anomaly. At day 1 there is also more vertical sinking at the location of the salinity anomaly (not shown). Because Equation (4.12) shows that sensitivity to salinity is positively related to sensitivity to density, I propose that the mechanism behind the positive sensitivity of SST to surface salinity is that the associated density anomaly introduces a convergent baroclinic pressure gradient anomaly that drives flow convergence and sinking, and evolves a cyclonic circulation anomaly. This process suppresses vertical upward mixing, pulls warm plume water in from the west and cold mixed water in from the east toward the perturbation site producing the dipole pattern of SST anomaly. This warmed surface water moves into the southern half of *A* and augments *J*.

However, the control mechanism is different beneath the surface. Figures 4.7a and 4.7b show sensitivity at day 0 to salinity and temperature at 10 m depth. Temperature sensitivity has opposite sign everywhere to the sensitivity to salinity and its absolute value is about 5 times smaller. Equation (4.12) is used to separate the density and advection effects at 10 m (Figure 4.7c and 4.7d, respectively). Clearly, the sensitivity due to temperature density effect dominates at this depth – the role of advection or diffusion is minor. To explore this further I show sensitivity to density at day 0 at depths of 10 m, 5 m, 2.5 m and 1.5 m in Figure 4.7e through 4.7h, respectively. At depth, there is a strong positive sensitivity to density close to the sensitivity region. Moving up through the water column, this region is displaced progressively further upstream along the plume trajectory consistent with a vertically sheared flow. I interpret this as showing, for each depth, the

horizontal location where water at that depth affects vertical mixing of water into the sensitivity region. The sensitivity is positive because more dense subsurface water corresponds to stronger stratification; this suppresses the mixing of cold water up to surface causing a warmer plume and eventually higher SST anomaly in the sensitivity region at day 3. The opposite effect occurs in the colder part of the frame where warmer surface water would decrease *J* as in Figure 4.5: denser water at that depth suppresses upward mixing, keeps the surface water warmer (surface cool water is still warmer than subsurface water), and decreases *J*, as shown by negative sensitivity to density in Figure 4.7g and h.

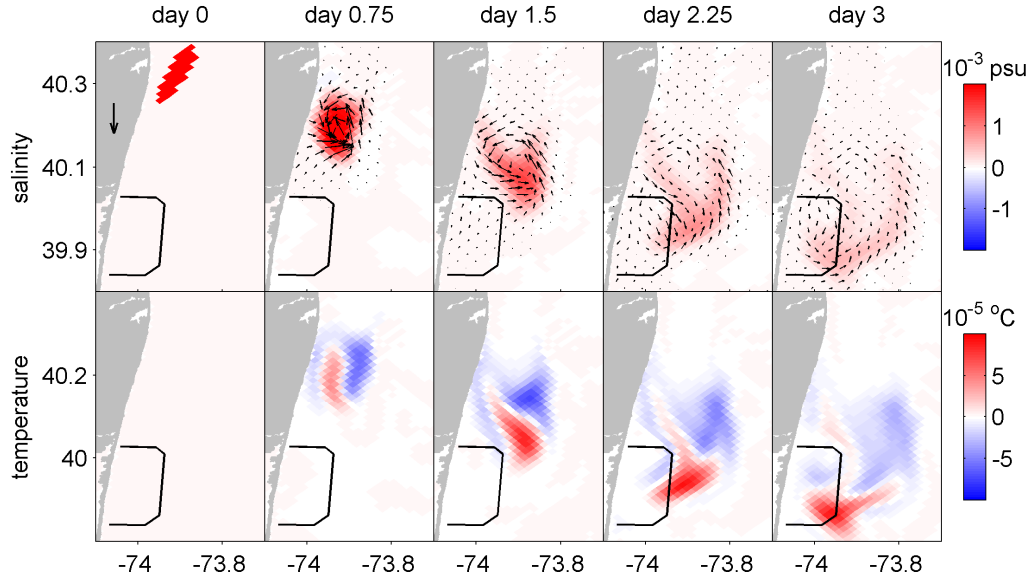

Figure 4.6. The difference in nonlinear forward model simulations when a 0.01 salinity perturbation is added to the surface initial conditions in the region shown in top left panel. Top row: Surface current difference superimposed on surface salinity difference. Bottom row: Surface temperature difference. The arrow in the top left panel is a scale for 10^{-5} m s^{-1}.

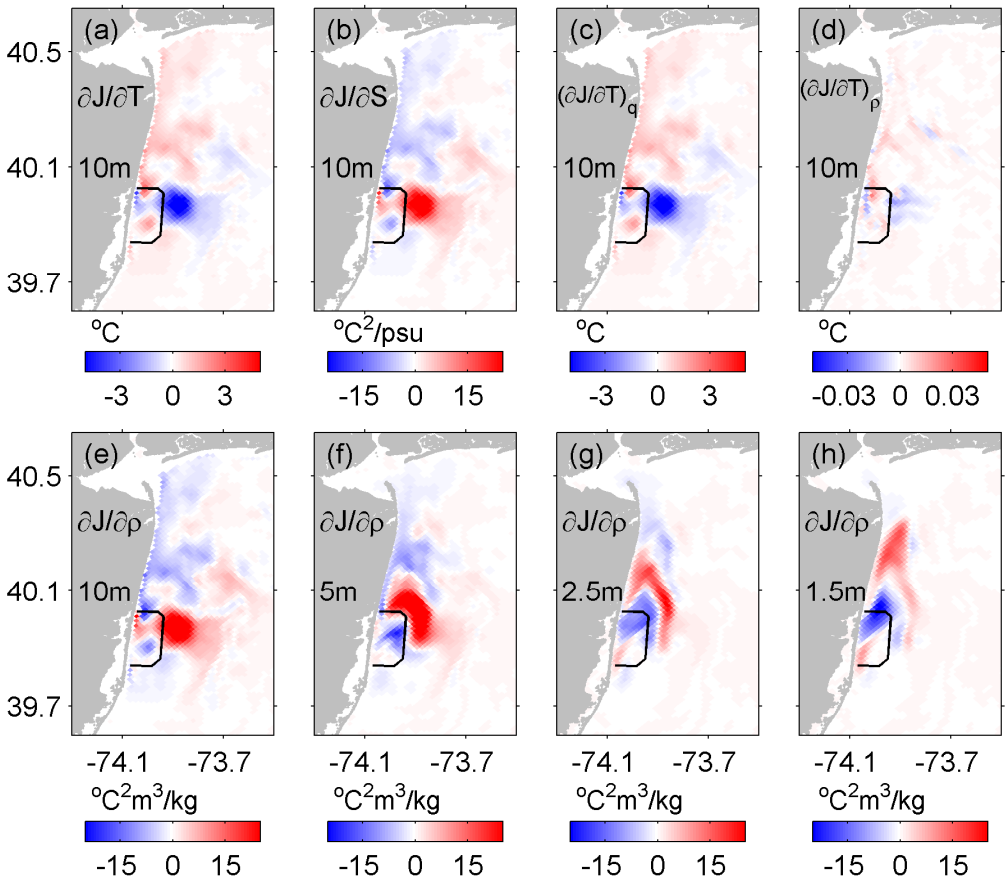

Figure 4.7. For Experiment 1 (no wind). Top row: Sensitivity to (a) temperature, (b) salinity, (c) temperature density effect and (d) temperature advection effect at 10 m depth. Bottom row: Sensitivity to density at different depths: (e) 10m, (f) 5m, (g) 2.5m, and (h) 1.5m. All plots are for sensitivity of *J* at the beginning (day 0) of the 3-day period. The Adjoint forcing area is indicated by the black frame. All the fields here are multiplied by 10^6.

4.4.2. Experiment 2: Southward down-welling wind

In Experiment 2, a moderate 5 m s^{-1} southward wind blows over the entire domain for 20 days. Onshore Ekman transport pushes the river plume against the New Jersey coast,

drives down-welling at the coast, and generates a geostrophically balanced southward coastal jet (Choi and Wilkin, 2007) that augments the river plume as shown in Figure 4.2b. Stronger vertical mixing is expected due to the effect of the wind, and there should be more water from offshore joining the plume along its path and eventually entering my chosen sensitivity area, *A*. A time sequence of sensitivity of *J* to SST (Figure 4.8) shows backward, or upstream, propagation that is faster and along a path that is closer to the coast than the unforced plume of Experiment 1.

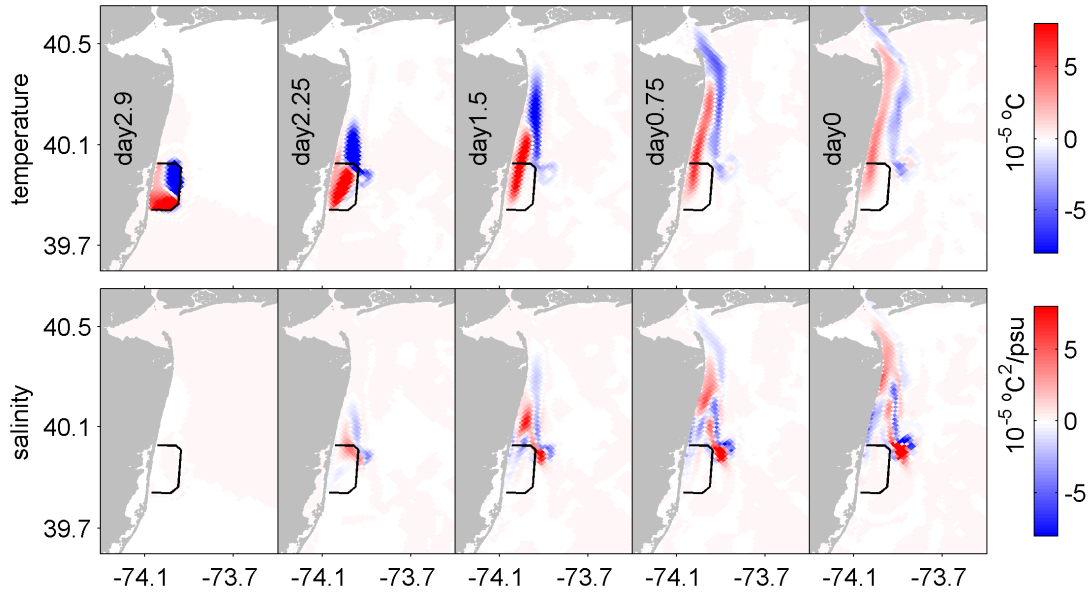

Figure 4.8. For Experiment 2 (southward wind), the sensitivity of *J* to surface temperature (top row) and salinity (bottom row) at different times during the three-day period. Time retreats backwards from left to right. The region *A* over which *J* is evaluated is indicated by the black frame.

In common with Experiment 1, at day 3 the pattern of sensitivity to SST has positive value in the southern half of region *A* and negative in the north. Both features propagate, backwards in time, along the plume track. The negative branch enters Raritan Bay and the

Hudson River mouth with a long trail on the east side of the plume, whereas the positive part stays in the coastal plume. A small persistent patch of sensitivity to SST lies just outside the northeastern corner of region *A* at day 0. This feature is more obvious in the sensitivity to surface salinity. Once again I separate the density and advection effects at day 0 using Equation (4.13) and (4.14) (Figure 4.9). This shows that the positive and negative sensitivity to SST within and adjacent to the plume trajectory are both due mainly to temperature advection, while the patch at the northeastern corner of the frame is associated mostly with the influence of temperature on density and vertical mixing.

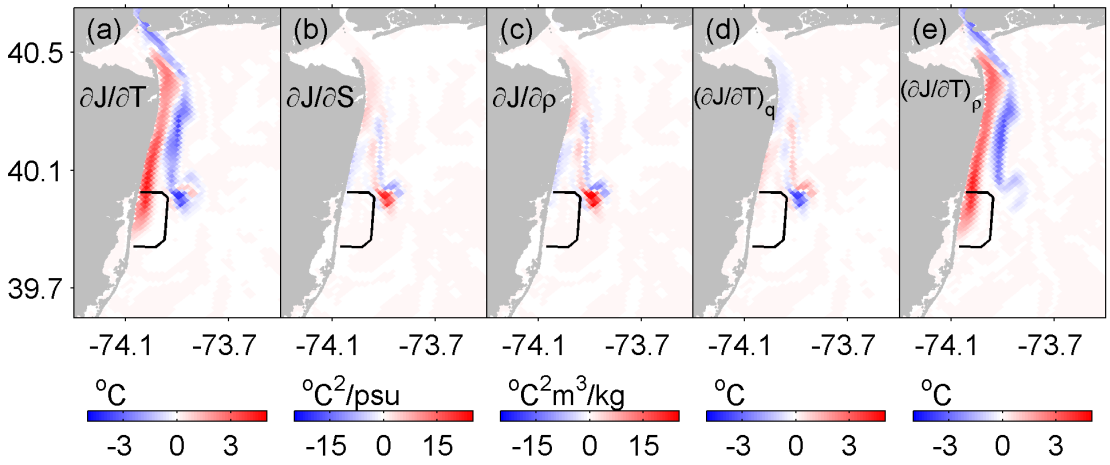

Figure 4.9. At day 0 of Experiment 2 (southward wind), the sensitivity, evaluated at the sea surface, of *J* with respect to (a) SST, (b) surface salinity, (c) density, (d) temperature density effect and (e) temperature advection and diffusion effect. All the fields here are multiplied by 10^5.

Revisiting Figure 4.8, we now see that surface water in region *A* consists of three water masses: (i) river plume water which is already at the coast at day 0, (ii) a mixture of new

water originating from the Hudson river after day 0 with cool surface water from east of the plume, and (iii) offshore surface water at northeast corner of the frame at day 0. The first two water sources affect the SST anomaly in the frame mainly through advection. Because the first source is warmer than mean SST in the frame at day 3, sensitivity of *J* to this part of the upstream temperature is positive. The opposite sign goes to that of the second source because it is colder than mean SST in the frame. For surface water at the northeast corner of the frame at Day 0, because density effect there is dominant and it is colder than the average, *J* would be larger if stratification there was decreased and vertical mixing was enhanced. Therefore the sensitivity of *J* to temperature of this patch of surface water is negative (Figure 4.9).

4.4.3. Experiment 3: Northward upwelling wind

In Experiment 3, a uniform 5 m s^{-1} wind blows to the north and pushes the river plume toward Long Island (Figure 4.2c). Along the New Jersey coast, offshore Ekman transport upwells deeper water to the surface (Choi and Wilkin 2007) and generates a coastal cold anomaly. Upward tilt of the thermocline and halocline at the coast associated with coastal upwelling can be seen in the temperature and salinity cross-section (upper panel in Figure 4.11) along the red line in Figure 4.2c. Note that relative low temperature and salinity difference in the vertical is expected because the strong surface heating, characteristic of summer time conditions in the NYB, is omitted, and there has been upwelling for a relatively long period during the spin-up which lowers vertical differences. In terms of the contribution to SST anomaly, strong vertical mixing due to the fact that deep cold water is brought up to the surface would lower the contribution from upstream water temperature advection. Figure 4.10 shows sensitivity of *J* to SST and surface salinity in the same format

as Figures 4.4 and 4.8 for the previous experiments. The sensitivity to SST at day 2.9, which we note again is simply the initial temperature anomaly $T_S - \overline{T}_S$, has three patches: negative sensitivity at the northern and

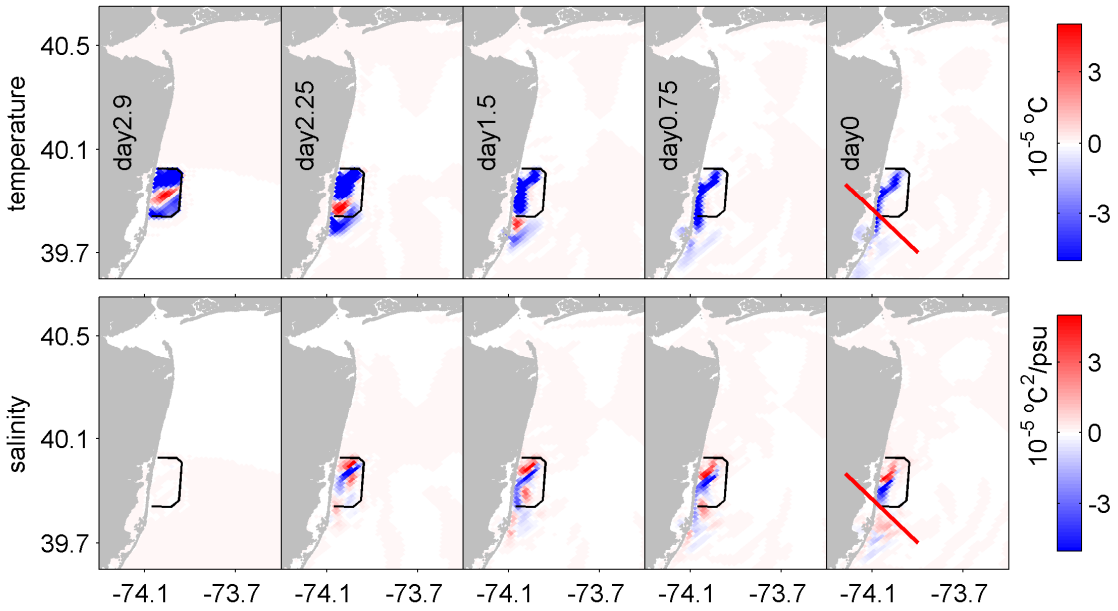

Figure 4.10. For Experiment 3 (northward wind), the sensitivity of J to surface temperature (top row) and salinity (bottom row) through time. The red line in the right-most panel indicates the position of the vertical cross-section for Figure 4.11.

southern ends of the frame, and positive in the middle. Both the negative and positive sensitivity signal in the south moves southward as time proceeds backward (in the upstream direction for the upwelling coastal jet) but disappears rather rapidly compared to Experiments 1 and 2; and the negative sensitivity in the north remains on the surface, and within the frame, through to day 0. Thus, the surface water in the frame at day 3 actually has water sources at day 0: water deep in the southern end of the frame and previously upwelled, offshore moving water (see the cool tongue in Figure 4.2). Almost the entire

southeast half of region *A* shows zero sensitivity to temperature at day 0 because these waters are swept out of the frame by Ekman transport and make no contribution to SST at day 3.

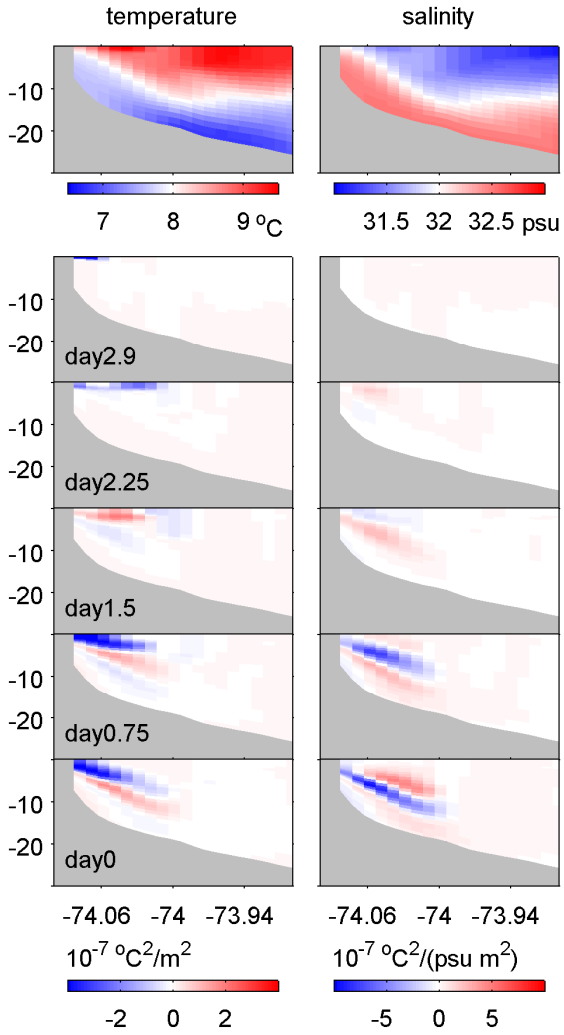

Figure 4.11. Top panel: forward model temperature and salinity along the vertical cross-section indicated in Figure 4.2c and Figure 4.10; Bottom panels: sensitivity to temperature (left) and salinity (right) along the cross-section at different time during the three-day period for Experiment 3 (northward wind).

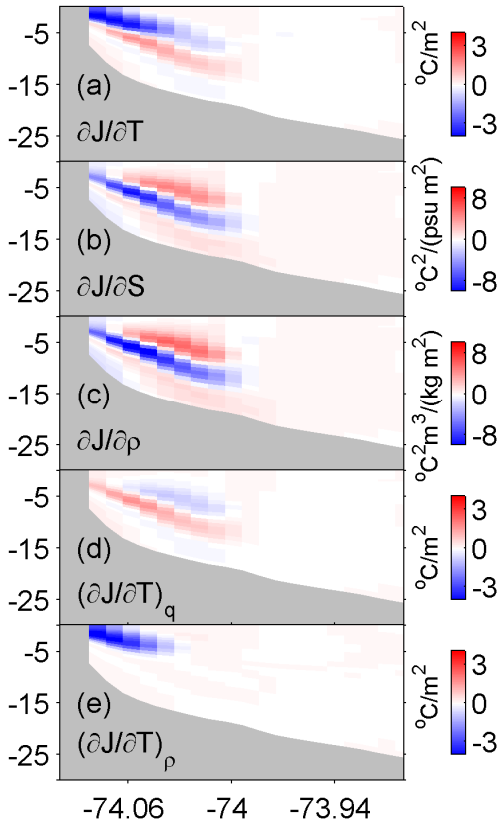

Figure 4.12. At day 0 of Experiment 3 (northward wind), the sensitivity to (a) temperature, (b) salinity, (c) density, (d) temperature density effect and (e) temperature advection and diffusion effect along the vertical cross-section indicated in Figure 4.10. All the fields are multiplied by 10^7.

To illustrate how adjoint sensitivity reveals the deep source of upwelling waters, cross-sections of sensitivity to temperature and salinity along the red line in Figure 4.10 are shown in Figure 4.11, along with cross-sections of the forward model temperature and salinity. Because of the stretched ROMS vertical coordinate the sensitivity here is scaled by the local vertical grid spacing to remove effects of the discrete grid size (Section 2b). Sensitivity to temperature and salinity gradually propagate to the deep and reach almost to

the seafloor at day 0. At that time, both temperature and salinity sensitivity show a two-layer pattern parallel to the thermocline. Applying Equations (4.13) and (4.14), the roles of density and advection in the temperature sensitivity are separated in Figure 4.12. These effects exert their influence at different depths: the sensitivity due to the dynamic role of density is positive and occurs mostly below 5 m, while above this there is negative sensitivity due to upwelling advection. A simple volume conservation calculation for the Ekman layer divergence indicates 5 m as the approximate distance the water would move vertically in 3 days. The sensitivity of J to temperature in the surface 5 m is negative because upwelling brings cold water to the surface and strengthens the southern cold anomaly in the frame. The reason for little dynamic density effect in this layer is presumably that small density changes to the water in the upper 5 m at day 0 cannot prevent the water from upwelling; the flow divergence is set by the wind stress. However, for the water beneath 5 m, SST at day 3 can be influenced through the effect of density stratification on vertical mixing, and subsequently on the SST anomaly.

Sensitivity to density exhibits a two-layer pattern with negative sensitivity lying beneath positive sensitivity (Figure 4.12c). To confirm this pattern, I follow a similar approach as presented in Figure 4.6 and add a 0.01 salinity perturbation at these layers in the initial conditions of a forward model run. The differences in SST between perturbed and unperturbed nonlinear model solutions at day 3 are shown in Figure 4.13 for perturbations to the lower and upper layer, respectively. Both figures show a tripole pattern of SST anomalies, with two positive patches bracketing a negative patch between them. Scrutiny of model state differences at other times (not shown) reveals that these patches originate subsurface and outcrop due to uplift driven by the diverging Ekman transport.

The pattern is displaced further offshore for salinity initial perturbation placed in the upper layer (Figure 4.13b), and the impact on SST anomaly differs: the outcome of the lower layer perturbation (Figure 4.13a) lowers the SST anomaly in the frame at day 2.9 (see Figure 4.10), and then sensitivity of J to salinity at that layer is negative; the upper layer perturbation (Figure 4.13b) enhances the SST anomaly in the frame and then sensitivity of J to salinity in that layer is positive.

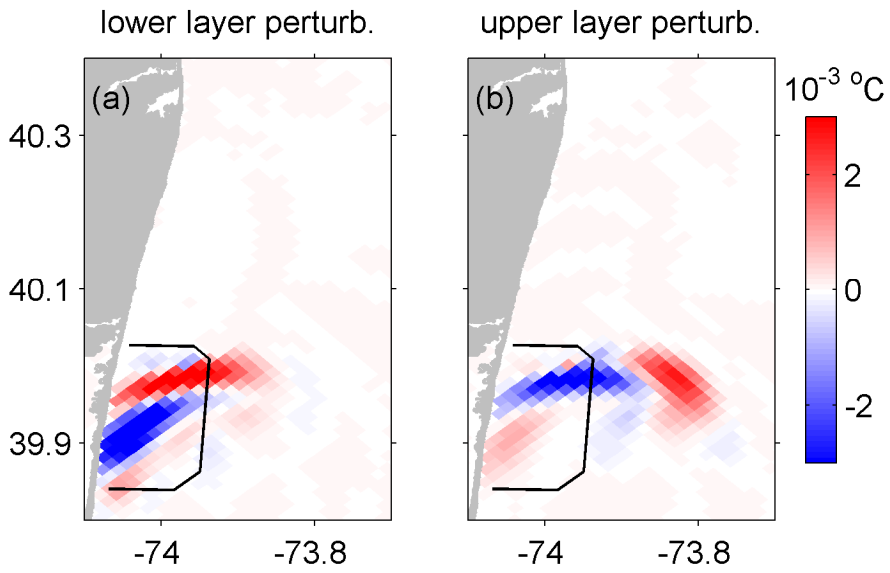

Figure 4.13. For Experiment 3 (northward wind), the difference in SST in forward model simulations when a salinity perturbation is added to the (a) upper layer, and (b) lower layer, initial conditions.

Table 4.1. Comparison of the magnitude of different contributions to J (coastal SST anomaly) for each of the 3 experiments

	X	Upstream temperature	Density	Surface current	Sea surface height	Vertical mixing of momentum	Vertical mixing of tracers	Wind stress
No wind	$\partial J/\partial X$	10^{-4}	10^{-5}	2×10^{-4}	3×10^{-5}	1	0.3	10^{-4}
	δX	2	1	10^{-1}	10^{-2}	10^{-5}	10^{-6}	--
	$\frac{\partial J}{\partial X}\delta X\,(°C^2)$	2×10^{-4}	10^{-5}	2×10^{-5}	3×10^{-7}	10^{-5}	3×10^{-7}	--
Southward wind	$\partial J/\partial X$	5×10^{-5}	2×10^{-4}	5×10^{-4}	3×10^{-4}	10	3×10^{-2}	5×10^{-4}
	δX	2	1	10^{-1}	10^{-2}	10^{-5}	10^{-4}	5×10^{-3}
	$\frac{\partial J}{\partial X}\delta X\,(°C^2)$	10^{-4}	2×10^{-4}	5×10^{-5}	3×10^{-6}	10^{-4}	3×10^{-6}	2.5×10^{-6}
Northward wind	$\partial J/\partial X$	10^{-4}	2×10^{-4}	5×10^{-4}	2×10^{-4}	5×10^{-1}	10^{-2}	3×10^{-4}
	δX	2	1	10^{-1}	10^{-2}	10^{-5}	10^{-4}	10^{-3}
	$\frac{\partial J}{\partial X}\delta X\,(°C^2)$	2×10^{-4}	2×10^{-4}	5×10^{-5}	2×10^{-6}	5×10^{-6}	10^{-6}	3×10^{-7}

X denotes model variables in their SI units; $\partial J/\partial X$ is the adjoint sensitivity in units $^{o}C^{2}/[X]$; δX is a small variation of X in units $[X]$.

4.4.4. Comparison of the different contributions to total δJ

Besides sensitivity to temperature and salinity, the adjoint model also gives the sensitivity of J to the other state variables, forcing, and parameters of the model. To quantitatively compare the different contributions to the total variation of J, terms in equation (4.8) are estimated for all three experiments and shown in Table 4.1. For Experiment 1 (no wind), the contribution of surface temperature dominates. Mixing is weak in this free river plume scenario, and SST anomaly in the frame is determined principally by the advection of warm water from upstream. From the perspective of observing system design, good estimation of upstream water temperature along the New Jersey coast over the proceeding 3 days is highly relevant to knowledge of the SST anomaly in region A.

For Experiment 2 (southward wind), Table 4.1 shows density makes the leading contribution, followed by upstream temperature advection and vertical mixing. The contribution of wind to SST anomaly variation over the 3 days is surprisingly small considering that the strong coastal current is mainly due to the down-welling favorable wind. An adjoint model simulation with a longer time window does show sensitivity to wind stress having a leading role in the variation of J. It can be interpreted as indicating the full strength of the coastal current takes several days to evolve, and is not strongly impacted by wind changes in the last 3 days of simulation. Once established, details of the SST patterns within the current itself become the main contributor to variation of the J defined here.

The same logic applies to Experiment 3, the upwelling scenario, for which Table 4.1 shows density and upstream temperature advection as the largest contributors. A leading contribution from density is to be expected because changes to the vertical stratification can alter both mixing and the depth from which upwelled water is drawn (Allen et al. 1995). Both these influences can change SST as explained in Section 4c on the 3-day timescale. Therefore, in this circulation scenario, observation of the vertical density distribution as well as the upstream water temperature over the preceding three days is significant for accurate simulation of the SST anomaly in the end of the period.

The quantitative comparison of the relative contributions of different state variables and forcing variables under different circulation scenarios, together with the spatially and temporally resolved adjoint sensitivity information in Section 4a-c, shed light on the timing and location of variations in the ocean state that are crucial for precise prediction of the future SST anomaly conditions as characterized by J. Observation of these variables at the identified times and locations can reasonably be expected to be of significantly greater value when seeking to adjust the model prior state through DA.

4.5. Summary

As a step toward building a coastal ocean forecast system for the New York Bight, I have undertaken an adjoint model study of the sensitivity of New Jersey coastal SST anomalies for three idealized wind forcing scenarios: no wind, upwelling favorable, and down-welling favorable wind. The adjoint sensitivity formulas were derived first to clarify how adjoint sensitivity has the capability to simultaneously compare the contribution from

different state variables, model forcing, and model parameters to the variation of some chosen model aspect characterized via a scalar functional, *J*, and then identify the main source of that variation.

To focus on characteristics of short-term wind-induced SST anomalies adjacent to the New Jersey coast, my scalar functional *J* was defined as the temporal and spatial mean of the square of SST anomaly in a frame area in a small central sector of the New Jersey coast for a brief prescribed time interval. Within this definition, ocean temperature can affect *J* through two different processes: the advection and diffusion of source waters of differing temperature into the frame region, and the effect that temperature has on circulation and mixing through its contribution to density. It was shown that these influences can be separated by deriving a decomposition based on applying the chain rule to the adjoint sensitivity analysis; the method essentially exploits the density information in the sensitivity to salinity at constant temperature. Prior to the adjoint sensitivity analysis, I verify that the linearization assumption of the adjoint model is valid by comparing the tangent linear model solution with the difference between two, slightly perturbed, nonlinear model solutions. The tangent linearization is valid for the 3-day time window of this study. Care is taken to normalize the adjoint sensitivity appropriately to remove effects of the vertical grid discretization before interpretation of the results.

In the first experiment, the Hudson River discharge generates a purely buoyancy driven coastal current in the nonlinear model (no wind). The adjoint sensitivity method shows that of all ocean state variables (temperature, salinity, velocity) and forcing, throughout the entire model domain and at all preceding times, temperature itself has the greatest impact on *J* in this experiment. The decomposition of sensitivity into advection and density

contributions shows that in this scenario advection dominates over the indirect role of temperature on circulation exerted through the influence of density on mixing and pressure gradients. The sensitivity of *J* to surface temperature identifies two sources of the surface water in the frame where the functional *J* is defined: warm plume water and cooler coastal ocean water that is partially surrounded by the river plume where it detaches from the coast. Analysis of the sensitivity to subsurface water temperatures shows these exert their influence principally through the dynamic density effect.

In Experiment 2 a 5 m s^{-1} southward wind blows and drives a strong coastal current in the same direction as the buoyancy driven circulation. Adjoint sensitivity highlights three significant sources of influence on *J*. Decomposition shows that two stretches of water parallel to the coast and of opposite sign in sensitivity act through temperature advection, while a small patch northeast of the sensitivity frame influences SST less directly due to the dynamic effect of density.

Deep water is uplifted to the surface in Experiment 3 due to a northward upwelling favorable wind. The sensitivity of *J* to SST rapidly diminishes at the coast as time proceeds backward in this scenario because surface waters to the south are swept offshore by Ekman transport and do not enter the sensitivity region where *J* is defined. A vertical cross-section of sensitivity to temperature confirms there is a deep source to the temperatures that influence SST anomaly, and clearly delineates its depth and offshore extent through time. Separation of the sensitivity to temperature into the respective contributions of advection and dynamics shows that influence of direct advection is restricted to mainly the top 5 m of the water column and some 10 km offshore (3 days

previously), while the indirect dynamic or density effect is beneath this (5 to 15 m depth) and over the same across-shelf extent.

The contributions from different variables and parameters to the total variation of J are quantitatively compared. For the no wind, unforced plume experiment, upstream surface temperature dominates. For the down-welling favorable wind experiment, density effect is shown to have the leading contribution followed by temperature advection and vertical mixing. Only when adjoint simulations are extended to a time window longer than 3 days do we find that wind stress can become the dominate source of sensitivity for the chosen J. For the upwelling scenario, density and upstream temperature advection contribute equally to J. The importance of density is expected in this case because upwelling is against the vertical stratification, and changes in vertical density structure alter details of the upwelling process and subsequently SST characterized by J.

The results obtained in this study demonstrate the ability of adjoint sensitivity to identify the oceanic conditions and forcing that are "dynamically upstream" to a region or feature of interest, water sources, the main contributors to variation of a defined model feature, and often the mechanisms behind these. The timing and location of variations in the ocean state that are crucial for subsequent prediction of the model features, as characterized by a chosen functional J, are clearly highlighted. It follows, therefore, that observation of these variables at the identified locations and times can be expected to have significant value when used to adjust the model prior state through DA. This property embodied in the adjoint model will underpin future DA and adaptive sampling studies.

CHAPTER 5. IS4DVAR DATA ASSIMILATION

5.1. Introduction

In this chapter ROMS IS4DVAR system is used to assimilate observational data collected in the NYB during spring 2006. The practice exposes some practical issues that need to be addressed when assimilating observational data, especially in real-time, evaluates the influences of different observations on the performance of the forecast system, and provides the best estimated ocean state that can be obtained.

The NYB is active in biogeochemical processes and the Hudson River is a major source of the biogeochemical tracers and contaminants in the NYB. Thorough understanding of the local biogeochemistry is an objective for some studies in this area (Schofield et al. 2008b), and numerical modeling is one of the approaches that have been taken in these studies (Cahill et al. 2008, Fennel et al. 2006). For the purpose of simulating biogeochemical processes, an accurate estimate of the ocean physical states is required. Improving estimates of the ocean state is one of the objectives of this chapter.

As described in Chapter 1, the NYB is one of the best observed coastal areas in the world and the target of pioneered deployments of new observing instruments including gliders, HF radar, and a cabled observatory. During spring 2006, interdisciplinary process studies of the Hudson River plume, the Lagrangian Transport and Transformation Experiment (LaTTE), were conducted (Chant et al. 2008a). A variety of observational platforms, including satellites, HF Radar network, a fleet of gliders, mooring arrays, surface drifters, R/V Cape Hatteras and R/V Oceanus, were used extensively to monitor the

NYB. Meanwhile, numerical simulation of the NYB with ROMS was used to guide the observations in real-time. These make the NYB an attractive location to explore the integration of advanced observation and modeling capabilities for the purposes of implementing coastal ocean DA and optimal observation systems. The first half of the integration is carried out in this chapter and the second in Chapter 6.

In DA observations are used to improve the model description of the oceans (Bennett 2002, Evensen 2007, Wunsch 2006). Time-dependent variational method (4DVAR) is one DA method and it takes the linearized dynamical model into consideration while adjusting model control variables to fit observations. Within the 4DVAR system a cost function is usually defined as the weighted mismatch between observations and model equivalent plus some extra constraints, such as the size of the adjustment to the model control variables. The ultimate goal of the 4DVAR DA system is to minimize the cost function. In principle, control variables to be adjusted can be any external constraints on the model, such as initial conditions, boundary conditions, and external forcings, or inside the model, such as vertical mixing parameters and missing physics.

Assuming the model physics is perfect ("strong" constraint (Talagrand and Courtier 1987)), there are two approaches to minimize the cost function: (i) IS4DVAR (Courtier et al. 1994), and (ii) representer-based 4DVAR (Bennett 2002) (also called 4D-PSAS (Courtier 1997)), which are essentially equivalent (Courtier 1997). However, they minimize the cost function in different spaces: IS4DVAR performs the minimization in model space and representer-based 4DVAR in observation space. In IS4DVAR an iterative scheme, e.g. conjugate gradient algorithm and quasi-Newtonian method, is used to minimize the cost function based on the information provided by Tangent Linear and

Adjoint models (Powell et al. 2008, Weaver et al. 2003). In each iteration a backward integration of the Adjoint model forced by the model-observation mismatch is conducted. It rides on nonlinear model trajectory over the period that a single continuous DA spans, the DA window, and gives the gradient of the cost function with respect to control variables. The gradient is then used to provide the direction of the cost function minimum search. Subsequent Tangent Linear model integration propagates the control variable adjustment forward over the DA window. The IS4DVAR algorithm was implemented in ROMS (Powell et al. 2008) and therefore used in this study.

In representer-based 4DVAR the minimum search is achieved through looking for the coefficients of the observational representers that give the model-observation mismatch (Bennett 2002). A representer is the covariance between an observed model state at an observation location and model states everywhere at any time. The covariance has dynamical components, and obtaining these components requires integration of Tangent Linear and Adjoint models. The process of solving the equations of representer coefficients hence employs Tangent Linear and Adjoint models. Courtier (1997) proved that the equations of representer coefficients are equivalent to the equations of control variable adjustment in IS4DVAR, and that to solve the equations of representer coefficients is essentially to minimize an objective function whose Hessian has the same condition number as that of the cost function in IS4DVAR. The integration of Tangent Linear and Adjoint models in both IS4DVAR and representer-base 4DVAR algorithms incorporates the time-dependent dynamics into the adjusting system, which is the very merit of the 4DVAR method.

Both 4DVAR algorithms have been applied in oceanography studies in different scales. In large scales IS4DVAR have been applied for methodology improvement (Vialard et al. 2003, Vossepoel et al. 2004, Weaver et al. 2003, Weaver et al. 2005) and state estimation (Stammer et al. 2004, Stammer et al. 2002, 2003, Wunsch and Heimbach 2007). In regional and coastal scales systems using 4DVAR algorithms have been developed and applied mostly in idealized setups (Di Lorenzo et al. 2007, Kurapov et al. 2007, Ngodock et al. 2007, Scott et al. 2000) with the exception of Hoteit and Köhl (2006), Powell et al. (2008) and Smith and Ngodock (2008). Given the difficulties associated with coastal applications, such as open boundary condition and strong nonlinearity, extra caution is required to build the 4DVAR system. At the same time, some coastal ocean DA works have been done with other methods, such as nudging or melding (Lewis et al. 1998, Wilkin et al. 2005), optimal interpolation (Oke et al. 2002), 3DVAR (Li et al. 2008), and ensemble Kalman filter (Hoffman et al. 2008).

This chapter is organized as follows: Section 5.2 describes the data collected in spring 2006 and the quality control; Section 5.3 describes the model configuration and Section 5.4 the DA system; Section 5.5 presents the results; Section 5.6 summarizes the chapter.

5.2. Observational Data

During spring 2006 there was a LaTTE field campaign in the NYB targeting the spring freshet of the Hudson River, similar to that in spring 2005 (Chant et al. 2008a). The sustained observatories including HF Radar, gliders, satellites were operated by the

Rutgers University Coastal Ocean Observation Laboratory (COOL) (Glenn and Schofield 2003).

Raw satellite data was acquired from the Advanced Very High Resolution Radiometer (AVHRR) aboard NOAA-12, 15, 17, 18 satellites by an L-Band satellite dish. On average, there are about 2 to 3 passes of the satellites over the NYB area in a day. The raw data were processed to 1km resolution SST data in COOL using the Multi-channel Sea Surface Temperature algorithm in SeaSpace terascan software. Clouds in the SST snapshot data were manually removed and the snapshots were then spatially averaged on to a 4-km resolution grid. An example of the SST snapshot is given in Figure 5.6a.

Glider data used in this study are temperature and salinity profiles. There were measured by SeaBird CTD aboard which operates at 0.5 Hz and gives vertical profiles at resolution of 0.25 m. Because the conductivity cells on the gliders are unpumped, there is thermal-lag associated with flushing of conductivity cell and heat stored in the wall of conductivity cell especially when gliders cross the thermocline (Lueck 1990). The thermal-lag was corrected using the algorithm proposed by Morison et al. (1994) and the data were then vertically averaged to profiles of 1 m resolution. The glider tracks are plotted in Figure 5.1 and an example of glider-measured temperature and salinity cross-sections is given in Figure 5.7.

HF radar data from 5 radio sites (Figure 5.1) are used to retrieve 3-hour averaged sea surface current once per hour. The azimuthal resolution of the raw data at all the sites is 5 degrees, and radial data from the sites was combined into total vector maps using the algorithm described by Kohut et al. (2001) and Kohut et al. (2006b). The product from the

COOL is surface currents on a 6 km resolution regular grid. An example of the HF Radar-measured surface current is given in Figure 5.6a. I choose 2.5 m to be the depth of the HF Radar-measured currents according to the effective depth of the HF Radar measurement (Stewart and Joy 1974).

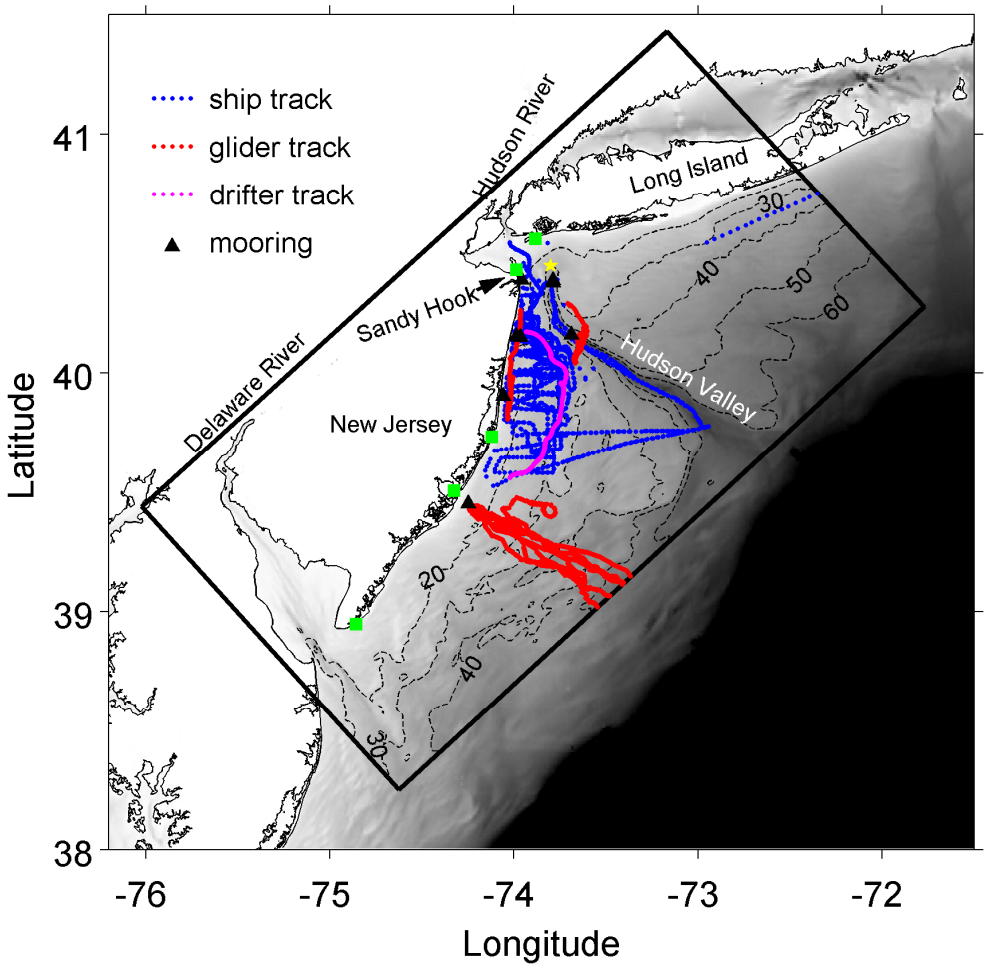

Figure 5.1. The study domain and observation locations. The black frame indicates the model domain; Bathymetry of the New York Bight is in grayscale; Black dash lines are contours of model isobaths in meters; the yellow pentagram indicates location of the Ambrose Tower; the green squares indicate locations of the five HF Radar stations.

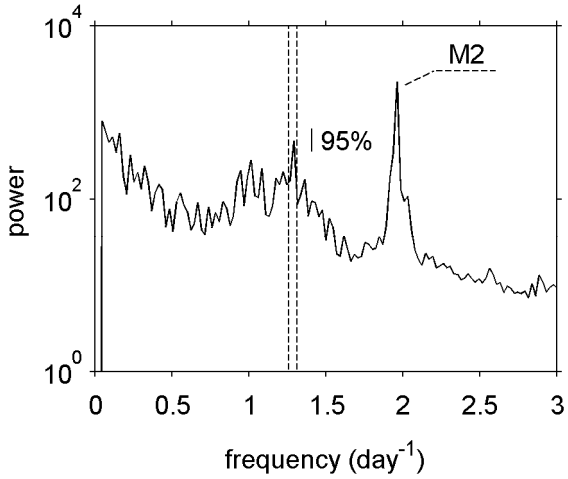

Figure 5.2. Averaged spectrum of HF-Radar-measured surface current. Dash lines indicate local inertial frequency band and the confidence limit applies to data within the inertial frequency band.

The averaged power spectrum of the HF Radar data in Figure 5.2 shows that the tidal signal dominates the observed surface current. Due to errors in either the model tidal harmonic boundary conditions, the HF Radar measurement, or both, tidal current in the model is different from that observed by HF Radar as we can see from the comparison of M2 tide in Figure 5.3. However, the DA system used in this study does not take model tidal harmonics as a control variable, that is, it cannot adjust the tidal harmonics on the open boundaries to fit the observed tidal currents. If the HF Radar data is assimilated directly the DA system would consider the tidal difference as the outcome of errors in control variables, i.e. initial conditions in this study. It would then adjust the initial conditions to minimize the difference in the tides, which would lead to overcorrection.

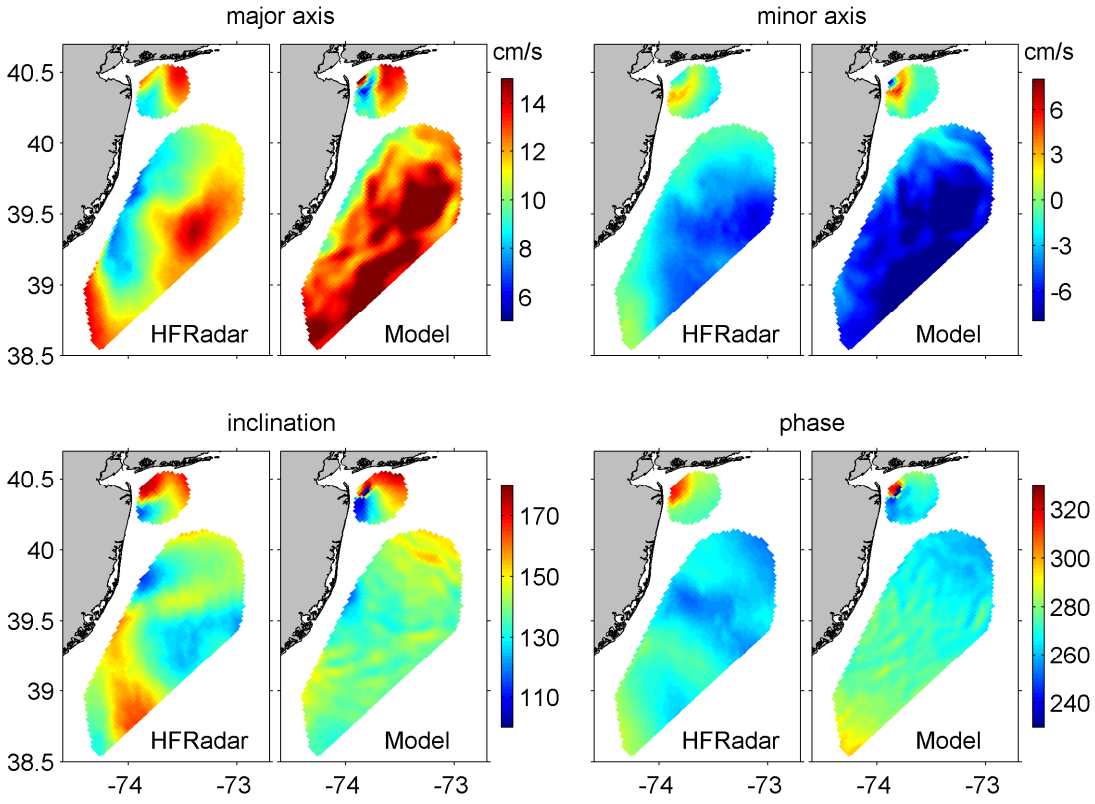

Figure 5.3. Comparison between HF Radar-observed and modeled M2 tide.

To overcome this problem, I filtered the tidal signal (O1, K1, Q1, M2, S2, N2 and K2) in the HF Radar data, extracted the tidal harmonics from a control model simulation over the period of observation, and then added the modeled tides to the detided HF Radar data. This merge guarantees the consistency between the tidal currents in the "observational data" and model. Assimilating the merged "observations" is essentially assimilating the subtidal currents measured by the HF Radar. Comparison of assimilating the original HF Radar data and the merged ones shows that assimilating the merged surface currents gives slightly better velocity fit and forecast skill (not shown).

Other observations used in this study include moorings, surface drifters, and ship surveys. Seven moorings as shown in Figure 5.1 were deployed from the beginning of April to the end of June. Each mooring contains an Acoustic Doppler Current Profile (ADCP) and two to three Conductivity/Temperature (CT) sensors at different depth. Two surface drifters were deployed between 4 and 8 May. They measured the surface water temperature while drifting. The shipboard surveys with the R/V Cape Hatteras and R/V Oceanus occurred between 2 and 8 May. A towed undulating vehicle, CTD and ADCP were used to measure the temperature, salinity and current along the tracks. All data from the towed undulating vehicle, ADCP, CTD, CT and drifters were averaged to resolution of 2 m on vertical, 5 km on horizontal and 12 minutes on temporal.

Figure 5.4a marks the types of observations we have each day during the experiment period and Figure 5.4b gives the total number of observations and numbers for each variable at each day. We have between 20,000 and 45,000 observations each day, among which velocity occupies the most and salinity the least. More than 60% of the velocity data is surface current measured by HF Radar and the rest is measured by ADCPs. More than 50% of the temperature data is SST data from satellites, about 13% is measured by gliders, and the rest is measured by moored and shipborne CTDs. About half of the salinity data is subsurface glider measurement and the other half is from moored and shipborne CTDs.

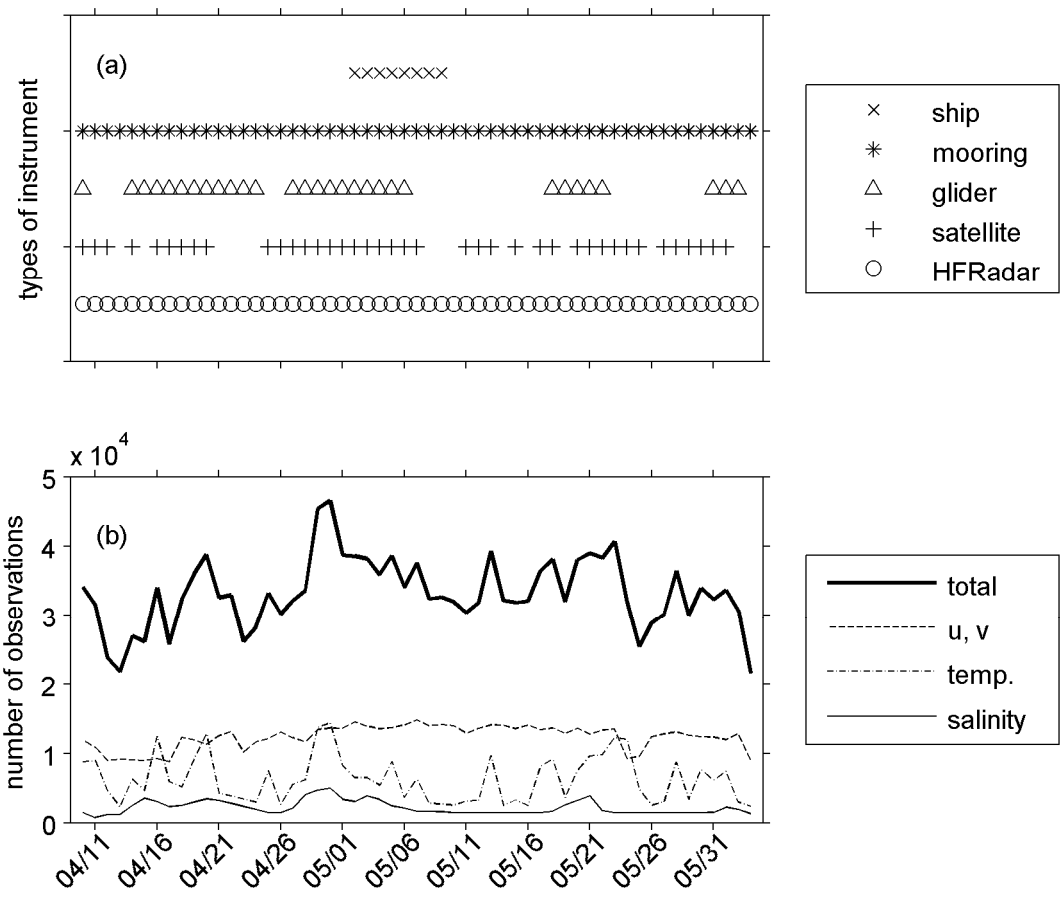

Figure 5.4. Types (a) and numbers (b) of observations over the data assimilation period.

5.3. Model Configuration

The model setup in this chapter is very similar to that in Chapter 2 as shown in Figure 5.1, and it is therefore described only briefly here emphasizing the changes from Chapter 2. Because of the massive computational demand of the IS4DVAR system (about 100 times the computation of a single forward model simulation), horizontal resolution in this study has been decreased to 2 km.

The control forward nonlinear model simulation (before DA) starts at Apr. 5th, 2006 with initial conditions obtained from the full physics simulation in Chapter 2. In all forward nonlinear model simulations Chapman (1985) and Flather (1976) open boundary conditions are used for sea level elevation and the barotropic component of velocity on the model perimeter, respectively. These conditions impose both a remotely forced along-shelf mean flow computed from the water-depth/flow-speed relationship deduced by Lentz (2008), and tidal harmonic variability (K1, O1, Q1, M2, S2, N2, K2) extracted from a regional ADCIRC simulation (Mukai et al. 2002). Gradient open boundary conditions are used for 3D velocity and tracers. Quadratic bottom drag was used with drag coefficient 0.003. General length scale method with *k-kl* scheme (Umlauf and Burchard 2003, Warner et al. 2005) was used for the vertical mixing. The forward models apply bulk formulae (Fairall et al. 2003) with meteorological forcings from the North American Mesoscale (NAM) model at NOMADS (Rutledge et al. 2006) to compute air-sea momentum and heat exchange. The meteorological variables were chosen to be the 6- to 30-hour daily forecasts in order to avoid the initial shocks at the beginning of the forecasts. The river discharge was obtained from USGS Water Data (U. S. Geological Survey 2007) and modified to include ungauged portions of the watershed. Figure 5.5 shows the river discharges and wind at the Hudson River mouth over the DA experiment period.

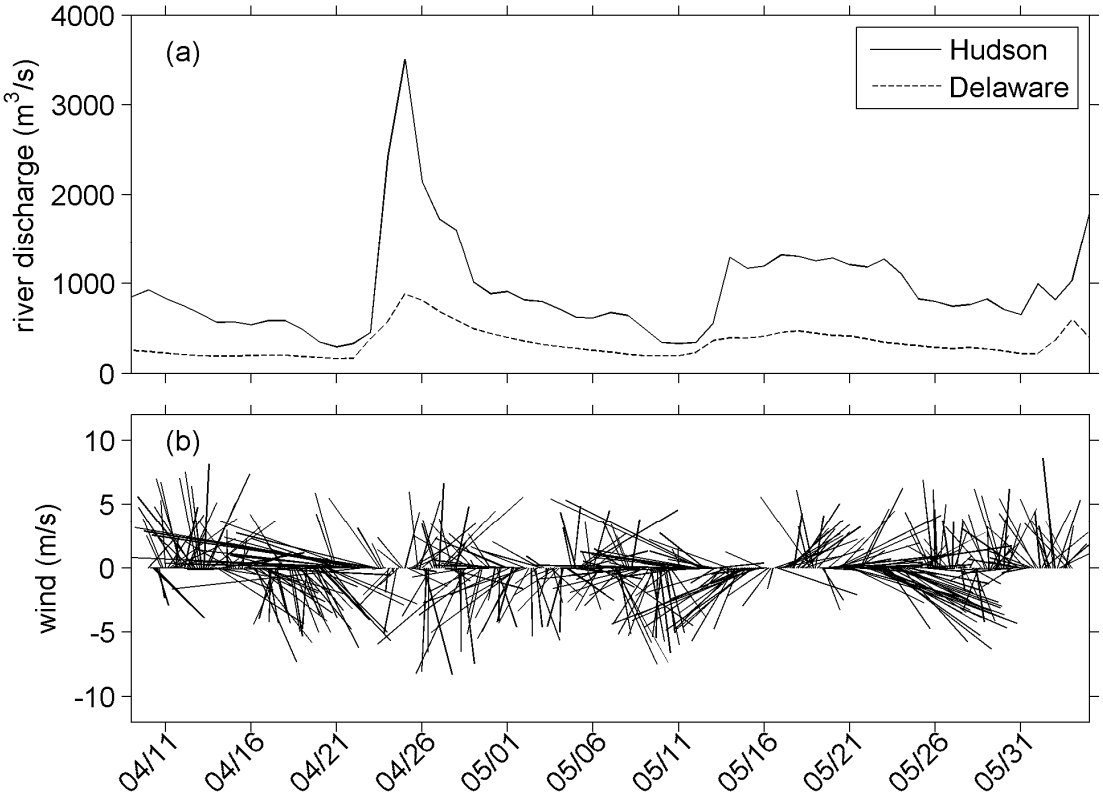

Figure 5.5. River discharges (a) and wind at the Hudson River mouth (b) over the experiment period.

5.4. Data Assimilation System

5.4.1. IS4DVAR Theory

Here I briefly describe the theory of IS4DVAR for completeness. Readers can refer to literatures for detailed description (Courtier 1997, Courtier et al. 1994, Powell et al. 2008, Weaver et al. 2003). The nonlinear ROMS can be presented as,

$$\begin{cases} \dfrac{\partial \mathbf{\Phi}(t)}{\partial t} = M(\mathbf{\Phi}(t)) + \mathbf{F}(t) \\ \mathbf{\Phi}(0) = \mathbf{\Phi}_i \\ \mathbf{\Phi}(t)\big|_{\Omega} = \mathbf{\Phi}_{\Omega}(t) \end{cases} \tag{5.1}$$

where M is the model nonlinear operator; $\mathbf{\Phi}(t)$ is a state vector $[\mathbf{u}\ \mathbf{v}\ \mathbf{T}\ \mathbf{S}\ \zeta]^{\mathrm{T}}$ comprised of the velocity, temperature, salinity and sea surface height at all model grid points at time t; $\mathbf{F}(t)$ is the external forcing; $\mathbf{\Phi}_i$ is the initial conditions; and $\mathbf{\Phi}_{\Omega}(t)$ are boundary conditions along boundary Ω. I assume the model is perfect (strong constraint). The objective of the DA is to adjust the control variables (i.e. initial conditions, boundary conditions and forcing) to minimize the mismatch between observations and model equivalent,

$$J_o = \frac{1}{2}\sum_{n=1}^{N_{\mathrm{obs}}} \left(\mathbf{H}_n \mathbf{\Phi}(t_n) - \mathbf{y}_n\right)^{\mathrm{T}} \mathbf{O}^{-1} \left(\mathbf{H}_n \mathbf{\Phi}(t_n) - \mathbf{y}_n\right), \tag{5.2}$$

where $\mathbf{H}$ is the sampling operator which samples the nonlinear model states at the observation locations, $\mathbf{O}$ is the observational error covariance matrix, and $\mathbf{y}$ is the observations. We let $\mathbf{\Phi}_0$ denote a solution to the nonlinear problem (5.1) and the mismatch between the model and observation is then $\mathbf{d} = \mathbf{y} - \mathbf{H}\mathbf{\Phi}_0(t)$. Assume $\mathbf{\Phi}_0$ is sufficiently "close" to the truth, that is, $\mathbf{d}$ is small and adjustment to initial conditions, $\boldsymbol{\varphi}_i = \delta\mathbf{\Phi}_i$, boundary conditions, $\boldsymbol{\varphi}_{\Omega}(t) = \delta\mathbf{\Phi}_{\Omega}(t)$, and external forcing $\mathbf{f}(t) = \delta\mathbf{F}(t)$ required to fit the observations is sufficiently small. Then the system can be linearized and the cost function is defined as

$$J = \frac{1}{2}\sum_{n=1}^{N_{\text{obs}}} \left(\mathbf{H}'_n \boldsymbol{\varphi}(t_n) - \mathbf{d}_n\right)^{\mathrm{T}} \mathbf{O}^{-1} \left(\mathbf{H}'_n \boldsymbol{\varphi}(t_n) - \mathbf{d}_n\right) + \frac{1}{2}\boldsymbol{\varphi}_i \mathbf{B}_i^{-1} \boldsymbol{\varphi}_i + \frac{1}{2}\boldsymbol{\varphi}_\Omega \mathbf{B}_\Omega^{-1} \boldsymbol{\varphi}_\Omega + \frac{1}{2}\mathbf{f}\mathbf{B}_f^{-1}\mathbf{f} \tag{5.3}$$

where N_{obs} is the number of observational data, $\mathbf{H}'$ is linearized $\mathbf{H}$, $\boldsymbol{\varphi}(t)$ is the perturbation state at time t, $\boldsymbol{\varphi}(t) = \boldsymbol{\Phi}(t) - \boldsymbol{\Phi}_0(t)$, $\mathbf{B}_i$, $\mathbf{B}_\Omega$ and $\mathbf{B}_f$ are the covariances of errors in initial conditions, boundary conditions and forcing, respectively. The first term in the right-hand-side of equation (5.3) is a measure of the model-observation mismatch, and the last three terms in equation (5.3) are to penalize the adjustment of the control variables to ensure them to be small.

The minimization of J is usually achieved iteratively (inner-loop) using a Conjugate Gradient algorithm. Because the system is linear, J is quadratic and the convergence of iterations is guaranteed. In each iteration the gradient of J with respect to control variables obtained from the adjoint model forced by the model-observation mismatch (Talagrand and Courtier 1987) provides the direction of the minimum search. There is also a layer of outer-loop which runs the nonlinear model using the adjusted control variables when an inner-loop is finished. This brings the nonlinearity into the system. In the end, corrected initial conditions, boundary conditions and forcing are obtained.

5.4.2. System Setup

The DA experiment in this chapter covers the period of April 10 to June 5, 2006. The DA window is chosen to be 3 days based on the Tangent Linear model linearization tests in Chapter 4. Following the practice of real-time numerical weather forecast, I choose to overlap consecutive DA cycles: the beginning of the DA window proceeds one day from

one cycle to the next, and there is therefore a two-day overlap between two consecutive cycles. The workflow is described as follows. The first DA cycle starts at April 10, 00:00 UTC (The times in this chapter are all UTC and UTC is neglected from now on.) with the first guess of the initial conditions from the control forward model simulation. The 3-day DA assimilates all the observational data within the period (April 10, 00:00– April 13, 00:00) and gives an adjusted initial conditions. An 18-day forward nonlinear model simulation is then launched with the adjusted initial conditions at April 10, 00:00. The model output within the first three days are analysis results and that for the following 15 days are forecasts. Note that the ocean forecasts here are forced by the sequentially merged 6- to 30-hour daily meteorological forecasts, and the forecast skill of the 4DVAR system in this study is therefore expected to be better than that in real time. The second DA cycle starts at April 11, 00:00 with the first guess of the initial conditions from the analysis of the first DA cycle. It then assimilates all the observational data within the window of April 11, 00:00 and April 14, 00:00 and produces adjusted initial conditions at April 11, 00:00. Note that the observations between April 11, 00:00 and April 13, 00:00 have been assimilated in both the first and the second DA cycles. Another 18-day forward nonlinear model simulation starting from the adjusted initial conditions at April 11, 00:00 is then launched. The cycles repeat. The last DA cycle starts at June 3, 00:00:00. In total, there are 55 overlapped cycles.

In this study, I adjust only the model initial conditions to fit the observations. The last two terms in equation (5.3) are therefore neglected. It is likely that errors exist in the external forcing and boundary conditions. But given the relatively short DA window, I expect the effects of initial conditions to dominate the effects of boundary conditions and

forcing in the subsequent evolution of oceanic tracers (temperature and salinity). Thus initial condition error is a major cause of the model-observation tracer mismatch. This is consistent with results in Chapter 4 in the context of comparing contributions of different sources to SST anomaly on the New Jersey coast. However, this argument is not necessarily correct for velocity as we will see later in this chapter. The capability of adjusting external forcing and boundary conditions has been recently added to ROMS. They will be applied in future studies and it presumably will improve the performance of the DA system.

Within each DA cycle, 3 outer-loops and 11 inner-loops are used. Tests with different number of outer-loops and inner-loops show that this combination is the best balance between system performance and affordability. Due to strong nonlinearity embedded in the generic length scale method and bulk formulae, their linearizations are not used in the Tangent Linear and Adjoint models. Instead, vertical viscosity and diffusivity, surface heat and moment fluxes computed in the first nonlinear model simulation of each cycle were stored and used by the Tangent Linear and Adjoint models in that cycle.

5.4.3. Error Statistics

The model-observation mismatch in the cost function (the first term in the right-hand-side of equation (5.3)) is weighted by observational error covariance. In this study I assume the observations are independent of each other, and the observational error covariance matrix **O** is then a diagonal matrix. An error value is assigned to each observation to represent observational error which includes instrument error, misrepresentation error associated with subgrid-scale physics missed by the model but

caught by the instruments, and model misrepresentation error associated with error in forcing and open boundary conditions. The error assigned for each observation is essentially to measure how much each of the observations can be trusted given the status of the model. To choose the observational error representation is a rather subjective and empirical task. On one hand, it should be based on the knowledge we have about the instruments and model characteristics. On the other hand, we need to choose the errors that will make the minimization in the DA system converge. Table 5.1 lists the error representation associated with each instrument type that is used in this study.

Table 5.1. Observational Error Representation

Observational Platform	Satellite	HF Radar	Glider	Mooring	Drifters	Shipborne
Velocity ($m\ s^{-1}$)	----	0.05	----	0.02	----	0.06
Temperature (^oC)	0.4	----	0.4	0.4	0.3	0.6
Salinity	----	----	0.4	0.4	----	0.6

The background error covariance $\mathbf{B}_i$ in Equation (5.3) is to take into account the interconnection between the initial condition adjustment in the same variable at different locations (univariate) and between the adjustment in different variables (multi-variate) (Derber and Bouttier 1999). It is essentially to spatially smooth the initial condition adjustment for this study. Because it is impossible to have the explicit form of $\mathbf{B}_i$ in a 4DVAR system given its prohibitive size ($O(10^6)\times O(10^6)$ for this study), it is usually

estimated based on an ensemble of model simulations (Li et al. 2008, Parrish and Derber 1992) or numerical simulation of diffusion equations (Weaver and Courtier 2001). The algorithm proposed by Weaver and Courtier (2001) was implemented in ROMS (Powell et al. 2008). It separates $\mathbf{B}_i$ into a multi-variate balance operator, background error standard deviations, and a univariate correlation matrix. The correlation matrix is further separated to horizontal and vertical correlations, and each of them is achieved by solving a diffusion equation (2 dimensional for horizontal and 1 dimensional for vertical).

Because the balance operator in ROMS is still under development, it is not used in this study. It is worth emphasizing that some of the dynamical connections between different variables can still be caught by the Tangent Linear and Adjoint model integrations. The background error standard deviations were calculated from a detided 3-month model simulation assuming that the uncertainty in initial conditions is similar to the subtidal variability. In computation of correlation 20 km horizontal and 2 m vertical decorrelation scales were chosen based on the length scales that local spatial variability has. Note that the length scale in ROMS is defined as the distance over which the correlation reaches about 0.7.

5.5. Results

In this section I am going to show two examples of the DA results first. Investigations of statistical measures of the model performance, i.e., the reduction of the model-observation mismatch in analysis and forecast modes, respectively, will then be presented. Note that the comparison in analysis mode will be conducted with only assimilated data and that in forecast mode with unassimilated independent data.

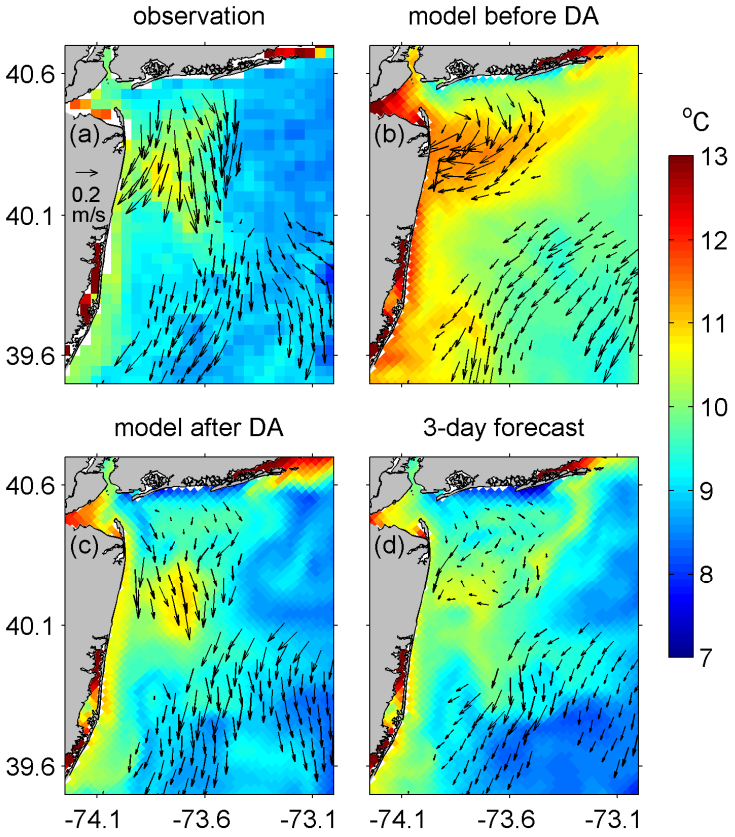

Figure 5.6. Comparison of observed and modeled sea surface temperature and current at 2006 April 20, 07:00:00.

5.5.1. Two Examples

Figure 5.6 and 5.7 show two examples of the DA result. In Figure 5.6, satellite-measured SST and HF-Radar-measured surface current at 2006 April 20, 07:00:00 are compared to their equivalent in the control simulation, the analysis given by the 10th cycle (DA window spans April 19 – 22, 00:00:00) and the forecast of the 6th cycle (DA window spans April 15 – 18, 00:00:00). The observational data were preprocessed as

described in Section 5.2. Comparison between Figure 5.6a and b clearly shows that SST in the control simulation is too warm everywhere, the warm Hudson River plume extends too much to the east, the coastal warm patch around 39.6^{o}N extends too offshore, and most of the surface current vectors are pointing to the right of the observed ones. The model errors have largely been removed in the analysis by the DA (Figure 5.6c): SST bias appears absent, the Hudson River plume sits at the right location, the warm patch along the New Jersey coast covers the right area, and most the surface current vectors point to the same direction as the observed ones. The 3-day forecast (Figure 5.6d) has SST and surface current pattern closer to the observations than the control simulation, but the forecast deviates more from the observations than the analysis, especially for the surface current in the Hudson River plume area.

Between April 27 and 29 a glider was deployed around the Hudson Shelf Valley area and its track is the one in Figure 5.1 across the Hudson Shelf Valley. In Figure 5.7, the measured temperature and salinity cross-sections are compared to the equivalent in the control simulation, the analysis given by the 20th cycle (DA window spans April 27 – 30, 00:00:00) and the forecast given by the 17th cycle (DA window spans April 24 – 27, 00:00:00). The comparison between observations and the control simulation shows about 1^{o}C surface warm bias, 1^{o}C subsurface cold bias and 0.5 psu saline biases in all depth in the model. In the analysis the biases have largely been removed and the temperature and salinity patterns have been mostly restored except that the subsurface saline bias in the Hudson Shelf Valley becomes worse. In the 3-day forecast, the biases in most areas are absent, but the spatial patterns divert from the observations much more than the analysis, especially salinity in the surface layer.

These two examples demonstrate that the DA system utilized in this study is capable of bringing the model closer to the observations and also giving somewhat improved forecasts comparing to the control simulation before DA.

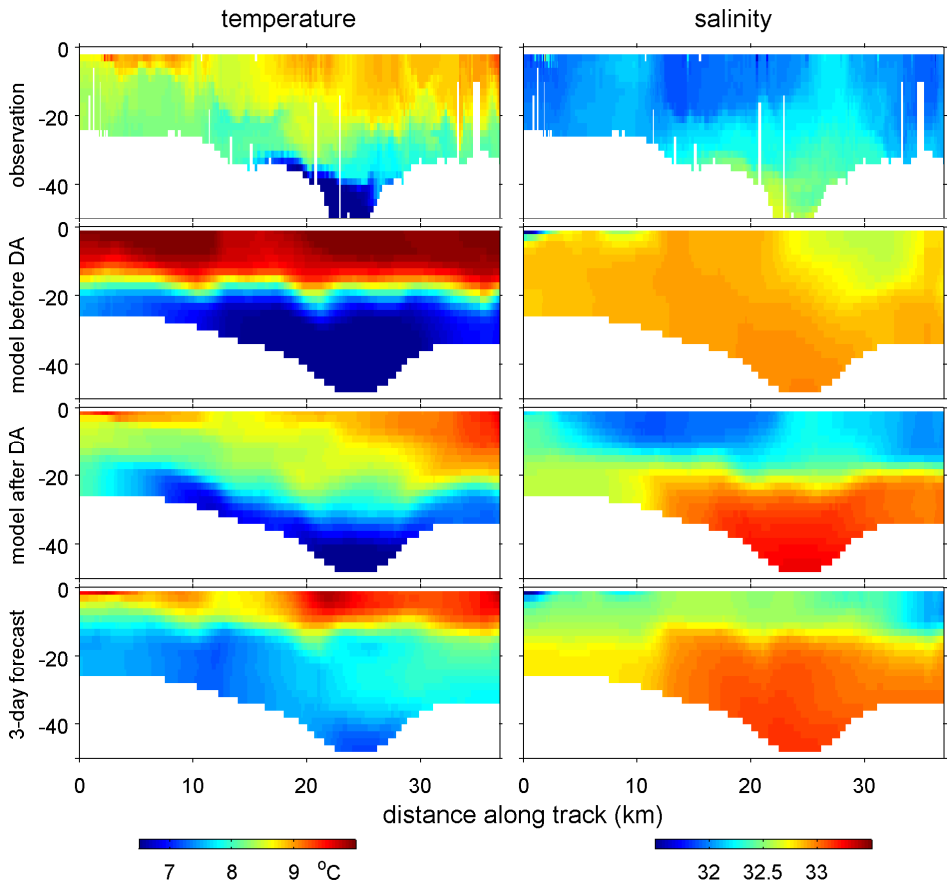

Figure 5.7. Comparison of glider-measured and modeled temperature and salinity along a glider track between April 27 and April 29, 2006 (The red line across the Hudson Shelf Valley in Figure 5.1).

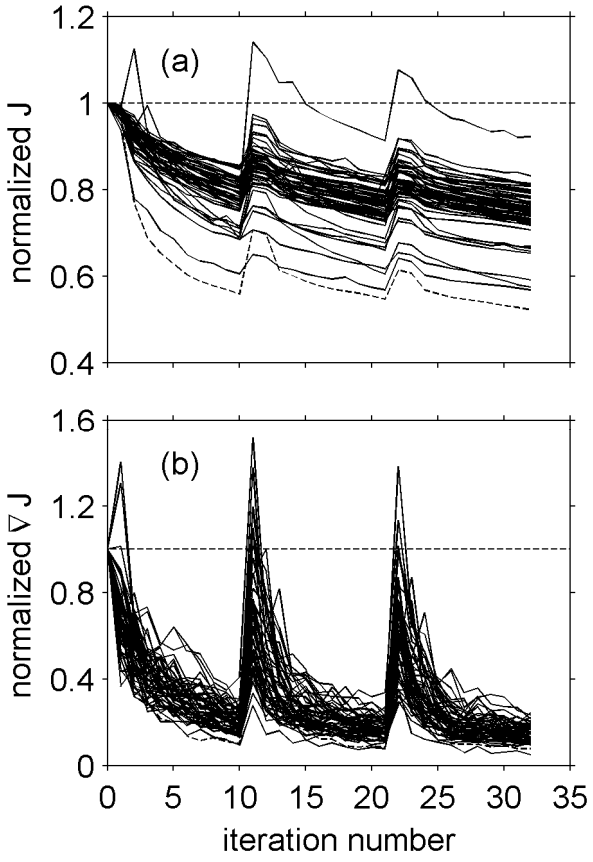

Figure 5.8. Normalized cost functions (a) and cost function gradient norm (b) at each iteration of all the 55 DA cycles. The dashed lines are from the first DA cycle. The normalization is achieved through dividing the cost functions and cost function gradient norms by their value at the beginning of each DA cycle.

5.5.2. Analysis Error Reduction

Figure 5.8 shows cost function value and cost function gradient norm after each iteration for all 55 cycles. They are normalized by their initial values at the beginning of each cycle. It can be seen that cost functions in all cycles decrease as the iterations proceed

and most of the cycles have more than 20% reduction of cost function after 33 iterations. The reason for such a low reduction of cost function is that, on average, 2/3 of the observations in each cycle have been assimilated by previous cycles. The dashed curve in Figure 5.8a has the largest decrease of cost function (about 50%) in 33 iterations and is from the first 3-day cycle within which all observations were assimilated for the first time. It is expected that most of the mismatch between the previously assimilated observations and the model is in the null space of the DA system, and it is caused by subgrid-scale dynamics, error in forcing or boundary conditions, etc. That is, it is impossible to adjust model initial conditions to reduce this part of the mismatch. Within 33 iterations, cost function gradient norms in all cycles have about an 80%-90% reduction. This indicates that the conjugate gradient algorithm has successfully found the minima of the cost functions.

Another distinct feature in Figure 5.8 is the surge of the cost functions and their gradient norms at the beginning of each outer-loop. This is caused by the update of the nonlinearity in the dynamical system. The minimization of the cost function within each outer-loop is based on linearization upon the nonlinear model trajectory given by the previous cycle (for the first outer-loop) or the previous outer-loop (for the second and third outer-loops). The nonlinearity update at the beginning of each outer-loop breaks the assumption and incorporates nonlinearity into the DA system. As the minimization proceeds, the surges of cost function become smaller. This indicates that the linear models are getting closer to the nonlinear models, suggesting that the linear assumption embedded in the Tangent Linear and Adjoint models is appropriate.

To further demonstrate reduction of the model-observation mismatch, I produced scatter plots of observation vs. the control simulation and the analysis for temperature, salinity and velocity u-component as in Figure 5.9. Comparison of model-observation RMS differences before and after the DA gives about 60% RMS reduction for temperature, 30% for salinity, and 25% for velocity u-component by the DA. The RMS reduction for velocity v-component is similar to u-component (not shown). From the temperature comparison we can see that the warm bias in the control simulation has been removed in the analysis and the scattering around the diagonal line has been reduced. The salinity comparison also shows reduction of the scattering around the diagonal line, although some large mismatch between analysis and observation remains. The large salinity mismatch between analysis and observation mostly occurs within the estuary (shipborne in-situ salinity measurements). Because the model resolution is too coarse to properly resolve the estuarine processes, large mismatch there is unsurprising. Scattering of the velocity u-component is also reduced by the DA, but it remains large. One possible reason for this is that the variability-to-span ratio of velocity is about 1, which is much larger than that of temperature and salinity. Presumably, model error is proportional to the natural variability and then the ratio of model error to span, which the plotted scattering really means, for velocity is larger than that for temperature and salinity. Another possible reason for the relatively larger error in modeled velocity is wind error and it will be discussed in the next section.

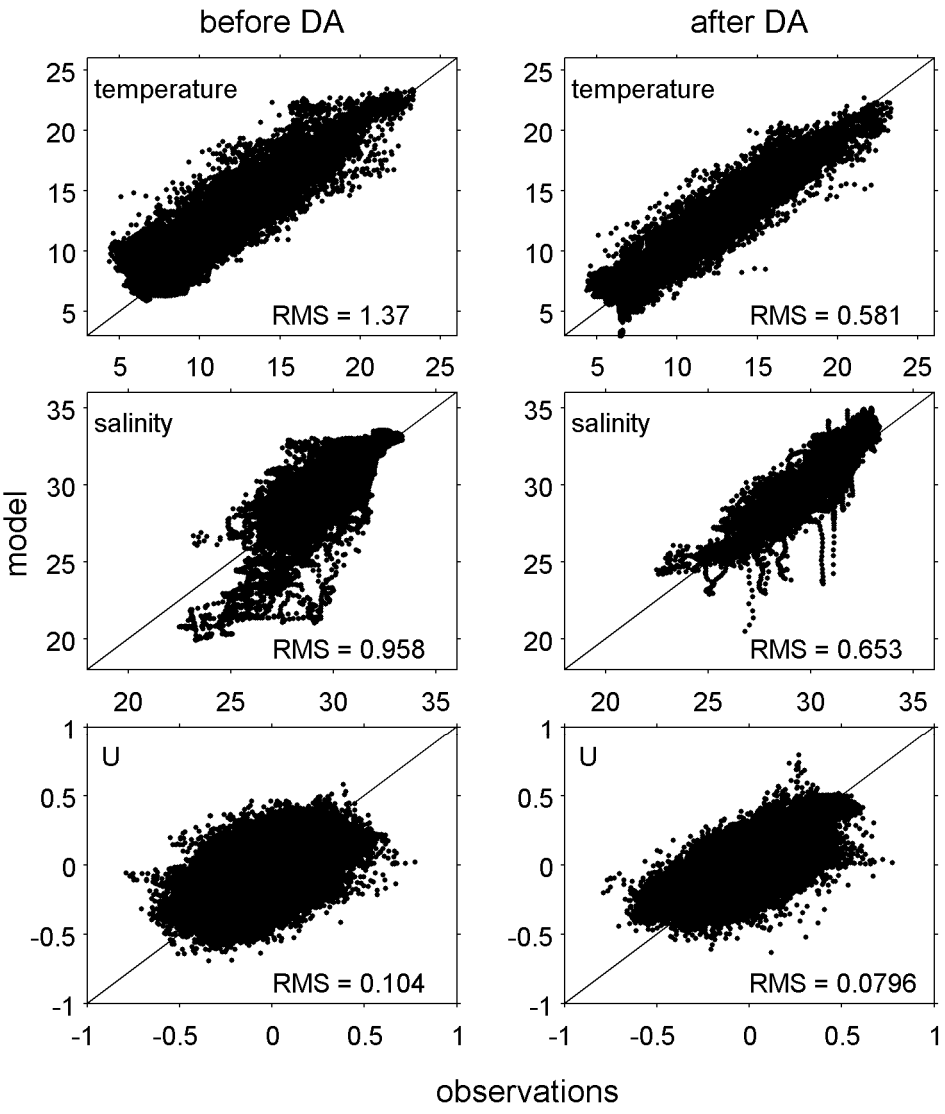

Figure 5.9. Comparison between observed and modeled temperature, salinity and U-velocity for model before (control run) and after data assimilation.

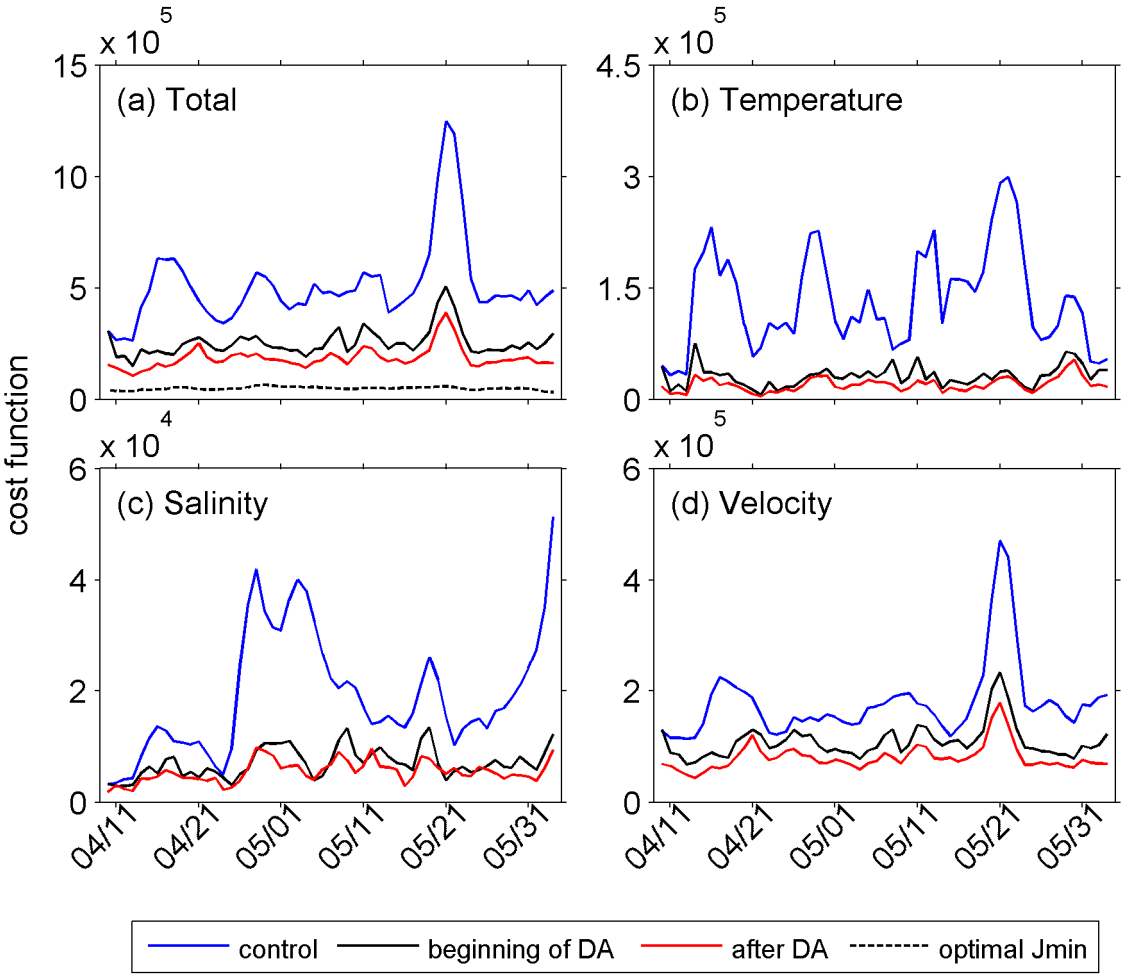

Figure 5.10. Cost function of the control run, at the beginning of each cycle and of the analysis and the Chi-squared-theory-predicted optimal minimum of cost function of each cycle.

Figure 5.10 presents the time series of the total cost function and the cost functions of temperature, salinity and velocity. The cost functions of the control simulation, at the beginning of each cycle and of the analysis are compared in each subplot. Note that the background cost function (the second term in the right-hand side of equation (5.3)) in this study starts with zero at the beginning of the minimization and is about one order smaller

than the observational cost function at the end of the minimization for all the cycles. The time series of cost functions in Figure 5.10 therefore approximately represent the change of observational cost functions (the first term in the right-hand-side of equation (5.3), i.e. a measure of the model-observation mismatch) over the experiment period. If the observational and background errors are Gaussian and their covariance **O** and $\mathbf{B}_i$ are correctly described in the 4DVAR system, the Chi-squared theory predicts that the minimum value of the cost function is half of the number of observational data assimilated, $N_{obs}/2$, with variance $1/N_{obs}$ (Bennett 2002, Powell et al. 2008, Weaver et al. 2003). Note that because the definition of cost function in Bennett (2002) is different from the one in this study, Powell et al. (2008) and Weaver et al. (2003) by a ½-factor, the minimum value of cost function in Bennett (2002) is N_{obs}. The Chi-squared predicted minimum cost functions are plotted in dash lines in Figure 5.10a with the associated variances neglected (they are too small to be shown).

The cost function comparison in Figure 5.10a shows a big drop of the total cost function from the control simulation to the beginning of each cycle for most of the cycles. Notice that they are the same for the first cycle because the oceanic state at the beginning of the first cycle is from the control simulation. From the beginning of the cycles to the analysis there is another drop of the cost function but to a smaller extent. As mentioned before, it is small because 2/3 of the observations in most of the cycles have been assimilated by previous cycles and most of the residual mismatch is in the null spaces. In the end, the analysis cost functions are 2 to 3 times larger than the optimal minimum values given by Chi-squared theory. Given the fact that the IS4DVAR system used here corrects only initial conditions, and the errors in surface forcing, boundary conditions and model

physics are neglected, this result is unsurprising. As will be presented in next subsection, there are substantial errors in wind forces. It certainly contributes to the discrepancies between minimized cost functions and the optimal minima.

Breaking down the cost functions to different variables I find that the model-observation velocity mismatch is the leading source of the total cost function, temperature mismatch is the second and the salinity mismatch is the smallest. For all of them, DA is able to substantially decrease the mismatch in all cycles. As previously reported, the largest decrease happens to temperature mismatch and the smallest decrease to velocity mismatch. The large remain of the velocity mismatch suggests that much of the velocity mismatch is in the null space of the DA system and can not be corrected by adjusting model initial conditions. As we will see in next subsection, it is, at least partially, due to the spatially coherent "error" in the surface current observations. The velocity error is really error in the model generated by error in wind forcing. But because surface forcing is not part of the control variables the DA system considers the model-observation discrepancy as "observational error".

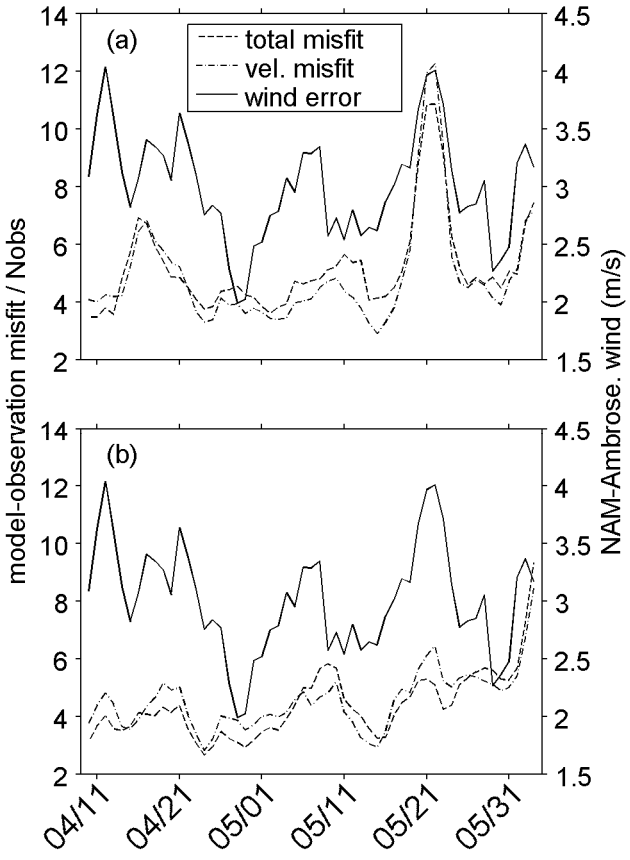

Figure 5.11. Magnitude of NAM wind error, normalized model-observation total misfit and normalized model-observation velocity misfit of the control run before (a) and after (b) the wind correction. All misfits are normalized by the number of corresponding observations assimilated in each cycle.

5.5.3. Effects of Wind Error

Another feature in Figure 5.10 is the spike increase of total cost function around May 21. The spike persists after DA. Similar spikes also exist in the control simulation cost function of temperature and velocity, and DA was able to eliminate it for temperature, but

not for velocity. This suggests that a significant part of the model-observation velocity mismatch falls into the null space of the DA system. To investigate the mechanism I computed the difference between the 3-hour averaged observed wind and the 3-hourly NAM wind at the nearest grid point to the wind observation. The observed wind was measured at about 20 m above the sea level by the Ambrose Tower which was maintained by National Data Buoy Center and its position is given in Figure 5.1. Note the NAM wind is 10 m wind. The apparent inconsistency here is neglected because the measurements that are required to compute the 10 m wind are missing. Part of the difference between NAM wind and observed wind is the error of the NAM wind at the area around Ambrose Tower. Averaged magnitude of the NAM wind error over each DA window is plotted in Figure 5.11a together with total cost function and velocity cost function of the control simulation. To eliminate the effect of different numbers of observations, I normalized the cost functions in Figure 5.11 by the number of corresponding observations assimilated in each cycle.

Because the number of observations in each day varies relatively little as shown in Figure 5.4b, the normalized cost functions in Figure 5.11a preserve the basic temporal variation in Figure 5.10 including the spike around May 21. Time series of averaged NAM wind error in Figure 5.11a show a similar jump around May 21. The overall correlation between averaged NAM wind error and normalized total cost function is about 0.48 and that between average wind error and normalized velocity cost function is about 0.62, both statistically significant at 95% confidence level. These suggest that error in wind forcing of the model is an important source of the model-observation mismatch, especially the mismatch in velocity. The reason can be easily seen in Figure 5.2, the averaged power

spectrum of surface current measured by HF Radar. There is a distinct peak within the inertial band, significant at the 95% level. It means that the ocean in this area reacts strongly to wind through inertial oscillation. Note that the highest peak in Figure 5.2 is M2 tide. Because tidal currents in HF Radar data have been replaced with ROMS tidal currents, I am essentially assimilating the detided surface current data. Then model-observation velocity mismatch in the inertial band is very likely to be a major part of the total velocity mismatch.

I further show this through a nonlinear forward model simulation forced with wind corrected in a simple way. I assume NAM wind error has a horizontal scale larger than the model domain. Wind error in the domain is then nearly uniform. I corrected the NAM wind by adding the difference between NAM-modeled and Ambrose-measured winds to NAM wind everywhere in the model domain. I then conducted a nonlinear forward model simulation same as the control one except using the corrected wind. The normalized total cost functions and velocity cost functions of the new nonlinear model are plotted in Figure 5.11b along with the NAM wind error. The comparison between Figure 5.11a and b demonstrates the effect of simple wind correction: model-observation mismatch has been decreased for most of the cycles and the mismatch spike around May 21 has been decreased substantially. However, the validity of the assumption about the scale of NAM wind error is unclear. The exercise here is just for demonstration purposes. Even if the assumption was valid, we would not have the observed wind available for real-time forecast which is one of the goals of this study. Therefore, other methods of correcting wind are needed if no better wind product is available.

Because of the error in the NAM wind, correcting model initial conditions through DA would not be able to totally remove the model-observation mismatch, as shown in Figure 5.10a and d. After DA, the spikes of the cost functions around May 21 remain, but the magnitude has been substantially reduced. It means that the IS4DVAR system adjusted initial conditions to minimize the mismatch caused by the wind error. Presumably, this is overcorrection and it degrades the performance of the system, especially the velocity forecast, as we will see in next section. Because the harmonics of wind-driven inertial oscillation are unsteady it is impossible to filter them out as with the tides. Another option to solve this problem is to correct the wind forcing through DA by including surface forcing in the control variables of the IS4DVAR system. This is the next step of this study. If correct error statistics are used, it will presumably correct the error in the surface forcing and give a better analysis, although the forecast is still limited to the use of the uncorrected wind forcing.

5.5.4. Improvement of the Forecast

Because one of the purposes of this study is to practice real-time ocean weather forecasting, I present the statistical measure of the skills of the DA system, i.e. forecast improvement, of each variable in Figure 5.12. The skill is defined as

$$S = 1 - \frac{\mathrm{RMS}_{\mathrm{afterDA}}}{\mathrm{RMS}_{\mathrm{beforeDA}}}, \tag{5.4}$$

where RMS is the root-mean-square of model-observation mismatch weighted by observational error. This RMS is equivalent to the square root of the observational cost function. Note that observational data within forecast windows are not assimilated by DA,

and they are therefore independent data. Given the skill definition, any skill value greater than 0 means improvement of the model performance and the maximum skill is 1. Skill was computed for each day of the analysis and forecast windows for all 55 cycles. The ensemble average and 95% confidence interval for each analysis and forecast day were computed from the 55 cycles and plotted in Figure 5.12.

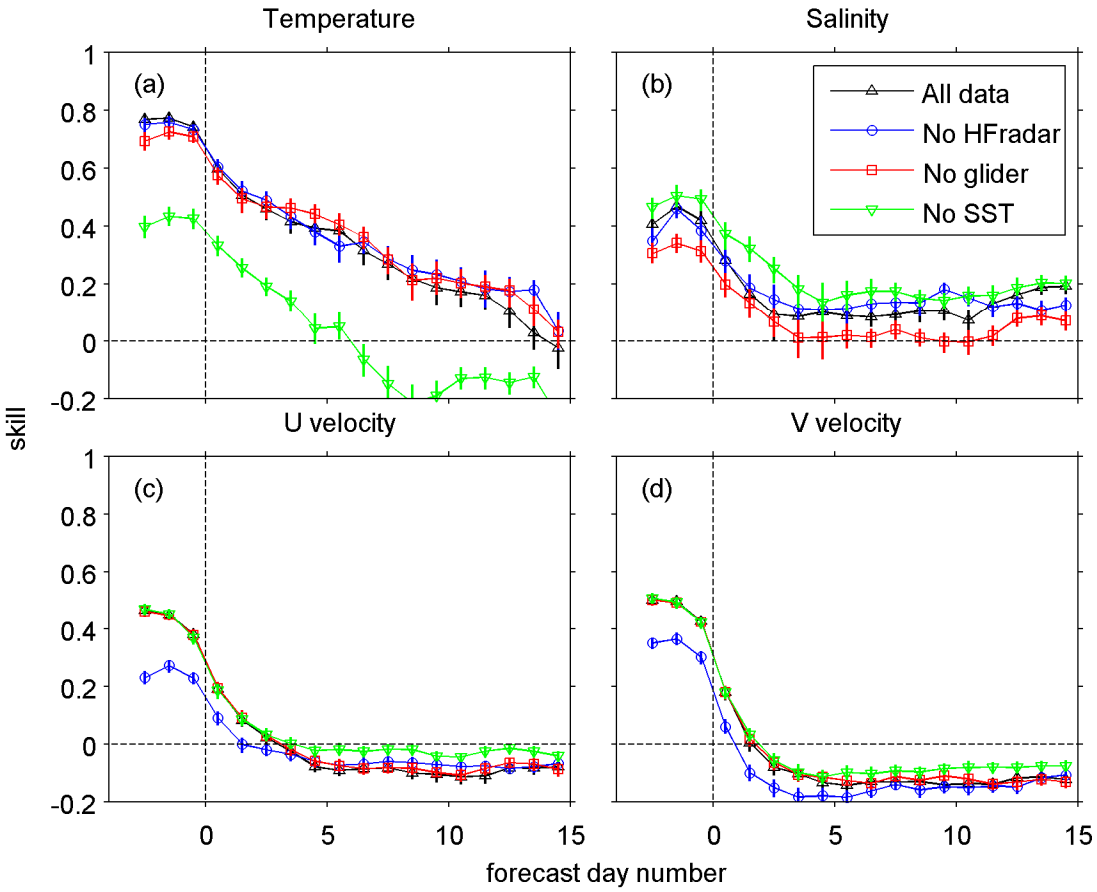

Figure 5.12. Ensemble average of the skills of different DA systems over analysis and forecast periods in term of different variables. Vertical bars indicate 95% confidence intervals of the skills. Vertical dash lines denote the boundary between analysis and forecast windows with analysis on the left and forecast on the right.

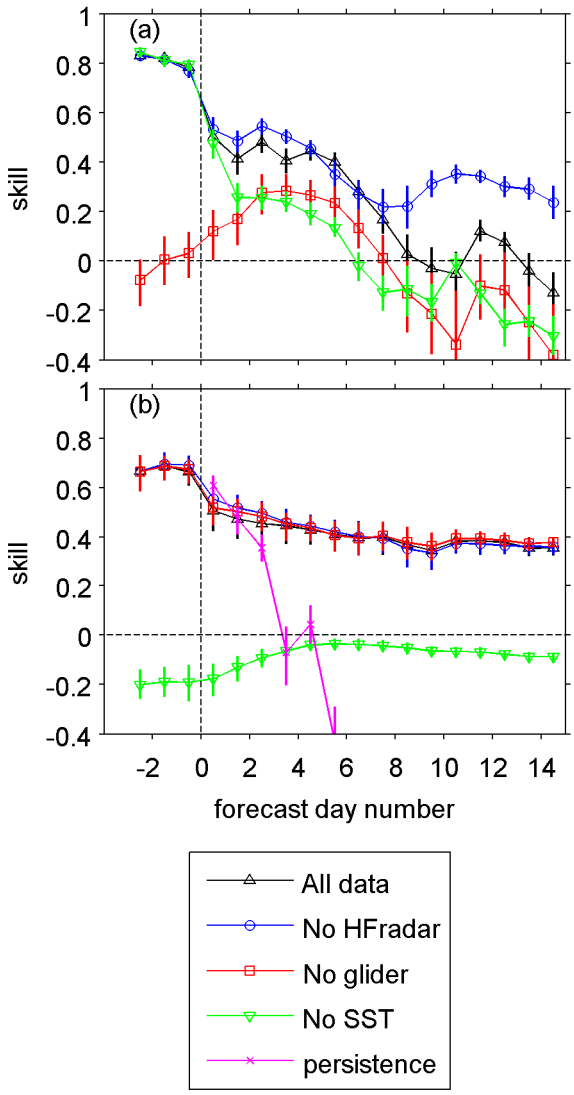

Figure 5.13. Ensemble average of the skills of different DA system over analysis and forecast periods in terms of glider-measured temperature (a) and satellite-measured SST (b). Vertical bars indicate 95% confidence intervals of the skills. Vertical dash lines denote the boundary between analysis and forecast windows with analysis on the left and forecast on the right.

In Figure 5.12, skills of the DA system that assimilates all available observational data are denoted by the black curves. In order to diagnose the effect of different data sets on the skills, I formed three other DA systems in which I withdrew HF Radar-measured velocity data, glider-measured temperature and salinity data, and satellite-measured SST data respectively from the assimilation. To make the explanation clear, I name the four DA systems All-data, No-HFradar, No-glider, and No-SST, respectively. Note that the skills shown in Figure 5.12 were computed from the comparison of models and all observational data even though some of the data were withdrawn from the DA systems.

Figure 5.12a shows that model-observation temperature mismatch in the analysis period is dramatically reduced (about 70% for the All-data, No-HFradar and No-glider systems and 40% for the No-SST system) and temperature forecast is substantial improved in all DA systems. The temperature forecast improvement of the All-data, No-HFradar and No-glider systems is about same, starts from 0.6 at the 1st day and gradually decreases to 0 at about the 14th day. In contrast, the No-SST system has the least forecast improvement. It starts with about 0.4 at the 1st day and drops to 0 at the 5th day. After the 5th day, the temperature forecast deteriorates slightly. The contrast between the No-SST system and others demonstrates the major impact SST data has on the temperature forecast improvement. It is expected to be, at least partially, an outcome of the fact that SST data occupies more than half of the temperature data.

To further diagnose the impact of different data sets, the temperature forecast improvement was separated to those of glider-measured temperature and satellite-measured SST as shown in Figure 5.13. Figure 5.13a shows that the forecast improvement of glider-measured subsurface temperature of the All-data system drops from

about 0.5 at the 1st day to 0 at the 8th day. Without assimilating HF Radar velocity data, there is no obvious change to the forecast improvement until 7 days into the forecast. Assimilating surface velocity decreases forecast improvement of subsurface temperature in the second week. Without assimilating glider data, although subsurface temperature mismatch between model and observation within the analysis window is preserved, the forecast gains skill for the first week. This is presumably caused by assimilating SST as we can see from the comparison between All-Data and No-SST system. Without assimilating SST data, the subsurface temperature forecast improvement drops for the entire forecast period even though the subsurface temperature mismatch between model and observation keeps same in the analysis period. This implies that the initial condition adjustment given by assimilating SST is able to propagate downward and improves subsurface temperature forecast.

In Figure 5.13b, we see that the All-data, No-HFradar, and No-glider systems have same performance on SST and the 0.4 forecast improvement is rather stable for the entire forecast period. Without assimilating the satellite-measured SST data, the skill of the DA system is constantly degraded. This means that assimilating other data sets does not improve SST forecast, although assimilating satellite-measured SST improves forecast of subsurface temperature. It suggests that model SST is not controlled by initial conditions of subsurface temperature or other variables.

Figure 5.13b also gives the persistence skill of the satellite SST observations. The persistence skill, a commonly used standard of reference for measuring the accuracy of the forecasts (Di Lorenzo et al. 2007, Murphy 1992), is computed by taking a SST map as the forecasts of subsequent fields of SST. The persistence skill starts around 0.6 for the first

day forecast and quickly approaches zero after 3 days. The comparison between the persistence skill and the skill of the DA system in Figure 5.13b suggests that the DA system was able to use the observations to correct the model dynamics through the model integration, rather than just fitting the observations.

Let us now move back to Figure 5.12 to look at the forecast improvement for other variables. Figure 5.12b shows that the All-data DA system reduces the model-observation salinity mismatch by about 40% and has forecast improvement about 0.3 at the 1st day and about 0.1 at the 3rd day. Forecast improvement after that stays around 0.1 for the rest of the 15 days forecast. Comparing the forecast improvement of different systems we see that assimilating glider-measured subsurface data improves salinity forecast improvement for the entire period, assimilating SST data decreases the salinity forecast improvement for the entire period, and assimilating surface velocity data has minimum impact on salinity forecast. The impact assimilating SST data has on salinity forecast reflects loss of freedom that model has to adjust its initial conditions to fit the observations.

Figure 5.12c and d show similar pattern: the All-data system reduces velocity mismatch between model and observations by about 45% and has velocity forecast improvement greater than 0 only for 2-3 days. Velocity forecast after that is deteriorated slightly. This weak skill of velocity forecast is presumably caused by the error in the surface wind as mentioned in previous subsection. Because surface wind stress is not one of the control variables and there is no other constraint on the initial condition adjustment than the overall departure, the DA system attributes model-observation velocity discrepancy to initial condition error. This behavior of adjusting the wrong field to fit observations is expected to degrade system performance. Negligible difference between

the skills of All-data, No-glider, and No-SST systems suggests that assimilating glider data and SST has little impact on the performance of the DA system on surface velocity. Nevertheless, the difference between All-data and No-HFradar systems suggests that assimilating HF Radar-measured surface current data improves velocity forecast by 1-2 days.

To show the evolution of skill over time, I present the Hovmöller plot of the RMS and cross-correlation (CC) ratios for different variables in Figure 5.14. Both RMS and CC are obtained from the comparisons between all available observational data and modeled equivalent (before DA and after All-data DA). Ratios are computed for each day in each DA cycle. Then each 45-degree tilted line in Figure 5.14 represents a DA cycle and all value with y-coordinate less than 0 is within analysis periods. The ratio for CC is chosen to be the ratio of 1-CC to make two ratios comparable: ratio less than 1 means improvement of the model relative to the observational data.

Both RMS and CC ratios of temperature have values much smaller than 1 in the analysis window for almost all cycles. In forecast periods, the RMS ratio remains less than 1 for most of the cycles except for several particular days and the CC ratio has intermittent patches of ratio greater than 1. The RMS ratio of salinity is less than 1 for most of the time except a period around April 25. Figure 5.5 indicates that the Hudson River had a peak discharge around the same time. Sudden injection of the large amount of freshwater into the shelf brings unusually large salinity variation, which is presumably hard to be simulated precisely. For both velocity components, RMS and CC ratios have values less than 1 in the analysis periods for most of the cycles, but the ratios become greater than 1 rather quickly after they enter the forecast periods, consistent with the statistical measure

of the velocity forecast improvement. The period in which it preserves its forecast improvement varies from 1 to 5 days.

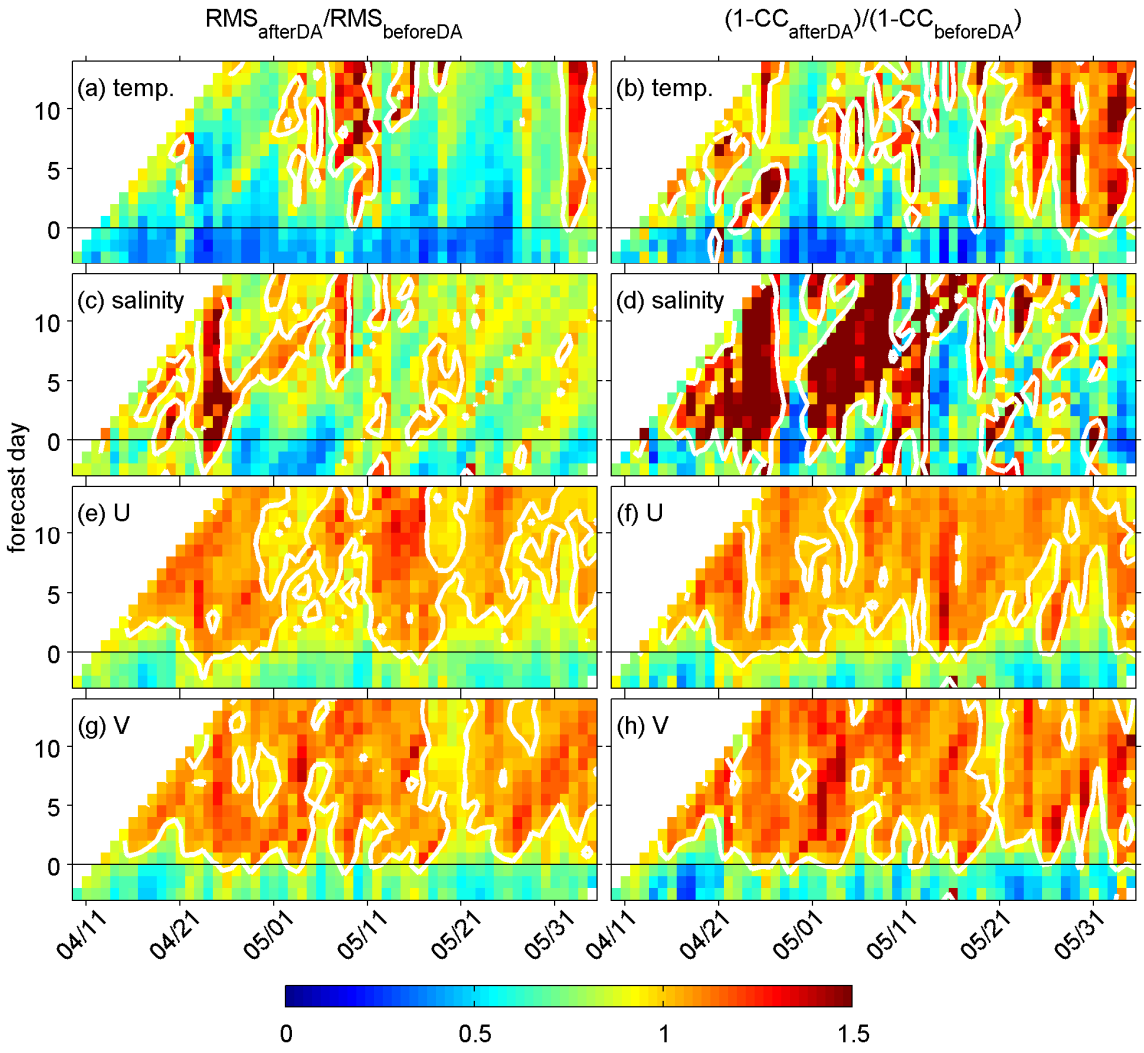

Figure 5.14. Hovmöller plot of RMS and cross-correlation ratios at each day of all cycles for the DA system assimilating all observational data. Thick white lines are contours of value 1.

5.6. Summary and Conclusions

As part of the project to build an integrated observation and modeling system for the New York Bight for the purpose of coastal ocean prediction and observing system design, this chapter carries out the 4D variational DA using ROMS in a realistic and pseudo-realtime setup.

In this chapter all the observations including temperature, salinity and velocity data collected by variety of platforms in spring 2006 during a campaign of field observation were assimilated. All observational data were preprocessed for quality control and to fit model spatial scales. Errors in observations were assumed to be independent and an error standard deviation was assigned to each observation according to instrumental error, model representation and the convergence of the DA system. ROMS IS4DVAR was used in this chapter with 3-day DA window to provide adjusted initial conditions. Simulations of diffusion equations were used with 20 km horizontal and 2 m vertical decorrelation scales to obtain the background error covariance. An overlapped DA cycling system was applied for the purpose of practicing real-time ocean forecast.

System performance was evaluated by looking into model-observation mismatch in analysis and forecast periods. Time series of cost functions and their gradient norms indicate that ROMS IS4DVAR converges towards cost function minima and reduces the model-observation mismatch in analysis periods successfully. The overall mismatch reduction is about 60% for temperature, 30% for salinity and 25% for velocity. Time series of the cost functions show that DA was able to reduce the cost functions for all 55 cycles, but the obtained minima of total cost functions are 2-3 times larger than the optimal minima given by the Chi-squared theory.

Significant correlation between wind forcing error and model-observation velocity mismatch suggests that a large portion of the velocity mismatch is actually caused by error in the wind used to force the model. A nonlinear model simulation forced with simply corrected wind shows improvement in the modeled velocities. A strong inertial response of the ocean to wind is hypothesized to be the reason. This finding emphasizes the importance of having accurate wind forcing in coastal ocean DA, especially when predicting surface velocity.

Skills of the DA system were obtained from comparing 15 days forecast of each cycle and unassimilated independent observations. Three new DA systems were designed to reveal the effects different data sets have on the skills. Overall, the DA system has positive forecast improvement for about 15 days for temperature and salinity and 2 – 3 days for velocity. Comparison between different DA systems indicates that assimilating satellite-measured SST improves not only the surface temperature forecast improvement substantially but also the forecast of subsurface temperature. It decreases the forecast improvement of subsurface salinity. Assimilating glider measurement improves the salinity forecast improvement but has little effect on the temperature forecast improvement. Assimilating HF Radar surface current data improves the velocity forecast improvement by 1-2 days even with the error in the wind forcing. The comparison also shows that assimilating HF Radar data worsens the forecast of subsurface temperature.

In all, this study demonstrates the ability of ROMS IS4DVAR to reduce model-observation mismatch and provide better forecast. It illustrates the importance of having accurate meteorological forcing and sheds the light on the benefit of correcting surface forcing through DA.

CHAPTER 6. OPTIMAL OBSERVATION

6.1. Introduction

The technology of ocean observation has undergone dramatic advances in recent decades. Numerous instruments are now monitoring the oceans and bringing unprecedented richness of data to oceanic research. While being used to study the oceans directly, observational data can also be used to correct numerical models with schemes of DA for state estimation or ocean weather forecasting. Increased investments in ocean observation also bolster the demand of evaluating existing observational strategies and objectively designing future observations. It is called targeted observation or adaptive sampling. The question of targeted observation for DA is to select the most efficient observation types and locations to improve model analysis or forecast of certain aspect of interest given instrumental and logistical constraints.

Targeted observation is an active research topic in the numerical weather forecast community (Langland 2005, Rabier et al. 2008). Berliner et al. (1999) synthesized the question thoroughly using the language of mathematics. There are different techniques of seeking targeted observations: Singular Vector-type (Leutbecher 2003, Palmer et al. 1998), adjoint sensitivity-type (Bergot 1999, Wu et al. 2007), observation sensitivity-type (Baker and Daley 2000, Langland and Baker 2004), and ensemble transform-type (Bishop and Toth 1999, Bishop et al. 2001) techniques.

Singular Vector techniques are to find the most rapidly growing error structures associated with a norm over a finite-time interval. The norm is chosen to describe an aspect of interest, e.g. forecast uncertainty or total energy. The argument is that to capture the

chosen aspect precisely the fastest-growing singular vector error structures in the model ought to be constrained by observations. Adjoint sensitivity techniques identify the variables and geographic locations to which a chosen aspect is most sensitive. The sensitive variables and locations are the dynamical upstream of the chosen aspect (Chapter 4), which is presumably the most effective target to observe for predicting the chosen aspect. Both adjoint sensitivity and singular vector approaches identify patterns that could cause large forecast error if they exist. But they do not take existing or planned observations into consideration. Existing observations may project onto the singular vectors or be located near the dynamical upstream, and they will subsequently change the pattern of the most effective observations.

The effect of existing observations on targeted observation can be addressed in observation sensitivity and ensemble transform techniques. The observation sensitivity provides the effect of each assimilated observation on analysis (forecast) of a chosen aspect using the adjoint of the data assimilation (forecast). Hence, effects of hypothetical observations can be obtained and compared although observation innovation (discrepancy between model and observation) needs to be estimated ahead. The ensemble transform-type techniques use ensembles of forecast simulations to retrieve the covariance of forecast and look for the optimal observation pattern which minimizes forecast uncertainty the most. It is most suitable for systems using ensemble-type DA schemes.

Unlike in meteorology, few works of targeted observation in oceanography have been published. Because most current studies of ocean DA emphasize state estimation, studies of targeted observation in oceanography pay more attention to better capturing certain ocean phenomena or variability (e.g. intraseasonal variability in the tropical oceans) in

analyses, instead of forecasts. Among the existing works, some (Ballabrera-Poy et al. 2007, Bennett 1990, Hackert et al. 1998, Oke and Schiller 2007, Sakov and Oke 2008) utilized ensemble transform-type techniques to study the designs of tropical mooring arrays in order to better capture the intraseasonal and interseasonal variability. Frolov et al. (2008) utilized a similar technique to assess and design fixed coastal and estuarine observatories. Barth and Wunsch (1990) utilized a simulated annealing technique to optimize the design of an acoustic array. Using the adjoint sensitivity technique, Shulman et al. (2005) identified the upstream of a bioluminescence patch and conducted a survey accordingly. Basing on array mode analysis, i.e. the eigen analysis of stabilized representer matrix (the sum of representer matrix and observational error matrix), McIntosh (1987) presented the optimal positioning of tide gauges in an open-ended channel and Bennett (1990) assessed an equatorial Pacific XBT observing program.

To reduce the computation load, Köhl and Stammer (2004) simplified the observation sensitivity technique using an assumption of large observational error. They applied the simplified technique to identify the optimal observation locations for determining the heat transport across the Greenland-Scotland ridge. Because the assumption of large observational error is inconsistent with the concept of DA being the step after targeted observation, interpreting their result as observation sensitivity as in Baker and Daley (2000) is probably inappropriate. However, from another prospective, their simplified technique is consistent with computing the representer of the chosen aspect. As we will see in next section, it gives the covariance and then correlation between the chosen aspect and ocean states at all locations at any time. Then it is logical to observe the places where the

correlation is the highest. This explains Köhl and Stammer's (2004) finding that their results are still valid even when the observational error is small.

The integration of observation and modeling shall be two-way. Chapter 5 demonstrates the use of observations to correct a numerical model with a 4DVAR scheme. In this chapter I will explore the use of the numerical model to assess and guide observations objectively. It provides a prototype for forecast-oriented targeted observation in a coastal setup. I stress here that the targeted observations will not be used to interpret physics directly and, instead, they are to be assimilated into a numerical model which will then describe the aspect of interest more precisely.

This chapter is organized as follows: Section 6.2 describes the theory of representer-based observing system design; Section 6.3 describes the system setup; Section 6.4 presents the application for predicting salt flux within the Hudson Shelf Valley (HSV); Section 6.5 compares the influences of different observations; Section 6.6 summarizes the chapter.

6.2. Representer-based Observing System Design

Denote ocean state vector $[\mathbf{u}\ \mathbf{v}\ \mathbf{T}\ \mathbf{S}\ \boldsymbol{\zeta}]^T$ comprised of the velocity, temperature, salinity and sea surface height at all grid points at time t as $\boldsymbol{\Phi}(t)$. A representer is the covariance between a single element of $\boldsymbol{\Phi}(t_0)$ (one variable at a particular grid point at a particular time t_0, I call it "point aspect of interest" in this chapter) and all elements of ocean state vector $\boldsymbol{\Phi}(t)$ (a 3-dimensional field at time t) (Bennett 2002, Kurapov et al. 2009). The covariance is not based on temporal variation of the ocean states but on different realization of randomly distributed ocean states in Bayesian statistics (van Leeuwen and Evensen 1996).

The ocean state obtained from a nonlinear numerical model is only one realization of all possible ocean states. We can transform the continuous space-based representer format in Bennett (2002) to a discrete space-based matrix format as

$$\text{Representer} = \mathbf{MBM}^{\mathrm{T}}\boldsymbol{\Delta}(\phi_0, \mathbf{x}_0, t_0), \tag{6.1}$$

where $\mathbf{M}$ is tangent linear model propagator and $\mathbf{M}^{\mathrm{T}}$ is the corresponding adjoint operator (Moore et al. 2004), $\mathbf{B}$ is the background error covariance matrix, $\boldsymbol{\Delta}$ is a impulse vector with the same length as $\boldsymbol{\Phi}$,

$$\boldsymbol{\Delta}(\phi_0, \mathbf{x}_0, t_0) = \begin{cases} 1 & \phi = \phi_0 \text{ and } \mathbf{x} = \mathbf{x}_0 \text{ and } t = t_0 \\ 0 & \phi \neq \phi_0 \text{ or } \mathbf{x} \neq \mathbf{x}_0 \text{ or } t \neq t_0 \end{cases},$$

ϕ_0 is the variable of interest ($\phi_0 \in [\mathrm{u\ v\ T\ S\ }\zeta]^{\mathrm{T}}$), $\mathbf{x}_0$ is the location of interest, and t_0 is the time of interest. Then $\phi_0(\mathrm{x}_0, t_0)$ is the point aspect of interest.

The representer is based on the linearization around a nonlinear model trajectory as the tangent linear and adjoint models imply. In variational DA, if the aspect of interest is a single observation, the corresponding representer describes the influence of the observation in the model (Bennett 1990, Egbert and Erofeeva 2002, Kurapov et al. 2009). To obtain a representer, as in equation (6.1), an adjoint model initialized with $\boldsymbol{\Delta}(\phi_0, \mathbf{x}_0, t_0)$ is integrated backward on time, model background error covariance is then applied and followed by forward integration of a tangent linear model. Here, $\boldsymbol{\Delta}(\phi_0, \mathbf{x}_0, t_0)$ can be considered as $\partial J_0/\partial\boldsymbol{\Phi}(t_0)$, where J_0 is an objective function of a point aspect of interest, $J_0 = \phi_0(\mathbf{x}_0, t_0)$. Hence, the representer gives the covariance between J_0 and $\boldsymbol{\Phi}(t)$, and equation (6.1) becomes

$$\mathrm{rep}\left(\frac{\partial J_0}{\partial \mathbf{\Phi}(t_0)}\right) = \mathbf{MBM}^{\mathrm{T}} \frac{\partial J_0}{\partial \mathbf{\Phi}(t_0)} = \mathrm{cov}(J_0, \mathbf{\Phi}(t)) . \tag{6.2}$$

Here I denote the linear representer operator as rep(·). Notice that both sides of the second equal sign give the same unit, $[J]\cdot[\mathbf{\Phi}]$. The middle term in equation (6.2) is very similar to Equation (13) in Köhl and Stammer (2004) except the sampling operator and observation error covariance matrix they applied after the representer.

Next, I am going to extend the representer concept to a more general circumstance. For a and b, any two independent point aspect of interest at time t_0, we can prove that (see Appendix)

$$\mathrm{rep}\left(\frac{\partial (a+b)}{\partial \mathbf{\Phi}(t_0)}\right) = \mathrm{cov}(a+b, \mathbf{\Phi}(t)) , \tag{6.3}$$

$$\mathrm{rep}\left(\frac{\partial (a-b)}{\partial \mathbf{\Phi}(t_0)}\right) = \mathrm{cov}(a-b, \mathbf{\Phi}(t)) , \tag{6.4}$$

$$\mathrm{rep}\left(\frac{\partial (ab)}{\partial \mathbf{\Phi}(t_0)}\right) \simeq \mathrm{cov}(ab, \mathbf{\Phi}(t)) , \tag{6.5}$$

and

$$\mathrm{rep}\left(\frac{\partial (a/b)}{\partial \mathbf{\Phi}(t_0)}\right) \simeq \mathrm{cov}(a/b, \mathbf{\Phi}(t)) . \tag{6.6}$$

Given equation (6.3) – (6.6), we expect

$$\mathrm{rep}\left(\frac{\partial J}{\partial \mathbf{\Phi}(t_0)}\right) = \mathrm{cov}(J, \mathbf{\Phi}(t)) \tag{6.7}$$

to be valid for J defined as any arithmetic function of ocean state variables at time t_0, $J = J(\mathbf{\Phi}(t_0))$. For J being a function of $\mathbf{\Phi}(t)$ over a time interval, $J = J(\mathbf{\Phi}(t))$, $t \in [t_1, t_0]$, in

discrete space its representer can be simply treated as a superposition of several representers associated with J's that are defined at instantaneous times, because the system is linear. Equation (6.7) is still valid. A special aspect of this representer is that $\partial J/\partial \mathbf{\Phi}(t)$, once the initial condition of the adjoint model, now has to be applied as forcing of the adjoint model over the time interval $[t_1, t_0]$ as in adjoint sensitivity (Chapter 3). Thereby, for a particular aspect of interest that can be expressed as an arithmetic function of model variables, e.g. salt transport across a cross-section, we can compute the corresponding representer to get the covariance between the aspect of interest and ocean variables at all locations at any time in the integration window. Note that the integration time window is limited by the linear assumption.

Suppose we are going to conduct some observations for knowing the aspect of interest better and there is no other observation available for this purpose, it is then logical to deploy instruments at the place where the observed variables have the highest correlation with the aspect of interest. Presumably, after assimilating the observations the model will describe the aspect of interest more precisely. Because there is no time constraint in the theory above except the linearization window, observations can be conducted ahead of, at the same time as, or after the happening of the aspect of interest. Hence, the representer-based observing system design can be applied for forecasts, nowcasts and hindcasts.

Like those in adjoint sensitivity-type and singular vector-type techniques, the assumption of having no other observation is a major drawback in the representer-based technique. Existing or routine observations will change the result of the targeted observation if their influences reach the aspect of interest in space and time. Nevertheless,

the result of the representer-based technique is useful when existing or routine observations are not close to the aspect of interest. Moreover, we can use the same representer-based technique to outline the influence area of existing or routine observations and check whether it covers the aspect of interest as in Section 6.5. If the aspect of interest is covered, how different the targeted observations would be is an interesting scientific question and can be addressed by the observation sensitivity technique. It is beyond the scope of this thesis but will be addressed in future studies since the machinery will soon be available.

6.3. System Setup

6.3.1. Model Configuration

The model domain as shown in Figure 6.1 is the same as the one in previous chapters. The nonlinear control simulation which the tangent linear and adjoint models are linearized based on covers the whole year of 2006 with initial condition from Chapter 2. It uses Chapman (1985) and Flather (1976) conditions for sea level elevation and the barotropic component of velocity on the model open boundaries, respectively. Steady along-shelf flow (Lentz 2008) and tidal elevation and current (K1, O1, Q1, M2, S2, N2, K2) extracted from a regional ADCIRC simulation (Mukai et al. 2002) were imposed on the open boundaries. Orlanski-type radiation condition (Orlanski 1976) was applied for 3D velocity and tracers. Vertical mixing was parameterized with the *k-kl* scheme of general length scale method (Umlauf and Burchard 2003, Warner et al. 2005) and quadratic bottom drag was used with drag coefficient 0.003. On the surface bulk formulae (Fairall et al. 2003) with meteorological forcings from the North American Regional Reanalysis (Mesinger et al. 2006) were applied to compute air-sea momentum and heat exchange. River discharges

were obtained from USGS Water Data (U. S. Geological Survey 2007) and modified to include ungauged portions of the watershed.

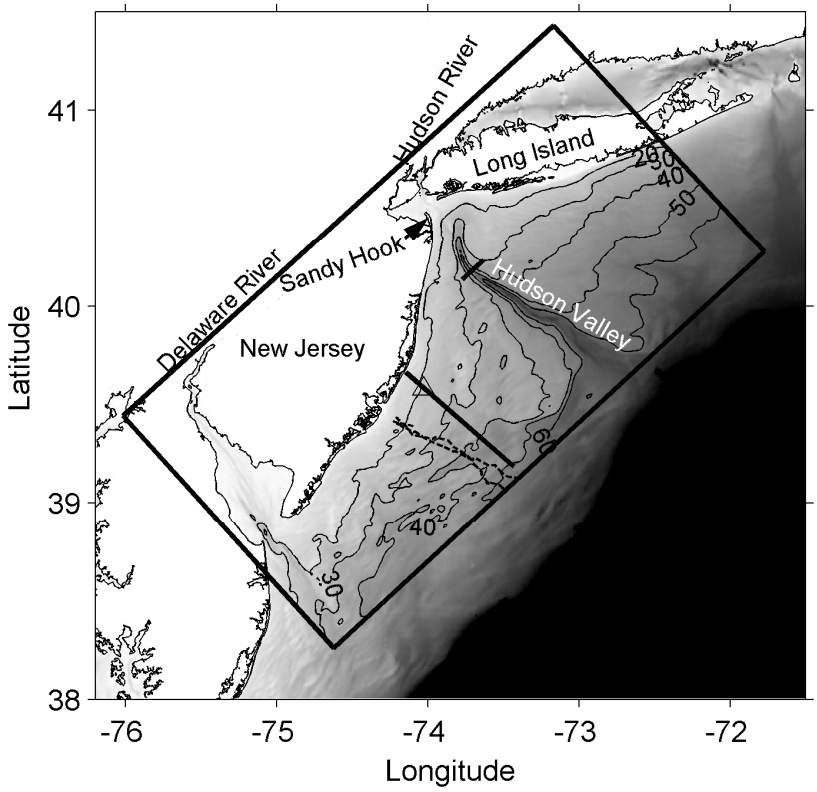

Figure 6.1. The model domain (black frame) and bathymetry of the New York Bight in grayscale. The short straight line across the Hudson Shelf Valley indicates the cross-section used in this chapter for computing salt transport within the valley; the dash line is a real glider track; the long straight line is the hypothetical glider track used in this chapter; and the triangle indicates the location of the hypothetical mooring.

6.3.2. Representer Computation

To compute the representer, as mentioned in the previous section, an adjoint model started with zero initial condition and forced by adjoint forcing is integrated backward for 3 or 4 days. A background error covariance, **B**, is then applied and followed by forward integration of a tangent linear model. The adjoint forcing, $\partial J/\partial \mathbf{\Phi}(t)$, is applied to the time interval over which J is defined. The length of adjoint and tangent linear model integration depends on the application as we will see later and it is constrained by the linearization. Chapter 4 tested the linear assumption in a model with the same domain but a higher horizontal resolution (1 km) and found that it is valid for 3 days. Because the tests were rather strict (perturbing initial condition with the fastest growing perturbation pattern obtained from optimal perturbation application) and model resolution in this study is lower, I expect the linear assumption in this chapter to be valid for a longer window. In the application of salt flux within the HSV, the adjoint model was integrated backward for 4 days in order to better simulate the glider deployment 2 days before the defined J.

The background error covariance describes the interconnection between variations of same variable at different locations (univariate) and variations of different variables (multi-variate) due to dynamical and statistical reasons. Only the univariate part is considered in this study and it is simulated by solving two diffusion equations (one for horizontal and the other for vertical) with horizontal decorrelation scale 20 km and vertical 2 m. More detailed description of background error covariance in ROMS can be seen in Powell et al. (2008) and Chapter 5.

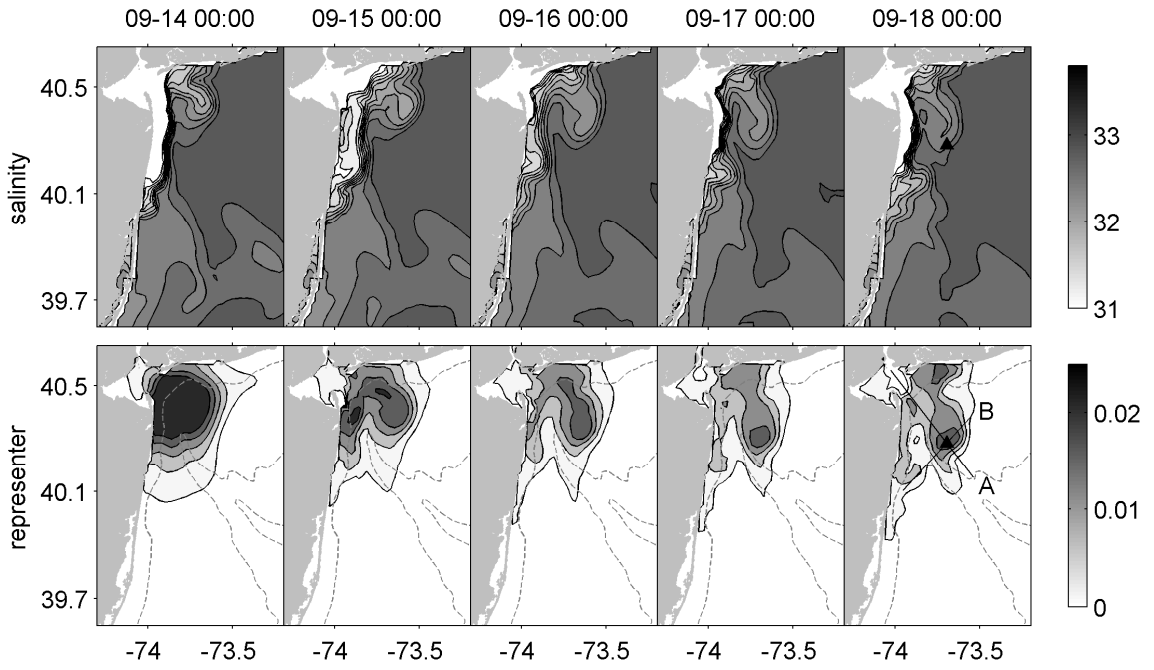

Figure 6.2. Surface salinity field (top) and surface salinity representer field (bottom) at different times. The triangles in the last column indicate the point of interest; the straight lines passing through that point in the last panel indicate the cross-sections plotted in Figure 6.3; and gray dashed lines are 20, 40 and 60 m isobaths.

To illustrate the physical meaning of the representer, a representer computation was conducted for a point aspect of interest. The results are shown in Figure 6.2 and 6.3. The aspect of interest, J, was chosen to be surface salinity at $\mathbf{x}_0$ = (73.7ºW, 40.3ºN) at t_0 = 2006-09-18 00:00 UTC. The location is shown by the triangle in Figure 6.2. The adjoint model in the representer computation was forced by $\partial J/\partial \mathbf{\Phi}(t_0) = \mathbf{\Delta}(S, \mathbf{x}_0, t_0)$ at t_0 and integrated backward for 4 days before applying the background error covariance. The surface salinity representer, surface salinity in the subsequent tangent linear model, at

different time is shown in the bottom row of Figure 6.2. Surface salinity fields at the same times in the nonlinear forward model are given in the top row of Figure 6.2.

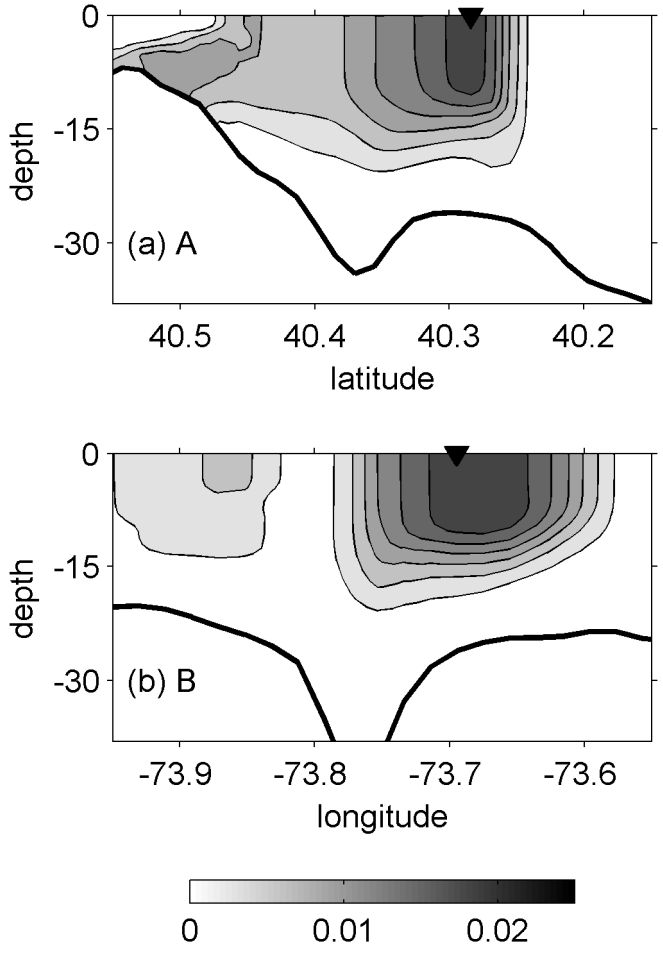

Figure 6.3. Cross-sections of the salinity representer field at 09-18 00:00, the time when J is defined. The positions of the cross-sections are depicted in Figure 6.2.

The surface salinity fields show that the river plume has two branches, one extends southeastward over the 4 days period and the other fresher one propagates southward along the New Jersey coast. The salty water between them is presumably caused by the ocean water shoreward intrusion along the HSV as shown in Chapter 2. At 09-18 00:00, the point

of interest is located at the tip of the southwestward-propagating branch. Given the common freshwater source, we expect properties of water at the point of interest to be highly correlated with properties of water in the two plume branches. Figure 6.2 shows the surface salinity representers with the covariance pattern just as expected. At 09-14 00:00 just after applying the background error covariance, the surface salinity representer gives a round shape of high covariance in the New York apex area. It results from the smoothing effect of the diffusion equations used to simulate the background error covariance. The covariance pattern then transforms gradually in a way similar to the freshwater propagation as time proceeds. By 09-18 00:00, the time when the aspect of interest is defined, the surface covariance patch develops into a two-branch pattern. The branch east of the HSV has high covariance value and is in a shape very similar to the plume branch there. The highest covariance value sits around the point of interest. The other branch along the New Jersey coast has relatively lower covariance value and is connected to the first branch at the estuary entrance. Overall, the surface salinity representer clearly outlines the area where water has the same source as the point of interest.

Figure 6.3 shows the vertical cross-section of the salinity representer at 09-18 00:00 along line A and B in Figure 6.2. On both cross-sections covariance concentrates in the surface 15 m and has the largest value around the point of interest. The 15 m depth is consistent with the average depth of the surface layer in this area. On cross-section A (Figure 6.3a), the covariance pattern extends into the estuary. Within the estuary (to the left of 40.5ºN) the covariance is positive on the bottom and zero on the surface. It results from the two-layer circulation in the estuary. The surface layer consists of newly discharged freshwater and is independent of the previously discharged freshwater which is

the source of the water at the point of interest; the bottom intrusion water is a mixture of ocean water and previously discharged freshwater and is therefore correlated with the water at the point of interest. On cross-section B (Figure 6.3b) which cuts through the HSV and bridges the two freshwater branches, the covariance exhibits a dipole pattern: high covariance value on both ends and zero covariance between. The shoreward intrusion of ocean water in the HSV brings in a different type of water and causes the dipole pattern.

Overall, the representer associated with the point aspect of interest gives covariance patterns highly consistent with the local circulation and, therefore, we can use the representer to help design and evaluate observations.

6.4. Application of Targeted Observation

In this section I will carry out the representer-based observing system design in a realistic setup. Note that it is just an example and the same system can be used for a broad range of applications.

6.4.1. Background

The HSV is a distinct feature in the NYB and cuts through almost the entire continental shelf. Flow within the HSV is highly correlated with local wind and sea level elevation (Mayer et al. 1982, Nelson et al. 1978) and the mean flow is shoreward along the valley. Because of the seasonal variation of the local wind and possibly that of the large-scale along-shelf circulation, the shoreward ocean water intrusion in the HSV intensifies in winter (Harris et al. 2003, Nelson et al. 1978). In Figure 6.4 I plot the season average of the salinity and current at 20 m depth from the nonlinear simulation of 2006.

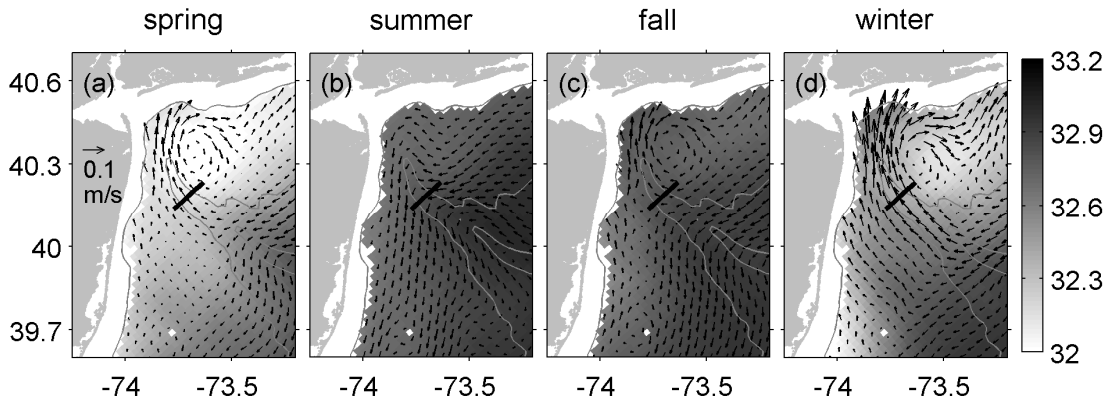

Figure 6.4. Seasonal average of salinity (in grayscale) and current (arrows) at 20 m. Gray lines are 20, 40, 60 m isobaths and the thick black lines indicate the cross-section of the Hudson Shelf Valley that is used to compute the salt flux.

At the cross-section (the short thick line in Figure 6.4) the seasonal mean current at 20 m is shoreward along the valley in winter and spring with the strongest intrusion in winter. In summer and fall, the circulation at the cross-section is roughly along the isobaths crossing the valley. Figure 6.5 shows time series of the vertically integrated subsurface (below 10 m) salt flux across the cross-section over 2006. It is evident that shoreward salt flux dominates the spring and winter seasons and the corresponding time period (October - April) is consistent with observations in Nelson et al. (1978). Shoreward flow in the HSV transports saline and nutrient-rich subsurface ocean water towards the inner shelf. It is expected to have consequences on the local biogeochemical processes. The shoreward flow in the HSV also erodes the sea floor and carries the resuspended sediment onshore (Harris et al. 2003, Manning et al. 1994).

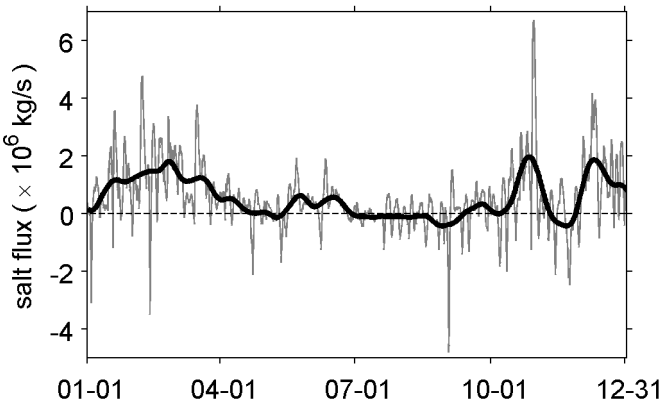

Figure 6.5. Time series of the vertically integrated subsurface (below 10 m) along-valley salt flux within the Hudson Shelf Valley over 2006. The thin gray line is the daily-averaged record and the thick black is low-pass filtered with 24-day window LOESS. Positive is shoreward.

6.4.2. Representer-based Glider Track Design

Given the effects the HSV has, it would be useful for studies of local biogeochemistry and sedimentation if precise knowledge of the transport within the HSV were known. Because gliders are commonly used in this area for monitoring the ocean, the example of representer-based observing system design in this section is chosen to be the search of optimal track for a routine glider mission. The question asked here is: where should the gliders be deployed in order to predict the along-valley salt flux across the cross-section 2 days in the future? The cross-section chosen to measure the along-valley salt flux is given by the short thick lines in Figure 6.4. To answer the question I define the objective function, J, as the vertically integrated subsurface salt flux 2 days after the glider deployment and I am going to apply the representer system to obtain the covariance and the

correlation between J and variables everywhere at the deployment time. The place where the correlation is the highest is the answer to the question. As previously mentioned, this application assumes there are no other observations available around the cross-section.

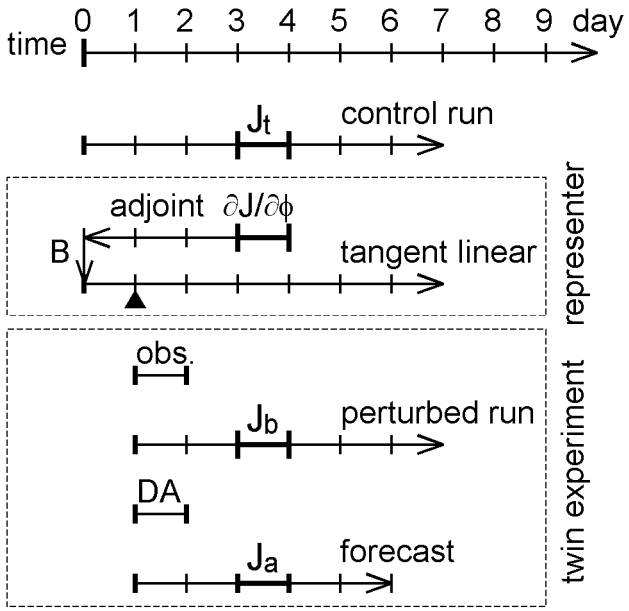

Figure 6.6. Flow chart of the representer computation and corresponding twin experiment. J_t is the "true" salt flux from the control run; $\partial J/\partial \phi$ indicates corresponding adjoint forcing; **B** is the background error covariance; triangle indicates the time of the presented representer (two days before J_t); 'obs.' indicates the observation window; J_b is the background salt flux from the perturbed simulation; 'DA' indicates the data assimilation; J_a is the salt flux forecast given by the models after data assimilation.

The flow of the representer-based observation design system is described in Figure 6.6. Firstly, a forward nonlinear simulation (control run) is carried out and I assume the simulated result is the truth. Secondly, J_t, the "true" subsurface salt flux across the

cross-section over a day period (the 4th day counting from the time of applying background error covariance) and the corresponding adjoint forcing, $\partial J/\partial \mathbf{\Phi}(t)$, are computed from the control run. Thirdly, a representer computation is conducted with 4-day adjoint model integration and 1-day tangent linear model integration. This gives a representer field two days ahead of the J. The last two steps are then repeated with J defined two days apart from the previous one. I repeated the process over the entire period of 2006 and obtained 180 representers in total. They were separated into two seasons, winter-spring (October – April) and summer-fall (May – September), according to the time when J is defined. The correlation associated with each salinity representer was then obtained by dividing the representer by standard deviations of J and detided model variables. RMS of all the correlation fields at 20 m in each season was then computed and presented in Figure 6.7.

The average correlation map of summer-fall season (Figure 6.7a) has highest correlation north of the cross-section and the correlation contours are nearly circular. In winter-spring season the highest correlation is located east of the cross-section and has an elongated pattern. Positions of the highest correlation relative to the cross-section are consistent with the seasonally averaged circulation in Figure 6.4. In summer and fall, because subsurface current is roughly along the isobaths, the upstream of the cross-section is somewhere in the northeast. In winter and spring, circulation at the cross-section is roughly shoreward along the HSV, and the upstream of the cross-section is therefore somewhere in the east or southeast. Moreover, the correlation in winter-spring season is much higher because the current within the HSV is much stronger at that time.

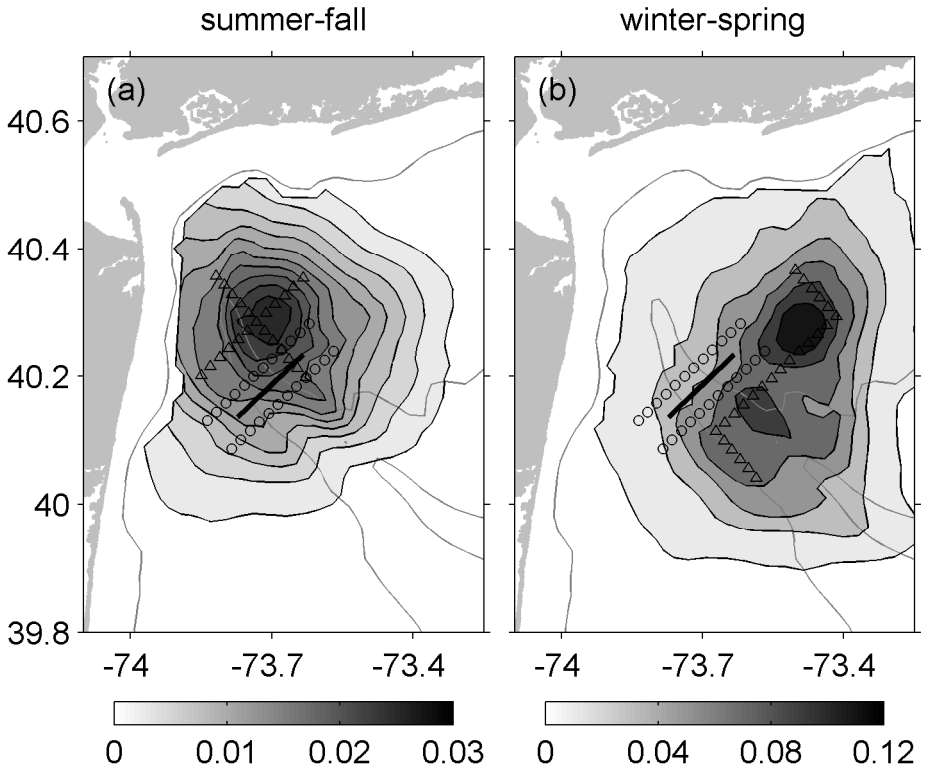

Figure 6.7. Averaged salinity correlation field at 20 m for different seasons. Gray lines are 20, 40 and 60 m isobaths and the thick black lines indicate the Hudson Shelf Valley cross-section where J is defined. Triangles indicate the optimal glider track and circles the traditional.

The glider track was then designed according to the correlation pattern. Figure 6.7 presents the optimal design of the glider track for each season (triangles) in contrast to a traditional design of glider track (circles) which are on both sides of the cross-section. I emphasize here that the optimal track is not obtained from a robust optimization algorithm but designed intuitively according to the correlation pattern. I call it "optimal" to distinguish it from the traditional track. The real optimization of the glider track would be

based on a robust mathematical algorithm and take all instrumental and logistical constraints of glider deployment into consideration, which is another topic of research.

6.4.3. Twin Experiments

I am now going to verify the result using DA twin experiments. Flow of the twin experiments is depicted in Figure 6.6. For each representer, I first took temperature and salinity vertical profiles from "true" states of the control run along two different sampling tracks (optimal and traditional). Note that the optimal track is different for different seasons. Both sets of observations were taken over the second day counting from the time of applying the background covariance. For a fair comparison, the two glider missions are set to take the same number of observations. I then conducted a perturbed nonlinear model simulation starting from the end of the first day with initial conditions obtained from model state 5 days prior (day -4 in Figure 6.6). Forcing of the perturbed simulation were kept the same as those of the control run, that is, there is no error in forcing, and errors exist only in initial conditions. The perturbed simulation gives a forecast of the subsurface salt flux across the cross-section at the 4^{th} day, J_b, different from the truth J_t given by the control run. Two IS4DVAR DA based on the perturbed simulation were carried out to assimilate two sets of observations measured by two different missions, one optimal and one traditional, respectively. The IS4DVAR system used here is same as the one used in Chapter 5. In this chapter the DA window is 1 day and only the "glider-measured" temperature and salinity profiles were assimilated. The corrected initial conditions given by the two DA systems were used to initialize two forecast simulations, respectively. Each of the post-DA forecast simulations has forecast of the subsurface salt flux across the

cross-section at the 4th day, J_a (the second forecast). Overall, I have 180 pairs of J_a and 180 J_t and J_b.

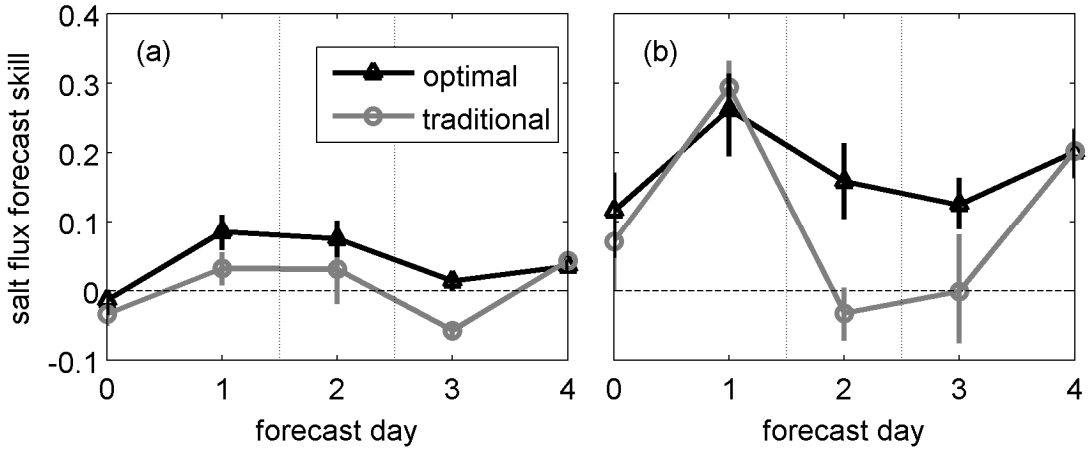

Figure 6.8. Skills of the two twin experiment systems in terms of predicting salt flux within the Hudson Shelf Valley for (a) summer-fall and (b) winter-spring seasons. Vertical bars are 95% confidence interval.

A statistical measure of the skills of the two DA systems in improving forecast of J is presented in Figure 6.8 for both seasons. The skill is defined as

$$S = 1 - \frac{|J_a - J_t|}{|J_b - J_t|}. \tag{6.8}$$

Positive skill means improvement of the J prediction by the DA and larger skill means better the prediction (the maximum skill is 1). Because the objective is to predict the salt flux 2 days after the observation, the focus here is on the second day forecast (between the dash lines in Figure 6.8). For both seasons, the system assimilated optimal observations has statistically better prediction of the salt flux than the one assimilated traditional

observations. The amount of prediction improvement is also consistent with the magnitude of the correlation in Figure 6.7. In summer-fall season the correlation contrast between the optimal track and traditional track is rather small (Figure 6.7a) and the improvement of the *J* prediction is little; in winter-spring season the correlation contrast is relatively large (Figure 6.7b) and the prediction improvement is substantial. Figure 6.8 also shows that assimilating the optimal observations does not necessarily give better prediction of the salt flux for other days. For example, in winter-spring season the first day predictions of salt flux in the two systems are indistinguishable. This suggests that precise definition of objective function is important in the representer-based observing system design. Overall, the DA twin experiments show the validity of the representer-based observing system design.

6.5. Comparison of Observation Influence

Observation influence is a measure operational oceanographer and policy makers have been concerned about for integrating observing systems (Kaiser and Pulsipher 2004), designing new observation networks (Oke and Schiller 2007) or evaluating existing observations (Frolov et al. 2008). In this section I am going to explore the use of the representer system to compare observation influences in a simple manner.

6.5.1. Therory

As mentioned in Section 1, the representer associated with a single observation describes the influence of that observation in a 4DVAR DA system. Similar to the derivation in Section 2, we can expand this concept to a broader circumstance. Suppose we

have a numerical model and a group of observations. Because of errors in initial conditions, boundary conditions, forcing, or model physics, modeled results are different from their observed counterpart. The idea of DA is to use the observations to correct the model. Let us assume that observational error is much smaller than model error and the analysis after DA is close to the truth. Part of the gain of assimilating the observations is to eliminate the model error in the observed variables at the observation locations and times. We can define a corresponding gain function *J*, similar to the objective function in Section 4. In a 4DVAR system, assimilating the observations corrects not only the observed variables at the observation locations and times, but also the model state at other locations and times through background error covariance and the dynamical connections embedded in the adjoint and tangent linear models. Because the representer system is linear, we can obtain the influence of a group of observations by superimposing the representers associated with each observation. The mathematical derivation is same as the one in Section 2. That is, for a group of observations, if we define the associated gain function, *J*, as an arithmetic function of state variables, we can obtain the influences of the observation group through the associated representer. In general, definition of the gain function can be any arithmetic function of model variables. Because different definitions of the gain function will result in different observation influences, interpretation of the influence should be consistent with the definition of the gain function.

Next, I will demonstrate three examples of the representer-based comparison of observation influence. I focus on the comparison of influence area and strength of two different observing strategies, of the same observations at different dynamical regimes, and also of the same observations with different DA windows. Note that the comparison in this

study is not for realistic design of an observational network but rather for domonstrating the representer-based observation comparison. As the first try of this system, this comparison is intended to understand what the representer system can give us and to qualitatively compare the influences of different observations.

6.5.2. Glider vs. Mooring

Because gliders and moorings are two commonly used instruments to monitor the NYB and both measure vertical profiles of temperature and salinity, I choose to compare their influences in this section. In Figure 6.1, I plot the track of a glider mission which is part of a routine cross-shelf glider section operated by the COOL (Castelao et al. 2008a). I put the hypothetical glider track north of the real track for the sake of space and assign the one-way mission to be 3 days which is roughly the time it takes a real glider to cross the shelf. The glider moves back and forth along the track. The hypothetical mooring is located at the 20 m isobath on the hypothetical glider track. The experiment was conducted for the period of April – May, 2006.

Firstly, both instruments sampled vertical temperature and salinity profiles in the nonlinear control model at every time step (180 seconds). The two-month period was then separated into 20 3-day windows and a representer computation was conducted in each window. If model error is proportional to ocean state anomaly, the gain of correcting the observed variables in the model at the observation locations and times is also proportional to the ocean state anomaly. I therefore defined the gain function as

$$J = \frac{1}{V\Delta t}\int_V \int_{\Delta t} \left[\frac{(T-\overline{T})^2}{\mathbf{O}_T} + \frac{(S-\overline{S})^2}{\mathbf{O}_S} \right] dtdV \,, \tag{6.9}$$

where Δt is 3 days, V is the volume of the observed space in 3 days, T and S are observed temperature and salinity, respectively, the overhead bars stand for a temporal mean at each observation location, and $\mathbf{O}_T$ and $\mathbf{O}_S$ are the error covariance matrices of temperature and salinity observations, respectively. Assume both error covariance matrices are the identity matrix for simplicity. Because my objective is to investigate the influence of observations in a 4DVAR system, I chose a quadratic gain function to be consistent with the cost function in 4DVAR.

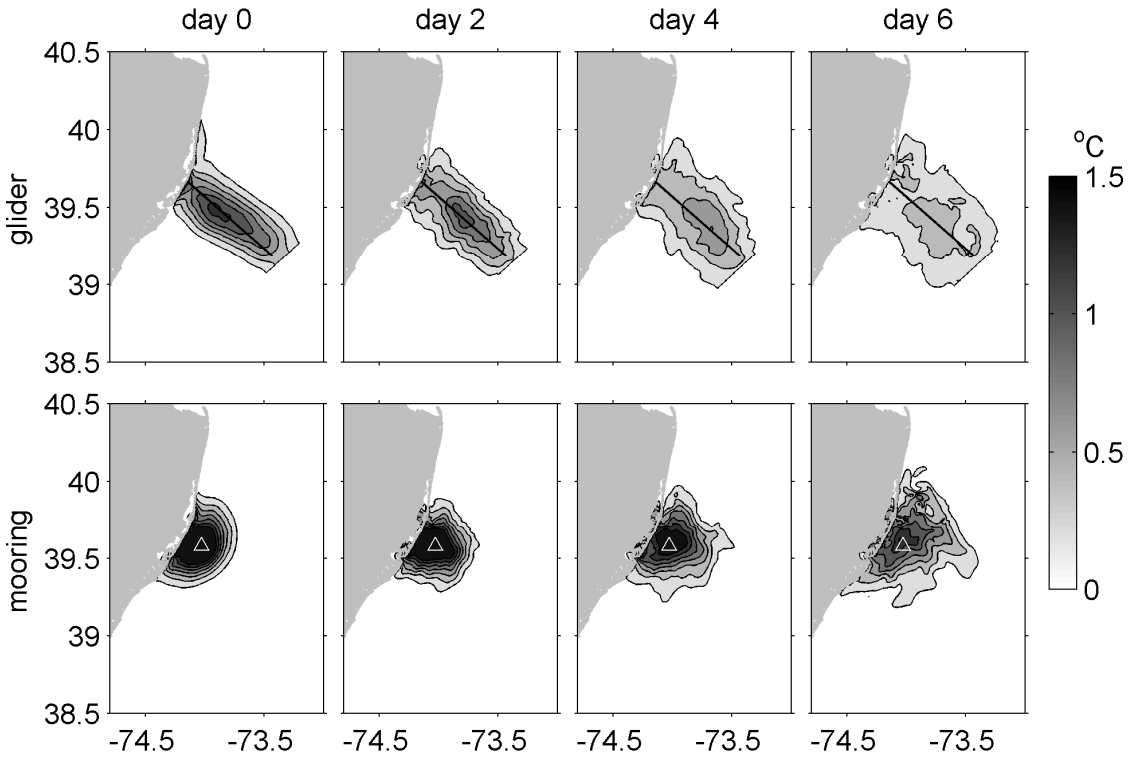

Figure 6.9. Averaged influence of a glider section (black straight lines in top row) and a fixed mooring (white triangle in bottom row) observations. The observations span from day 0 to day 3. Counting of the days starts from the time of applying background error covariance (see Figure 6.6).

The procedure of representer computation is same as the one in Section 4. For each representer, the adjoint model was integrated backward for 3 days with adjoint forcing covering the whole period. After applying the background error covariance, the tangent linear model was integrated for 6 days in order to show the observation influences in both analysis (the first 3 days) and forecast (the last 3 days) periods. RMS of the 20 representer fields was then computed for different time in the 6-day window. Figure 6.9 shows the RMS of the surface temperature representer at different times of the 6-day window.

Generally, comparison in the analysis period (the first two columns in Figure 6.9) shows that glider observation has a larger influence area than a mooring but the influential strength of the mooring at the observation location is about twice as stronger as that of the glider observation. During the forecast period (the last two columns in Figure 6.9), the influence of glider observation quickly decays away, while that of mooring observation stays strong. At day 6, 3 days into the forecast, the influence of mooring observation at observation location is more than 3 times stronger than that of glider observation. Moreover, the influence area of mooring observation expands quickly along the shelf over the forecast period, but that of glider observation expands little. At day 6, it is not obvious that the glider observations have larger influence area than the mooring.

In Figure 6.10, I plot the vertical cross-section of the RMS influences of the two instruments. The cross-sections are along the glider track. Comparison within the analysis period tells the same story as that in Figure 6.9: the glider observation has larger influential coverage across the shelf and the mooring observation has stronger influence at the observation location. Cross-sections of glider observation influence within the forecast period shows that decay of the influence mainly happens in the surface 15 m. One

interesting feature in Figure 6.10 is that at day 0 both cross-sections show strong influence in the surface and bottom boundary layer and relatively weaker influence at mid-depth. The two boundary layers merge next to the coast. This feature is consistent with the strong temperature and salinity variability in the surface and bottom boundary layers caused by the wind-driven coastal upwelling and down-welling.

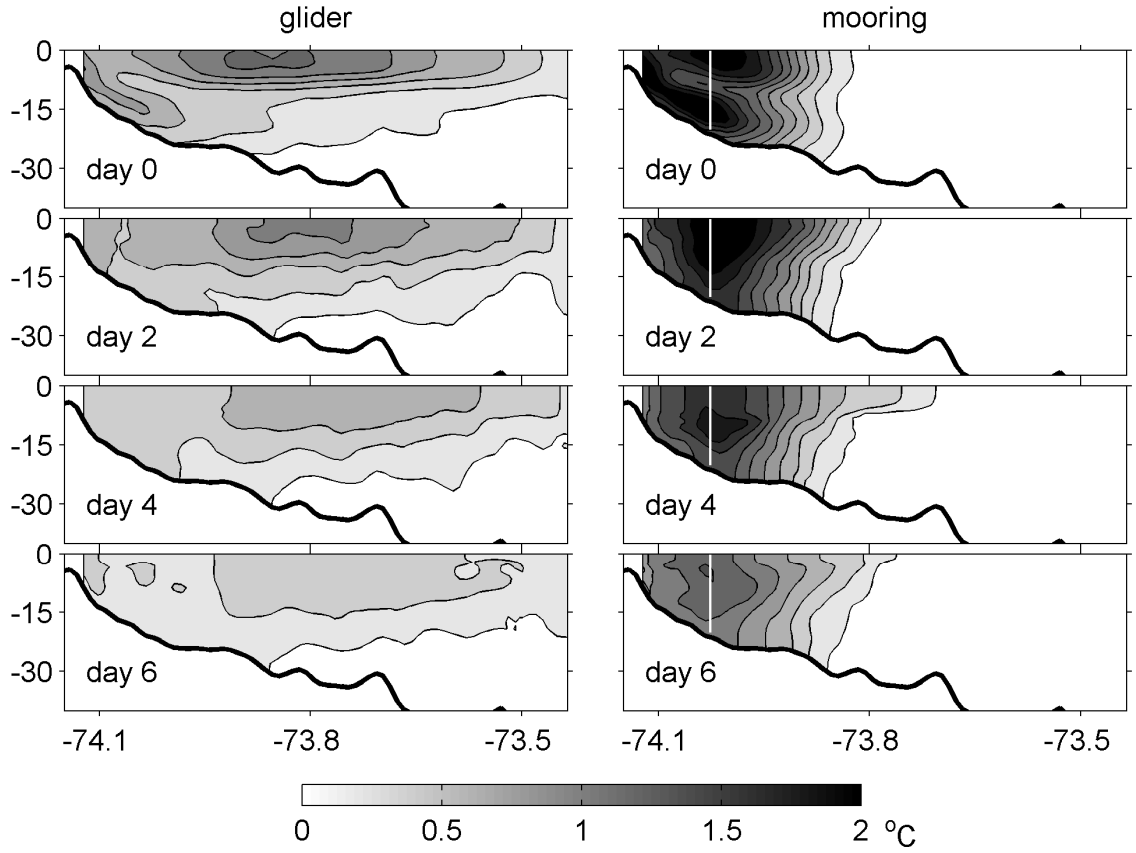

Figure 6.10. Cross-sections of the averaged influence at different time along the glider track in Figure 6.9. The white lines in the second column indicate the mooring location. The observations span from day 0 to day 3.

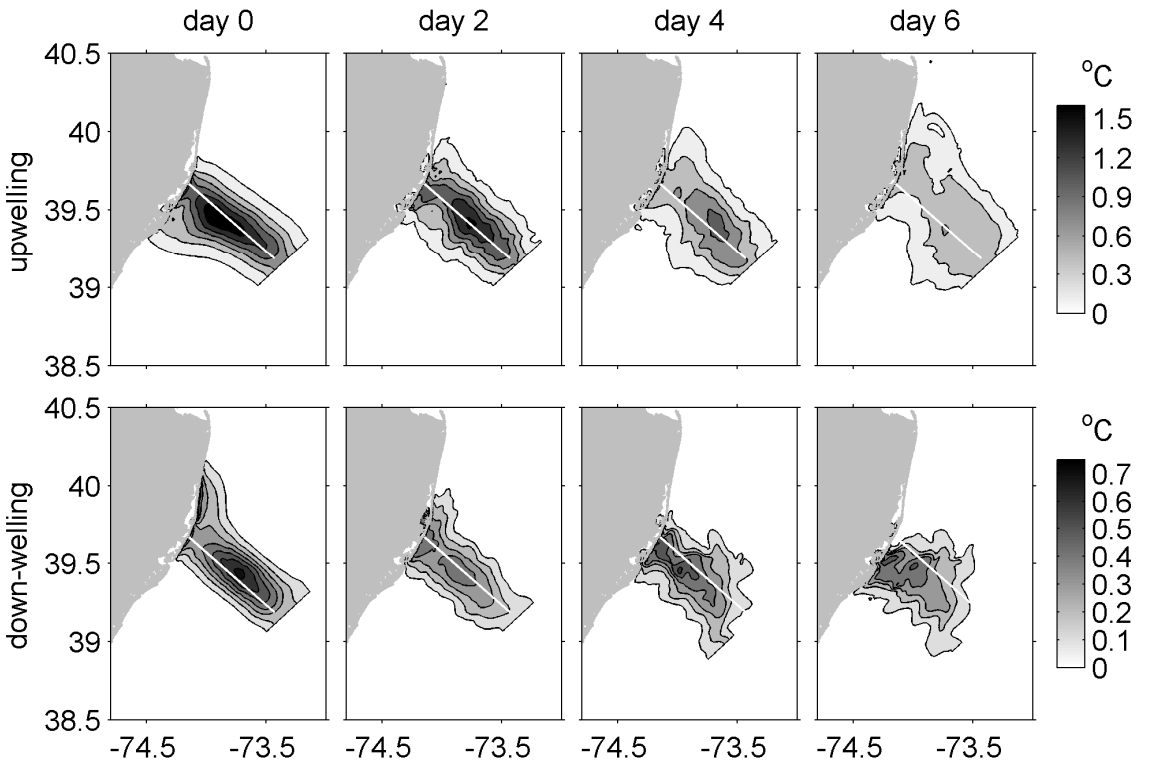

Figure 6.11. Averaged surface influence of a glider section (white lines) in wind-driven coast upwelling (top row) and down-welling (bottom row) regimes. The observations span from day 0 to day 3.

6.5.3. Comparison of Different Wind Regimes

Because wind-driven coastal upwelling and down-welling are common phenomena in the inner shelf of the NYB (Castelao et al. 2008b, Wong 1999, Yankovsky and Garvine 1998), differences between the influences of observations in the two dynamical regimes are of particular interest for operational oceanography. This subsection takes the hypothetical glider section in Section 5.1 as an example and demonstrates its different influences in upwelling and down-welling regimes. I separated the 20 glider representers

in Section 6.5.2 into two groups according to the wind direction in the 3-day observation windows (southerly wind drives upwelling on the coast and northerly wind down-welling). The RMS of the representers in each group were then computed and presented in Figure 6.11.

In general, the influence within the analysis window (Day 0-3) in the upwelling regime is about twice as strong as that in the down-welling regime. Because coastal upwelling pulls deep cold water up to the surface and down-welling pushes offshore surface water on shore, the surface temperature anomaly associated with upwelling is much stronger. Model temperature error on the surface in an upwelling regime is consequently larger since model error is assumed to be proportional to the ocean state anomaly. Therefore, the influence of the glider observations in an upwelling regime on correcting model errors is also larger.

At day 0, the influence area of the observation extends southward along the coast in the upwelling regime and northward along the coast in the down-welling regime. It reflects that model state at the dynamical upstream of the observed quantities in a 4DVAR system is influenced by the observations. In the upwelling regime, coastal surface water south of the glider track is pushed northeastward and, therefore, surface glider observation at the end of the 3-day window captures the properties of the water that had been located south of the track on the surface next to the coast at day 0. In the down-welling regime, coastal surface water north of the glider track is pushed into the bottom boundary layer and moves southward. Subsurface glider observation at the end of the window thus captures the properties of the water that had been located north of the track on the surface next to the coast at day 0. The upstream coverage of the representer-based observation influence is

consistent with the identification of dynamical upstream by adjoint sensitivity as in Chapter 4. As time proceeds into the forecast window (the last two columns in Figure 6.11), the influence area propagates downstream along the coast, northward in upwelling regime and southward in down-welling regime.

Results in this subsection and the previous one can be used to help the design of an observation network if the observations are taken for the purpose of DA. Details of instrument spacing, especially for permanently mounted instruments, can be studied using representer-based systems before the instruments are deployed.

6.5.4. Comparison of Different Data Assimilation Windows

One major advantage of 4DVAR DA is its ability to propagate information, e.g. observation innovation, over time, backward and forward. Ideally, we would like the information to be propagated as long as possible in order to capture as many dynamical connections as possible. But the longest time period for which the information can propagate, i.e. the DA window, is always constraint by the linear assumption used in 4DVAR systems. The length of the DA window is thus always an issue in 4DVAR DA. For the same observation, different lengths of the DA window will result in different observation influences. To show this, I conducted a simple example using the representer-based observation influence. I formed 4 groups of representers of glider observations along the same track as in the previous section. Each group has 20 representers. The adjoint models in the 4 groups were initialized at the same times and integrated for 0, 1, 2 and 3 days, respectively. The tangent linear models were integrated for 3, 4, 5 and 6 days, respectively. To make the comparisons fair, I designed all glider

observations to be instantaneous at the initial times of the adjoint models and then all representer windows include the same observations.

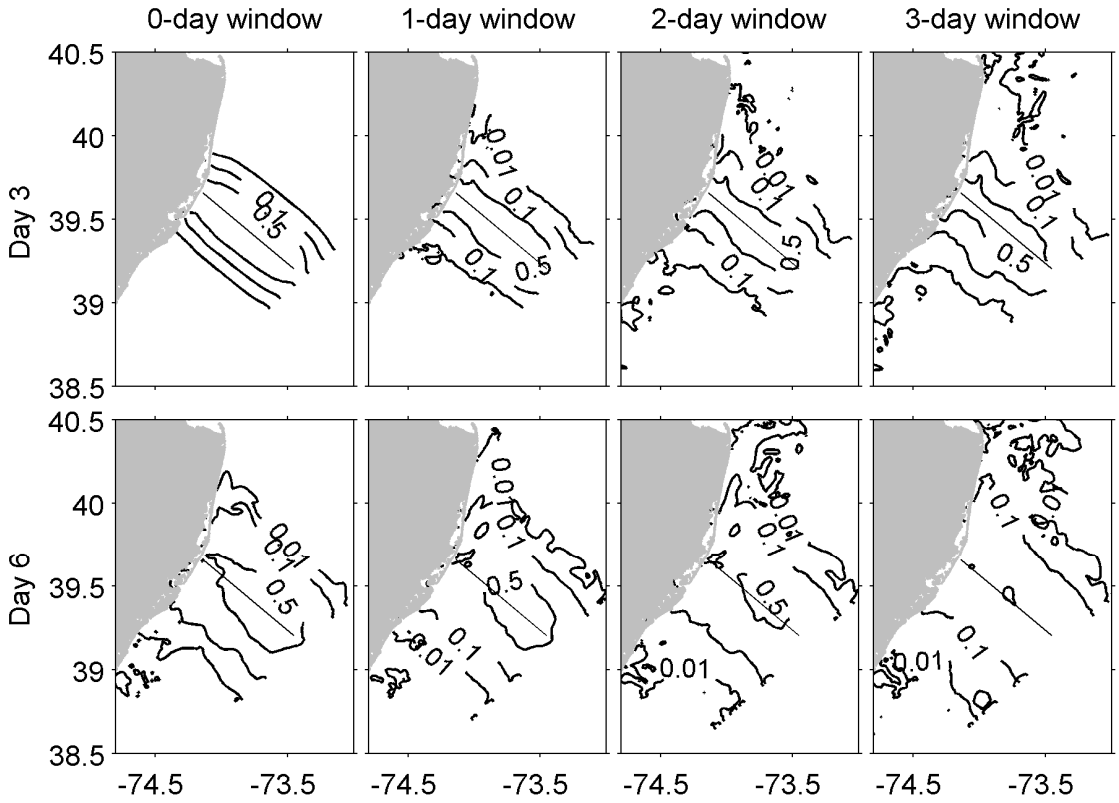

Figure 6.12. Contours of the averaged influence of a glider section (black straight lines) at day 3 (top row) and day 6 (bottom row) in systems with different data assimilation window. The contour lines are 0.01, 0.1, 0.5 ^{o}C, repectively. The instantaneous observations were taken at Day 3.

The RMS of the representers in each group at different time were computed and the surface average temperature influences are presented in Figure 6.12. In Figure 6.12, Day 3 is the observation time and Day 6 is the ending time of the tangent linear integration (3

days after observations). The comparison at both times shows that longer DA windows have larger influence areas. At Day 3, the average influence in the 0-day window group is confined around the glider track. As the window becomes longer, the influence spreads out, especially along the coast. The average influence in the 3-day window group covers almost the entire New Jersey coast. Note that the small covariance value (0.01) at the edges of the influence area results from the RMS averaging process. The influence value in individual representer is much larger but the corresponding influence area is smaller.

The RMS averaged influence of the 0-day window group at Day 3 has a very smooth pattern because it is just after applying the background error covariance. The representer of the 0-day window is a measure of observation influences in sequential DA, i.e. 3DVAR, Kalman Filter-type DA methods. In these methods, information about the dynamical upstream is lost because there is no backward propagation of observation innovation, and all the information obtained from the observations are through the statistical and dynamical connections described by the background error covariance. In 4DVAR DA, the adjoint model propagates the observation innovation backward according to linear dynamics and points out the corrections needed to be made in the dynamical upstream in initial conditions, boundary conditions or surface forcing.

6.6. Summary

This chapter is the part of the project to build an integrated observation and modeling system for the NYB for the purpose of coastal ocean prediction and observing system design. Chapter 5 carried out the 4DVAR DA using ROMS in a realistic and

pseudo-realtime setup. This chapter is dedicated to the observation-modeling integration in the opposite direction: representer-based observing system design.

It is well known that representer describes the covariance between a point aspect of interest and variables at all locations at any time. In 4DVAR DA, a representer provides the influences of single assimilated observation and can be used in the process of cost function minimization in observation space (Bennett 2002). To extend the application of representer to broader circumstances, I first showed that the representer associated with any arithmetic function of model variables describes the covariance between the aspect of interest described by the arithmetic function and model variables at all locations at any time. The place where the correlation is the highest is presumably the optimal place to observe in order to estimate the aspect of interest more precisely if there is no other observation available in nearby locations. Applying the same theory to observation influence, I found that the representer associated with a group of observations outlines the influences of the observation group in a 4DVAR DA system.

To exam the consistency between representer and local dynamics I computed the representers associated with a point aspect of interest in the Hudson River plume. Time series of representers show the propagation of covariance in a pattern similar to the river plume. The representer at the time of interest indicates high covariance confined in the area where water has the same source as the point of interest.

In the application of observing system design, I seek the optimal glider track for better model prediction of salt flux across a cross-section of the Hudson Shelf Valley 2 days after the glider deployment. 180 representers were computed and grouped into two seasons, summer-fall and winter-spring. The RMS of the correlation in the summer-fall group is the

highest north of cross-section and for the winter-spring group it is east and southeast of the cross-section. Optimal glider tracks were then picked intuitively for both seasons according to the correlation maps. In contrast, the traditional glider track was designed to be on both sides of the cross-section for all year. DA twin experiments were used to verify the result. Glider observations taken from a control nonlinear simulation along the optimal and traditional tracks were then assimilated respectively into 4DVAR systems based on a perturbed nonlinear model. Skills of the two DA systems in term of predicting the salt flux 2 days after the observations were obtained. For both seasons, the system assimilated the optimally positioned observations gives statistically better prediction of the salt flux than the one assimilated the traditional observations. The difference in the improvement of the forecast in two seasons reflects the difference in the magnitude of seasonally averaged correlation.

This example shows the usefulness of representer-based system in finding optimal observing locations in the situation of no other available observation. The question of how much different the optimal pattern would be if other observations are available is an interesting scientific question and can be addressed using the observation sensitivity technique.

The representer-based system was used to outline the influences of a group of observations in a 4DVAR DA system and compare the influences of different observing strategies. I first compared the influences of a routine glider cross-shelf section and a fixed mooring. 20 representers were computed for each instrument type. Comparison of the representer RMS shows that the glider section has a broader influence area and the

mooring has stronger influence at the observation location. Meanwhile, in the forecast mode, influence of the mooring persists and extends dramatically along the shelf.

The influences of the same routine glider section in different dynamical regimes were then compared: wind-driven coastal upwelling and down-welling. It was shown that influence area of the glider observation tends to cover the dynamical upstream: southward along the coast in the upwelling regime and northward along the coast in the down-welling regime. The influence is stronger in upwelling regime because of the strong surface temperature anomaly associated with the coastal upwelling.

In the last part, I compared the influences of the same glider section in DA systems with different window lengths, 0 to 3 days. The result agrees with intuition that a longer DA window brings more dynamical connections and gives the same observations larger influence area.

In all, this work demonstrates the ability of representer system in finding an optimal observation pattern and outlining the influence of observations. It can potentially be used to help design the positioning of single observation or observation networks. Of course, the real optimization of observations is a multi-aspect task and will have to consider other constraints, instrumental and logistical, as well. The work in this chapter approaches the goal from one perspective.

Appendix: Derivation of Equations (6.3) – (6.6)

Suppose a and b are two independent variables at particular locations of interest, $\mathbf{x}_1$ and $\mathbf{x}_2$ respectively, at time t_0, that is, $a = \phi_1(\mathbf{x}_1, t_0)$ and $b = \phi_2(\mathbf{x}_2, t_0)$, and N is the number of all possible ocean states. I assume that (i) the ocean states given by the nonlinear model is the mean of the randomly distributed ocean states in Bayesian statistics and (ii) the deviation of all possible ocean states from the mean is small and the product of two or more state deviations (e.g. $a'b'$) is negligible. The first condition is reasonable because distribution of model errors is usually assumed to be Gaussian and the nonlinear model states which the tangent linear and adjoint models are linearized based on are normally the best ones we can get. The second condition agrees with the small background error assumption we have in variational DA.

Overhead bars in following derivation stands for the mean of the randomly distributed ocean states.

Derivation of equation (6.3):

$$\begin{aligned}
\mathrm{rep}\left(\frac{\partial(a+b)}{\partial\boldsymbol{\Phi}(t_0)}\right) &= \mathrm{rep}\left(\frac{\partial a}{\partial\boldsymbol{\Phi}(t_0)}\right) + \mathrm{rep}\left(\frac{\partial b}{\partial\boldsymbol{\Phi}(t_0)}\right) \\
&= \mathrm{cov}(a, \boldsymbol{\Phi}(t)) + \mathrm{cov}(b, \boldsymbol{\Phi}(t)) \\
&= \frac{1}{N}\sum_{i=1}^{N}\left[(a-\bar{a})(\boldsymbol{\Phi}(t)-\overline{\boldsymbol{\Phi}(t)})\right] + \frac{1}{N}\sum_{i=1}^{N}\left[(b-\bar{b})(\boldsymbol{\Phi}(t)-\overline{\boldsymbol{\Phi}(t)})\right]. \\
&= \frac{1}{N}\sum_{i=1}^{N}\left[(a+b-(\bar{a}+\bar{b}))(\boldsymbol{\Phi}(t)-\overline{\boldsymbol{\Phi}(t)})\right] \\
&= \mathrm{cov}(a+b, \boldsymbol{\Phi}(t))
\end{aligned}$$

Derivation of equation (6.4) is very similar to that of equation (6.3) and, therefore, neglected here.

Derivation of equation (6.5):

$$
\begin{aligned}
\mathrm{rep}\left(\frac{\partial(ab)}{\partial\boldsymbol{\Phi}(t_0)}\right) &= b\,\mathrm{rep}\left(\frac{\partial a}{\partial\boldsymbol{\Phi}(t_0)}\right) + a\,\mathrm{rep}\left(\frac{\partial b}{\partial\boldsymbol{\Phi}(t_0)}\right) \\
&= \bar{b}\,\mathrm{cov}(a,\boldsymbol{\Phi}(t)) + \bar{a}\,\mathrm{cov}(b,\boldsymbol{\Phi}(t)) \\
&= \frac{1}{N}\sum_{i=1}^{N}\left[\left(\bar{b}(a-\bar{a})+\bar{a}(b-\bar{b})\right)(\boldsymbol{\Phi}(t)-\overline{\boldsymbol{\Phi}(t)})\right] \\
&= \frac{1}{N}\sum_{i=1}^{N}\left[\left(a'\bar{b}+\bar{a}b'\right)(\boldsymbol{\Phi}(t)-\overline{\boldsymbol{\Phi}(t)})\right] \\
&= \frac{1}{N}\sum_{i=1}^{N}\left[\left(\bar{a}\bar{b}+a'\bar{b}+\bar{a}b'+a'b'-\bar{a}\bar{b}+\overline{a'b'}\right)(\boldsymbol{\Phi}(t)-\overline{\boldsymbol{\Phi}(t)})\right] \\
&= \frac{1}{N}\sum_{i=1}^{N}\left[\left(ab-\overline{ab}\right)(\boldsymbol{\Phi}(t)-\overline{\boldsymbol{\Phi}(t)})\right] \\
&\simeq \mathrm{cov}(ab,\boldsymbol{\Phi}(t))
\end{aligned}
$$

Derivation of equation (6.6) (first-order Taylor series expansion applied):

$$
\begin{aligned}
\mathrm{rep}\left(\frac{\partial(a/b)}{\partial\boldsymbol{\Phi}(t_0)}\right) &= \frac{1}{b}\,\mathrm{rep}\left(\frac{\partial a}{\partial\boldsymbol{\Phi}(t_0)}\right) - \frac{a}{b^2}\,\mathrm{rep}\left(\frac{\partial b}{\partial\boldsymbol{\Phi}(t_0)}\right) \\
&= \frac{1}{\bar{b}}\,\mathrm{cov}(a,\boldsymbol{\Phi}(t)) - \frac{\bar{a}}{\bar{b}^2}\,\mathrm{cov}(b,\boldsymbol{\Phi}(t)) \\
&= \frac{1}{N}\sum_{i=1}^{N}\left[\left(\frac{a'}{\bar{b}}-\frac{\bar{a}b'}{\bar{b}^2}\right)(\boldsymbol{\Phi}(t)-\overline{\boldsymbol{\Phi}(t)})\right] \\
&= \frac{1}{N}\sum_{i=1}^{N}\left[\left(\frac{\bar{a}+a'}{\bar{b}}-\frac{\bar{a}b'+a'b'}{\bar{b}^2}-\frac{\overline{a+a'}}{\bar{b}}+\frac{\overline{\bar{a}b'+a'b'}}{\bar{b}^2}\right)(\boldsymbol{\Phi}(t)-\overline{\boldsymbol{\Phi}(t)})\right] \\
&= \frac{1}{N}\sum_{i=1}^{N}\left[\left(\frac{\bar{a}+a'}{\bar{b}}(1-\frac{b'}{\bar{b}})-\frac{\overline{\bar{a}+a'}}{\bar{b}}(1-\frac{b'}{\bar{b}})\right)(\boldsymbol{\Phi}(t)-\overline{\boldsymbol{\Phi}(t)})\right] \\
&\simeq \frac{1}{N}\sum_{i=1}^{N}\left[\left(\frac{\bar{a}+a'}{\bar{b}}\frac{1}{1+\frac{b'}{\bar{b}}}-\frac{\overline{\bar{a}+a'}}{\bar{b}}\frac{1}{1+\frac{b'}{\bar{b}}}\right)(\boldsymbol{\Phi}(t)-\overline{\boldsymbol{\Phi}(t)})\right] \\
&\simeq \frac{1}{N}\sum_{i=1}^{N}\left[\left(\frac{a}{b}-\frac{\overline{a}}{b}\right)(\boldsymbol{\Phi}(t)-\overline{\boldsymbol{\Phi}(t)})\right] \\
&= \mathrm{cov}(a/b,\boldsymbol{\Phi}(t))
\end{aligned}
$$

CHAPTER 7. SUMMARY

The overarching theme of this dissertation is to develop a prototype for the implementation of an integrated coastal ocean observing and modeling system for the NYB. It utilizes ROMS component models (Nonlinear, Tangent Linear and Adjoint models) and drivers for adjoint sensitivity, residence time, IS4DVAR DA, and representer-based optimal observation. The results demonstrate how these tools can be applied to reveal the dominant physical processes in shelf regions such as the NYB, give more precise oceanic state estimation for forecasting and re-analysis, and improve the design of observational systems.

Chapter 2 investigates the spatial and temporal dispersal patterns of the Hudson River plume in the NYB. Analysis of the two-year duration model simulation first provides the background dynamics and shows strong seasonal variations of the freshwater dispersal. It is shown that the Hudson River source water propagates in the NYB in three major pathways: (i) a southward pathway along the New Jersey coast dominant in winter and spring seasons; (ii) a eastward pathway along the Long Island coast mainly happening in fall; and (iii) a direct southeastward off-shore pathway dominant in the summer. A series of reduced physics simulations demonstrate the effects different forces have on the dispersal pattern. Wind is the major force for the spreading of river source freshwater to the mid- and outer-shelf; the ambient current pushes the freshwater southwestward along the shelf; and the HSV intensifies the bulge recirculation at the apex area of the NYB.

Chapter 3 investigates the time scales (age and residence time) associated with the dispersal of the Hudson River plume in the NYB. The spatial and temporal variability of the time scales are shown to be consistent with those of the freshwater pathways

discovered in Chapter 2. Correlations of the time scales with river discharge and wind show that both age and residence time of the surface water in the NYB are largely affected by the variations of the river discharge and wind. Easterly winds increase surface water age and extend the duration waters along the Long Island coast remain in the NYB apex. Southerly winds increase age along the New Jersey coast, yet drive a decrease in age of offshore surface waters and prolong the time surface waters close to the New Jersey coast stay in the NYB apex. Comparison between modeled surface water age and an age proxy, the ratio of satellite measured irradiance in two channels, shows qualitative agreement. A least squares fit gives empirical relationship between the band ratio and modeled mean age for NYB waters.

Chapter 4 uses adjoint sensitivity analysis to study physics in the NYB for three idealized situations: an unforced buoyant river plume, and upwelling and down-welling wind forcing. Coastal SST variability is considered and the adjoint scalar index is defined as the temporal-spatial mean squared SST anomaly on a segment of the New Jersey coast at the conclusion of a 3-day period. The adjoint method identifies the oceanic conditions and forcing that are "dynamically upstream" to a region or feature of interest, and compares the relative roles of the prior ocean state, forcing, and dynamical influences on forming the feature of interest. In the absence of wind, surface temperature advection dominates SST anomaly with two sources of surface water identified. Down-welling favorable winds amplify upstream advective influence. For upwelling conditions, it is shown that coastal SST is controlled by both advection from the south and subsurface, but above 5 m depth, and temperature-related density stratification between 5 m and 15 m, out to 10 km offshore.

Chapter 5 carries out the 4D variational DA in the NYB using ROMS IS4DVAR system. It assimilates a number of observations collected by a variety of instruments during spring 2006 to correct model initial conditions. An overlapped cycling system with 3-day DA window is used. The DA system reduces the model-observation mismatch substantially for all variables. It is shown that error in model wind forcing is a major cause of the velocity mismatch. Because surface forcing quantities are not among the control variables, the DA system is unable to reduce the mismatch associated with surface forcing errors. Comparisons between model forecasts and independent observations show improvement of forecast for about 15 days for temperature and salinity and 2 – 3 days for velocity. Comparison between different DA systems that assimilated different sets of data indicates that assimilating SST improves the forecast of surface and subsurface temperature but worsens salinity forecast. Assimilating glider measurement improves the salinity forecast but has little effect on the temperature forecast. Assimilating surface current data improves the velocity forecast for 1-2 days and worsens the forecast of subsurface temperature.

Chapter 6 explores the representer-based observing system design in the NYB. Because the representer of an observation describes the covariance between the observed quantity and ocean states at all locations at any time, it can be used to measure the influence of the observation in a 4D Variational (4DVAR) DA system. A representer-based system is applied to identify the optimal glider track for better predicting salt flux in the Hudson Shelf Valley 2 days in the future. Twin experiments assimilating observations along the optimal track give better prediction of the salt flux than the ones assimilating observations along a traditional track. The same system was used to compare the influences of different

observation strategies. Comparison of the influences of a routine glider section and a mooring shows that the glider section influences a larger area and the mooring has stronger influence at the observation location; Comparison of the glider section in different dynamical regimes shows different coverage of the observations in a 4DVAR system. Comparison of the influences of the glider section in a DA system with different window lengths shows that longer DA window lets the system catch more dynamical connections and allows the observations to influence a larger area.

Bibliography

Adams, D. A., J. S. O'Connor, and S. B. Weisberg, 1998: Sediment quality of the NY/NJ harbor systemEPA/902-R-98-001.

Allen, J. S., P. A. Newberger, and J. Federiuk, 1995: Upwelling Circulation on the Oregon Continental Shelf. Part I: Response to Idealized Forcing. *J. Phys. Oceanogr.*, **25,** 1843–1866

Austin, J. A. and J. A. Barth, 2002: Variation in the position of the upwelling front on the Oregon shelf. *J. Geophys. Res.*, **107,** 3180,doi:10.1029/2001JC000858.

Avicola, G. and P. Huq, 2003a: The role of outflow geometry in the formation of the recirculating bulge region in coastal buoyant outflows. *J. Mar. Res.*, **61,** 411-434

——, 2003b: The characteristics of recirculating bulge region in coastal buoyant outflows. *J. Mar. Res.*, **61,** 435-463

Baker, N. and R. Daley, 2000: Observation and background adjoint sensitivity in the adaptive observation-targeting problem. *Q. J. R. Meteorol. Soc.*, **126,** 1431-1454

Ballabrera-Poy, J., E. Hackert, R. Murtugudde, and A. J. Busalacchi, 2007: An observing system simulation experiment for an optimal moored instrument array in the tropical Indian Ocean. *J. Clim.*, **20,** 3284-3299,doi: 10.1175/JCLI4149.1.

Barth, N. and C. Wunsch, 1990: Oceanographic experiment design by simulated annealing. *J. Phys. Oceanogr.*, **20,** 1249-1263,doi: 10.1175/1520-0485(1990)020<1249:OEDBSA>2.0.CO;2.

Beardsley, R. C. and W. C. Boicourt, 1981: On estuarine and continental shelf circulation in the Middle Atlantic Bight. *Evolution of Physical Oceanography*, B. A. Warren and C. Wunsch, Eds., The MIT Press, 198-223.

Bennett, A. F., 1990: Inverse methods for assessing ship-of-opportunity networks and estimating circulation and winds from tropical expendable bathythermograph data. *J. Geophys. Res.*, **95,** 16,111-16,148

——, 2002: *Inverse Modeling of the Ocean and Atmosphere*. Cambridge University Press, 234 pp.

Bergot, T., 1999: daptive observations during FASTEX : A systematic survey of upstream flights. *Q. J. R. Meteorol. Soc.*, **125,** 3271-3298

Berliner, L. M., Z.-Q. Lu, and C. Snyder, 1999: Statistical design for adaptive weather observations. *J. Atmos. Sci.*, **56,** 2536-2552,DOI: 10.1175/1520-0469(1999)056<2536:SDFAWO>2.0.CO;2.

Bertsekas, D. P., 1982: *Constrained optimization and Lagrange multiplier methods*. Academic Press, 395 pp.

Bishop, C. H. and Z. Toth, 1999: Ensemble transformation and adaptive observations. *J. Atmos. Sci.*, **56,** 1748-1765,10.1175/1520-0469(1999)056<1748:ETAAO>2.0.CO;2.

Bishop, C. H., B. J. Etherton, and S. J. Majumdar, 2001: Adaptive sampling with the Ensemble Transform Kalman Filter. Part I: theoretical aspects. *Mon. Weather Rev.*, **129,** 420-436,doi: 10.1175/1520-0493(2001)129<0420:ASWTET>2.0.CO;2.

Brooks, D. A., M. W. Baca, and Y.-T. Lo, 1999: Tidal circulation and residence time in a macrotidal estuary: Cobscook Bay, Maine. *Est. Coast. Shelf Sci.*, **49,** 647-665

Broquet, G., C. A. Edwards, A. M. Moore, B. S. Powell, M. Veneziani, and J. D. Doyle, 2009: Application of 4D-Variational data assimilation to the California Current System. *Dyn. Atmos. Oceans***,** in press

Cahill, B., O. Schofield, R. Chant, J. Wilkin, E. Hunter, S. Glenn, and P. Bissett, 2008: Dynamics of turbid buoyant plumes and the feedbacks on near-shore biogeochemistry and physics. *Geophys. Res. Lett.*, **35,** L10605, doi:10.1029/2008GL033595

Castelao, R. M., O. Schofield, S. Glenn, R. J. Chant, and J. Kohut, 2008a: Cross-shelf transport of fresh water on the New Jersey Shelf. *J. Geophys. Res.*, **113,** C07017,doi:10.1029/2007JC004241.

Castelao, R. M., S. Glenn, O. Schofield, R. J. Chant, J. Wilkin, and J. Kohut, 2008b: Seasonal evolution of hydrographic fields in the central Middle Atlantic Bight from glider observations. *Geophys. Res. Lett.*, **35,** L03617, doi:10.1029/2007GL032335

Chant, R. J., 2001: Evolution of near-inertial waves during an upwelling event on the New Jersey inner shelf. *J. Phys. Oceanogr.*, **31,** 746-764

Chant, R. J., S. Glenn, and J. Kohut, 2004: Flow reversals during upwelling conditions on the New Jersey inner shelf. *J. Geophys. Res.*, **109,** C12S03, doi:10.1029/2003JC001941.

Chant, R. J., W. R. Geyer, R. Houghton, E. Hunter, and J. Lerczak, 2007: Estuarine Boundary Layer Mixing Processes: Insights from Dye Experiments. *J. Phys. Oceanogr.*, **37,** 1859-1877

Chant, R. J., S. M. Glenn, E. Hunter, J. Kohut, R. F. Chen, R. W. Houghton, J. Bosch, and O. Schofield, 2008a: Bulge formation of a buoyant river flow. *J. Geophys. Res.*, **113,** C01017, doi:10:1029/2007JC004100

Chant, R. J., J. Wilkin, W. Zhang, B.-J. Choi, E. Hunter, R. Castelao, S. M. Glenn, J. Jurisa, O. Schofield, R. Houghton, J. Kohut, T. K. Frazer, and M. A. Moline, 2008b: Dispersal of the Hudson River Plume in the New York Bight: synthesis of observational and numerical studies during LaTTE. *Oceanography*, **21,** 148-161

Chapman, D. C., 1985: Numerical treatment of cross-shelf open boundaries in a barotropic ocean model. *J. Phys. Oceanogr.*, **15,** 1060-1075

Chapman, D. C. and R. C. Beardsley, 1989: On the origin of shelf water in the Middle Atlantic Bight. *J. Phys. Oceanogr.*, **19,** 384-391

Choi, B.-J. and J. L. Wilkin, 2007: The effect of wind on the dispersal of the Hudson River plume. *J. Phys. Oceanogr.*, **37,** 1878-1897

Ciotti, Á. M., C. Odebrecht, G. Fillmann, and O. O. Möller, 1995: Freshwater outflow and Subtropical Convergence influence on phytoplankton biomass on the southern Brazilian continental shelf. *Cont. Shelf Res.*, **15,** 1737-1756

Courtier, P., 1997: Dual formulation of four-dimensional variational assimilation. *Q. J. R. Meteorol. Soc.*, **123,** 2449-2461

Courtier, P., J.-N. Thépaut, and A. Hollingsworth, 1994: A strategy for operational implementation of 4DVAR using an incremental approach. *Q. J. R. Meteorol. Soc.*, **120,** 1367-1388

Deleersnijder, E., J.-M. Campin, and E. J. M. Delhez, 2001: The concept of age in marine modelling: I. Theory and preliminary model results. *J. Mar. Syst.*, **28,** 229-267

Delhez, E. J. M., 2006: Transient residence and exposure time. *Ocean Sci.*, **2,** 1-9

Delhez, E. J. M. and E. Deleersnijder, 2006: The boundary layer of the residence time field. *Ocean Dynam.*, **56,** 139-150,doi:10.1007/s10236-006-0067-0.

Delhez, E. J. M., A. W. Heemink, and E. Deleersnijder, 2004: Residence time in a semi-enclosed domain from the solution of an adjoint problem. *Est. Coast. Shelf Sci.*, **61,** 691-702

Delhez, E. J. M., J.-M. Campin, A. C. Hirst, and E. Deleersnijder, 1999: Toward a general theory of the age in ocean modeling. *Ocean Model.*, **1,** 17-27

Delhez, E. J. M., E. Deleersnijder, A. Mouchet, and J.-M. Beckers, 2003: A note on the age of radioactive tracers. *J. Mar. Syst.*, **38,** 277-286

Derber, J. and F. Bouttier, 1999: A reformulation of the background error covariance in the ECMWF global data assimilation system. *Tellus A*, **51,** 195-221

Di Lorenzo, E., A. M. Moore, H. G. Arango, B. D. Cornuelle, A. J. Miller, B. Powell, B. S. Chua, and A. Bennett, 2007: Weak and strong constraint data assimilation in the inverse Regional Ocean Modeling System (ROMS): development and application for a baroclinic coastal upwelling system. *Ocean Model.*, **16,** 160-187

Duarte, A. S., J. L. Pinho, M. A. Pardal, J. M. Neto, J. P. Vieira, and F. S. Santos, 2001: Effect of residence times on River Mondego estuary eutrophication vulnerability. *Water Sci. Technol.*, **44,** 329-336

Dutkiewicz, S., M. Heimbach, M. Follows, and J. Marshall, 2006: Controls on ocean productivity and air-sea carbon flux: an adjoint model sensitivity study. *Geophys. Res. Lett.*, **33,** L02603, 10.1029/2005GL024987

Egbert, G. D. and S. Y. Erofeeva, 2002: Efficient inverse modeling of barotropic ocean tides. *J. Atmos. Oceanic Technol.*, **19,** 183-204,10.1175/1520-0426(2002)019<0183:EIMOBO>2.0.CO;2.

England, M. H., 1995: The age of water and ventilation timescales in a global ocean model. *J. Phys. Oceanogr.*, **25,** 2756-2777

Errico, R. M., 1997: What is an adjoint model? *Bull. Am. Meteorol. Soc.*, **78,** 2577-2591

Errico, R. M. and T. Vukicevic, 1992: Sensitivity analysis using an Adjoint of the PSU-NCAR mesoscale model. *Mon. Weather Rev.*, **120,** 1644-1660

Evensen, G., 2007: *Data Assimilation: The Ensemble Kalman Filter*. Springer, 208 pp.

Fairall, C. W., E. F. Bradley, J. E. Hare, A. A. Grachev, and J. Edson, 2003: Bulk Parameterization of Air–Sea Fluxes: Updates and Verification for the COARE Algorithm. *J. Clim.*, **16,** 571-591

Farrell, B. F. and A. M. Moore, 1992: An adjoint method for obtaining the most rapidly growing perturbation to oceanic flows. *J. Phys. Oceanogr.*, **22,** 338-349

Fennel, K., J. Wilkin, J. Levin, J. Moisan, J. O'Reilly, and D. Haidvogel, 2006: Nitrogen cycling in the Middle Atlantic Bight: Results from a three-dimensional model and implications for the North Atlantic nitrogen budget. *Global Biogeochem. Cy.*, **20,** doi:10.1029/2005GB002456

Fine, R. A., 1995: Tracers, timescales, and the thermohaline circulation: the lower limb in the North Atlantic Ocean. *Rev. Geophys.*, **33 Suppl.,** 1353-1365

Flather, R. A., 1976: A tidal model of the northwest European continental shelf. *Mem. Soc. Roy. Sci. Liege, Ser. 6*, **10,** 141-164

Fong, D. A. and W. R. Geyer, 2001: Response of a river plume during an upwelling favorable wind event. *J. Geophys. Res.*, **106,** 1067-1084

——, 2002: The alongshore transport of freshwater in a surface-trapped river plume. *J. Phys. Oceanogr.*, **32,** 957-972

Frolov, S., A. Baptista, and M. Wilkin, 2008: Optimizing fixed observational assets in a coastal observatory. *Cont. Shelf Res.*, **28,** 2644-2658,doi: 10.1016/j.csr.2008.08.009.

Galanti, E. and E. Tziperman, 2003: A Midlatitude-ENSO Teleconnection Mechanism via Baroclinically Unstable Long Rossby Waves. *J. Phys. Oceanogr.*, **33,** 1877-1888

Gao, Y., H. Drange, M. Bentsen, and O. M. Johannessen, 2005: Tracer-derived transit time of the waters in the eastern Nordic Seas. *Tellus*, **57B,** 332-340

García Berdeal, I., B. M. Hickey, and M. Kawase, 2002: Influence of wind stress and ambient flow on a high discharge river plume. *J. Geophys. Res.*, **107,** 3130, doi:10.1029/2001JC000932,doi:10.1029/2001JC000932.

Garvine, R. W., 1999: Penetration of buoyant coastal discharge onto the continental shelf: a numerical model experiment. *J. Phys. Oceanogr.*, **29,** 1892-1909

——, 2004: The vertical structure and subtidal dynamics of the inner shelf off New Jersey. *J. Mar. Res.*, **62,** 337-371,doi:10.1357/0022240041446182.

Garvine, R. W. and M. M. Whitney, 2006: An estuarine box model of freshwater delivery to the coastal ocean for use in climate models. *J. Mar. Res.*, **64,** 173-194

Geyer, W. R., J. D. Woodruff, and P. Traykovski, 2001: Sediment transport and trapping in the Hudson River Estuary. *Estuaries*, **24,** 670-679

Glenn, S. M. and O. Schofield, 2003: Observing the oceans from the COOLroom: Our history, experience. *Oceanography*, **16,** 37-52

Hackert, E. C., R. N. Miller, and A. J. Busalacchi, 1998: An optimized design for a moored instrument array in the tropical Atlantic Ocean. *J. Geophys. Res.*, **103,** 7491-7509

Haidvogel, D. B., H. Arango, W. B. Budgell, B. D. Cornuelle, E. Curchitser, E. Di Lorenzo, K. Fennel, W. R. Geyer, A. J. Hermann, L. Lanerolle, J. Levin, J. C. McWilliams, A. J. Miller, A. M. Moore, T. M. Powell, A. F. Shchepetkin, C. R. Sherwood, R. P. Signell, J. C. Warner, and J. Wilkin, 2008: Ocean forecasting in terrain-following coordinates: formulation and skill assessment of the regional ocean modeling system. *J. Comput. Phys.*, **227,** 3595-624

Haine, T. W. N. and T. M. Hall, 2002: A generalized transport theory: water-mass composition and age. *J. Phys. Oceanogr.*, **32,** 1932-1946

Haine, T. W. N., A. J. Watson, M. I. Liddicoat, and R. R. Dickson, 1998: The flow of Antarctic bottom water to the southwest Indian Ocean estimated using CFCs. *J. Geophys. Res.*, **103,** 27637-27653

Hall, T. M. and R. A. Plumb, 1994: Age as a diagnostic of stratospheric transport. *J. Geophys. Res.*, **99,** 1059-1070

Hall, T. M. and T. W. N. Haine, 2002: On ocean transport diagnostics: the idealized age tracer and the age spectrum. *J. Phys. Oceanogr.*, **32,** 1987-1991

Harris, C. K., B. Butman, and P. Traykovski, 2003: Winter-time circulation and sediment transport in the Hudson Shelf Valley. *Cont. Shelf Res.*, **23,** 801-820

Hickey, B., S. Geier, N. Kachel, and A. MacFadyen, 2005: A bi-directional river plume: The Columbia in summer. *Cont. Shelf Res.*, **25,** 1631-1656

Hill, C., V. Bugnion, M. Follows, and J. Marshall, 2004: Evaluating carbon sequestration efficiency in an ocean circulation model by adjoint sensitivity analysis. *J. Geophys. Res.*, **109,** C11005, doi:10.1029/2002JC001598

Hoffman, R. N., R. M. Ponte, E. J. Kostelich, A. Blumberg, I. Szunyogh, S. V. Vinogradov, and J. M. Henderson, 2008: A simulation study using a local ensemble transform Kalman filter for data assimilation in New York Harbor. *J. Atmos. Oceanic Technol.*, **25,** 1638-1656,10.1175/2008jtecho565.1.

Hofmann, E., J.-N. Druon, K. Fennel, M. Friedrichs, D. Haidvogel, C. Lee, A. Mannino, C. McClain, R. Najjar, J. O'Reilly, D. Pollard, M. Previdi, S. Seitzinger, J. Siewert, S. Signorini, and J. Wilkin, 2008: Eastern US continental shelf carbon budget, Integrating models, data assimilation, and analysis. *Oceanography*, **21,** 86-104

Hohmann, R., M. Hofer, R. Kipfer, F. Peeters, D. M. Imboden, H. Baur, and M. N. Shimaraev, 1998: Distribution of helium and tritium in Lake Baikal. *J. Geophys. Res.*, **103,** 12823-12838

Holzer, M. and T. M. Hall, 2000: Transit-time and tracer-age distributions in geophysical flows. *J. Atmos. Sci.*, **57,** 3539-3558

Hoteit, I. and A. Köhl, 2006: Efficiency of reduced-order, time-dependent adjoint data assimilation approaches. *J. Oceanogr.*, **62,** 539-550

Howarth, R. W., R. Marino, D. P. Swaney, and E. W. Boyer, 2006: Wastewater and watershed influences on primary productivity and oxygen dynamics in the lower Hudson River estuary. *The Hudson River Estuary*, J. S. Levington and J. R. Waldman, Eds., Cambridge University Press, 121-139.

Jenkins, W. J., 1987: ^{3}H and ^{3}He in the Beta Triangle: Observations of Gyre ventilation and oxygen utilization rates. *J. Phys. Oceanogr.*, **17,** 763-783

Johnson, D. R., J. Miller, and O. Schofield, 2003: Dynamics and optics of the Hudson River outflow plume. *J. Geophys. Res.*, **108,** 3323, doi:10.1029/2002JC001485

Junge, M. M. and T. W. N. Haine, 2001: Mechanisms of North Atlantic Wintertime Sea Surface Temperature Anomalies. *J. Clim.*, **14,** 4560-4572

Kaiser, M. J. and A. G. Pulsipher, 2004: The potential value of improved ocean observation systems in the Gulf of Mexico. *Mar. Policy*, **28,** 469-489,doi: 10.1016/j.marpol.2003.11.002.

Khatiwala, S., 2007: A computational framework for simulation of biogeochemical tracers in the ocean. *Global Biogeochem. Cy.*, **21,** GB3001,doi:10.1029/2007GB002923.

Köhl, A. and D. Stammer, 2004: Optimal observations for variational data assimilation. *J. Phys. Oceanogr.*, **34,** 529-542

Kohut, J., S. Glenn, and R. J. Chant, 2004: Seasonal current variability on the New Jersey inner shelf. *J. Geophys. Res.*, **109,** C07S07, doi: 10.1029/2003JC001963

Kohut, J. T., S. M. Glenn, and D. E. Barrick, 2001: multiple HF-radar system development for a regional longterm ecosystem observatory in the New York Bight. *American Meteorological Society: Fifth Symposium on Integrated Observing Systems*, Albuquerque, New Mexco, 4-7.

Kohut, J. T., H. J. Roarty, and S. M. Glenn, 2006a: Characterizing Observed Environmental Variability with HF Doppler Radar Surface Current Mappers and Acoustic Doppler Current Profilers: Environmental Variability in the Coastal Ocean. *IEEE J. Oceanic Eng.*, **31,** 876-884

Kohut, J. T., S. M. Glenn, and J. Paduan, 2006b: The inner-shelf response to tropical storm Floyd. *J. Geophys. Res.*, **111,** C09S91,doi: 10.1029/2003JC002173.

Kurapov, A. L., G. D. Egbert, J. S. Allen, and R. N. Miller, 2007: Representer-based variational data assimilation in a nonlinear model of nearshore circulation. *J. Geophys. Res.*, **112,** C11019,doi: 10.1029/2007JC004117.

——, 2009: Representer-based analyses in the coastal upwelling system. *Dyn. Atmos. Oceans***,** in press,doi:10.1016/j.dynatmoce.2008.09.002.

Lanczos, C., 1961: *Linear Differential Operators*. D. Van Nostrand Company Ltd.

Langland, R. H., 2005: Issues in targeted observations. *Q. J. R. Meteorol. Soc.*, **131,** 3409-3425,doi: 10.1256/qj.05.130.

Langland, R. H. and N. L. Baker, 2004: Estimation of observation impact using the NRL atmospheric variational data assimilation adjoint system. *Tellus A*, **56,** 189-201,doi: 10.1111/j.1600-0870.2004.00056.x.

Lentz, S. J., 2008: Observations and a model of the mean circulation over the Middle Atlantic Bight continental shelf. *J. Phys. Oceanogr.***,** 1203-1221

Lentz, S. J. and D. C. Chapman, 2004: The importance of nonlinear cross-shelf momentum flux during wind-driven coastal upwelling. *J. Phys. Oceanogr.*, **34,** 2444-57

Lerczak, J. A., W. R. Geyer, and R. J. Chant, 2006: Mechanisms Driving the Time-Dependent Salt Flux in a Partially Stratified Estuary&#042. *J. Phys. Oceanogr.*, **36,** 2296-2311

Leutbecher, M., 2003: A reduced rank estimate of forecast error variance changes due to intermittent modification of the observing network. *J. Atmos. Sci.*, **60,** 729-742,10.1175/1520-0469(2003)060<0729:ARREOF>2.0.CO;2.

Lewis, J. K., I. Shulman, and A. F. Blumberg, 1998: Assimilation of Doppler radar current data into numerical ocean models. *Cont. Shelf Res.*, **18,** 541-559

Lewis, J. M., K. D. Raeder, and R. M. Errico, 2001: Vapor flux associated with return flow over the Gulf of Mexico: a sensitivity study using adjoint modeling. *Tellus A*, **53,** 74-93, doi:10.1034/j.1600-0870.2001.01108.x

Li, X. and C. Wunsch, 2004: An adjoint sensitivity study of chlorofluorocarbons in the North Atlantic. *J. Geophys. Res.***,** C01007, doi:10.1029/2003JC002014

Li, Z., Y. Chao, J. C. McWilliams, and K. Ide, 2008: A three-dimensional variational data assimilation scheme for the Regional Ocean Modeling System: implementation and basic experiments. *J. Geophys. Res.*, **113,** C05002,doi: 10.1029/2006JC004042.

Losch, M. and P. Heimbach, 2007: Adjoint Sensitivity of an Ocean General Circulation Model to Bottom Topography. *J. Phys. Oceanogr.*, **37,** 377-393

Lueck, R. G., 1990: Thermal inertia of conductivity cells: theory. *J. Atmos. Oceanic Technol.*, **7,** 741-755

Madsen, O. S., 1977: A realistic model of the wind-induced Ekman boundary layer. *J. Phys. Oceanogr.*, **7,** 248-255

Malone, T. C. and M. B. Chervin, 1979: The production and fate of phytoplankton size fractions in the plume of the Hudson River, New York Bight. *Limnol. Oceanogr.*, **24,** 683-696

Manning, J. P., L. Y. Oey, D. Packer, J. Vitaliano, T. W. Finneran, K. W. You, and S. Fromm, 1994: Observations of bottom currents and estimates of resuspended sediment transport at the New York Bight 12-mile dumpsite. *J. Geophys. Res.*, **99,** 10,221-10,239

Marotzke, J., R. Giering, Q. K. Zhang, D. Stammer, C. N. Hill, and T. Lee, 1999: Construction of the adjoint MIT ocean general circulation model and application to Atlantic heat transport sensitivity. *J. Geophys. Res.*, **104,** 29,529-29,548

Mayer, D. A., G. C. Han, and D. V. Hansen, 1982: Circulation in the Hudson Shelf Valley: MESA physical oceanographic studies in New York Bight, 1. *J. Geophys. Res.*, **87,** 9563-9578

McIntosh, P. C., 1987: Systematic design of observational array. *J. Phys. Oceanogr.*, **17,** 885-902,doi: 10.1175/1520-0485(1987)017<0885:SDOOA>2.0.CO;2.

Mesinger, F., G. DiMego, E. Kalnay, K. Mitchell, P. C. Shafran, W. Ebisuzaki, D. Jovi, an, J. Woollen, E. Rogers, E. H. Berbery, M. B. Ek, Y. Fan, R. Grumbine, W. Higgins, H. Li, Y. Lin, G. Manikin, D. Parrish, and W. Shi, 2006: North American Regional Reanalysis. *Bull. Am. Meteorol. Soc.*, **87,** 343-360

Moline, M. A., T. K. Frazer, R. J. Chant, S. Glenn, C. Jacoby, J. R. Reinfelder, J. Yost, M. Zhou, and O. M. Schofield, 2008: Biological responses in a dynamic, buoyant river plume. *Oceanography*, **21,** 70-89

Monsen, N. E., J. E. Cloern, L. V. Lucas, and S. G. Monismith, 2002: A comment on the use of flushing time, residence time, and age as transport time scales. *Limnol. Oceanogr.*, **47,** 1545-1553

Moore, A. M. and B. F. Farrell, 1993: Rapid perturbation growth on spatially and temporally varying oceanic flows determined using an adjoint method: application to the Gulf Stream. *J. Phys. Oceanogr.*, **23,** 1682-1702

Moore, A. M., H. G. Arango, E. Di Lorenzo, A. J. Miller, and B. D. Cornuelle, 2008: An adjoint sensitivity analysis of the Southern California Current circulation and ecosystem. Part I: The physical circulation. *J. Phys. Oceanogr.*, in press

Moore, A. M., H. G. Arango, E. Di Lorenzo, B. D. Cornuelle, A. J. Miller, and D. J. Neilson, 2004: A Comprehensive Ocean Prediction and Analysis System Based on the Tangent Linear and Adjoint of a Regional Ocean Model. *Ocean Model.*, **7,** 227-258

Morison, J., R. Andersen, N. Larson, E. D'Asaro, and T. Boyd, 1994: The correction for thermal-lag effects in Sea-Bird CTD data. *J. Atmos. Oceanic Technol.*, **11,** 1151-1164

Mountain, D. G., 2003: Variability in the properties of Shelf Water in the Middle Atlantic Bight, 1977–1999. *J. Geophys. Res.*, **108,** 3014,doi:10.1029/2001JC001044.

Mukai, A. Y., J. J. Westerink, R. A. Luettich, and D. Mark, 2002: Eastcoast 2001, A tidal constituent database for the western North Atlantic, Gulf of Mexico and Caribbean Sea, Tech. Rep. ERDC/CHL TR-02-24, 196 pp.

Münchow, A. and R. J. Chant, 2000: Kinematics of inner shelf motion during the summer stratified season off New Jersey. *J. Phys. Oceanogr.*, **30,** 247-268

Murphy, A. H., 1992: Climatology, persistence, and their linear combination as standards of reference in skill scores. *Weather Forecast.*, **7,** 692-698

Nelson, T. A., P. E. Gadd, and T. L. Clarke, 1978: Wind-induced current flow in the upper Hudson Shelf Valley. *J. Geophys. Res.*, **83,** 6073-6082

Ngodock, H. E., S. R. Smith, and G. A. Jacobs, 2007: Cycling the representer algorithm for variational data assimilation with a nonlinear reduced gravity ocean model. *Ocean Model.*, **19,** 101-111

Nof, D. and T. Pichevin, 2001: The ballooning of outflows. *J. Phys. Oceanogr.*, **31,** 3045-3058

Oke, P. R. and A. Schiller, 2007: A model-based assessment and design of a tropical Indian Ocean mooring Array. *J. Clim.*, **20,** 3269-3283,doi: 10.1175/JCLI4170.1.

Oke, P. R., J. S. Allen, R. N. Miller, G. D. Egbert, and P. M. Kosro, 2002: Assimilation of surface velocity data into a primitive equation coastal ocean model. *J. Geophys. Res.*, **107,** 3122,doi:10.1029/2000JC000511.

Orlanski, I., 1976: A simple boundary condition for unbounded hyperbolic flows. *J. Comput. Phys.*, **21,** 251-269

Palmer, T. N., R. Gelaro, J. Barkmeijer, and R. Buizza, 1998: Singular Vectors, Metrics, and Adaptive Observations. *J. Atmos. Sci.*, **55,** 633–653

Parrish, D. F. and J. C. Derber, 1992: The National Meteorological Center's Spectral Statistical-Interpolation Analysis System. *Mon. Weather Rev.*, **120,** 1747-1763

Powell, B. S. and A. M. Moore, 2008: Estimating the 4DVAR analysis error of GODAE products. *Ocean Dynam.***,** in press,doi: 10.1007/s10236-008-0172-3.

Powell, B. S., H. G. Arango, A. M. Moore, E. Di Lorenzo, R. F. Milliff, and D. Foley, 2008: 4DVAR data assimilation in the Intra-Americas Sea with the Regional Ocean Modeling System (ROMS). *Ocean Model.*, **25,** 173-188,doi: 10.1016/j.ocemod.2008.08.002.

Powell, B. S., A. M. Moore, H. Arango, E. Di Lorenzo, R. Milliff, and R. R. Leben, 2009: Near real-time assimilation and prediction in the Intra-Americas Sea with the Regional Ocean Modeling System (ROMS). *Dyn. Atmos. Oceans***,** In press

Rabier, F., P. Gauthier, C. Cardinali, R. Langland, M. Tsyrulnikov, A. Lorenc, P. Steinle, R. Gelaro, and K. Koizumi, 2008: An update on THORPEX-related research in data assimilation and observing strategies. *Nonlin. Processes Geophys.*, **15,** 81-94

Ramadurai, R., 2008: Water mass classification using band ratios, Institute of Marine and Coastal Sciences, Rutgers, The State University of New Jersey, 101.

Rutledge, G. K., J. Alpert, and W. Ebisuzaki, 2006: NOMADS: A climate and weather model archive at the National Oceanic and Atmospheric Administration. *Bull. Am. Meteorol. Soc.*, **87,** 327-341

Sakov, P. and P. R. Oke, 2008: Objective array design: application to the tropical Indian Ocean. *J. Atmos. Oceanic Technol.*, **25,** 794-807,doi: 10.1175/2007JTECHO553.1.

Santer, B. D., T. M. L. Wigley, and P. D. Jones, 1993: Correlation methods in fingerprint detection studies. *Clim. Dynam.*, **8,** 265-276

Sarmiento, J. L., G. Thiele, R. M. Key, and W. S. Moore, 1990: Oxygen and Nitrate new production and remineralization in the North Atlantic subtropical gyre. *J. Geophys. Res.*, **95,** 18303-18315

Schlosser, P., J. L. Bullister, R. A. Fine, W. J. Jenkins, R. Key, J. Lupton, W. Roether, and W. M. Smethie Jr., 2001: Transformation and age of water masses. *Ocean Circulation and Climate*, G. Siedler, J. Church, and J. Gould, Eds., Academic, 431-454.

Schofield, O., J. Kohut, and S. M. Glenn, 2008a: Evolution of coastal observing networks. *Sea Technology*, **49,** 31-36

Schofield, O., J. Bosch, S. M. Glenn, G. Kirkpatrick, J. Kerfoot, M. A. Moline, M. Oliver, and P. Bissett, 2007: Bio-optics in integrated ocean observing networks: potential for studying harmful algal blooms. *Real Time Coastal Observing Systems for Ecosystem Dynamics and Harmful Algal Blooms*, M. Babin, C. Roesler, and J. J. Cullen, Eds., UNESCO, 85-108.

Schofield, O., R. Chant, B. Cahill, R. Castelao, D. Gong, A. Kahl, J. Kohut, M. Montes-Hugo, R. Ramadurai, P. Ramey, Y. Xu, and S. M. Glenn, 2008b: The decadal view of the Mid-Atlantic Bight from the COOLroom: Is our coastal system changing? *Oceanography*, **21,** 108-117

Schofield, O. M., M. A. Moline, B. Cahill, T. K. Frazer, E. Hunter, A. Kahl, M. Oliver, J. R. Reinfelder, S. Glenn, and R. J. Chant, 2009: Regulation of primary productivity in the turbid Hudson River plume. *J. Geophys. Res.***,** in revision

Scott, R. K., J. S. Allen, G. D. Egbert, and R. N. Miller, 2000: Assimilation of surface current measurements in a coastal ocean model. *J. Phys. Oceanogr.*, **30,** 2359-2378

Shchepetkin, A. F. and J. C. McWilliams, 1998: Quasi-monotone advection schemes based on explicit locally adaptive diffusion. *Mon. Weather Rev.*, **126,** 1541-1580

——, 2003: A Method for Computing Horizontal Pressure-Gradient Force in an Oceanic Model with a Non-Aligned Vertical Coordinate. *J. Geophys. Res.*, **108,** 3090, doi:10.1029/2001JC001047

——, 2005: The regional oceanic modeling system (ROMS): a split-explicit, free-surface, topography-following-coordinate oceanic model. *Ocean Model.*, **9,** 347-404

Shulman, I., D. J. McGillicuddy, M. A. Moline, S. H. D. Haddock, J. C. Kindle, D. Nechaev, and M. W. Phelps, 2005: Bioluminescence intensity modeling and sampling strategy optimization. *J. Atmos. Oceanic Technol.*, **22,** 1267-1281,doi: 10.1175/JTECH1760.1.

Smith, S. R. and H. E. Ngodock, 2008: Cycling the Representer Method for 4D-variational data assimilation with the Navy Coastal Ocean Model. *Ocean Model.*, **24,** 92-107,10.1016/j.ocemod.2008.05.008.

Stammer, D., K. Ueyoshi, A. Köhl, W. G. Large, S. A. Josey, and C. Wunsch, 2004: Estimating air-sea fluxes of heat, freshwater, and momentum through global ocean data assimilation. *J. Geophys. Res.*, **109,** C05023,doi: 10.1029/2003JC002082.

Stammer, D., C. Wunsch, R. Giering, C. Eckert, P. Heimbach, J. Marotzke, A. Adcroft, C. N. Hill, and J. Marshall, 2002: Global ocean circulation during 1992-1997, estimated from ocean observations and a general circulation model. *J. Geophys. Res.*, **107,** 3118,doi: 10.1029/2001JC000888.

——, 2003: Volume, heat, and freshwater transport of the global ocean circulation 1993-2000, estimated from a general circulation model constrained by World Ocean Circulation Experiment (WOCE) data. *J. Geophys. Res.*, **108,** 3007,doi: 10.1029/2001JC001115.

Stewart, R. H. and J. W. Joy, 1974: HF radio measurements of surface currents. *Deep-Sea Res.*, **21,** 1039-1049

Talagrand, O. and P. Courtier, 1987: Variational assimilation of meteorological observations with adjoint vorticity equation. I: Theory. *Q. J. R. Meteorol. Soc.*, **113,** 1321-1328

Thiele, G. and J. L. Sarmiento, 1990: Tracer dating and ocean ventilation. *J. Geophys. Res.*, **95,** 9377-9391

Tilburg, C. E. and R. W. Garvine, 2003: Three-dimensional flow in a coastal upwelling zone: Convergence and divergence on the New Jersey Shelf. *J. Phys. Oceanogr.*, **33,** 2113-2115,doi:10.1175/1520-0485(2003)033<2113:TFIASC>2.0.CO;2.

Tilburg, C. E., J. T. Reager, and M. M. Whitney, 2005: The physics of blue crab larval recruitment in Delaware Bay: A model study. *J. Mar. Res.*, **63,** 471-495

U. S. Geological Survey, 2007: Water-resources data for the United States, Water Year 2006: U.S. Geological Survey Water-Data Report WDR-US-2006, accessed April 1, 2007, http://pubs.water.usgs.gov/wdr2006.

Umlauf, L. and H. Burchard, 2003: A generic length-scale equation for geophysical turbulence models. *J. Mar. Res.*, **61,** 235-265

van Leeuwen, P. J. and G. Evensen, 1996: Data assimilation and inverse methods in terms of a probabilistic formulation. *Mon. Weather Rev.*, **124,** 2898-2913

van Oldenborgh, G. J., G. Burgers, S. Venzke, C. Eckert, and R. Giering, 1999: Tracking Down the ENSO Delayed Oscillator with an Adjoint OGCM. *Mon. Weather Rev.*, **127,** 1477-1496

Veneziani, M., C. A. Edwards, and A. M. Moore, 2009: A Central California coastal ocean modeling study. Part II: Adjoint sensitivities to local and remote driving mechanisms. *J. Geophys. Res.***,** In press

Vialard, J., A. T. Weaver, D. L. T. Anderson, and P. Delecluse, 2003: Three- and four-dimensional variational assimilation with a general circulation model of the tropical Pacific Ocean. Part II: Physical validation. *Mon. Weather Rev.*, **131,** 1379-1395

Vossepoel, F. C., A. T. Weaver, J. Vialard, and P. Delecluse, 2004: Adjustment of near-equatorial wind stress with four-dimensional variational data assimilation in a model of the Pacific Ocean. *Mon. Weather Rev.*, **132,** 2070-2083

Warner, J. C., C. R. Sherwood, H. G. Arango, R. P. Signell, and B. Butman, 2005: Performance of four turbulence closure models implemented using a generic length scale method. *Ocean Model.*, **8,** 81-113

Waugh, D. W., T. M. Hall, and T. W. N. Haine, 2003: Relationships among tracer ages. *J. Geophys. Res.*, **108,** 3138,doi:10.1029/2002JC001325.

Weaver, A. T. and P. Courtier, 2001: Correlation modelling on the sphere using a generalized diffusion equation. *Q. J. R. Meteorol. Soc.*, **127,** 1815-1846

Weaver, A. T., J. Vialard, and D. L. T. Anderson, 2003: Three- and four-dimensional variational assimilation with an ocean general circulation model of the tropical Pacific

Ocean. Part 1: Formulation, internal diagnostics and consistency checks. *Mon. Weather Rev.*, **131,** 1360-1378

Weaver, A. T., C. Deltel, E. Machu, S. Ricci, and N. Daget, 2005: A multivariate balance operator for variational ocean data assimilation. *Q. J. R. Meteorol. Soc.*, **131,** 3605-3625,doi: 10.1256/qj.05.119

Weiss, R. F., E. C. Carmack, and V. M. Koropalov, 1991: Deep-water renewal and biological production in Lake Baikal. *Nature*, **349,** 665-669,doi:10.1038/349665a0.

Wilkin, J. L., H. G. Arango, D. B. Haidvogel, C. S. Lichtenwalner, S. M. Glenn, and K. S. Hedström, 2005: A Regional Ocean Modeling System for the Long-term Ecosystem Observatory. *J. Geophys. Res.*, **110,** doi:10.1029/2003JC002218,doi:10.1029/2003JC002218.

Wong, K. C., 1999: The wind driven currents on the Middle Atlantic Bight inner shelf. *Cont. Shelf Res.*, **19,** 757-773,doi: 10.1016/S0278-4343(98)00107-1.

Wu, C.-C., J.-H. Chen, P.-H. Lin, and K.-H. Chou, 2007: Targeted observations of tropical cyclone movement based on the Adjoint-Derived Sensitivity Steering Vector. *J. Atmos. Sci.*, **64,** 2611-2626,doi: 10.1175/JAS3974.1.

Wunsch, C., 2002: Oceanic age and transient tracers: Analytical and numerical solutions. *J. Geophys. Res.*, **107,** 3048,doi:10.1029/2001JC000797.

——, 2006: *Discrete inverse and state estimation problems with geophysical fluid applications*. Cambridge University Press, 371 pp.

Wunsch, C. and P. Heimbach, 2007: Practical global oceanic state estimation. *Physica D*, **230,** 197-208,doi: 10.1016/j.physd.2006.09.040.

Yankovsky, A. E., 2003: The cold-water pathway during an upwelling event on the New Jersey shelf. *J. Phys. Oceanogr.*, **33,** 1954-1966,doi: 10.1175/1520-0485(2003)033<1954:TCPDAU>2.0.CO;2.

Yankovsky, A. E. and R. W. Garvine, 1998: Subinertial Dynamics on the Inner New Jersey Shelf during the Upwelling Season. *J. Phys. Oceanogr.*, **28,** 2444-2458

Yankovsky, A. E., R. W. Garvine, and A. Munchow, 2000: Mesoscale Currents on the Inner New Jersey Shelf Driven by the Interaction of Buoyancy and Wind Forcing. *J. Phys. Oceanogr.*, **30,** 2214-2230

Yelland, M. and P. K. Taylor, 1996: Wind Stress Measurements from the Open Ocean. *J. Phys. Oceanogr.*, **26,** 541-558

Curriculum Vita

Weifeng Zhang

EDUCATION

2003 – 2009 Institute of Marine and Coastal Sciences
Rutgers University, New Brunswick, NJ

Field: Physical Oceanography
Ph.D. awarded October 2009

1996 – 2003 Department of Engineering Mechanics
Zhejiang University, Hangzhou, Zhejiang Province, China

Field: Fluid Mechanics
M.S. awarded March 2003
B.E. awarded June 2000

PROFESSIONAL EXPERIENCES

2004 – 2009 Graduate Assistant
Institute of Marine and Coastal Sciences, Rutgers University

2005 Teaching Assistant, *Physical Oceanography*
Institute of Marine and Coastal Sciences, Rutgers University\

2003 – 2004 Graduate Fellow
Institute of Marine and Coastal Sciences, Rutgers University

PUBLICATIONS

Zhang, Weifeng, John Wilkin, 2009, Towards building an integrated observation and modeling system in the New York Bight using variational methods, Part II: representer-based observing system design, to be submitted to *Ocean Modelling*.

Zhang, Weifeng, John Wilkin, 2009, Towards building an integrated observation and modeling system in the New York Bight using variational methods, Part I: 4DVAR data assimilation, to be submitted to *Ocean Modelling*.

Zhang, Weifeng, John Wilkin, Oscar Schofield, 2009, Simulation of age and residence time in the New York Bight, *Journal of Physical Oceanography*, accepted with minor revisions.

Zhang, Weifeng, John Wilkin, Julia Levin, Hernan Arango, 2009, An Adjoint Sensitivity Study of Buoyancy- and Wind-driven Circulation on the New Jersey Inner Shelf, *Journal of Physical Oceanography*, 39, 1652-1668.

Zhang, Weifeng, John Wilkin, Robert Chant, 2009, Modeling of the pathways and mean dynamics of river plume dispersal in New York Bight, *Journal of Physical Oceanography*, 39, 1167-1183.

Chant, R. J., J. Wilkin, **W. Zhang**, B.-J. Choi, E. Hunter, R. Castelao, S. Glenn, J. Jurisa, O. Schofield, R. Houghton, J. Kohut, T.K. Frazer, and M.A. Moline, 2008, Dispersal of the Hudson River Plume in the New York Bight: synthesis of observational and numerical studies during LaTTE, *Oceanography*, 21(4): 148-161.

Wilkin, John, **Weifeng Zhang**, 2007, Modes of mesoscale sea surface height and temperature variability in the East Australian Current, *Journal of Geophysical Research*, 112, C01013, doi:10.1029/2006JC003590.

Zhang Shanliang, Lin Jianzhong, **Zhang Weifeng**, 2007, Numerical research on the fiber suspensions in a turbulent T-shaped branching channel flow, *Chinese Journal of Chemical Engineering*, 15(1), 30-38, doi:10.1016/S1004-9541(07)60030-5.

Lin Jianzhong, Zhang Lingxin, **Zhang Weifeng**, 2006, Pheological behavior of fiber suspensions in a turbulent channel flow, *Journal of Colloid and Interface Science*, 296(2): 721-728.

Zhang Lingxin, Lin Jianzhong, **Zhang Weifeng**, 2006, Theoretical model of particle orientation distribution function in a cylindrical particle suspension subject to turbulent shear flow, *Progress in Natural Science*, 16(1): 16-20.

Lin Jianzhong, Li Jun, **Zhang Weifeng**, 2005, Orientation distribution of fibres in a channel flow of fibre suspension, *Chinese Physics*, 14: 2529-2538, doi:10.1088/1009-1963/14/12/026.

Lin, Jianzhong, Wang Yelong, **Zhang Weifeng**, 2005, Sedimentation of short cylindrical pollutants with mechanical contacts, *Journal of Environmental Sciences*, 17(6): 906-911.

You, Zhenjiang, Lin, Jianzhong, Shao, Xueming, **Zhang, Weifeng**, 2004, Stability and drag reduction in transient channel flow of fibre suspension, *Chinese Journal of Chemical Engineerin*g, 12(3):319-323.

Lin, Jianzhong, Li, Jun, **Zhang, Weifeng**, 2004, The force for cylindrical particles in an elongational-shear flow, *International Journal of Nonlinear Sciences and Numerical Simulation*, 5(1): 9-16.

Lin, Jianzhong, **Zhang, Weifeng**, Yu, Zhaosheng, 2004, Numerical Research on the orientation distribution of fibers immersed in laminar and turbulent pipe flows, *Journal of Aerosol Science,* 35: 63-82.

Zhang, Weifeng, Lin, Jianzhong, 2004, Research on the Motion of Particles in the Turbulent Pipe Flow of Fiber Suspensions, *Applied Mathematics and Mechanics*, 25(7): 417-750.

Zhang, Weifeng, Lin, Jianzhong, 2003, Research on the Orientation of Cylindrical Particles in Gas-Solid Two-Phase Pipe Flows, *ACTA Aerodynamica Sinica* 21(2): 237-243. (In Chinese)

Lin, Jianzhong, **Zhang, Weifeng**, Wang, Yelong, 2002, Research on the orientation distribution of fibers immersed in a pipe flow, *Journal of Zhejiang University SCIENCE (English Edition)* 3(5): 501-506.